STRUCTURAL ANALYSIS OF RIBOSOMAL RESCUE COMPLEXES IN BACTERIA

Inaugural-Dissertation

to obtain the academic degree

Doctor rerum naturalium (Dr. rer. nat.)

submitted to the Department of Biology, Chemistry, Pharmacy

of Freie Universität Berlin

by

Annika Balke

2022

The present work was performed from Januar 2016 - Januar 2022 in the laboratories of Prof. Christian Spahn at the Institute of Medical Physics and Biophysics, Charité Berlin.

1st reviewer: Prof. Dr. Christian Spahn

2nd reviewer: Prof. Dr. Markus Wahl

Date of defense: 02.06.2022

Danksagung

My special thanks go to my thesis advisor Prof. Christian M.T. Spahn, in whose working group I was given the opportunity to do the work for this dissertation. Besides an excellent working environment, I would also like to thank for the helpful suggestions, discussions and especially, the great support in very challenging scientific situations.

I would like to thank Prof. Markus Wahl for the friendly communication and motivation to take over the second review of this thesis.

I would like to thank all colleagues of the AG Spahn and of the whole Institute of Medical Physics and biophysics for their practical and theoretical support over the years and for the always familiar atmosphere. I like to thank Dr. Hiroshi Yamamoto and Dr. Helge Paternoga for the scientific discussions, Dr. Justus Loerke for support in cryo-EM data processing, Dr. Magdalena Schacherl for the great support in structural modelling, Dr. Sofia Banchenko and Dr. Marylena Dabrowski for the detailed review and support in general, Dr. Thorsten Mielke and Jörg Bürger for their support with electron microscopy. In addition, a special thanks goes to Karin Chiluvane and Christine Gotthold the great support in organizational and general topics.

Many thanks to my family and friends, without whom I would not have survived the numerous setbacks during the work. In particular, I would like to thank Siddhartha for his patience, understanding and support during the whole time.

Selbstständigkeitserklärung

Hiermit versichere ich, Annika Balke, die vorliegende Arbeit selbstständig verfasst und keine anderen als die angegebenen Hilfsmittel verwendet zu haben. Ein Teil der beschriebenen Ergebnisse wurde in Zusammenarbeit mit Dr. Hiroshi Yamamoto, Dr. Justus Loerke, Jörg Bürger und Prof. Dr. Christian M.T. Spahn (Institut für Medizinische Physik und Biophysik, Charité – Universitätsmedizin Berlin) und Dr. Thorsten Mielke (Max-Planck-Institut für molekulare Genetik, Berlin) sowie Dr. Helge Paternoga und Prof. Dr. Joaziero (Zentrum für Molekulare Biologie der Universität Heidelberg, ZMBH) erarbeitet.

Berlin, 10. Januar 2022 _____

Annika Balke

Contents

List of figures

List of tables

Zusammenfassung

Die Proteinbiosynthese oder Translation ist ein grundlegender Prozess in den Zellen aller Organismen, der von den Ribosomen in Zusammenarbeit mit zahlreichen Proteinfaktoren durchgeführt wird. Die translatierenden Ribosomen können jedoch durch verschiedene Mechanismen blockiert werden, z. B. durch das Vorhandensein von beschädigten, abgeschnittenen oder Stopcodon-fehlenden Boten-RNAs (mRNAs). Um die Anhäufung von blockierten Ribosomen zu verhindern und somit den Pool aktiver Ribosomen zu minimieren, haben alle Organismen ribosomale Rettungsmechanismen entwickelt. Dazu gehören die *Trans*-Translation und die Ribosomen-assoziierte Qualitätskontrolle (RQC). Beide Wege bewirken den Abbau der unvollständigen und potenziell toxischen naszierenden Polypeptidkette, die an die transfer-RNA (tRNA) gebunden ist und retten blockierte Ribosomen.

Ein entscheidender Punkt bei der RQC ist die Erkennung der Peptidyl-tRNA enthaltenden großen ribosomalen Untereinheit, die bei Eukaryoten von Rqc2/NEMF und bei Prokaryoten von RqcH (dem Rqc2-Homolog) durchgeführt wird. Im Gegensatz zu Eukaryoten fehlten zu diesem Zeitpunkt Strukturdaten für prokaryotische RQC-Komplexe.

Ein Projekt dieser Doktorarbeit konzentrierte sich auf die Visualisierung von RqcH auf ribosomalen 50S-Untereinheiten mittels Kryo-EM. Die Strukturanalyse von *B. subtilis* 50S-Untereinheiten, die mit Wildtyp-RqcH aufgereinigt wurden, ergab keine Dichte für diesen Faktor, was möglicherweise auf seine Flexibilität zurückzuführen ist. Die Struktur lieferte jedoch wichtige und ergänzende Beweise für die Studie von Lytvynenko et al. 2019, da sie darauf hindeutet, dass peptidyl-tRNA-50S-Untereinheiten Substrate für RqcH sind, und damit RqcH im prokaryotischen RQC involviert zu sein scheint.

In einem zweiten Versuch, RqcH sichtbar zu machen, wurde das in seiner NFACT-N-Domäne mutierte RqcH-Protein gemeinsam mit 50S-Untereinheiten aufgereinigt und vor der EM-Analyse zusätzlich quervernetzt, um die Flexibilität zu verringern. Die anschließende Kryo-EM-Analyse ergab eine mutierte RqcH-50S-Struktur mit einer Auflösung von 3,1 Å. Die Struktur stellt wahrscheinlich den ersten Erkennungsschritt im prokaryotischen RQC dar und zeigt, wie die einzelnen Domänen von RqcH (NFACT-N-HhH, CC1-M-CC2 und NFACT-R) mit dem P-tRNA-50S-Komplex interagiert.

Die identifizierten RqcH-Bindungsstellen innerhalb der Struktur wurden durch funktionelle Experimente getestet, die von Dr. Helge Paternoga (ZMBH) durchgeführt wurden. Die kombinierte Struktur-Funktions-Analyse lieferte Hinweise auf spezifische RqcH-Regionen, die für die P-tRNA-50S-Bindung und die RqcH-Funktion innerhalb des RQC-Wegs funktionell relevant sind. Der Vergleich mit bestehenden RQC-Strukturen zeigt, dass RqcH durch seine M-CC2-Region an der 50S-Untereinheit verankert wird und als potenzieller Drehpunkt für die NFACT-N-HhH- und NFACT-R-Domänen dient, die flexibler zu sein scheinen.

Während RQC auf blockierte ribosomale Untereinheiten abzielt, strebt die *Trans*-Translation die Rettung von blockierten 70S-Ribosomen. Die *Trans*-Translation erfordert das kleine Protein SmpB und eine transfer-messenger RNA (tmRNA) und ermöglicht es durch die Aminosäure-Kodierungssequenz in der mRNA-ähnlichen Domäne (MLD) der tmRNA die entstehenden Polypeptidkette zu verlängern und für den Abbau zu markieren.

Der zweite Teil dieser Doktorarbeit befasste sich mit der Kryo-EM-Analyse der *E. coli* 70S-tmRNA-EF-G-FA-Probe, die zuvor in der Kryo-EM-Studie von Ramrath et al. (2012) verwendet wurde. Die Verwendung fortschrittlicher Technologien für die Kryo-EM-Analyse derselben Probe führte zu hochaufgelösten Strukturen und ergab darüber hinaus zusätzliche *Trans*-Translationszustände. Die fünf Kryo-EM-Strukturen wurden bis auf 3,5 Å bis 3,8 Å aufgelöst und geben Aufschluss über die Bewegungen des tmRNA-SmpB-Komplexes im Ribosom, von seiner Unterbringung in der ribosomalen A-Stelle über die Translokation zur ribosomalen P-Stelle bis zum Passieren der E-Stelle.

Die Beobachtung des Zustands vor der Translokation (tmRNA-PRE) und Zustände (PAST-E-TI-POST und PAST-POST) von nachfolgender Translokation ergänzen ähnlichen Strukturdaten und stimmen mit ihnen überein. Die tmRNA-SmpB-Translokation und auch der Prozess des Ladens der mRNA-ähnliche Domäne (MLD) wurden jedoch nur unzureichend erfasst. Die vorliegenden Strukturen zeigen, wie das tmRNA-SmpB-Modul spezifisch auf das Ribosom einwirkt und geben neue Einblicke, wie die Translation von der alten defekten mRNA auf das Leseraster der MLD gewechselt wird. Die Zwischenzustände (tmRNA-TI-POST I und II), die während der ersten Runde der Translokation gebildet werden, weisen eine Dichte für das komplette SmpB-Protein und die MLD auf, was neue Einblicke in den Prozess der MLD-Beladung in den mRNA-Kanal ermöglicht.

Darüber hinaus liefern die Strukturen molekulare Einblicke in den Prozess, durch den der große tmRNA-SmpB-Komplex die physikalischen Barrieren innerhalb des Ribosoms während der *Trans*-Translation überwindet.

Summary

Protein biosynthesis or translation is a basal process in the cells of all organisms, which is performed by the ribosomes in cooperation with numerous protein factors. However, translating ribosomes can be stalled by various mechanisms, such as the presence of damaged, truncated, or stop codon lacking messenger-RNAs (mRNAs). To prevent accumulation of stalled ribosomes and thus minimize the pool of active ribosomes, all organisms have evolved ribosomal rescue mechanisms. These include *trans*-translation and ribosome-associated quality control (RQC). Both pathways cause the degradation of the incomplete and potentially toxic nascent polypeptide chain attached to the transfer RNA (tRNA) and rescue stalled ribosomes.

A crucial point in RQC is the recognition of the peptidyl-tRNA-containing large ribosomal subunit, which is performed by Rqc2/NEMF in eukaryotes and RqcH (the Rqc2 homolog) in prokaryotes. Unlike for eukaryotes, structural data for prokaryotic RQC complexes were lacking at this time.

One project of this doctoral thesis aimed for the visualization of RqcH on ribosomal 50S subunits using cryo-EM. The structural analysis of *B. subtilis* 50S subunits co-purified with wild-type RqcH did not show a density for this factor, possibly due to its flexibility. However, the structure provided important and complementary evidence for the study in Lytvynenko et al. 2019, as it suggests that peptidyl-tRNA 50S subunits are substrates for RqcH, and thus RqcH appears to be involved in prokaryotic RQC.

In a second attempt to visualize RqcH, the RqcH protein mutated in its NFACT-N domain was co-purified with 50S subunits and additionally crosslinked before EM analysis, both to decrease flexibility. The subsequent cryo-EM analysis revealed a mutant RqcH-50S structure with a resolution of 3.1 Å. The structure likely represents the initial recognition step in prokaryotic RQC and shows how the individual domains of RqcH (NFACT-N-HhH, CC1-M-CC2 and NFACT-R) interact with the P-tRNA-50S complex.

The identified RqcH binding sites within the structure were tested by functional experiments which were performed by Dr. Helge Paternoga (ZMBH). The combined structure-function analysis provided evidence for specific RqcH region that are functionally relevant for P-tRNA-50S binding and RqcH function within the RQC pathway. Comparison with existing RQC structures

indicate that the M-CC2 region anchors RqcH to the 50S subunit and serves as a potential pivot point for the NFACT-N-HhH and NFACT-R domains which seem to be more flexible.

While RQC targets stalled ribosomal subunits, *trans*-translation aims to rescue stalled 70S ribosomes. *Trans*-translation requires the small protein SmpB and a transfer-messenger RNA (tmRNA) and allows by using the amino acid coding sequence in the mRNA-like domain (MLD) in the tmRNA to elongate and tag the nascent polypeptide chain for degradation.

The second part of this doctoral thesis focused on the cryo-EM analysis of the *E. coli* 70S-tmRNA-EF-G-FA specimen previously used in the cryo-EM study in Ramrath et al., 2012. Using advanced technologies for the cryo-EM analysis of the same specimen resulted into high-resolution structures and moreover revealed additional *trans*-translation states. The five cryo-EM structures were resolved to 3.5 Å to 3.8 Å and shed light on the movements of the tmRNA-SmpB complex in the ribosome, from its accommodation into the ribosomal A-site to the translocation towards the ribosomal P-site and passed the E-site.

The observation of a state before translocation (tmRNA-PRE) and states (PAST-E-TI-POST and PAST-POST) of subsequent translocation complement and are consistent with the similar structural data. However, the tmRNA-SmpB translocation and also the process of MLD (mRNA-like domain) loading were poorly understood. The structures in this work show how the tmRNA-SmpB module specifically acts on the ribosome revealing new insights of how the translation is switched from the old defective mRNA to the reading frame of the MLD. The intermediate states (tmRNA-TI-POST I and II) that formed during the first translocation round show density for the complete SmpB protein and the MLD allowing to gain new insights of the process of MLD loading into the mRNA channel.

In addition, the structures provide molecular insights into the process by which the large tmRNA-SmpB complex overcomes the physical barriers within the ribosome during the *trans*-translation.

1 Introduction

In living cells, the genetic information is transferred from the deoxyribonucleic acid (DNA) via the ribonucleic acid (RNA) as a mediator to the protein (Crick, 1970). All forms of RNA are synthesized by transcribing the DNA using RNA polymerases, a process that is called transcription. Ribonucleic acids such as transfer RNA and or ribosomal RNAs (tRNA or rRNA) perform various functions in the cell directly (Giegé, 2008) or are used as templates for translation as in the case of messenger RNA, the mRNA (Kozak, 2005). An example for the interplay of different RNAs, involved into the same process is the translation, in which the mRNA nucleotide sequence is translated into the sequence of amino acids which are delivered by tRNA molecules. The translation is a multi-step process and takes place in the cytosol at a large molecular complex, the ribosome (Palade, 1955). The growing peptide emerging from ribosome starts folding already co-translationally using chaperons. Protein folding into its three-dimensional (3D) structure is required to obtain full functionality. In rare cases, the mRNA lacks the signal to terminate the protein synthesis causing an arrest of the translation process which results in a stalled polypeptide-bound ribosome. These stalled ribosomes can be rescued in alternative processes, such as the Ribosome-associated quality control (RQC) or the *trans*-translation pathway (Buskirk & Green, 2017; Keiler et al., 1996). Ribosome-mediated processes involve the interaction of various protein factors and the ribosomes as well as its tRNA substrates underly extensive conformational changes. Many of these dynamic structural events on ribosomes have been characterized and visualized by biochemical and structural methods (Huter et al., 2017). In the recent decade, the new technological advances in x-ray crystallography and cryogenic electron microscopy (cryo-EM) facilitated the solving of biological structures at near-atomic to atomic resolution. The high-resolution structures provide enlightening insights into the complex molecular processes that are mediated by the ribosome (Müller et al., 2021).

1.1 The structure of the ribosome

All ribosomes have the conserved function to catalyze the synthesis of proteins. In all living cells, they exist freely in the cytoplasm or are bound to the membrane of the endoplasmic reticulum (rough ER). Ribosomes are macromolecular complexes composed of proteins and RNAs. The ribosomal proteins have structural and regulatory functions, while highly conserved rRNA elements perform catalytic functions, thus making the ribosome to a ribozyme, a non-coded RNA molecule with enzymatic activity (Noller et al., 1992). The function of ribosomes is universally conserved, whereas the composition of ribosomes varies between different domains of life (Figure 1).

Commonly, ribosomes are characterized by their sedimentation behavior (expressed in S = Svedberg units or coefficient), which depends on the size and shape of the macromolecule (Slonczewski at al., 2009). Accordingly, one distinguishes eukaryotic 80S-type and the prokaryotic 70S-type of the ribosome. The smaller 70S-type also includes ribosomes from mitochondria and plastids, which according to the endosymbiont theory evolved from prokaryotes and were taken up by eukaryotes (Wallin, 1922). Both types of ribosomes are composed of a large subunit (LSU; 50S in prokaryotes or 60S in eukaryotes) and a small subunit (SSU; 30S in prokaryotes or 40S in eukaryotes), which assemble to form a translation competent complex (80S or 70S ribosome) (Ban et al., 2000; Schluenzen et al., 2000; Wimberly et al., 2000). In the following chapters only the prokaryotic 70S is discussed and their small and large ribosomal subunit are abbreviated as SSU or 30S and LSU or 50S, respectively.

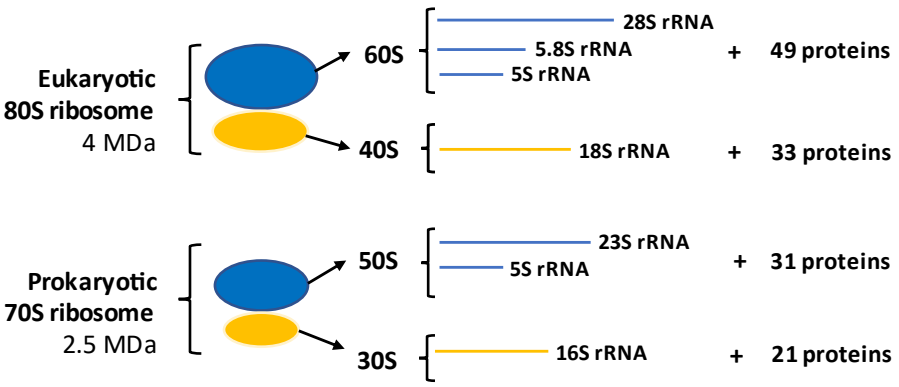

Figure 1: Eukaryotic and prokaryotic ribosomes differ in size and composition.

The first 3D structures of ribosomes were determined in 1995 by cryo-EM revealing its overall shape (Frank et al., 1995; Stark et al., 1995). Under the electron microscope, ribosomes appear

as oval to round particles with a diameter of 200 Angstrom (Å) in prokaryotes to 300 Å in eukaryotes. In many following cryo-EM studies it has been shown that the general architecture of ribosomes is preserved in all kingdoms.

The structure of the SSU is divided into two large segments, the head, and the body, which are connected by the neck (Figure 2A). Characteristic features of the body are the left and right foot, the shoulder, and the platform. The head has a pointed protrusion that resembles a bird's beak.

The LSU in its characteristic "crown view" shows structural landmarks including the central protuberance (CP) and two stalks, the L1 stalk and L7/L12 stalk (Figure 2B). These three elements are composed of distinct ribosomal proteins and helices of either the 5S rRNA (CP) or 23S rRNA (L1 and L7/12 stalk) of the LSU (Ban et al., 2000). In the crown view, the L1 stalk is located to the left and L7/L12 to the right of the CP, respectively.

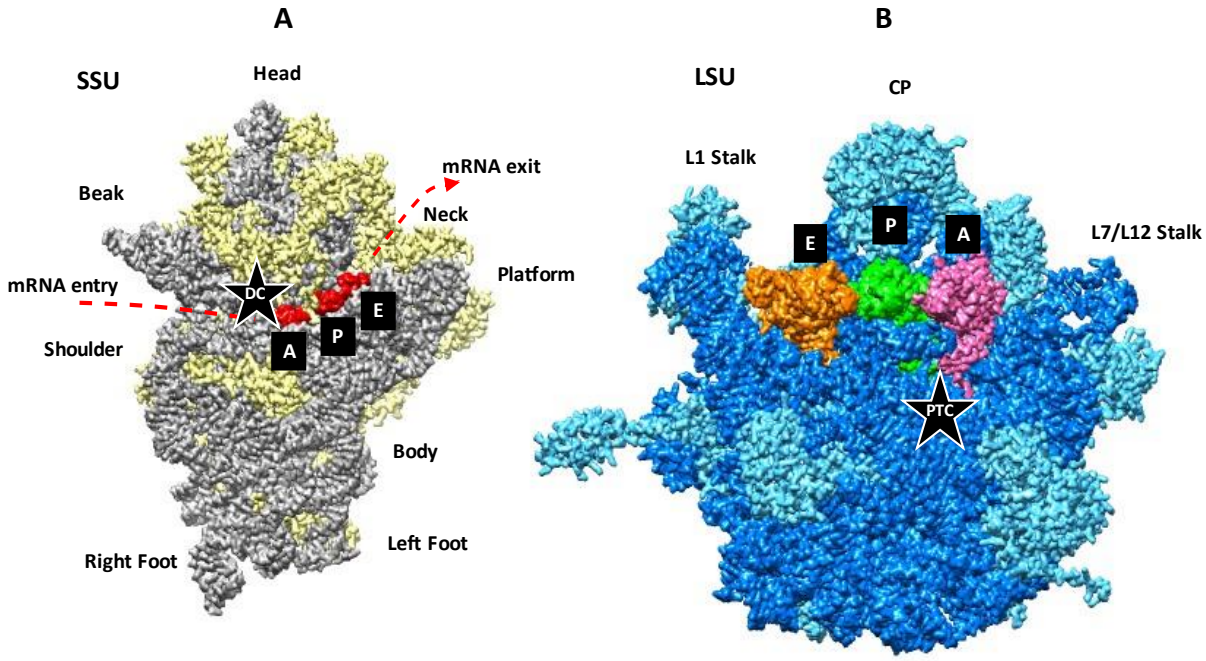

Figure 2: Model of a bacterial ribosome (70S) of *Thermus thermophilus* (Ramakrishnan et al., 2006, PDB-ID:4V51). A) Subunit interfaces of the 30S ribosomal subunit (SSU) and B) 50S ribosomal subunit ("crown view" of LSU). The ribosomal proteins of the SSU are shown in yellow, RNA in grey, the LSU proteins in cyan, and RNA in blue. The binding sites for the A-site, P-site, and E-site tRNA are indicated in pink, green, and orange respectively. The mRNA and its channel are shown in red, the catalytic active center (DC = decoding center, PTC = peptidyl-transfer center) are indicated by asterisks. Important landmarks for orientation are labeled (head, beak, shoulder, neck, platform, body, right and left foot, CP=central protuberance, L1 and L7/L12 stalk).

1.2 Function of the ribosome

Ribosomes carry out protein biosynthesis (translation) along with tRNA, mRNA and other varying translation factors. To describe functional centers of the ribosome, it is needed to describe the tRNA and mRNA first. The translation process itself is described in detail in chapter 1.3.

1.2.1 mRNA and tRNA

Both DNA and RNA are nucleic acid polymers, which comprise of nucleoside-phosphate units linked by phosphoric acid di-ester bonds. The DNA is composed of four nucleobases, which are adenine, cytosine, guanine, and thymine. Uracil is used instead of thymine during the transcription of the DNA into an RNA molecule. The mRNA sequence is read in the form of nucleotide triplets that are called codons (Crick et al., 1961). The codon sequence determines the sequence of the amino acids of the polypeptide chain to be formed, which determine the primary structure of a particular protein. Theoretically $4^3 = 64$ possible codon combinations exist, of which 61 encode the 20 canonical proteinogenic amino acids, while the remaining three function as stop codons (UAA, UAG or UGA) for the termination of translation (Lagerkvist, 1978).

The mRNA contains regions that are not translated into proteins, termed untranslated regions (UTRs), which are located at the 5' or 3' end of the protein coding sequence. In prokaryotes, the 5'UTR contains a ribosomal binding site (RBS) that includes the Shine-Dalgarno (SD) sequence, 5'–GGAGGU–3' (Shine & Dalgarno, 1974). The SD sequence is positioned 7 - 10 nucleotides upstream of the mRNA start codon, AUG (Figure 3). The complementary base pairing of the SD sequence with the anti-SD sequence (5'-ACCUCC-3') located at the 3' end of the ribosomal 16S rRNA marks the starting point of translation.

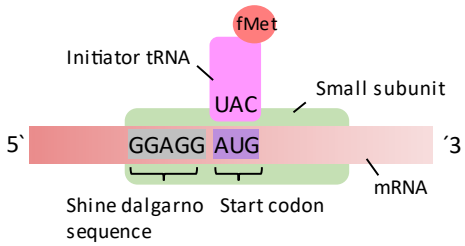

Figure 3: Shine-Dalgarno Sequence. The small ribosomal subunit is bound by the Shine-Dalgarno sequence of the mRNA, thereby fixing the start point of the translation. The initiator tRNA binds the AUG start codon which is located at the ribosomal P-site. Figure was prepared using Microsoft Office.

Beside the ribosomal contacts, the mRNA interacts with tRNAs. The tRNAs consists of 73 to 95 nucleotides and form a cloverleaf-shaped secondary and a L-shaped tertiary structure due to intramolecular base pairing (Holley et al., 1965; Kim et al., 1973). The structure of tRNA is divided into specific domains, each of which performs a different function (Figure 4). The acceptor arm is responsible for binding the respective amino acid and the anticodon arm provides the anticodon for complementary binding of the mRNA codon (Lorenz et al., 2017). The other two arms were named due to the presence of modified nucleotides as DHU arm (dihydro uridine) and TΨC arm (T: thymidine, Ψ: pseudo uridine, C: cytidine), which are mainly used to stabilize the tRNA molecules.

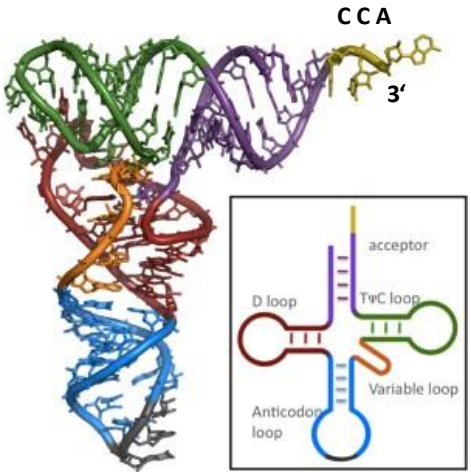

Figure 4: The general tertiary and secondary structure of tRNAs. The RNA loops and helices in the tertiary and secondary tRNA structure are colored as follows: TΨC arm in green, the variable loop in orange, the anticodon arm is blue, the D-arm is red, and the acceptor arm is purple. The 3'end CCA-end of the amino acid acceptor arm is yellow. The figure was adopted from Shareghi et al., 2012.

Before being delivered to the ribosome, amino acids need to be activated and loaded to the tRNA in both prokaryotic and eukaryotic cells. The process, called amino acylation, is catalyzed by an amino-acid specific aminoacyl-tRNA synthetases (AAS) (Ibba and Soll, 2000).

First, the AAS binds an amino acid and adenosine triphosphate (ATP) to form an aminoacyl adenylate (aminoacyl-adenosine monophosphate = aminoacyl-AMP), thereby releasing an inorganic pyrophosphate (PP_i). Then, the appropriate tRNA molecule is bound by the aminoacyl-adenylate via its D arm, and the activated amino acid is transferred from the aminoacyl-AMP to the OH group of the ribose of the tRNA nucleotide at the 3'-end (Figure 4). This two-step reaction can be summarized as:

- amino acid + ATP → aminoacyl-AMP + PP_i (amino acid activation)
- aminoacyl-AMP + tRNA → aminoacyl-tRNA + AMP (tRNA loading)

The resulting aminoacyl-tRNA (aa-tRNA) can now be used for the translation process on the ribosome or, in case of the prokaryotic initiator tRNA, the methionine-charged tRNA (Met-$tRNA^{Met}$) produced by methionine synthetase, needs to be further modified. This is done by the methioninyl-tRNA-formyltransferase (FMT), which formylates the methionine to formyl methionine on the Met-loaded tRNA, resulting into fMet-$tRNA^{Met}$. The N-formylation in fMet-$tRNA^{Met}$ provides a specific feature that is recognized by the initiation factor 2 required to start the translation process (see chapter 1.3.1).

1.2.2 Functional elements of the ribosome

The catalytically active center of the ribosome includes two regions: the decoding center (DC), which is located on the SSU (Figure 2A) and the peptidyl-transferase center (PTC), which is located on the LSU (Figure 2B). Both regions, DC, and PTC, are widely conserved with some differences observed in the surrounding regions (Ben-Shem et al., 2011; Wilson et al., 2012; Anger et al., 2013). During protein synthesis, the DC monitors the complementarity of tRNA and mRNA, while the PTC catalyzes the peptide bond formation and peptide release. Interaction between the codon on the mRNA at the DC and the amino acid at the PTC is accomplished by tRNAs.

The ribosome has three tRNA binding sites, the aminoacyl (A), peptidyl (P), and exit (E) sites, located at the interface of both ribosomal subunits (Figure 2). Binding of the tRNA to the A-site requires reading the mRNA codon by the anticodon of the tRNA. Then the peptide chain is transferred from the P-site bound tRNA to the 3'CCA -end of the tRNA bound to the A-site. The peptide chain charged tRNA of the A-site and the deacylated P-site tRNA are subsequently translocated one nucleotide triplet further to the P and E-site, respectively. Other functional sites of the ribosome include the mRNA channel located on the small subunit (Figure 2A) and the peptide tunnel that extends from the PTC through the LSU.

1.2.3 Structural dynamics of the ribosome

The dynamic nature of the ribosome can be interpreted with the help of an energy landscape (Munro et al., 2009a). According to this, the ribosome can adopt intermediate conformational

states that are in equilibrium at room temperature. In the energy landscape, these intermediate states represent local energy minima (Figure 5). The rate of transition from one state to the other depends on the activation energy that must be applied to reach one state or the other. The stability of individual intermediate states and/or the level of activation energy can be modulated by ligands (e.g., translation factors, antibiotics) and environmental parameters (ion concentrations, temperature).

The energy landscape has a hierarchical character to be able to capture macroscopic (e.g., transition from pre-translocational to post-translocational state), mesoscopic (e.g., dynamics of the L1 and L7/L12 stalk or spontaneous movement of tRNAs from the classical into the hybrid state), and microscopic (e.g., movements of individual protein side chains) structural rearrangements. The prokaryotic ribosome appears to have several degrees of freedom with respect to global conformational change, such as the 30S subunit rotation, 30S head domain rotation, L1 and L7/L12 stalk movement and conformational changes of the ribosomal intersubunit bridges. In the following, each degree of freedom is briefly described.

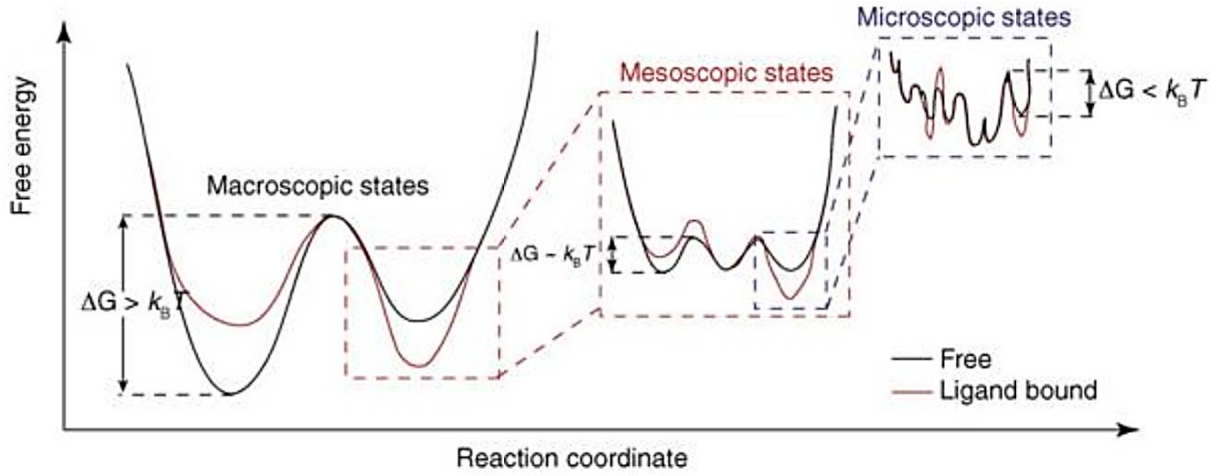

Figure 5: Hierarchical and metastable energy landscape. The ribosome has the intrinsic ability to reversibly adopt different natural conformations. The local minima of free energy describe macroscopic, mesoscopic, and microscopic substates of conformations. The conformational substates are defined by their individual conformational degrees of freedom within the ribosome. The energy landscape is shown before (black) and after ligand binding (red). The figure is adopted from Munro at al., 2009.

1.2.3.1 Conformational changes of the 30S ribosomal subunit

The most prominent large-scale rearrangements in prokaryotes occur on the ribosomal 30S subunit: the intersubunit rotation and head swivel. Both conformational changes are required

in the elongation phase of translation (see chapter 1.3.2), in which the coupled movement of mRNA and tRNAs on the ribosome is catalyzed by the elongation factor G (EF-G).

The subunit rotation also termed ratcheting (Figure 6A), was first visualized in pre-translocational (PRE) 70S complexes and described as a counterclockwise movement of the 30S subunit relative to the 50S subunit (Frank and Agrawal, 2000; Valle et al., 2003; Horan and Noller, 2007). The ratchet-like subunit rearrangement is accompanied with the movement of the tRNAs on the large subunit, from the classical (A/A and P/P) to hybrid (A/P and P/E) tRNA configuration (the first and second letter indicate the tRNA position on the small and large subunit, respectively) (Moazed and Noller, 1989; Agirrezabala et al., 2008). The resulting hybrid state is in a thermodynamic equilibrium with the nonrotated state.

The subunit rotation-mediated transition is a spontaneous and reversible reaction between these two states. Binding of EF-G additionally induces the 30S head swivel movement (Frank and Agrawal, 2000; Valle et al., 2003; Spahn et al., 2004; Connell et al, 2007). The head swivel describes a rotation of the small subunit head domain relative to the small subunit body/platform domain, which is roughly orthogonal to the intersubunit rotation (Ramrath et al., 2013; Ratje et al., 2010; Schuwirth et al., 2005; Spahn et al., 2004a, 2004b) (Figure 6B). Head swiveling leads to the formation of chimeric intra–subunit ap/P and pe/E hybrid tRNA binding sites (a and p indicate tRNA contacts to the A-site and P-site of the 30S, respectively; P and E indicate tRNA contacts to the P-site and E-site of the 50S, respectively) (Ramrath et al., 2013; Ratje et al., 2010).

Furthermore, during the transition of the chimeric bound tRNAs to the classical P/P and E/E configuration, the head can tilt about an axis that is parallel to the mRNA entry channel displacing it away from the 30S–50S interface (Ramrath et al., 2012; Nguyen et al., 2016) (Figure 6C). The 30S head tilting was first discovered in the ribosomal tmRNA-70S rescue complex and is proposed to open steric barriers which are required to complete the translocation of the mRNA–tRNA complex on the ribosome (Ramrath et al., 2012).

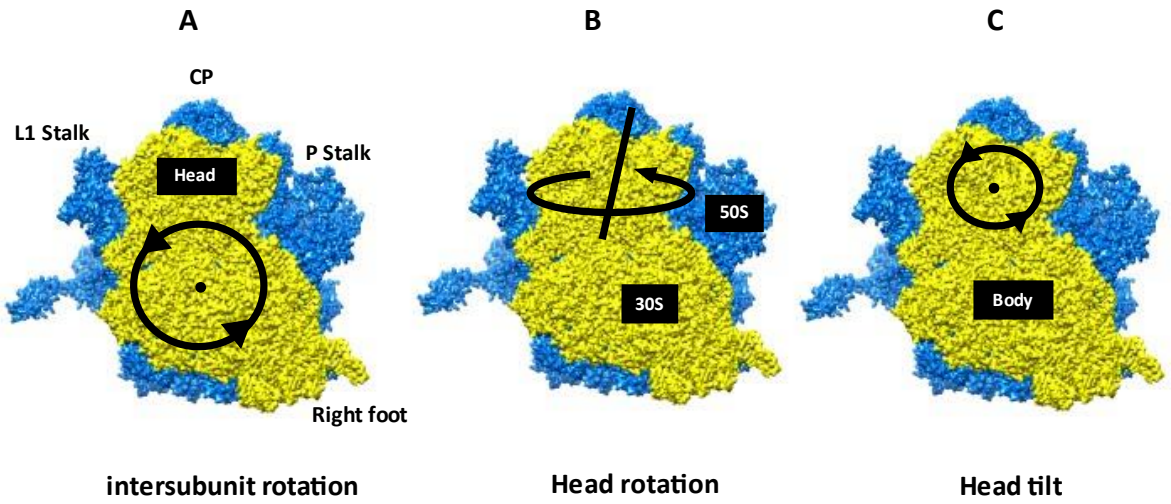

Figure 6: Large-scale conformational changes of the ribosomal 30S subunit. Shown are the subunit rotation (A), head rotation (B) and head tilt (C) of the 30S subunit (yellow) relative to the 50S subunit (blue). The electron density was simulated from the X-ray crystal structure of the 70S *Thermus thermophilus* (Ramakrishnan et al., 2006, PDB-ID:4V51) and visualized in Chimera. Elements of the 50S subunit (right foot, CP = central protuberance, L1 and L7/L12 stalk) are shown for orientation.

1.2.3.2 Conformational changes of the 50S ribosomal subunit

The largest movement within the 50S subunit is performed by the L1 stalk (formed by rRNA helices 76, 77, 78 and protein L1), which moves outwards or inwards the ribosomal intersubunit space adopting four distinct L1 stalk conformations (Figure 7A). The open conformation, in which the L1 stalk is extended away from the 50S subunit, was found in ribosomes with an empty E site or in isolated 50S subunit (Harms et al., 2001; Schuwirth et al., 2005; Agirrezabala et al., 2008; Dunkle et al., 2011). The release of the deacylated tRNA from the ribosomal E-site presumably occurs on transition to the open L1 state (Mohan and Noller, 2017).

The closed conformation, where the L1 stalk moves towards the intersubunit space and thereby contacting the elbow of the E-site tRNA, was found in ribosomes with classical bound E/E-tRNA (Korostelev et al., 2006; Selmer et al., 2006) or hybrid bound P/E tRNA (Valle et al., 2003; Gao et al, 2003). The intermediate L1 stalk conformations were observed during tRNA movement into the chimeric pe/E tRNA state (intermediate 1, Korostelev et al. 2006; Zhou et al., 2012) and into classical E/E state (intermediate 2 or half closed, Mohan and Noller, 2017).

A further mobile element of the 50S subunit of the ribosome is the L7/L12 stalk, which is formed by the stalk base (23S rRNA helices H43 and H44, and ribosomal protein uL11) as well as multiple copies of protein bL12 (originally named L7/L12) (Diaconu et al., 2005). The L7/L12

stalk can move towards or away the ribosomal A-site occupying the inward or outward position, respectively (Yusupova et al., 2006; Yusupov et al., 2001; Korostelev et al., 2006) (Figure 7A). Its motion results from binding canonical guanosine triphosphatases (GTPases), such as elongation factor Tu (EF-Tu), elongation factor G (EF-G), and release factor 3 (RF3) to the GTPase-associated center (GAC).

The GAC is formed by the 23S rRNA helices 42-44 and protein uL11 as well as the universally conserved sarcin-ricin-loop (SRL, formed by helix 95 of the 23S rRNA) (Valle et al., 2002; Gao et al., 2003, 2007; Connell et al., 2007) (Figure 7B).

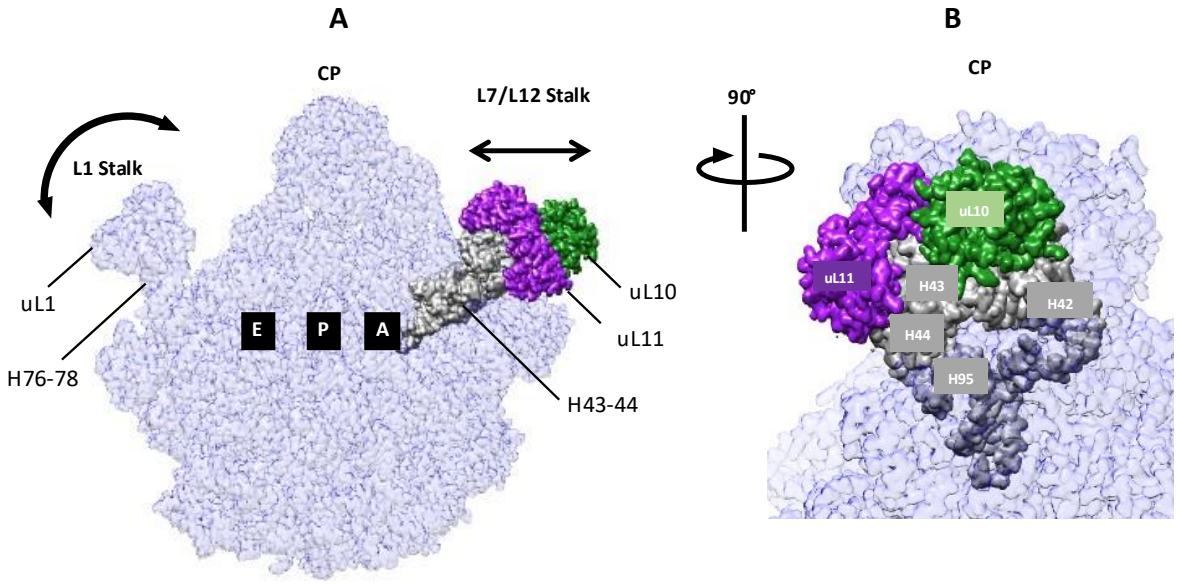

Figure 7: Motions of L1, L7/12 stalks and elements of the GTPase-associated center. A) Motion direction of the L1 stalk (uL1, rRNA helices H76-78) and L7/12 stalk (uL10 (green), L11 (purple), rRNA helices H43-44 (grey)). B) The side view shows the composition of the GTPase-associated center (GAC) formed by 23S rRNA helices H42-H44 and H95 (grey) and protein uL11 (purple). The remaining blue colored density belongs to the 50S subunit. The tRNAs binding sites for the A-site, P-site and E-site and LSU landmarks (L1 stalk, CP = central protuberance) are indicated for orientation. The figures were made in Chimera using mutant RqcH-50S structure model and cryo-EM map form this work.

1.2.3.3 Ribosomal inter-subunit bridges in prokaryotes

The dynamic movements occurring in various steps of translation are facilitated by several interactions between the ribosomal subunits, known as inter-subunit bridges (Figure 8). The ribosomal bridges observed in the classical state can be disrupted by rotation of the 30S subunit and head, resulting in new interactions between the two subunits.

For example, the bridges B1a and B1b are formed by the interaction of protein uS13 with the A-site finger (ASF; H38 in 23S rRNA) and with uL5, bL31 of the LSU, respectively. Both bridges are observed in classical (non-rotated) ribosomes, in which they stabilize the contact between the CP and the 30S head domain (Yusupov et al. 2001). While in hybrid-state ribosomes with 30S head swiveled, the B1a and B1b bridges are disrupted (Liu and Fredrick et al., 2016).

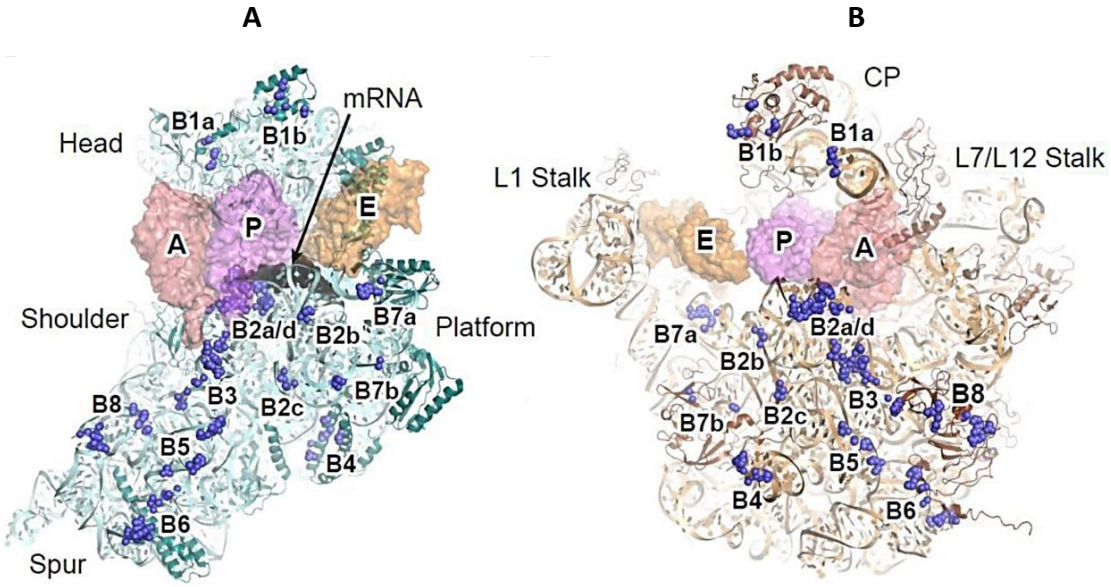

Figure 8: Inter-subunit bridges of the prokaryotic ribosome. The subunit interfaces of A) the 30S (green) and B) the 50S (brown) showing the inter-subunit bridge elements (blue spheres). The A-site (red), P-site (pink) and E-site (orange) tRNAs, mRNA (black) and landmarks (head, shoulder, platform, spur, CP = central protuberance, L1 and L7/L12 stalk) are indicated. Figures were taken from Liu and Fredrick et al., 2016.

1.3 The bacterial translation cycle

Protein synthesis or translation comprises four steps: initiation, elongation, termination, and recycling (Wilson and Nierhaus, 2003; Schmeing and Ramakrishnan, 2009).

During initiation, the ribosomal subunits assemble to form an initiation complex in which the initiator-tRNA base-pairs with the start codon of the mRNA. The following elongation is an iterative process of adding amino acids one-by-one to the growing polypeptide chain. The termination of the translation occurs when the elongation complex reaches a stop codon in the mRNA, which leads to the release of the polypeptide from the ribosome-bound tRNA. In the recycling phase the post-terminated ribosome is split into its subunits, which can be reused for subsequent translation rounds.

Each translation phase consists of multiple steps (Figure 9), which require numerous extra-ribosomal translation factors and several large-scale intra- and inter-subunit rearrangements of the ribosome (Korostelev et al., 2008; Dunkle and Cate, 2011; Ratje et al., 2010; Zhou et al., 2013). The factors and precise mechanism of each translational phase vary between the different kingdoms of life.

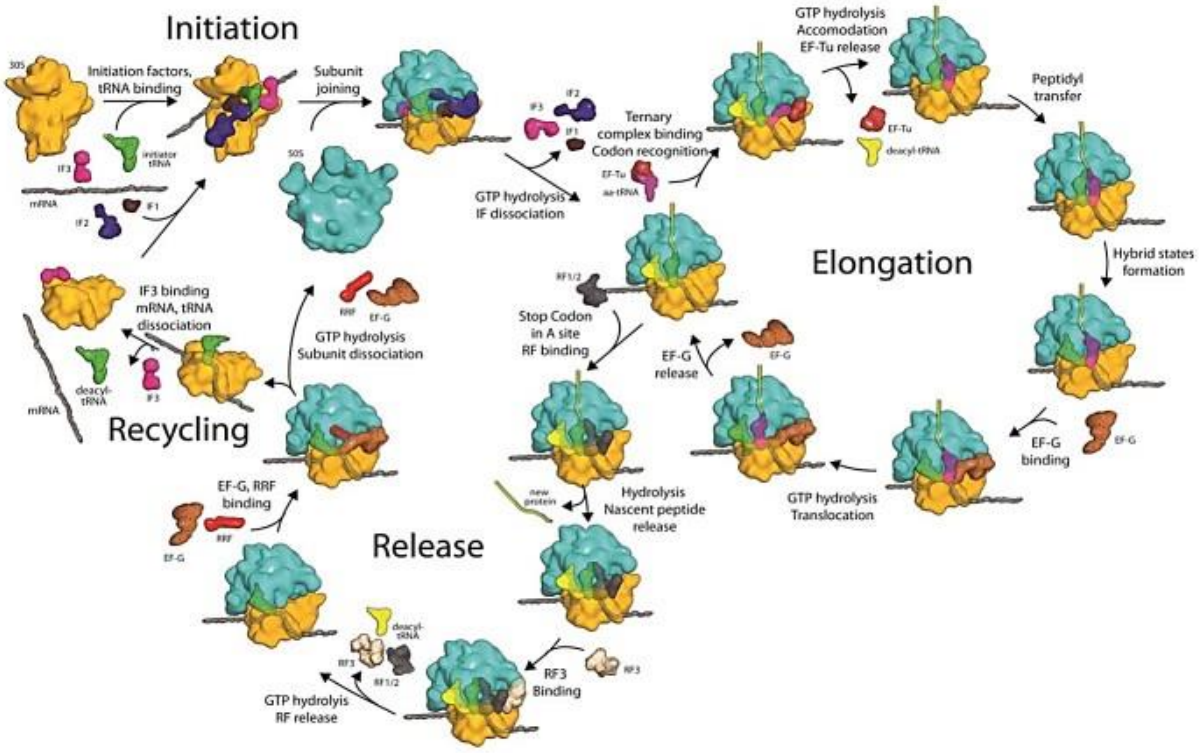

Figure 9: Schematic representation of the bacterial translation. The translation is a four-step process that comprises initiation, elongation, termination, and recycling. All steps are explained detailed in the following chapters. The figure was taken from Schmeing and Ramakrishnan, 2009.

1.3.1 Initiation of bacterial translation

The initiation of bacterial translation aims to form a ribosomal complex containing an mRNA with a start codon in the P-site that is bound to the initiator tRNA fMet-tRNA^{Met}. The initiation starts with the formation of the 30S-initiation complex (30S-IC), in which initiation factors 1, 2, and 3 (IF1, 2, and 3) as well as the initiator tRNA are bound to the ribosomal 30S subunit (Figure 9).

IF1 binding blocks the ribosomal A-site until the elongation starts. Both, IF3 and IF2 are responsible for the selection of the proper tRNA and its binding to the 30S subunit, which leads to the formation of the 30S-IC. IF-2 provides a specific docking site for the formyl group leading to a

direct bond of the fMet-tRNA$_i^{Met}$ to the 30S-IC (Canonaco et al., 1986; Gualerzi and Pon, 2000). IF3 controls additionally the mRNA binding to the P-site of SSU and in the further step promotes together with IF2 the joining of 30S-IC and 50S into a 70S initiation complex (70S-IC).

Formation of the 70S-IC triggers the hydrolysis of guanosine triphosphate (GTP) in IF2, which results in the dissociation of all initiation factors (Antoun et al., 2006; Grigoriadou et al., 2007; Milon et al., 2008). The initiation process may not be linear and the precise order of 30S factor binding might happen in a flexible manner (Hussain et al., 2016; Milon et al., 2010; Milón et al., 2012).

1.3.2 Elongation of bacterial translation

The elongation is a very complex process that basically translates the genetic information encoded in the mRNA into the corresponding amino acid sequence. The elongation is highly conserved among prokaryotes and eukaryotes, in contrast to the initiation and termination, which are distinctly different (Kozak 1999; Berg and Tymoczko; 2002; Petry et al., 2008). In this process new amino acids are iteratively incorporated into the growing polypeptide chain. They are delivered by the amino-acylated tRNAs in a manner specified by the codons in the mRNAs.

The elongation in bacteria is controlled by two elongation factors (EFs), the translocational GTPases EF-Tu and EF-G. Each elongation cycle is subdivided into decoding, peptidyl-transfer, and translocation. Decoding ensures the binding of the amino acid-loaded tRNA in the ribosomal A site. Subsequent peptidyl transfer leads to the linkage of the amino acid to the nascent peptide chain. And translocation catalyzes the movement of tRNAs along the mRNA to the next codon. The following chapters describe elongation steps in detail.

1.3.2.1 Decoding

Decoding describes the process of selecting the proper aminoacyl-tRNA (aa-tRNA) in the ribosomal A site. This step is catalyzed by elongation factor Tu (EF-Tu) and involves various steps: initial tRNA binding, mRNA codon recognition, GTP activation, and GTP hydrolysis (Schmeing et al., 2009; Schuette et al., 2009; Voorhees and Ramakrishnan, 2013). Decoding starts with the delivery of the ternary complex, comprising an aa-tRNA, EF-Tu and GTP, to the vacant A-site of non-rotated ribosomes carrying a peptidyl-tRNA in the P-site.

The initial binding of the ternary complex does not require mRNA, but rather the interaction of EF-Tu with ribosomal L7/L12 proteins. The bound aa-tRNA adopts a deformed and high-energy A/T conformation (Stark et al., 1997; Valle et al., 2003). This tRNA configuration enables the aa-tRNA anticodon loop to interact with the mRNA codon located in the A site and, simultaneously, EF-Tu binding near the sarcin-ricin loop of 23S rRNA in the large ribosomal subunit (Valle et al., 2002; Moazed et al., 1989; Stark et al., 1997).

EF-Tu's maintained association with the amino acyl end of the aa-tRNA prevents a premature engagement with the peptidyl-transfer center (PTC) (Schmeing and Ramakrishnan et al., 2009), while positioning of the anticodon loop of the aa-tRNA at the decoding center (DC) allows the sensing the mRNA for a matching codon (codon recognition). Successful codon–anticodon recognition leads to conformational changes of highly conserved ribosomal 16S RNA nucleotides G530, A1492 and A1493 at the DC of the 30S subunit (Ogle et al., 2001).

The excess energy released during base pair recognition is used to drive conformational changes in the ternary complex and the ribosomal 30S subunit. The change within the ribosome is called 30S subunit domain closure, which comprises a downward movement of the 30S head and an inward rotation of the 30S shoulder closer to EF-Tu (Ogle et al., 2002). The 30S subunit domain closure, combined with conformational rearrangement within the ternary complex, stimulates the GTP-hydrolysis in EF-Tu (Pape at al., 1998; Ogle et al., 2001 and 2002).

The subsequent EF-Tu-GDP dissociation releases the tRNA acceptor end, which moves into the PTC of the ribosomal A-site, a step called accommodation (Whitford et al., 2005). Once the accommodation has completed, the CCA'3-ends of both, A-site and P-site tRNA are positioned at the PTC, where they participate in a rapid peptide bond formation (see next chapter 1.3.2.2).

1.3.2.2 Peptide bond formation

After decoding, the ribosome contains an aminoacyl-tRNA at the A-site and the peptidyl-tRNA at the P-site, with both acyl residues attached to the last nucleotide at the 3' -end of the respective tRNA via an ester bond. In the following peptidyl transfer reaction, the nascent peptide is transferred from the P-site tRNA to the A-site tRNA. During this reaction, the ester bond of the carbonyl carbon in the peptidyl-tRNA is nucleophilically attacked by the amino-group

of the aminoacyl-tRNA in the A-site (Schmeing et al., 2005a) forming a transition state and finally transferring the peptidyl residue to the aminoacyl group of the A-site tRNA (Figure 10).

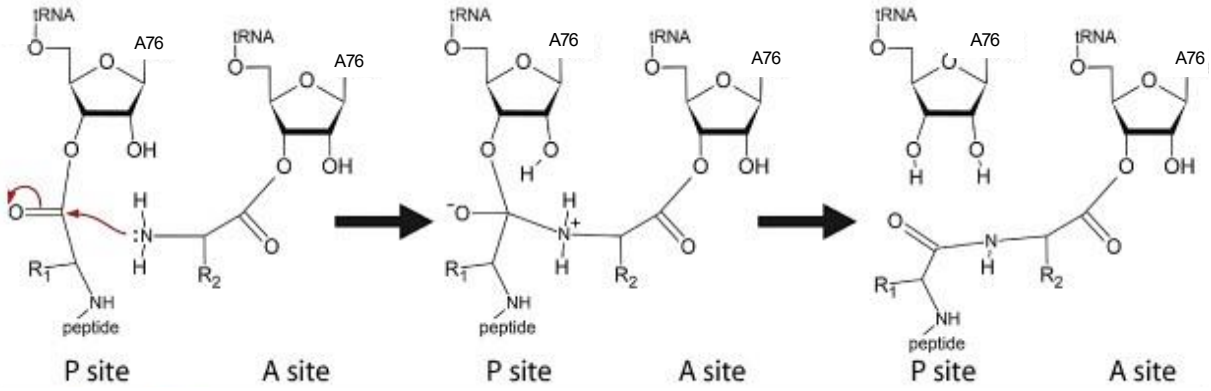

Figure 10: Reaction mechanism of the peptide-bond formation. Shown is the reaction between the acyl residues at the amino acid acceptor 3'ends of the tRNA in the P-site and A-site. Left: The carbonyl carbon of the ester bond of the amino acid in the P-site is nucleophilic attacked by the free electron pair of the amino group of the amino acid attached to the A-site tRNA. Subsequent deacylation of the tRNA in the P site and peptide transfer to the A site tRNA converts the transition state (middle) to the final products (right). The figure was adopted from Schmeing et al., 2005a.

Compared to an un-catalyzed reaction, the ribosome additionally accelerates the reaction by at about 10^5-fold (Sievers et al., 2004). The catalytic mechanism is based on entropic effects within the ribosome, which are mainly caused by substrate positioning and water exclusion within the active site. The catalytically active site is formed by the PTC of the large ribosomal subunit, which is entirely made up of rRNA (Ban, 2000; Nissen et al., 2000). The ribosomal catalytic power provided for the peptide-bond formation results through conformational re-arrangements in the PTC, which are established by a substrate induced-fit mechanism occurring during the accommodation (Sievers et al., 2004).

In an unaccommodated state with an empty A-site, the PTC provides an environment, where the ester group of the peptidyl-tRNA is protected by water from a nucleophilic attack, thus preventing a premature deacylation. But the binding of the aa-tRNA in the A-site induces a fit between the PTC and acceptor arm of both, the A-site and P-site tRNA, thereby exposing and positioning them properly for the peptidyl transfer reaction (Schmeing et al., 2005).

After this reaction, the ribosomal A site contains a peptidyl tRNA with its peptide extended by one amino acid, and the P site binds the deacylated tRNA. Removing the peptide chain of the P-tRNA overcomes the steric obstacles and thus, increases the specificity required for binding

the deacylated tRNA in the ribosomal E-site ensuring that the translocation can only occur after peptidyl transfer (Schmeing et al., 2003).

1.3.2.3 Translocation

Before translocation, the ribosome is found in a pre-translocational state (PRE state) with a peptidyl-tRNA in the A-site and a deacylated tRNA in the P-site (Figure 12A). During translocation the mRNA and tRNAs are synchronously moved by one codon shifting the A- and P-site tRNA into the ribosomal P- and E-site, respectively. The resulting post-translocational state (POST state) exposes the mRNA codon in the empty A-site required for the delivery of the next tRNA.

The translocation is catalyzed by EF-G, which hydrolyzes GTP during the reaction. It is the most complex step in elongation (Spirin, 1985) and involves large conformational changes within the ribosome leading to various post-translocational intermediates (TI-POST states defined by distinct tRNA binding positions and specific degrees of SSU head and body rotation, see Figure 12). The translocational states, described in the following text, are consistent with previous structural studies (Frank and Agrawal, 2000; Brilot et al., 2013; Fischer et al., 2010; Ramrath et al., 2013; Rundlet et al., 2021) and with single molecule FRET data (Chen et al., 2011; Wasserman et al., 2016; Rundlet et al., 2021).

In the classical state PRE ribosomal complexes, the acceptor ends of the A - and P-site tRNA can move spontaneously to P and E sites of the LSU, respectively (Moazed and Noller, 1989). Consequently, the tRNAs adopt intra-subunit A/P and P/E hybrid binding states, in which the tRNAs are bound to different sites with respect to the SSU and LSU. The anticodon steam loop (ASL) of the tRNAs remain the contact on the SSU, while their acceptor arms contact the P-site and E-site on the LSU, respectively. The formation of tRNA hybrid binding states is accompanied with the rotational movement of the SSU in the forward direction (clockwise movement) and to different degrees relative to the LSU (as described in chapter 1.2.3.1; Valle et al., 2003; Cornish et al., 2008; Rundlet et al., 2021). This intersubunit rotation combined with the presence of A/P and P/E tRNAs characterize the hybrid state of PRE ribosomal complexes (Figure 12A).

The tRNA hybrid state formation favors the translocation catalysis by lowering the energy barrier for it (Semenkov et al., 2000). Moreover, it has been shown that the hybrid state PRE

complexes are stabilized by binding of EF-G (Blanchard et al., 2004; Dorner et al., 2006; Frank and Agrawal, 2000; Munro et al., 2009b, 2010; Spiegel et al., 2007; Valle et al., 2003). However, whether EF-G-mediated translocation occurs from the classical state and/or hybrid state PRE complexes is still controversial (Chen et al., 2011; Wasserman et al., 2016; Belardinelli et al., 2016; Rodnina et al., 2018).

EF-G is composed of five domains (Figure 11; Czworkowski et al., 1994; Ævarsson et al., 1994): the GTP-binding domain I, the highly conserved domain II, the domain III which is required for the GTP-hydrolysis in EF-G (Martemyanov et al., 2000), domain IV that mimics the anticodon stem-loop of a tRNA (Lindahl et al., 1994; Nissen et al., 1995) and domain V.

EF-G can adopt a compact or elongated conformation by large movement of domain III, IV and V (Figure 11A and B; Lin et al., 2015). The favored conformation of non-bound EF-G is controlled by the biochemical environment, while ribosome-bound EF-G was found predominantly in the elongated conformation -except for the initial binding complex (Czworkowski et al., 1994, Salsi et al., 2016).

During translocation, EF-G binding is stabilized by its interaction with multiple elements of the 70S ribosome (Figure 11C; Zhou et al., 2013; Gao et al., 2009). The domain I, domain III and domain V are bound at the GTPase associated center (GAC; see chapter 1.2.3.2), domain II is positioned at the 30S shoulder and domain IV extends over the ribosomal A-site.

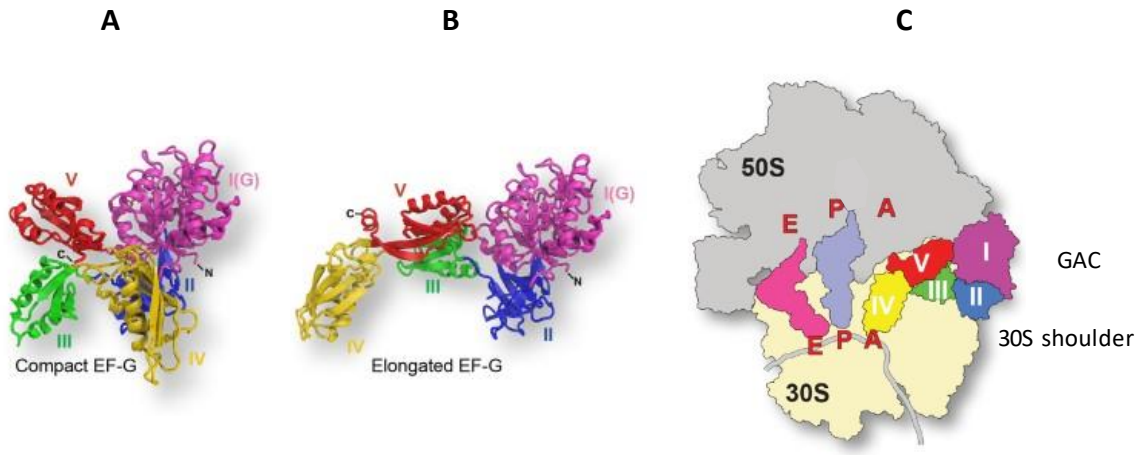

Figure 11: Cartoon representations of EFG. A) The compact EF-G conformation. B) The elongated EF-G conformation. C) EF-G bound to a post-translocational intermediate state. The Figure was adapted from Lin et al., 2015.

Binding of EFG to PRE ribosomal complexes causes conformational changes of the SSU in which the SSU body and SSU head rotate stepwise in the opposite directions (Zhou et al., 2013, 2014; Ramrath et al., 2013; Ratje at al., 2010). Early translocation intermediates contain EFG-GTP and exhibit hybrid A/P and P/E tRNA configurations (Ratje et al., 2010; Rundlet et al., 2021). It is suggested that the following EF-G-induced GTP hydrolysis causes an uncoupling of the SSU head and body movements (Zhou et al., 2013; Ramrath et al., 2013; Rundlet et al., 2021). The SSU head continues to move in the forward direction, while the SSU body progressively moves backward (counterclockwise), forming translocational intermediate states with chimeric bound ap/P and pe/E tRNA (see also chapter 1.2.3.1 and Figure 12B), originally termed post-translocational intermediate state (TI-POST) (Ratje et al., 2010).

The structural rearrangement within the ribosome leading to the chimeric states may facilitate the coupled tRNA-mRNA movement by opening ribosomal regions e.g., the ribosomal subunit interface and decoding region that stabilizes the position of tRNA and mRNA in the A and P sites (Savelsbergh et al., 2003; Ramrath et al., 2013). During the ribosomal rearrangements in the translocation intermediates, EF-G is proposed to function as a doorstop via its domain IV inserted in the A site that prevents reverse translocation of tRNA during reverse rotations of the SSU head and body domains (Connell et al., 2007; Ratje et al., 2010).

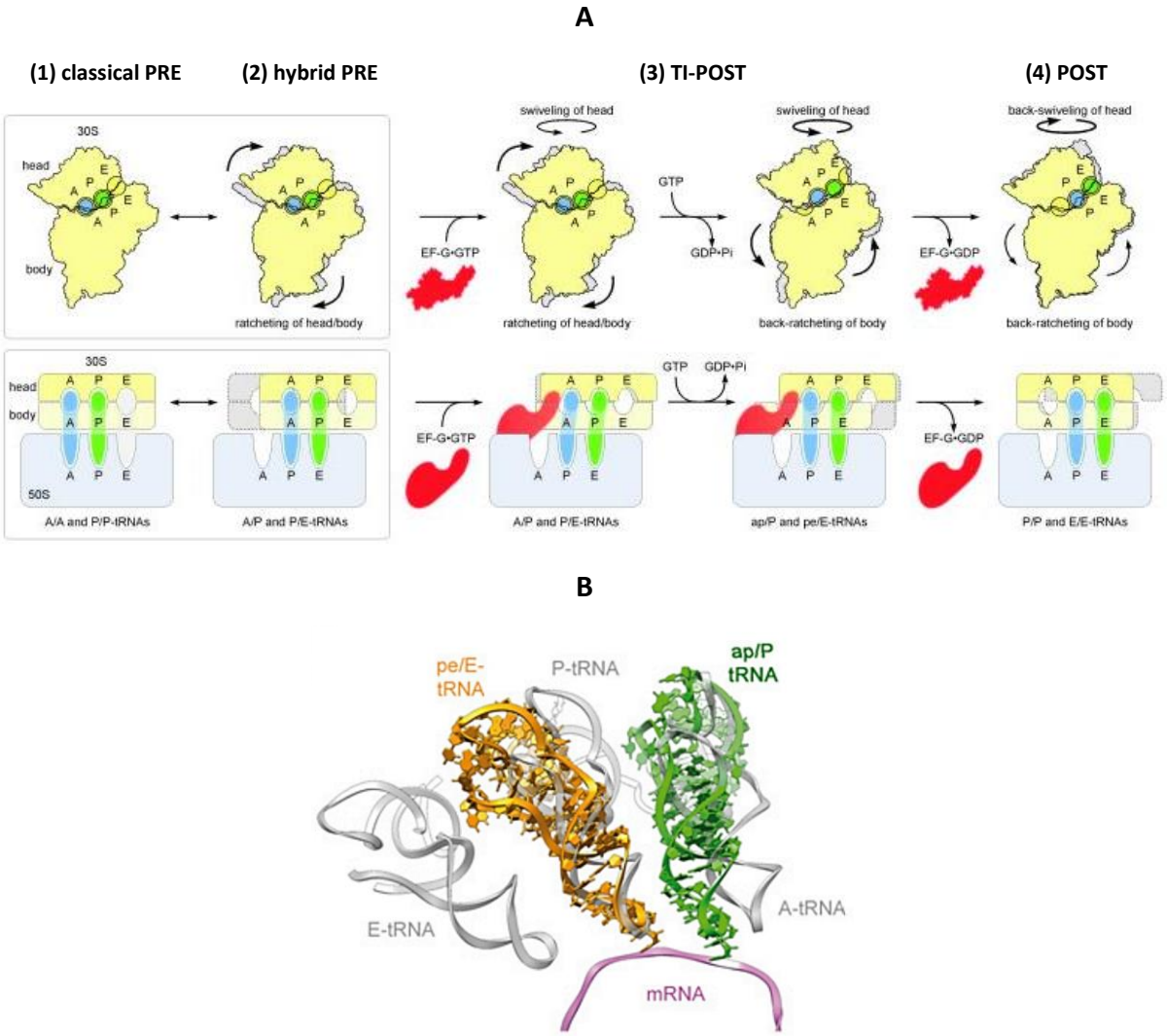

Figure 12: Translocation complexes. A) Model of the translocation. In the pre-translocation state, the ribosome alternates between the (1) classical conformation with classical A/A and P/P tRNAs and (2) the rotated conformation with hybrid A/P and P/E tRNAs. (3) Binding of EF-G-GTP to the rotated conformation of the ribosome causes head swiveling. Subsequent rotational movement of the head and back rotation of the 30S body brings the tRNAs from the A/P and P/E states to the chimeric ap/P and pe/E states within the subunit. (4) Complete back-rotation of the 30S subunit and dissociation of EF-G-GDP leads to the formation of the POST state. Figure was adopted from Ratje et al, 2010. B) Overlay of the ligands from the TI-POST complex (ap/P tRNA: green, pe/E tRNA: orange, mRNA: pink) with tRNAs in classic A, P, and E-site (grey) upon 30S head alignment. Figure was taken from Ramrath et al., 2013.

In the final steps of translocation, the SSU head and body rotate back completely, and EF-G-GDP dissociates from the ribosome. The resulting POST state with classically bound P/P - and E/E - tRNA can enter the next elongation cycle, unless no stop codon is present in the A-site (Ratje et al., 2010; Ermolenko and Noller, 2011; Belardinelli et al., 2016, Rundlet et al., 2021).

A spontaneous translocation without EF-G can occur in both directions but is extremely slow (Konevega et al, 2007; Shoji et al, 2006). But the interaction of EF-G on the ribosome provides the directionality of the translocation and lowers the energy barrier for the mRNA-tRNA translocation (Adio et al., 2015). Moreover, to understand fully the EF-G catalyzed translocation mechanism, the translocation steps as well as their timing remain to be further investigated.

1.3.3 Termination of bacterial translation

The elongation stops when reaching one of the three universal stop codons (UAG, UAA, UGA). The following termination reaction involves the class I release factors, RF1 and RF2 and the class II release factor RF3 (Figure 9). Class I release factors are proteins that recognize stop codons and remove the peptide-chain from the P-site bound tRNA. While the class 2 release factors are GTPases that facilitate the class 1 RFs to dissociate from the ribosome (Jakobsen et al., 2001).

RF1 and RF2 read the codons UAG/UAA and UGA/UAA, respectively. The binding of RF1 and RF2 to their respective stop codon takes place via their characteristic recognition motif, PAT in RF1 and SPF in RF2, which are in the domain II of these factors (Ito et al., 2000). The hydrolysis of the ester bond linking the tRNA to the peptide chain involves the peptidyl transferase center and the action of the universally conserved GGQ motif in domain III of RF1 and RF2 (Moffat und Tate, 1994; Zavialov et al., 2002).

The resulting so-called post-termination complex consisting of a deacylated tRNA in the P site and RF1/2 in the A site is bound by RF3 in its GDP-form (Zavialov et al., 2001; Zhou et al., 2012). The ribosome-mediated nucleotide exchange induces conformational changes in RF3. This leads to the dissociation of class-I release factors, GTP-hydrolysis in RF3 and subsequent RF3-GDP dissociation from the ribosome (Peske et al. 2014).

1.3.4 Recycling in bacterial translation

The post-terminal ribosomal complexes must be freed from both mRNA and tRNA and split into its ribosomal subunits, which then can be used again for further translations. This process is termed ribosome recycling, which requires an interaction of the ribosome recycling factor (RRF), the elongation factor G (EF-G) and the initiation factor IF3 (Figure 9; Hirashima and Kaji, 1973). Ribosome recycling starts when RRF docks to the ribosomal A-site (Gao et al. 2005)

before EF-G binding (Borg et al. 2016). There are two models that describe the next events of the recycling process.

One model suggests that ribosome splitting into their subunit is accomplished by EF-G-induced GTP-hydrolysis and the subsequent release of inorganic phosphate (Pi). The resulting SSU is still carrying the mRNA and tRNA is bound by IF3 inducing the release of both, mRNA and tRNA (Seo et al. 2004; Peske et al. 2005; Savelsbergh et al. 2009; Borg et al. 2016; Fu et al. 2016; Prabhakar et al. 2017). However, the usage of an mRNA without Shine-Dalgarno sequence, which is known to stabilize the codon-anticodon interaction, leads to an alternative model (Chen et al. 2017). This model proposes a novel function of EF-G, namely where EF-G promotes the release of mRNA by GTP-hydrolysis. This, in turn, facilitates the dissociation of the tRNA from the ribosome which subsequently is split into its subunits (Chen et al. 2017). Further studies are needed to clarify the correct order of events and whether multiple different recycling pathways are possible.

1.4 Ribosomal stalling during translation

During protein synthesis, ribosomes can stall (stalling = stopping the translation process) due to various reasons, such as mRNA frameshifting, read-through of the stop-codon, or the presence of damaged, truncated or stop-codon lacking mRNAs. Stalled ribosomes cannot undergo canonical elongation or termination, ultimately forming a nonstop complex that would reduce the pool of active ribosomes if not resolved.

Moreover, ribosome stalling produces incomplete and potentially toxic nascent proteins (Shoemaker and Green, 2012; Keiler, 2015). In order to maintain protein homeostasis and cellular fitness, all organisms have evolved strategies to sense and rescue stalled ribosomes and target the associated aberrant proteins for degradation (Bengston and Joaziero, 2010; Brandman et al., 2012; Defenouillère et al., 2013; Verma et al., 2013).

In the following chapters (1.4.1 and 1.4.2), two pathway ways to rescue stalled ribosomal complexes in prokaryotes are described in detail, since they are the focus of the PhD thesis.

1.4.1 *Trans*-translation

When the ribosome reaches the 3'-end of an mRNA lacking a stop codon, the translation cannot be continued efficiently because no stop codon is present (Keiler et al., 1996). The resulting ribosomal complex containing the P-site bound peptidyl-tRNA is stalled on the defective mRNA. To rescue such stalled ribosomes, bacteria have evolved a remarkable mechanism known as *trans*-translation, which is performed by a complex of transfer-messenger RNA (tmRNA) and small protein B (SmpB) (Keiler et al., 1996; Moore and Sauer, 2007; Janssen and Hayes, 2012; Giudice and Gillet, 2013).

The tmRNA, encoded by the gene ssrA, is a highly conserved, about 400 nucleotide long RNA molecule that contains a tRNA-like domain (TLD), an mRNA-like domain (MLD), and four pseudo-knots (PK 1-4) (Figure 13).

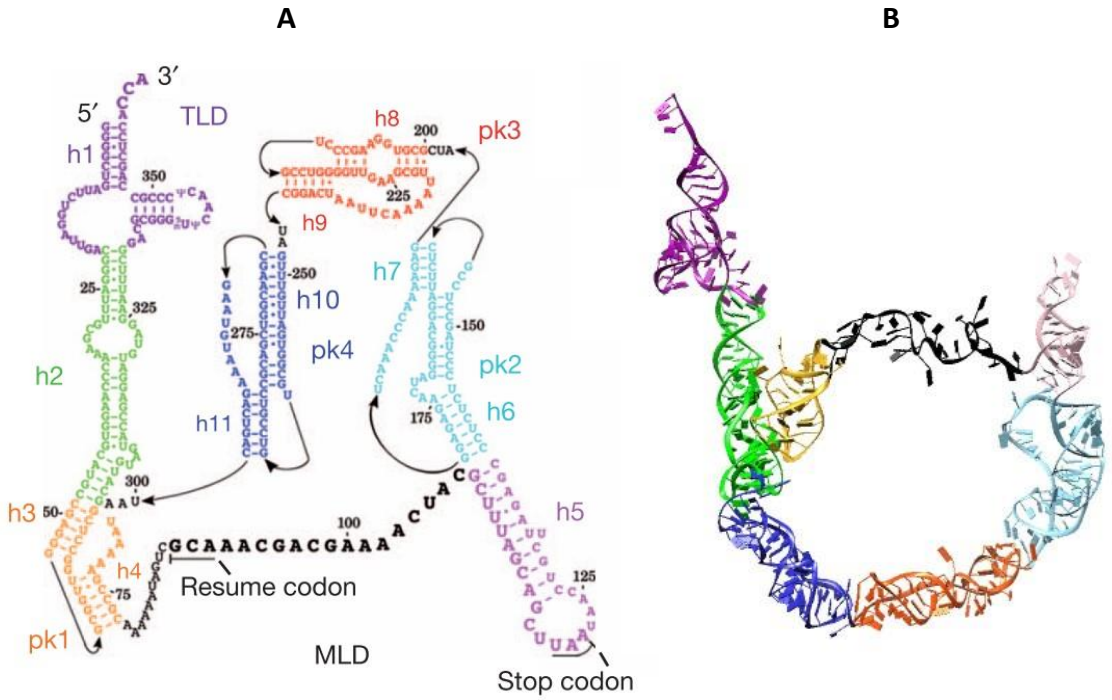

Figure 13: Composition and structure of the tmRNA. The *E. coli* tmRNA is shown as A) secondary structure (Ramrath et al., 2012) and as B) three-dimensional structure (this work), both color-coded according to their components, TLD (purple), helix 2 (green), pk1 (orange), pk2 (cyan), pk3 (red), pk4 (blue) and the MLD (black). The resume codon and stop codon are indicated.

The tmRNA TLD structurally and functionally mimics the acceptor and T-arms of the tRNA, while the anticodon arm- and D-loop are replaced by the globular domain of its interaction partner SmpB, distinguishing the tmRNA from a typical tRNA molecule (Figure 14).

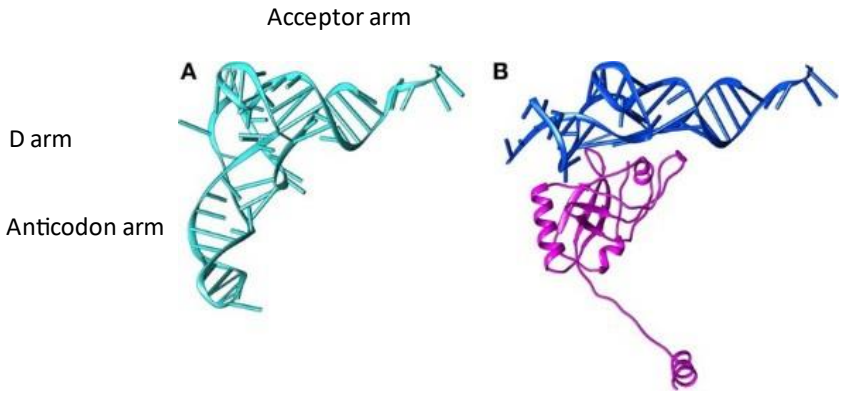

Figure 14: Comparison of a normal tRNA (A) and TLD/SmpB of the tmRNA (B). The upper part of the tRNA, formed by the acceptor arm (= T stem loop) and D arm (= D stem loop), matches the TLD (blue) consisting of the acceptor arm, but a reduced D-loop with lacking D stem. The lower part of the tRNA, formed by the anticodon arm (= anticodon stem loop) and D arm, is replaced by SmpB (magenta), which binds the elbow region of the TLD. The figure was adopted from Giudice et al., 2014.

SmpB comprises 160 amino acids in *E. coli*, that forms in solution an unstructured C-terminal tail and a globular domain (Dong et al., 2002). The structure of the globular domain consisting of an antiparallel β-barrel and three alpha-helices is preserved after binding to the ribosome. Whereas the SmpB C-terminal tail (in *E. coli*, residues 131 to 160) was observed to form an α-helix on PRE ribosomes (Himeno et al., 2014; Neubauer et al., 2012). The globular domain of SmpB possess a binding site at the ribosomal A-site and P-site, whereas the SmpB C-terminal was observed to occupy the mRNA channel (Kurita et al, 2010; Neubauer et al., 2012).

Binding of SmpB to the tmRNA prevents it from being degraded and helps in its aminoacylation (Hanawa-Suetsugu et al., 2002). As for canonical tRNA (see chapter 1.2.1), the aminoacylation of tmRNA occurs at its 3'-end by an appropriate aminoacyl-tRNA synthetase before delivery to the ribosome. The tmRNA is aminoacylated with an alanine by the alanyl-tRNA synthetase (Komine et al., 1994; Ushida et al., 1994).

The *trans*-translation is initiated by EF-Tu mediated delivery of the Ala- tmRNA-SmpB conjugate, which senses and then enters the vacant ribosomal A-site of the nonstop complex (Figure 15; Barends et al., 2002; Miller at al., 2014). Release of EF-Tu induces the tmRNA-SmpB accommodation into the A-site which is followed by the transfer of the nascent peptide from the P-site tRNA to the alanine of the tmRNA 3'CCA end. The canonical GTPase EF-G translocates the TLD-SmpB module from the A-site to the P site (Ramrath et al., 2012), which leads to the replacement of the defective mRNA by the MLD of the tmRNA.

The MLD encodes a resume codon to continue the translation and provides a proteolysis-inducing tag as well as a stop codon. Thus, the *trans*-translation leads to a conventional termination, the release of aberrant peptide chain, which is labeled for degradation. The degradation sequence of tmRNA-tagged proteins includes the last four amino acids, ALAA (alanine-lysine-alanine-alanine), which are targeted by cellular proteases (Herman et al., 1998; Choy et al., 2007). After termination the ribosome is recycled in the canonical way.

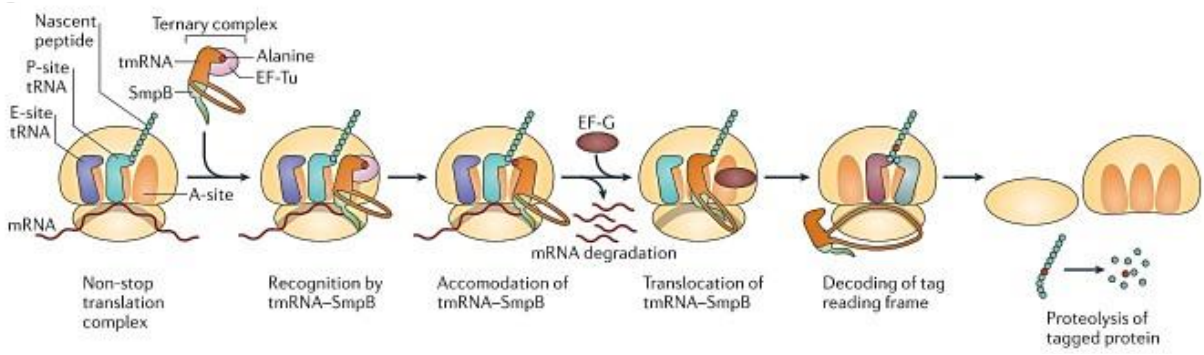

Figure 15: Schematic mechanism of *trans*-translation. The tmRNA/SmpB complex is delivered by EF-Tu-GTP to the ribosomal non-stop complex. The C-terminal tail of SmpB recognizes the empty mRNA channel and binds the ribosomal A-site resulting in the formation of the pre-accommodated state. After release of EF-Tu, the TLD is placed into the PTC causing the full accommodation mRNA–SmpB complex into the ribosomal A-site. The nascent peptide is transferred from the P-site bound tRNA to the alanine attached to the tmRNA. EFG induces translocation of the peptidyl-tmRNA–SmpB positioning the MLD of the tmRNA into the mRNA channel. The translation continues and terminates using the resume and stop codon encoded by the MLD of the tmRNA, respectively. The protein tagged for the proteolytic degradation is released and the ribosome can be recycled. The figure was taken from Keiler, 2015.

The *trans*-translation system is unique to prokaryotes but is not present and essential for all bacteria (Himeno et al., 2014). Since it has been shown that the absence of the *trans*-translation system would lead to loss of pathogenic potency of some infectious bacteria, it is targeted for antibiotics (Ramadoss et al., 2013).

Those bacterial species that do not naturally possess the *trans*- translation system, use alternative ribosome protein factors, e.g., ArfA, ArfB, or BrfA which rescue stalled ribosomes by promoting the peptidyl-tRNA hydrolysis. But these rescue factors do not target the nascent polypeptide chains for degradation (Keiler and Feaga, 2014; Goralski, Kirimanjeswara and Keiler, 2018; Shimokawa-Chiba et al., 2019). However, recently an alternative rescue factor RqcH was discovered, which functions in the proteolytic degradation of the aberrant nascent chains (Lytvynenko et al., 2019; see also next chapter 1.4.2). Unlike the tmRNA targeting

stalled 70S ribosomes, RqcH targets 50S subunits obstructed with a peptidyl-tRNA arisen from splitting of stalled ribosomes.

Various cryo-EM structures presenting the pre-accommodated state (Valle et al., 2003), pre-translocational state (Weis et al., 2010), the post-translocational intermediate state (Ramrath et al., 2010) and the post-translocational state (Fu et al., 2010; Weis et al., 2010) revealed that ribosomal complexes bound by tmRNA-SmpB undergo specific conformational changes along the cycle of *trans*-translation. However, due to their low resolution, the structures show only the overall shape and binding positions of the bound ligands within the *trans*-translation complex.

At this time, the highest resolution with 8.3 Å of a *trans*-translation structure was achieved in the cryo-EM study of the tmRNA-SmpB complex bound to the post-translocational intermediate state (Ramrath et al., 2012). Compared to the canonical TI-POST state, Ramrath et al., 2012 found an extra-large 30S head rotation in the post-translocational intermediate state bound to tmRNA-SmpB (here abbreviated to tmRNA-TI-POST state). This large 30S head rotation was proposed to be crucial for the coupled tmRNA-translocation and MLD loading. Due to the limited resolution, the interplay of the MLD and SmpB's C-terminal tail in the tmRNA-TI-POST structure couldn't be visualized.

1.4.2 Ribosome-associated quality control (RQC) in eukaryotes and prokaryotes

In eukaryotes, nonstop translation complexes are sensed by factors such as Hbs1, Dom34 and Hel2 (Hbs1L, Pelota and ZNF598 in mammals, respectively), which promote ribosomal subunit splitting (Buskirk and Green, 2017; Inada, 2017; Joazeiro, 2017). As a result of their action, the mRNA is released from the 40S subunit and subsequently degraded, but the peptidyl-tRNA remains associated with the 60S subunit. This obstructed complex provides a substrate for the process known as ribosome-associated quality control (RQC).

In the RQC pathway, the disassembly of the nascent chain-obstructed 60S complex is performed in a multi-step reaction (Figure 16) involving various factors (Bengston and Joaziero, 2010; Brandman et al., 2012).

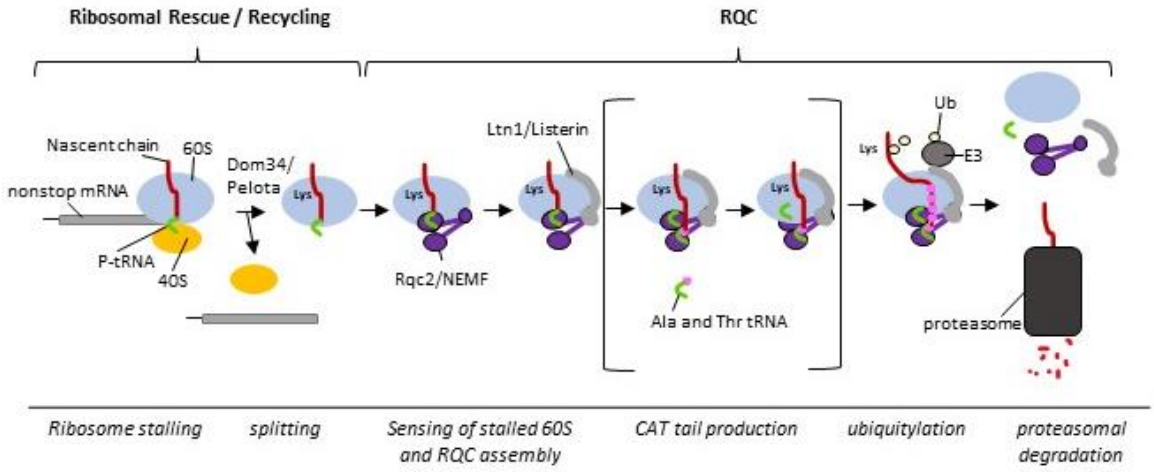

Figure 16: Overview of ribosomal rescue and RQC in eukaryotes. Components involved in ribosomal splitting, rescue and degradation are shown. Splitting of 80S ribosomes with nonstop-mRNA is performed by Dom34/Pelota. The resulting peptidyl-tRNA-60S complex is bound by Rqc2/NEMF, which help in recruitment of the E3 ligases, Ltn1/Listerin. The brackets refer only to Rqc2/Ltn1: In the case that Ltn1 does not have access to lysine ubiquitylation sites, Rqc2 can produce CAT tails. In the course of this, lysine residues leave the peptide exit tunnel and become accessible for ubiquitylation by Ltn1. The degradation of ubiquitylated nascent chains is carried out by the proteasome. Figure was prepared using Microsoft Office.

Rqc2 (yeast) / NEMF (mammals) initiates RQC by selectively recognizing the exposed, nascent-chain-conjugated tRNA on obstructed 60S subunits (Lyumkis, 2014). Subsequently, Rqc2/NEMF recruits and stabilizes the E3 ligase Ltn1 (yeast) / Listerin (mammals) which ubiquitylates the nascent polypeptide exiting the LSU, priming it for degradation at the proteasome (Bengtson and Joazeiro, 2010; Brandman et al., 2012; Defenouillère et al., 2013; Shao et al., 2015).

Additionally, Rqc2 possesses the unique ability to mediate mRNA-independent elongation of the nascent chain by C-terminal addition of alanine/threonine (Ala/Thr) residues (CAT-tailing) via recruitment of Ala- and Thr-tRNA to the A-site (Shen et al., 2015). This process is thought to assist Ltn1/Listerin-mediated ubiquitylation by pushing out lysine residues hidden within the ribosomal peptide exit tunnel (Kostova et al, 2017).

A recent study has uncovered a homologous mechanism to CAT-tailing in bacteria, whereby RqcH (the Rqc2 homolog) mediates the mRNA-independent elongation of nascent chains obstructing the 50S subunit by adding C-terminal alanine extensions (Ala tails) (Lytvynenko et al., 2019). The bacterial Ala tail itself acts as degron that signals proteolysis of the tagged nascent chain. Rqc2 homologs (RqcH, Rqc2, Caliban in Drosophila, and NEMF) define the NFACT family

of RNA-binding proteins, which can be traced to the LUCA (last universal common ancestor) (Doherty et al., 1996; Burroughs and Aravind, 2014). All NFACT family members display the same structural architecture formed of an N-terminal NFACT domain (NFACT-N), a helix-hairpin-helix domain pair (HhH), coiled-coil helices (CC1 and CC2) linked by a middle domain (M domain), and followed by an NFACT-R domain ("R" for predicted function in RNA binding). Eukaryotes and archaea possess an additional C-terminal domain, NFACT-C (Figure 17).

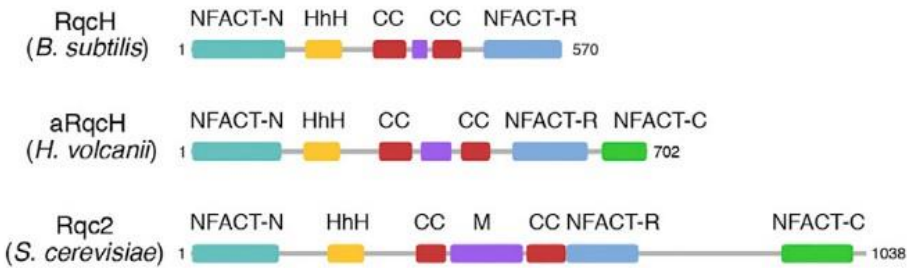

Figure 17: Domain organization of Rqc2 protein homologs. Shown are the protein domain compositions of *B. subtilis* RqcH, the homolog in *archaeon H. volcanii* (aRqcH), and *S. cerevisiae* Rqc2: NFACT*-N in cyan (N for N-terminal), HhH (helix-hairpin-helix; yellow), middle domain (M; purple), coiled coil (CC, red), and NFACT*-R in blue (R for RNA binding) and NFACT*-C in green (C for C-terminal). *NFACT is an abbreviation for NEMF, FbpA, Caliban, Tae2. The figure was taken from Lytvynenko et al., 2019.

Cryo-EM studies of eukaryotic RQC complexes revealed that Rqc2 and NEMF bind similarly to the 60S subunit-interface, using the NFACT domains to contact bound tRNAs; in addition, the coiled-coil helices form a spacer that crosses the A site and anchors the factor around the stalk base (Lyumkis et al., 2014; Shao et al., 2015; Shen et al., 2015). Furthermore, in each of the structures, the E3 Ligase Ltn1/Listerin was docked to the M domain of Rqc2/NEMF. At this time, no structural information of bacterial RQC complexes were available. However, immunoprecipitation studies of FLAG-tagged RqcH revealed that RqcH binds the 50S ribosomal subunits (Lytvynenko et al., 2019).

1.5 Cryogenic electron microscopy (Cryo-EM)

The method of cryogenic electron microscopy (cryo-EM) uses temperatures below -160°C to image frozen-hydrated samples. In combination with single and multi-particle approaches for image processing, it is a powerful tool for analyzing structures of intrinsically flexible and heterogenous functional assemblies like ribosomal complexes (Frank et al., 1996; Grigorieff,

2016; Hohn et al., 2007; Loerke et al., 2010; Lyumkis et al., 2013; Penczek et al., 2006, 2011, Scheres, 2012, 2016; Spahn and Penczek, 2009).

The modern cryo-EM analysis is divided into three steps: cryogenic sample preparation, transmission electron microscope (TEM) imaging, and data processing and analysis. In the first step, an electron microscopy grid carrying a thin film with a sample solution is quickly frozen into liquid ethane. In the second step, the sample is recorded on detectors using a TEM with low electron doses at liquid nitrogen temperature. The third step refers to later computational processing that reconstructs a three-dimensional (3D) density map from the 2D projections (also called particle images) and atomic model building from the reconstructed map.

An overview of the complete cryo-EM process from sample preparation to interpretation of the final 3D structure is given in Figure 18.

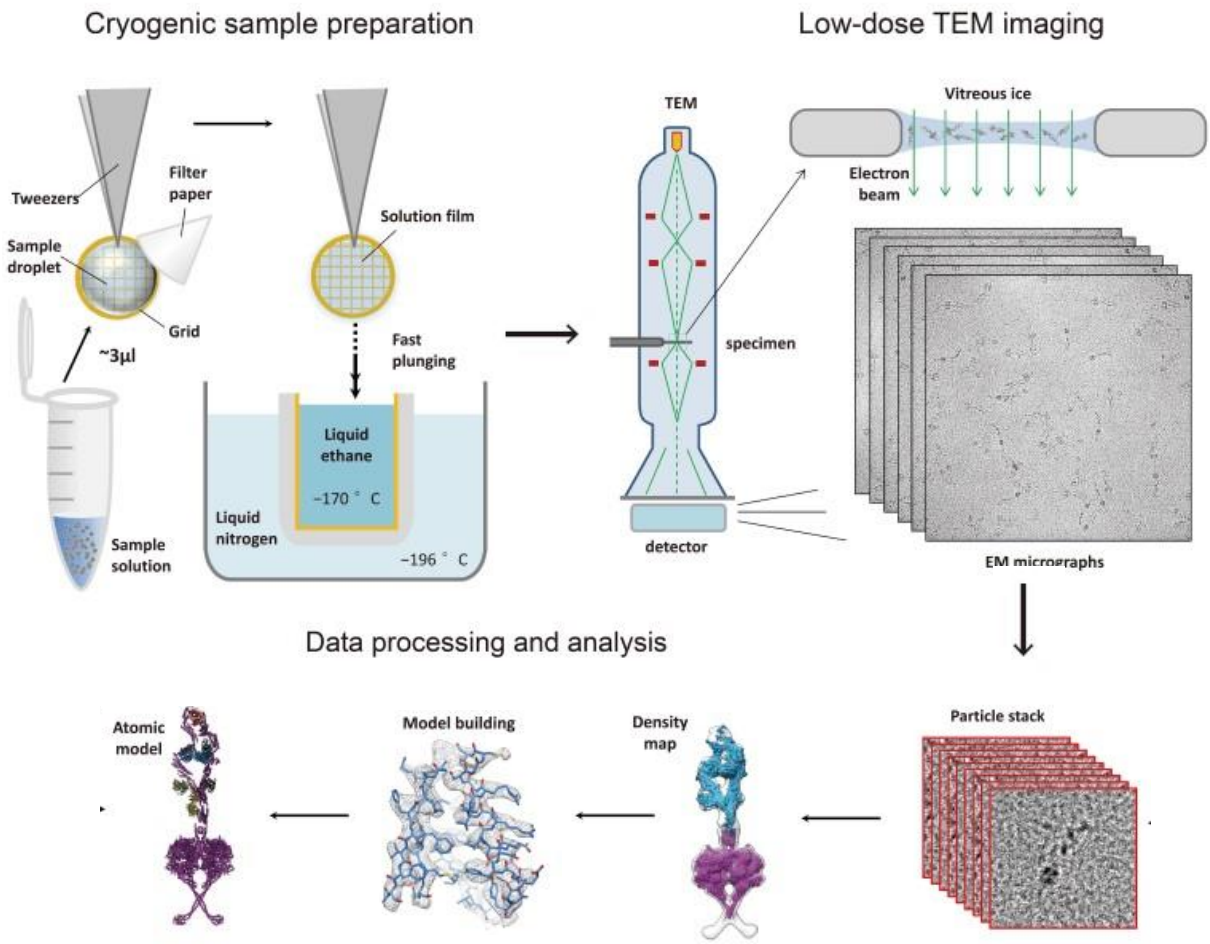

Figure 18: Overview of the process for cryo-EM analysis. The overview shows the cryo-EM process from sample preparation to interpretation of the final three-dimensional structure. Figure was adopted from Zhang and Liu, 2018.

1.5.1 Setup of an electron microscope

The first electron microscope (EM) was developed in 1931 at the Technische Hochschule Berlin by Max Knoll and his PhD student Ernst Ruska (Knoll and Ruska, 1932). The latter was awarded the Nobel Prize for Physics in 1986. Despite technological innovations, the principles and composition of the EM prototype still govern modern EMs. The basic composition of any EM is identical and analogous to that of a light microscope (Orlova and Saibil, 2011).

At the top of the electron microscope is a radiation source, followed by a series of lenses inside of the column, and an image detecting system at the bottom of the column (Figure 19). The radiation source of an EM is called cathode, also known as filament or electron gun, which contains tungsten, lanthanum hexaboride or cerium hexaboride crystals as electron emission material. There are two electron gun types, the thermionic electron gun where the electrons are emitted after heating the solid (e.g., tungsten wire), and the cold field emission gun (FEG) where a strong electromagnetic field is used to extract the electrons from a tungsten or hexaboride crystals. After heating (tungsten wire) or through a high electromagnetic field (in case of the FEG), the cathode emits electrons, which are accelerated by an electric field in the field direction (towards the positive anode).

The principle of the following electron optical lenses is the deflection of electrons by an electromagnetic force. The condenser lens focuses the primary electron beam onto the sample, the objective lens creates a magnification of 20 to 50-fold, and the projection lens additionally enlarges the intermediate image. In this lens arrangements, there is an objective aperture at the back focal plane of the objective lens that prevents electron scattering at high angles, which improves the image contrast. The images are viewed on a fluorescent screen or detected by a digital camera.

Electron microscopes are operated under a vacuum to protect the electron source from oxidation or the electron beam from interfering with air molecules. In order to maintain the vacuum system, various pumps, and their associated measurement equipment, as well as power supplies are needed.

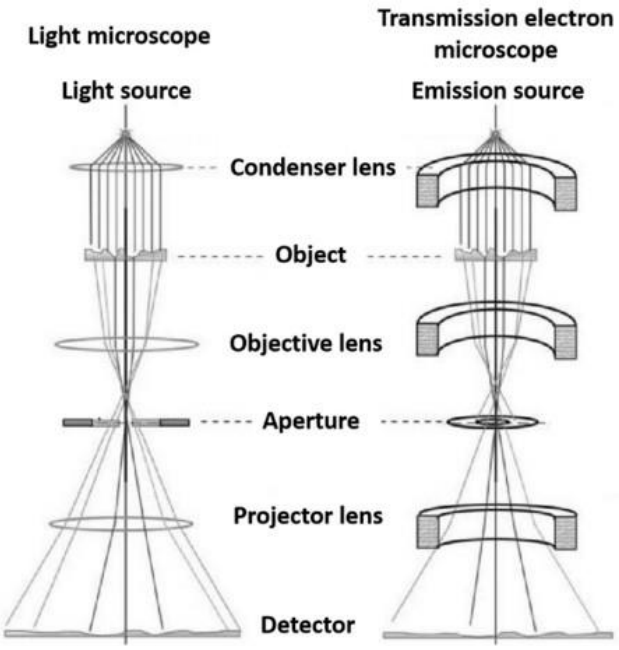

Figure 19: Comparison of a light and an electron microscope. The basic components of a light and electron microscope are shown. Figure was taken from Orlova and Saibil, 2011.

1.5.2 Image formation in TEM

By using electrons, which combine the properties of waves and particles (Broglie, 1924), it is possible to achieve much higher resolutions than with visible light. The highest attainable resolution (dmin) is inversely proportional to the wavelength (λ) of the radiation divided by the numerical aperture of the microscope (NA) (Abbe, 1873):

$$dmin = \frac{\lambda}{2NA}$$

The wavelengths of electrons directly depend on the acceleration voltage of the emission source. The higher the acceleration voltage, the better the theoretically achievable resolution (Milne et al., 2013). At a voltage of 300kV, typically used in cryo-EM, the wavelength of an electron is 0.002 nm which is five orders of magnitude smaller than that of visible light (λ~400-700 nm). Thus, the electron microscopy technique enables very high resolution, potentially allowing the identification of single atoms (atomic resolution).

In transmission electron microscopy (TEM), the electrons of the electron beam are emitted by the electron source which can pass through the specimen with or without interacting with its atoms (Figure 20).

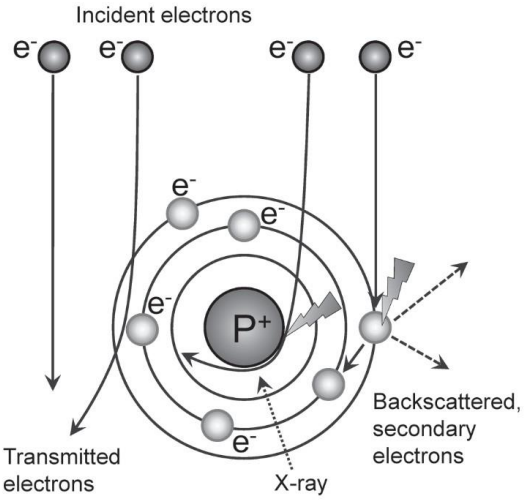

Figure 20: Interaction between the electron beam and the specimen. The incoming electrons can be deflected at the atomic electrons without energy loss, termed elastic scattering, or collide with atomic electrons or nuclei resulting into energy loss which is called inelastic scattering. Figure was taken from Orlova and Saibil, 2011.

All of them, the absorbed, transmitted, and scattered electrons contribute to the formation of the image and contrast. The contrast of an image is determined by the nature and the extent of the interactions between the electron beam and the sample (Hanszen, 1971). Contrast is defined as relative difference in intensity between the image points and its environments. The three-dimensional structural information of the object plane is transformed into two-dimensional projections of the object in the image plane. Depending on the orientation of the particles in the ice, the resulting two-dimensional images are projections of different views.

Generally, one distinguishes two types of scattering interactions of the electron beam with the specimen (Orlova and Saibil, 2011). The elastic scattering where the electrons are deflected by the atomic electrons without energy-loss and the inelastic electron which are scattered by the atomic electrons or nuclei leading to energy-loss. The energy of the inelastic scattered electrons can be transferred to cloud electrons resulting the ionization, X-ray emission, secondary electron scattering or chemical bond rearrangement of the atoms which leads to a radiation damage of the specimen. In order to keep the radiation damage to a minimum, the low-dose imaging is used as a standard method in cryo-EM. In this method, the electron exposure of the region of interest is kept as low as possible before imaging it at high resolution. This is achieved by performing the search of an appropriate area under low electron dose conditions and determining a suitable focus outside of the selected area (Sun and Li, 2010).

Moreover, the inelastic scattered electrons are focused by the electromagnetic lenses in plane higher up in the microscope than the electrons that are elastically scattered due to their loss of energy after collision with the specimen. Focusing rays varying in wavelength at different positions in the focal plane is known as chromatic aberration which produces additional background and blurring (noise) in the image. However, the noise of the image can be reduced by using an energy filter that eliminates most of the inelastically scattered electrons (De Bruijn et al., 1993).

The scattering angle of electrons is dependent on the coulomb force and voltage. Decreasing distance between the electron and atomic nucleus, increasing atomic numbers (e.g., heavy metal contrasting) as well as decreasing velocity of the electron lead to larger scattering angles (Orlova and Saibil, 2011). Electrons scattered with large angles can be removed by the objective aperture. This improves the image contrast, but the removal of strongly scattered electrons also reduces the resolution of the image.

The remaining elastically scattered, as well as unscattered electrons emerging the specimen are focused by electromagnetic lenses onto the image plane and produce the scattering contrast, also known as amplitude contrast in the image. However, the proportion of scattering contrast in images is relatively low. The beam electrons hardly interact with the sample atoms because of their large velocity caused by the high operation voltage used in cryo-EM. Moreover, the specimen consisting of the biological sample on the carbon film that embedded in vitrified ice is entirely made of low atomic number elements, such as H, C, N, O, P and therefore, interact only weakly with the incoming electrons.

To improve the image contrast, one uses the wave properties of the electrons and the resulting phase contrast (Orlova and Saibil, 2011). Scattering of the electrons at varying angles produces electrons waves varying in their path lengths after emerging the specimen. In cryo-EM, the most image contrast results from the interference between the elastically scattered and unscattered electron waves passing through the sample. While the inelastically scattered electrons do not contribute to the scattering or phase contrast because of their very small scattering angles and changed wavelength, respectively.

The phase alterations in the exit wave provide the most structural information of the cryo-EM samples. However, they must be converted into amplitude variations because the sensor detects intensities (square of the amplitudes) only, but the amplitude of the emerging electron wave is not changed by the cryo-EM object.

Biological samples used in cryo-EM scatter electrons at small angles, therefore they are referred to as weak phase objects that produce only slight phase shifts with respect to the undeflected electron beam (Zhang et al. 2021). Thus, the importance of phase contrast increases, the smaller the object to be examined or the higher the microscope magnification.

Typically, the phase contrast of biological objects is enhanced using the combined effects of spherical aberration and image defocus (Erickson and Klug 1971). Both, the slight defocus, usually -0.5-5 µm, moving the image plane away from exact focus and differently strong ray refraction at the objective lens (spherical aberration) induce additional phase shifts between scattered and unscattered electrons.

Thus, it is important to know the correct microscope parameters such as spherical aberration, defocus, astigmatism (results from an asymmetric magnetic field in the lenses) and the acceleration voltage to get a good image quality.

1.5.3 Contrast transfer function

The imaging properties of the electron microscope are described by the contrast transfer function (CTF), a periodic sine function in reciprocal space (Figure 21) that modulates the image information (Wade, 1992). The CTF takes different aberrations (e.g., spherical aberration) as well as defocus of the object into account. It represents a curve oscillating around the zero point, whose maxima and minima provide the most image information. Extrema at high-spatial frequencies correspond to fine structural details, while low frequencies represent rough object structures.

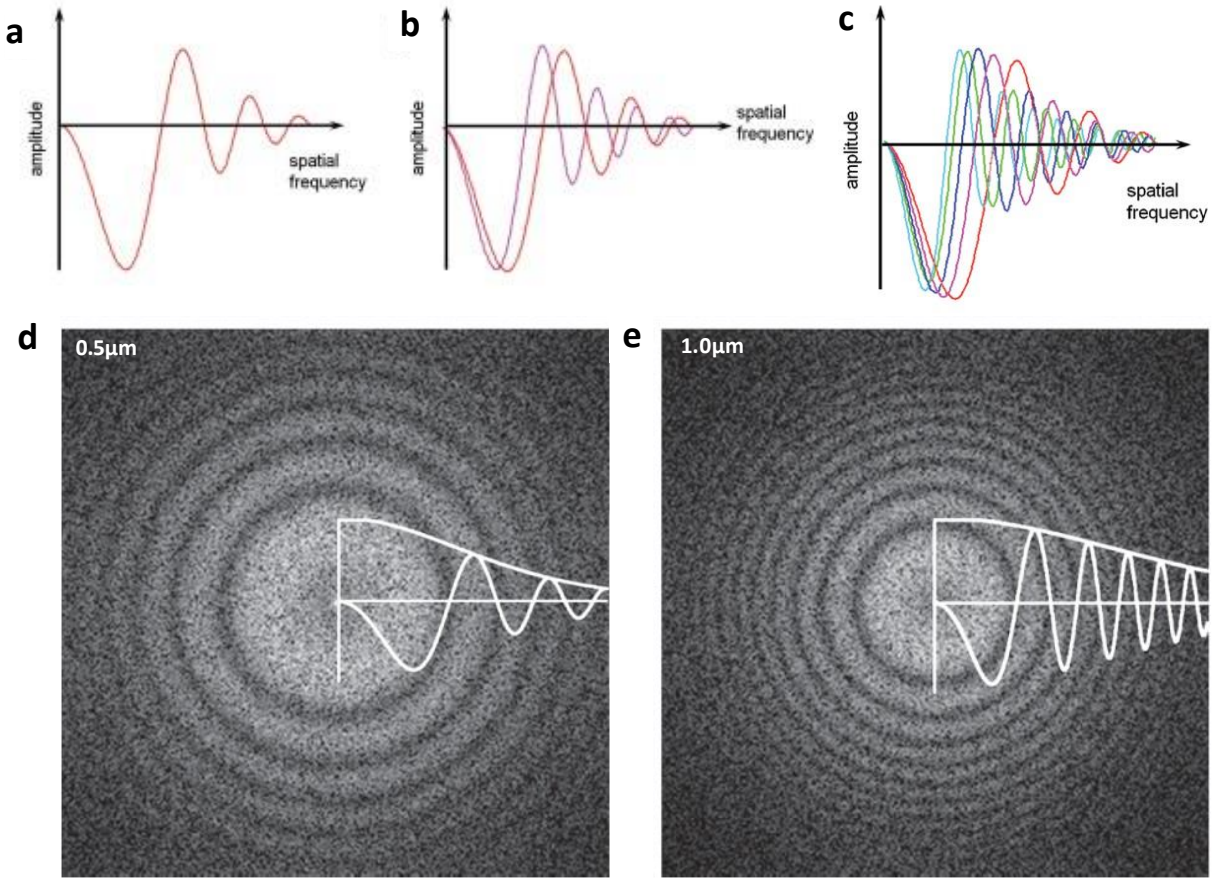

Figure 21: The contrast transfer function. (a) The CTF curves for a certain defocus value. (b) Overlay of CTF curves of two different defocus values. The red curve oscillates faster as the orange curve which represents an image that is closer to focus. (c) Overlay of several defocus values where the red curve is closest to focus, and the cyan curve correspond to images with the highest defocus. (d), (e) The two-dimensional power spectra of images of carbon film displaying Thon rings with corresponding CTF curves at d) 0.5 µm and e) 1 µm defocus. As the defocus increases, the oscillation of the CTF is amplified. The figures were taken from Orlova and Saibil, 2011.

The information content at the respective spatial frequency decreases as the CTF approaches the zero point. Every time the CTF crosses the x-axis, the contrast is inverted. At the zero points of the function no more information at this spatial frequency is transmitted. These information gaps can be recovered by altering the defocus from image to image (Penczek et al., 2006; Zhu et al., 1997). The different defocus values are chosen in such a way that the zeros of the corresponding functions are shifted against each other. The averaging of many single particle images varying in its defocus values allows to obtain the information for all spatial frequencies which improves the resolution of the reconstruction.

The influence of various instabilities (e.g., the electron beam, the detection system or drift) that attenuate the CTF with increasing frequencies and suppresses the information obtained

for high-spatial frequencies is described by the envelope function (Chiu and Glaeser, 1977). The point where the envelope function damps the CTF to zero represents the information limit of the microscope. The envelope function causes an underrepresentation of the fine structural details, which are of great interest in the field of structure biology. To improve the contrast and resolution of an image, the damped CTF components are recovered by a procedure that is called CTF-correction (Penczek, 2010).

CTF-correction requires a precise determination of the CTF which is done by measuring the defocus and astigmatism within each micrograph (Rohou et al., 2015). A simple method for CTF-correction is the phase-flipping operation, in which those Fourier components of an image that have negative amplitude values in the CTF are either multiplied by -1 or their phases are flipped by 180° (Orlova and Saibil, 2011). This reverses the negative values of the CTF to positive values, which then contribute to the image contrast.

Another method, called Wiener filtering, corrects both, the Fourier phases and amplitudes of the image using a filter for noise suppression (Wiener, 1964; Penczek, 2010). This method also helps to correct the CTF decay at high spatial frequencies. High-spatial frequency enhancement is also used for map sharpening, a standard method for visualizing high-frequency details in which the amplitude decay is rescaled according to the amplitude spectrum of an atomic reference structure (Schmid et al., 1999)

1.5.4 Revolutionary developments of the cryo-EM

The development of the cryo-EM opened a new era in biochemistry. This method facilitates imaging of biomolecules without crystallizing or applying structure-altering fixatives allowing the visualization of its native state and atomic details. For the development of this revolutionary method Joachim Frank, Richard Henderson and Jacques Dubochet received the Nobel Prize in Chemistry in 2017.

Frank invented the single particle analysis in EM: the improvement of the resolution and structural information in EM images by averaging the individual particle images (Frank, 1975). Henderson applied the EM technique on a protein complex for the first time (Henderson and Unwin, 1975). And Dubochet used the frozen hydration technique to preserve the structural integrity of biological samples (Taylor and Glaeser, 1974) for the EM (Dubochet and McDowall, 1981; Dubochet, et al., 1982).

The electron optic system of modern EMs itself is of sufficient quality to image radiation resistant material, typically inorganic samples, at subatomic resolution (better than 1 Ångström). The great improvement of the resolution in the single-particle cryo-EM, was achieved especially due to technological advances of the electron detectors.

The performance of the detector can be qualitatively determined by considering the Thon rings (Thon, 1966) or by the detectable quantum efficiency (DQE). Thon rings, calculated from recorded micrographs of carbon film, indicate the approximate frequency/resolution to which signal is visible (Bammes et al., 2011; Milazzo et al., 2011). The DQE, originally defined as the "useful quantum efficiency" (Rose, 1946), describes how efficiently an electron is detected at a given resolution.

Previously, micrographs of frozen-hydrated samples were acquired using photographic film or scintillator-based digital cameras, like charge-coupled device (CCD) or complementary metal-oxide semiconductor (CMOS) cameras. Compared to films, CMOS/CCD cameras enabled the digitalization of the images allowing an automated data acquisition. Additionally, they have a better low-frequency DQE resulting into an increased image contrast, but their high-frequency DQE is poorer (Li X et al., 2013; McMullan et al., 2014). Those digital cameras can detect only about 10% of the signal at high frequencies.

The loss of signal, thus the loss of resolution is manly caused by signal blurring, also known as point-spread-function (PSF) resulting from the conversion of signals from incident electrons into photons using the scintillator of the CMOS/CCD cameras. At present, the combined usage of direct electron detection device (DDD) cameras and beam-induced motion correction algorithms significantly improved the image quality in single particle cryo-EM (Brilot et al., 2012; Li X et al., 2013; Zheng et al., 2017). DDDs detect the charge distribution generated by each electron event which is very small minimizing the PSF, thus improving the camera performance at low and high resolution (McMullan et al.; 2009).

The technological advances of DDD revolutionized the single-particle cryo-EM (Kühlbrandt, 2014; Li X et al., 2013; McMullan et al., 2014). The so-called movie mode of DDD cameras allow to fractionate the total electron dose into a series of image frames which then can be aligned to compensate for specimen drift and beam-induced movement (Brilot et al., 2012; Campbell et al., 2012; Li et al., 2013a).

1.6 Aims of the presented work

Ribosomes that stall during translation must be rescued to preserve the protein synthesis capacity of the cell (Shoemaker and Green, 2012). In eukaryotes, the rescue pathway, ribosome quality control (RQC), starts after splitting of the ribosomes stalled. The mRNA is degraded, and the small subunit can be recycled, while the large subunit needs to be freed from the still associated unfinished peptide which is achieved by targeting the nascent chain for proteolytic degradation.

Most biochemical and structural studies dealt with the investigation of the eukaryotic RQC complexes (Lyumkis et al., 2014, Shen et al., 2015, Shao et al., 2015). They identified the eukaryotic factors NEMF/Rqc2 as key players in the recognition and degradation of nascent chain stalled ribosomal subunits. In contrast, the prokaryotic RQC pathway has been little studied so far.

Biochemical studies showed that the Rqc2 homolog (RqcH) in *B. subtilis* can bind to stalled 50S subunits suggesting that it recognizes the association of a P-site tRNA with a free 50S subunit as a characteristic of 50S obstruction (Lytvynenko et al., 2019). However, structural information of prokaryotic RQC complexes were lacking entirely. Therefore, and as part of the study in Lytvynenko et al., 2019, we used the wild-type RqcH-co-immunoprecipitated 50S subunit complex for cryo-EM analysis to gain structural insights of how RqcH binds to the 50S ribosomal subunit.

In bacteria, the primary system for freeing ribosomes stalled on mRNA lacking a stop-codon is the *trans*-translation pathway (Keiler at al., 1996; Karzai et al., 1999). It comprises a transfer-messenger RNA (tmRNA) and its attached protein SmpB which take over the translation in *trans* by using its own ORF encoded in the mRNA-like domain (MLD) of the tmRNA, thereby targeting the nascent peptide for proteolysis.

First information of how the tmRNA-SmpB module accomplishes MLD positioning during movement through the ribosome was provided by a cryo-EM structure of the *E. coli* ribosome in complex with tmRNA-SmpB and EF-G (Ramrath et al., 2013), the tmRNA-TI-POST state. However, due to the technical limitation at this time, the tmRNA-TI-POST structure was only resolved to 8.3 Å, resulting to a lack of density for the MLD in the tmRNA and the C-terminus in SmpB. Therefore, we revisited the cryo-EM study of the tmRNA-TI-POST state in Ramrath et

al., 2013 and used advanced EM technologies, to visualize the full-length molecules of SmpB and tmRNA. This structural information, together with a more detailed analysis of the translocation states, is needed to enlighten the mechanism of the tmRNA-SmpB-translocation within the *trans*-translation process.

2 Material and Methods

2.1 Material

2.1.1 Bacterial strains

Table 1: Bacterial strains

stain	Relevant genotype	SOURCE
B. subtilis Wild-type 168 1A700	*trpC2*	BGSC
B. subtilis 168 Δ*rqcH*	*trpC2*	Lytvynenko *et al.* 2019
B. subtilis 168 *ΔrqcH ΔssrA*	*trpC2*	Lytvynenko *et al.* 2019

Table 2: Plasmids

Plasmid	Relevant information	Source
pHT01	amp^r, Cm^r, lacI, repA	MoBiTec
pHT01 RqcH-WT	P_{rqcH} RqcH-FLAG wild type T_{rqcH}	Lytvynenko *et al.* 2019
pHT01 RqcH-EIM	P_{rqcH} RqcH-FLAG EIM121AGG T_{rqcH}	Lytvynenko *et al.* 2019
pHT01 RqcH-YF376AA	P_{rqcH} RqcH-FLAG YF376AA T_{rqcH}	ZMBH, Joaziero lab
pHT01 RqcH-patch	P_{rqcH} RqcH-FLAG R476A R480A R534A T_{rqcH}	ZMBH, Joaziero lab
pHT01 RqcH-YF/patch	P_{rqcH} RqcH-FLAG YF376AA R476A R480A R534A T_{rqcH}	ZMBH, Joaziero lab
pHT01 RqcH-282-415	P_{rqcH} RqcH-FLAG aa 282-415 T_{rqcH}	ZMBH, Joaziero lab
pHT01 RqcH-loop1	P_{rqcH} RqcH-FLAG KYLRPK430GSGSGS T_{rqcH}	ZMBH, Joaziero lab
pHT01 RqcH-loop2	P_{rqcH} RqcH-FLAG KKPNGAK537GSGSGSG T_{rqcH}	ZMBH, Joaziero lab
pHT01 RqcH-loop1/loop2	P_{rqcH} RqcH-FLAG KYLRPK430GSGSGS KKPNGAK537GSGSGSG T_{rqcH}	ZMBH, Joaziero lab

2.1.2 Chemicals and Materials

Table 3: Chemicals and Materials.

Chemical and Materials	Source
ANTI-FLAG M2 Affinity Gel	Sigma
DNF-471 standard sensitivity RNA Analysis Kit (15nt)	Agilent
FLAG peptide	Sigma
Glutaraldehyde	Thermo Fisher Scientific
Holey carbon grids	Quantifoil
LDS sample buffer	Thermo Fisher Scientific
Mobicol ‘F’ column with a filter of 35 mmpore size	MoBiTec
MOPS buffer	Thermo Fisher Scientific
Ni-NTA agarose	QIAGEN
NuPAGE Bis-Tris gels (4–12%)	Thermo Fisher Scientific
Protease inhibitor (cOmplete ULTRA Tablets, EDTA-free)	Roche
RNAse-free water	Gibco Ultrapure (UP), Invitrogen
SERVA Blue G250	Thermo Fisher Scientific
Spermidine	Sigma-Aldrich
Spermine	Sigma-Aldrich
Stericup vacuum filters (22mm)	Millipore Sigma
Superose 12 column	GE Healthcare
TRIzol reagent	Life Technologies
Uranyl acetate	Fluka/Balzers Union AG
Yeast extract	Bacto

2.1.3 Buffers, solutions, and media

A10 binding buffer
10 mM magnesium acetate
4 mM β-mercaptoethanol
20 mM HEPES-KOH at pH 7.6
150 mM ammonium acetate
2 mM spermidine
0. 05 mM spermine

B4.5 binding buffer
4.5 mM magnesium acetate
4 mM β-mercaptoethanol
20 mM HEPES-KOH at pH 7.6
150 mM ammonium acetate
2 mM spermidine
0.05 mM spermine

Dissociation buffer
20 mM HEPES-KOH at pH 7.5
1mM magnesium acetate
200mM Ammonium acetate
4mM β-Mercaptoethanol

Elution buffer
50 mM Tris/HCl pH 7.5 at 4°C
100 mM potassium chloride
3 mM magnesium chloride
1 mM DTT

IP buffer
50 mM Tris/Cl pH 7.5 at 4°C
100 mM sodium chloride
3 mM magnesium chloride
5% Glycerol (v/v)
0.1% NP-40 (v/v)
1 mM DTT

LB-media
10 g/l BactoPepton
5 g/l yeast extract
10 g/l sodium chloride

Re-association buffer
20mM HEPES-KOH, pH=7.5
20mM magnesium acetate
30mM potassium acetate
4mM β-Mercaptoethanol 4 mM

Sample buffer for wilde-type RqcH-50S
50mM Tris/HCl pH 7.5
100mM sodium chloride
3mM magnesium chloride

Sample buffer for mutant RqcH-50S
20mM HEPES pH 7.5
100mM potassium chloride
5mM magnesium chloride
1mM DTT

Tico buffer
20mM HEPES-KOH, pH=7.5
6mM magnesium acetate
30mM ammonium acetate
4mM β-Mercaptoethanol 4 mM

2.1.4 Devices and Tools

Table 4: Devices and Tools.

Tools and Devices	Source
CM100 Electron microscope	Philips
Chromatography column	BioRad
Eagle CCD camera (Tietz	Tietz
FastScan-F114 CCD camera	Tietz
Fragment AnalyzerTM Automated CE System	Invitrogen
K2 Summit DED Camera	Gatan
Laboratory supplies	Roth, Eppendorf
Microfluidizer	EmulsiFlex C5; Avestin
Photometer Nanodrop 1000	Peqlab
Plasma Cleaner PDC002	Harrick
Pipettes	Gilson
SS-34 rotor (RCFavg = 22548.5)	Thermo Scientific
Table centrifuge 5415 D, R	Eppendorf
Tecnai G2 Polara F30 Electron microscope	FEI Company
Tecnai G2 Spirit F30 Electron microscope	FEI Company
Titan Krios Electron microscope	FEI Company
Turning wheel	Labinco
Vitrobot	FEI Company

2.1.5 Software and online tools

Table 5: Software and online tools.

Software/Tool	Reference	Link
Adobe CC	-	http://adobe.com/
Chimera	Pettersen et al., 2004	https://www.cgl.ucsf.edu/chimera
CisTEM	Grant et al., 2018	https://cistem.org/
Clustal Omega	-	https://www.ebi.ac.uk/Tools/msa/clustalo/
Coot	Emsley and Cowtan, 2004	https://www2.mrc-lmb.cam.ac.uk/personal/pemsley/coot/

Software/Tool	Reference	Link
CryoSPARC	Punjani et al., 2017	https://cryosparc.com
CTFFIND4	Rohou and Grigorieff, 2015	https://grigoriefflab.umassmed.edu/
EMAN2	Tang et al., 2017	https://ncmi.bcm.tmc.edu/ncmi/software
EM database	-	https://www.ebi.ac.uk/emdb/
ERRASER	Chou et al., 2012	https://www.phenix-online.org/documentation/reference/erraser.html
ExPASy	Gasteiger et al., 2005	https://www.expasy.org/
Microsoft Office	-	http://products.office.com/en/
Molprobity	-	http://molprobity.manchester.ac.uk/
MotionCor2	Zheng et al., 2017	https://msg.ucsf.edu/em/software
Phenix	Adams et al., 2010	https://www.phenix-online.org/
Pubmed	-	https://pubmed.ncbi.nlm.nih.gov/
Phyre2	Kelley et al., 2015	http://www.sbg.bio.ic.ac.uk/phyre2/html/page.cgi?id=index
RCSB PDB	-	https://www.rcsb.org/
RCSB PDB Validation	-	https://validate-rcsb-2.wwpdb.org/
Relion	Scheres, 2015	https://www3.mrc-lmb.cam.ac.uk/relion
ResMap	Kucukelbir et al., 2014	http://resmap.sourceforge.net/
SerialEM	Mastronarde, 2005	https://bio3d.colorado.edu/SerialEM/
SPIDER	Frank et al., 1996	https://spider.wadsworth.org/
Uniprot	-	https://www.uniprot.org/

2.2 Biochemical purification and analysis of the RqcH-FLAG variants

The biochemical purification of the RqcH-FLAG variants and associated biochemical experiments were performed by Dr. Helge Paternoga from the Joaziero laboratory at Heidelberg University. The *B. subtilis* strains and RqcH mutants used for purification as well as biochemical analysis were created by the Joaziero laboratory at Heidelberg University as described in Lytvynenko *et al.* 2019.

2.2.1 Co-Immunoprecipitation (Co-IP) of the RqcH-FLAG 50S complexes

Co-immunoprecipitation (Co-IP) is a proper method to detect physiologically relevant protein-protein/nucleic acid interactions. Therefore, target protein-specific antibodies are used to indirectly detect proteins bound to a specific target protein. In this work, the Co-IP of FLAG-tagged RqcH complexes were performed using Anti-FLAG M2 affinity gel. The Anti-FLAG M2 affinity gel contains covalently linked antibodies that bind the FLAG affinity tag expressed by the RqcH proteins. Subsequent addition of competing FLAG peptides allows the elution of the RqcH-FLAG proteins and associated binding partners. The eluate containing co-immunoprecipitated FLAG-tagged-RqcH-50S complexes were further used for biochemical and structural analysis to identify the protein and nucleic acid binding partners.

2.2.1.1 Co-Immunoprecipitation of wild-type RqcH-FLAG complexes

Cells of the genomically-tagged RqcH-FLAG strain were grown in LB medium supplemented with 5 mg/ml chloramphenicol. 4x2 L cell cultures were grown at 37°C, 120 rpm to OD600 = 1.5 (OD = optical density). The cells were subsequently harvested, frozen in liquid nitrogen, and stored at -20°C. For lysis, the cells were resuspended in in sterile filtrated IP buffer, mixed with protease inhibitor and lysed using a microfluidizer. The lysates were clarified for 22min. at 17 krpm in a SS-34 rotor (RCFavg = 22548.5). Then, the supernatant was mixed with 4x200 mL pre-washed ANTI-FLAG M2 Affinity Gel and incubated at 4°C for 2h on a turning wheel. The beads were collected by centrifugation and washed three times with IP buffer. Subsequently, the beads were transferred to one Mobicol ‘F’ with a filter of 35 mmpore size and washed by gravity flow with Elution Buffer. For, RqcH-FLAG elution, the beads were added with 100 mL Elution buffer containing 0.3 mg/ml 3X FLAG peptide and incubated for 45min. on a turning wheel in the cold room. The eluate was collected by centrifugation at 18000 RCF and 4°C for 15min. The supernatant containing the RqcH-FLAG and associated components was collected in a fresh microcentrifuge tube. One portion of it was used for SDS-PAGE analysis and the other portion was flash-frozen into liquid nitrogen and shipped on dry-ice for cryo-EM analysis.

2.2.1.2 Co-Immunoprecipitation of mutant RqcH-FLAG complexes

For FLAG purification, pHT01 RqcH-FLAG variants were transformed into the ΔrqcH strain. Cells were grown in LB medium supplemented with 5 µg/ml chloramphenicol. 1.5 l cultures

were grown at 37 °C, 120 rpm to OD600 of ~1.2-1.6 after which cells were harvested, frozen in liquid nitrogen, and stored at -20 °C. For lysis, cells were resuspended in IP buffer and mixed with protease inhibitor. Cells were using a microfluidizer and lysates were clarified for 22min. at 17 krpm in a SS-34 rotor (RCFavg = 22548.5). Afterwards, 100 µl of the supernatant were collected for RNA extraction (see chapter 2.2.4), the remaining supernatant was mixed with 120 µl pre-washed ANTI-FLAG M2 Affinity Gel and incubated for 90min. at 4°C on a turning wheel. Then, the beads were collected by centrifugation and washed three times with 20 ml of buffer. Next, the beads were transferred to a Mobicol 'F' with a filter of 35 µm pore size and washed extensively by gravity flow. Elutions were performed by addition of 200 µl Elution buffer containing 0.2 mg/ml 3x FLAG peptide for 45min. on a turning wheel in the cold room. The eluate was split into three equal volumes, of which one half was precipitated with 10% TCA and subsequently analyzed on 4–12% NuPAGE gels using MOPS buffer (chapter 2.2.2) . The second half was used for RNA extraction and analysis (see chapter 2.2.3). The third portion was flash-frozen into liquid nitrogen and shipped on dry-ice for EM analysis.

2.2.2 SDS-polyacrylamide gel electrophoresis (SDS-PAGE)

To separate proteins by gel electrophoresis under denaturing condition, 4–12% polyacrylamide gels were used. The samples were mixed with 1x LDS sample buffer and heated for 10 min. at 70°C before loading on the gel. The electrophoresis was run at 200 V in MOPS buffer. The proteins were visualized in the gel by staining with Coomassie solution.

2.2.3 RNA extraction and analysis

The RNA was extracted from the FLAG input and eluate using the TRIzol reagent (Life Technologies) according to the manufacturer's instructions. The TRIzol reagent is a single-phase denaturing solution of acid phenol and guanidine isothiocyanate (GTC). GTC is a chaotropic salt that is very effective at denaturing and inactivating proteins. Acid phenol not only removes proteins, but by lowering the pH, it also removes DNA.

For analysis of the size distribution of the RNA fragments, an amount of 500-600 ng of isolated RNA from each RqcH mutant sample were analyzed using the Fragment Analyzer™ Automated CE System equipped with the DNF-471 standard sensitivity RNA Analysis Kit (15nt) following the manufacturer's instructions. The Fragment Analyzer Automated CE System is an

instrument that uses fluorescence-based capillary electrophoresis for analysis of concentration, integrity, length of nucleic acid fragments using an intercalating dye and a LED light source. Capillary gel electrophoresis, CE, is separation method in which charged molecules, such as RNA, are separated by size in capillaries filled with porous gel matrix.

2.2.4 Photometric estimation of the concentration

The concentration of proteins or nucleic acids within a sample was estimated using a photometer device such as the Nanodrop. The photometric measurement is based on the Lambert-Beer law:

$$E_\lambda = \varepsilon \times c \times d.$$

The extinction E describes the attenuation of intensity of radiation when passing through a medium exhibiting a certain layer of thickness (d). The extinction is direct proportional to the concentration (c) of the absorbing substances such as proteins, RNA and DNA and their extinction coefficient (ε). The protein concentrations were estimated by reading out the absorption maximum at 280nm. The extinction coefficient was determined on the basis of the amino acid sequence with Protparam (ExPASy) (Gasteiger et al., 2005). The concentration of nucleic acids is estimated by reading out the absorption at 260nm and using the following simplifications:

1 A260nm = 50µg / ml double stranded DNA

1 A260nm = 33 µg/ml single stranded DNA or RNA

1 A260nm = 40 µg / ml oligonucleotide

2.2.5 Growth analysis

Growth analysis was performed to examine the effect on the *in vivo* phenotypes by RqcH mutations introduced in the ΔrqcH ΔssrA double deletion strain. Therefore, the cells were grown at 37°C to exponential phase in LB medium supplemented with 5 µg/ml chloramphenicol. The optical density (OD) of the bacterial suspension was measured at 600nm. The OD measurement of a bacterial suspension is based on light scattering, which was detected using a spectrometer. After OD measurement, the cell culture was diluted to an OD600 of 0.1 using LB medium supplemented with 5 µg/ml chloramphenicol and spotted in 10-fold serial dilution on

LB-agar plates containing 5 µg/ml chloramphenicol. The plates were incubated at 37°C and 45°C for one day. The initial spot shown in the figures corresponds to an OD600 of 0.01.

2.2.6 Sample preparation for high-resolution cryo-EM

For cryo-EM grid preparation, the wild-type RqcH-50S sample was diluted to a concentration of 33 nM using a buffer consisting of 50mM Tris/HCl pH 7.5., 100 mM NaCl, 3 mM MgCl2.

For the mutant RqcH-50S complex, the sample was adjusted to a concentration of 91nM using a buffer consisting of 20mM HEPES pH 7.5, 100mM KCl, 5mM MgCl2, 1mM DTT, with 0,5% glutaraldehyde added prior freezing.

2.3 Preparation the 70S-tmRNA-SmpB-EF-G-FA complex

The sample preparation of the 70S-tmRNA-SmpB-EF-G-FA complex for cryo-EM was performed by Dr. Hiroshi Yamamoto, a previous member from the Spahn laboratory at the Charite Berlin. The individual components, including tmRNA, SmpB, EF-G, and AlaRS, expressed using the T7 expression system were first purified and then reconstituted *in vitro* which is described in Ramrath et al., 2012.

2.3.1 Chromatography

Chromatography is used for separation of proteins, nucleic acids, or small molecules from a mixture. One variant is the affinity chromatography that is based on the interaction between two molecules, such as the Ni-NTA affinity chromatography which is suitable for purifying recombinant proteins carrying a His tag. Here, the His-tagged proteins of *E. coli*, including the AlaRS, SmpB, EF-Tu, and EF-G were purified using Ni-NTA agarose accordingly to the manufacturer's instructions. His-tagged proteins form coordination bond with the Nickel 2+ ion of the Nitrilotriacetic acid (NTA) matrix. This coordination bond can be dissolved by changing the buffer composition resulting in the elution of the proteins.

Another type is the size-exclusion chromatography, also called gel filtration in which molecules are separated according to their size and shape. The basis of gel filtration is a column filled with a special gel matrix which consists of a polymeric organic compound (e.g., dextran,

agarose, polyacrylamide) containing hydrophilic pores. This type of chromatography was for further purification of SmpB using a Superose 12 column.

2.3.2 Sucrose gradient centrifugation for preparation of reassociated 70S ribosomes

A sucrose gradient is a common method for separating polysomes, monosomes and ribosomal subunits. Depending on the gradient composition, the sucrose allows the separation of particles of different size, shape, and molecular weight from a sample.

For isolation of crude 70S ribosomes, frozen *E.coli* cells dissolved in Tico buffer were used. The isolation of 70S ribosomes was carried out using *E. coli* cell cultures after the method described in Bommer et al., 1997.

The isolated, “crude” 70S ribosomes usually hold fragments of mRNAs and tRNAs and are therefore not suitable for the reconstitution of ribosomal complexes. The isolated 70S ribosome are first further purified by centrifugation using a linear sucrose (0 % - 40 %). Then, the 70S peak containing fractions are pooled and centrifuged to separate the tight coupled 70S free from the soluble factors.

For subunit dissociation, the pelleted 70S ribosomes are incubated in dissociation buffer (low Mg concentration) and centrifugated a second time by the same linear sucrose as before. The subunits purified in this way are free of cellular ligands such as proteins, tRNA, mRNA, etc. and can be reassociated to 70S ribosomes under physiological salt conditions. The 50S and 30S subunits containing fractions obtained from the second centrifugation are pooled and centrifuged to pellet them.

For subunit re-association, the pellet containing ribosomal subunits are dissolved in re-association buffer to form re-associated 70S ribosomes, which are needed for functional assays. The reassociated 70S are again applied to a linear sucrose gradient (0 % - 40 %). Then the 70S peak is collected from the gradient. The reassociated particles are pelleted by centrifugation. The resulting pellets are finally dissolved in Tico buffer and can be aliquoted, flash frozen and stored at - 80 °C for later use.

2.3.3 Preparation of the 70S-tmRNA-SmpB-EF-G-FA complex

Before complex assembly, the tmRNA was purified by a denaturing gel as described in Felden et al., 1997. The extracted and purified tmRNA was subsequently heated 2 min. at 70 °C in binding buffer A10, cooled for 20 min. to room temperature, and stored on ice until its use.

For the tmRNA alanylation and preparation of the quaternary complex (Ala-tmRNA-SmpB-EF-Tu-GTP), a 10µl reaction mix containing A10 binding buffer, 50 pmol AlaRS, 4.5 mM ATP, 300 pmol alanine, 10 pmol tmRNA, 20 pmol SmpB, 15 pmol EF-Tu, 2.25 mM GTP, 7.5 mM acetylphosphate were incubated for 20 min. at 37 °C.

The stalled 70S ribosomes were obtained by incubating the binding buffer B4.5 with 10 pmol of reassociated 70S ribosomes, 20 pmol of initiator tRNA (N-formyl methionine- $tRNA^{fMet}$) and 80 pmol of mRNA in a 15µl reaction volume for 10min. at 37°C. The used mRNA was purchased from IBA life sciences. It contains the sequence 5'-*GGCAAGGAGGU*AAAA**AUG**UA-3', where the initiation AUG codon is bold and its Shine-Dalgarno sequence is in italics.

The 15 µl stalled ribosome and 10 µl tmRNA reactions were mixed and incubated for 10 min. at 37 °C. To the resulting ribosome-tmRNA mixture was then added with 30 pmol of EF-G and fusidic acid added at a final concentration of 1 mM and incubated for 10 min. at 37 °C. This reaction mixture was then stored in aliquots at -80 °C until its use.

2.3.4 Sample preparation for high-resolution cryo-EM

Cryo-EM grid preparation for the 70S-tmRNA-SmpB-EF-G-FA sample was performed by Dr. David Ramrath, a former member of the Spahn laboratory at Charite Berlin, as described in chapter 2.4.1. The 70S-tmRNA-SmpB-EF-G-FA complex (prepared as described in chapter 2.3.3) was diluted to a final concentration of 30 nM using buffer A10 before applying to the EM grid.

2.4 Electron microscopy (EM) analysis

The typical workflow for structural analysis starts with negative-stain EM to test the quality of the sample and to estimate the concentration for the cryo-EM data collection. The subsequent low-resolution data collection under cryogenic conditions is performed to get initial structural information of the sample. The next step is the high-resolution data collection, which is usually performed if the low-resolution map looked reasonable. Data processing is performed using

different software packages. The final map(s) is interpreted using appropriate models for creating the final model.

2.4.1 Grid preparation

For both, negative-stain, and cryo-samples, the so-called "holey carbon grids" from Quantifoil were used. These grids consisted of a 300-copper mesh which is coated with a 2nm carbon film containing holes with a diameter of 2 µm. Before usage, the grids were washed with chloroform to remove the thin plastic film. The grids were subsequently glow-discharged for 30 s at 0.3 mbar using the plasma cleaner. Glow-discharging creates a hydrophilic carbon surface which improves the sample adsorption. Grids prepared in this way were immediately used for negative-staining or freezing the samples.

For negative-staining, 3.5 µL of the sample was placed on the grid and incubated for 45 s. Then 3.5µl of a 2% uranyl acetate stain solution was added to the sample. After an incubation time of 20-30s, the stain was gently removed using the wedge of filter paper allowing the grid to dry before EM imaging.

For the cryo-samples, 3.5 µL were applied to the grid, 30-45s incubated and rapidly vitrified in liquid ethane at -196 °C using the Vitrobot at 4 °C and approx. 90 % humidity. Removal of the excess liquid by blotting (2-8s) was followed by the immediate transfer into liquid ethane. Until use, the grids were stored in liquid nitrogen.

Rapid cooling in ethane prevents the formation of ice crystals damaging biological molecules, instead it produces amorphous ice preserving the native, hydrated state of the molecules (Dubochet et al., 1988). Ethane is cooled by liquid nitrogen, to obtain the temperature of more than -150°C required for vitrification of water. Moreover, ethane is much more suitable for rapid cooling than nitrogen due to its higher heat capacity, even though its melting point of -183°C is higher (nitrogen: - 210 °C).

2.4.2 EM data collection

In this work, four different microscopes were used to collect the EM data.

For negative contrasting, the CM100 microscope was used, because the samples do not require cooling. The images were recorded with an acceleration voltage of 100 kV at a magnification of 28,500x with a FastScan-F114 CCD camera with a format of 1024 x 1024 pixels and a physical pixel size of 14 µm.

For initial structure determinations of cryo-samples the Tecnai G2 Spirit microscope at 120 KV equipped with an Eagle CCD camera (format: 4096 x 4096 pixels and pixel size: 15µM) was used. The images were recorded under electron low-dose conditions (25 $e^-/Å^2$), with a magnification of 42,000x resulting in a pixel size of 2.65 Å on the object scale. The micrographs were collected automatically with Leginon (Suloway et al., 2005) at a defocus range of -2.0 to -4.0 µm.

Cryo-EM data for high-resolution structures of the RqcH-50S complexes were obtained using the Tecnai G2 Polara at 300 kV equipped with a K2 Summit DED camera (Gatan, pixel size: 0.6275 Å). The images were acquired in electron-counting mode, with a magnification of 31,000x and an electron dose of 30 $e^-/Å^2$. Images were collected automatically with Leginon at a defocus range of -0.9 to -2.0 µm.

The high resolution cryo-EM data for 70S-tmRNA-SmpB-EF-G-FA-complex was obtained from a Titan Krios microscope at 300 kV equipped with a K2 Summit DED camera (Gatan, pixel size: 0.66 Å). The images were acquired in super-resolution mode, with a magnification of 31,000x and an electron dose of 30 e-/$Å^2$. The images were automatically collected using SerialEM (Mastronarde et al., 2005) at a defocus range of -0.6 to -2.4 µm.

2.4.3 Pre-Processing of the cryo-EM data

For high-resolution cryo-EM data, MotionCor2 (Zheng et al., 2017) was used for background correction using a reference image obtained at the beginning of data acquisition (gain correction), electron dose weighting of later acquired frames, and correction of beam-induced sample motion by aligning the frames in the movie stack. Low-resolution cryo-EM data were not recorded in movie mode, thus were used directly for the visual inspection using e2display and e2boxer.py of the EMAN2 software package (Tang et al., 2007). The criteria that were evaluated to exclude the micrographs were the following: low particle numbers, high number of particle aggregates and ice contamination, and power spectra with Thon rings of limited radius, astigmatism, and drift. The remaining micrographs were used for CTF estimation by

CTFfind4 (Rohou and Grigorieff, 2015) in case of the low-resolution data or by GCTF (Zhang, 2016) for high-resolution data. The particle images of the low-resolution data were semiautomatically picked in e2boxer.py, and then extracted, normalized and 2-fold decimated using SPIDER (Frank et al., 1996). The particle images obtained from high-resolution data were picked and extracted using GAUTOMATCH (developed by Kai Zhang, MRC Laboratory), their normalization and decimation was performed in RELION (Scheres, 2015).

2.4.4 3D Reconstruction of single particle images

The reconstruction of a three-dimensional structure requires the existence of single particle images representing different orientations of the object (projection directions) in order to obtain a complete description of the structure. Before the 3D-reconstruction the 2D particles images need to be assign with orientation parameters (Euler angle), which is accomplished by comparison of the experimental projections with reference projections of a known structure (Frank, 2006; Penczek, 2010). The Euler angles are used for the back-projection of the 2D particle images into the 3D structure. The initial maps are subsequently refined by modifying the orientation parameters of the particle images to achieve an improved match with reprojections determined from the current structure. The refinement ends until the alignment reaches convergence, i.e., when the resolution and orientation parameters stay unchanged in the final volumes.

For the low-resolution data, the 3D reconstructions were created in SPIDER (Frank et al., 1996) using the 2-fold decimated particle stacks and an empty 50S subunit from *B. subtilis* (PDB-ID: 3J9W) as reference. In case of high-resolution data sets, 3-fold decimated images were subjected to the ab initio procedure or homogenous refinement in CryoSPARC (Punjani et al., 2017) to generate initial 3D reconstructions. In the homogenous refinement an empty 70S of *E. coli* (generated from PBD-ID: 4V6T) and a 50S subunit (generated form PBD-ID: 3J9W) were used as references to align the particle images of the tmRNA-70S and RqcH-50S data sets, respectively. For the mutant RqcH-50S dataset, the ab initio procedure was applied before the homogenous refinement to exclude false positive particle images that formed an artefactual 3D-reconstruction. The cryo-EM maps were visualized using Chimera (Pettersen et al., 2004).

2.4.5 Sorting and Refinement

In single-particle EM thousands of identical particle images are averaged for 3D structure determination. However, samples of ribosomal complexes often contain particles exhibiting different conformation or composition (heterogeneity). A common procedure for reducing compositional heterogeneity is chemical cross-linking, for example with glutaraldehyde. *In silico*, different classification methods are available to separate the data into more homogeneous substates.

In this work, the 3D classification was performed using the multiparticle approach (Loerke et al., 2010) and focused reassignment (Penczek et al., 2006), both implemented in SPIDER (Frank et al., 1996; Shaikh et al., 2008). In case of the high-resolution data obtained from the mutant RqcH-50S sample, the 3D classification and focused classification were performed in CisTEM using the maximum-likelihood approach (Lyumkis et al., 2013).

The heterogeneity in the maps were evaluated using the 3D variability analysis (Behrmann et al., 2015). A binary mask covering highly variable regions were used for focused classification.

The final maps obtained from the high-resolution data were sharpened at DC2 level using PDB enhancement. The method of PDB enhancement applies a computationally simulated frequency spectrum of an atomic model to the experimentally obtained density map to enhance high-frequency information that is expected to be present in the experimental data.

2.4.6 Resolution assessment for EM maps

The resolution of the cryo-EM maps was assessed using the Fourier Shell Correlation (FSC) (Harauz and van Heel, 1986). In this procedure, the data are divided according to even and odd image numbers into half-data sets from which their 3D reconstruction is generated. The two half-volumes are correlated shell by shell in reciprocal space to produce a 1D curve of FSC coefficients as a function of spatial frequency. High FSC values in the curve indicate consistent signals, while FSC values close to zero indicate unreliable signals. In this work, the resolution was taken at the FSC cut-off value of 0.143 (Rosenthal and Henderson, 2003), which is commonly used for cryo-EM maps of resolution better than 10 Å.

Since the resolution is determined using a single value, it represents the average resolution of the entire volume and is therefore also referred to as the overall or global resolution. However, the resolution varies in most maps, e.g., due to the heterogeneity of the samples. The evaluation of the local resolution in maps helps in interpretation of EM-maps. In this work, the local resolution was estimated using the unfiltered half maps in ResMap (Kucukelbir et al., 2014). This algorithm is based on the determination of a sine wave above the noise level for each point within the map.

2.5 Building and validation of atomic models

The building of atomic models for cryo-EM maps depends on the resolution. At high resolution (better than 4 Å), the information is sufficient to build a model directly from the density map (Malhotra et al., 2019). Low (~ 10 -25 Å) and intermediate (~ 4 - 10 Å) resolution allow the fit of the model as rigid body into the electron density. The integration of information of different methods (integrative modelling) and local refinement may improve the rigid-body fitted model (Koukos and Bonvin, 2019).

The source of models which were used in this work are listed in table S1 and S2 (see chapter 6). Homology models were created in Phyre2 (Kelley et al., 2015) using a related model as template and the known sequence of the relevant bacterial species. The models for ribosomal proteins, RNA or factors were separately fitted as rigid bodies into the density maps using Chimera. Model elements that were absent in the density map, were removed. The subsequent adjustment of the remaining elements was done by iterative model building into the density using Coot (Emsley et al., 2010), phenix.real_space_refine program in Phenix (Adams et al., 2010) and in case of RNA by ERRASER (Chou et al., 2012).

The validation of the model was performed using the RCSB PDB Validation (https://validate-rcsb-2.wwpdb.org/), Molprobity (http://molprobity.manchester.ac.uk/) and the cryo-EM validation tools in Phenix.

A complementary method for assessing the map quality is the calculation of the cross-resolution between the final map and the map simulated from the respective model. The cross-resolution calculates the correlation between the final map and the map simulated from the respective model but uses the FSC cutoff at 0.5.

3 Results

This work focused on the structural analysis of two ribosomal rescue factors in bacteria, the RqcH protein which is supposed to bind stalled 50S ribosomal subunits (see introduction, chapter 1.4.2) and the tmRNA and its attached protein SmpB that recognize stalled 70S ribosomes (see introduction, chapter 1.4.1).

For analysis of RqcH-50S subunit binding, RqcH was co-purified with ribosomal 50S subunits from *B. subtilis* lysate and used for electron microscopy analysis (following chapters 3.1 – 3.2). However, the wild-type RqcH couldn't be visualized on the ribosomal 50S subunit. Subsequent EM-analysis using mutant RqcH co-immunoprecipitated 50S complexes and chemical cross-linking allowed to visualize RqcH binding to 50S ribosomal subunits (following chapters 3.3 – 3.5). The identified binding interfaces between RqcH and the 50S subunit in the built atomic model were additionally analyzed by appropriate RqcH mutation experiments that were performed from Dr. Helge Paternoga.

The cryo-EM analysis of the specimen containing *E. coli* 70S-tmRNA-SmpB-EF-G complexes stalled with fusidic acid from a previous study (Ramrath et al., 2012) revealed five structures representing distinct translocation states (following chapters 3.6 – 3.7). The advanced technologies in EM and data processing allowed to obtain high-resolution cryo-EM maps exhibiting the densities for the complete molecules of the tmRNA and SmpB on the 70S ribosome. The built atomic model allowed a detailed characterization of the individual states and their integration into the process of translocation within the *trans*-translation pathway.

3.1 Wilde-type RqcH co-immunoprecipitates with 50S subunits

As described in the introduction (chapter 1.4.2) structural data was only available for eukaryotic RQC rescue factors, such as Rqc2 in yeast of NEMF in mammals which target stalled ribosomal subunits for degradation (Shen et al., 2015; Shao et al., 2015). Since co-immunoprecipitation experiments showed that the bacterial Rqc2 homolog, RqcH in *B. subtilis* can bind to 50S ribosomal subunits, it was suggested a RQC pathway exists in bacteria, too (Lytvynenko et al., 2019). To explore the structure of bacterial RQC complexes, the RqcH-50S subunit complex was purified by affinity chromatography of the FLAG-tagged wild-type RqcH protein from the *B. subtilis* cell lysate. The binding of RqcH to the ribosomal proteins of the 50S subunit was

shown by Coomassie staining after separation in polyacrylamide gel (Figure 22). The biochemical preparation and analysis were performed by Dr. Helge Paternoga as described (for details see chapter 2.2).

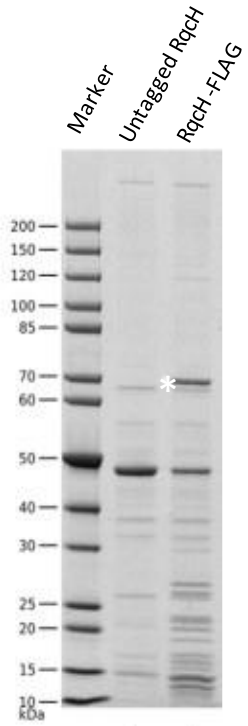

Figure 22: SDS-PAGE of wild-type RqcH-co-immunoprecipitated 50S sample. The band corresponding to RqcH-FLAG is indicated by an asterisk. Coomassie staining of the sample utilized for EM structural determination. The experiments were performed by Dr. Helge Paternoga.

The purification and subsequent binding experiments confirm to have produced the desired ribosomal complex consisting of the 50S subunit in complex with wild-type RqcH suitable for the structural analysis using EM.

3.2 EM analysis of wild-type RqcH co-immunoprecipitated 50S complexes

To evaluate the sample and to estimate the appropriate concentration for cryogenic conditions, a negative contrasting with uranyl acetate was performed (Figure 23A). The particle distribution is homogenous, i.e., the particles appear with the same sizes (around 200 Å) and shapes (mostly spherical) as expected for ribosomal 50S subunits (Figure 23). The used concentration of 33nM revealed a number of about 230 particles on each Spirit TEM micrograph which is sufficient for data processing (Figure 23B).

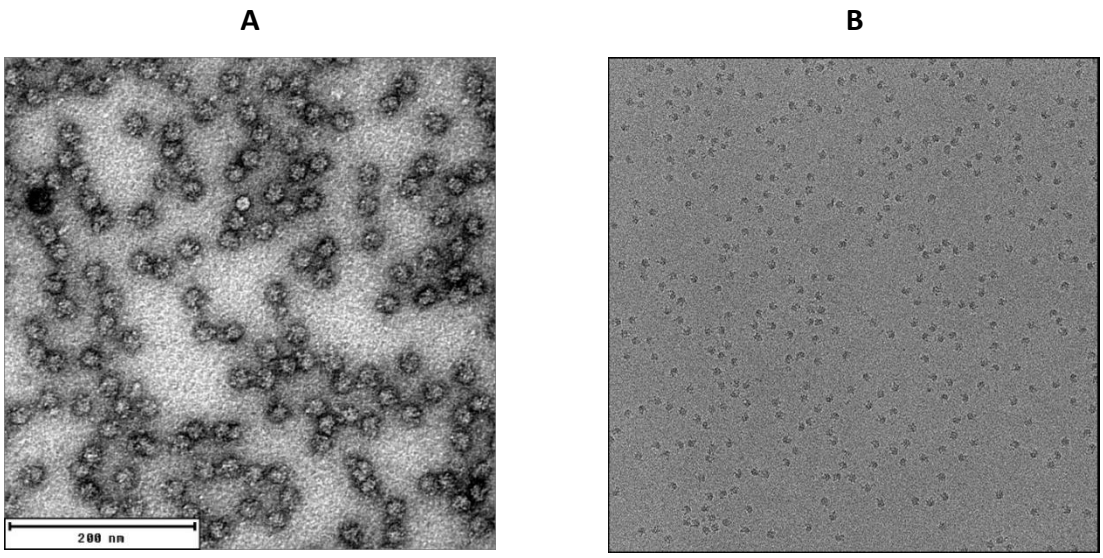

Figure 23: Electron micrographs obtained from the wild-type RqcH-50S sample. A) Negative contrast image of sample stained with uranyl acetate B) Cryo-EM image of sample vitrified in ice.

The obtain initial structural information the low-resolution data set consisting of 301 micrographs were processed (as described in the methods, chapters 2.4.3 - 2.4.4). The final 3D-reconstruction comprised 57k particle images (99.8 % of the total number of particle images) and had a resolution of 17 Å. The map represented the ribosomal 50S subunit with an undefined extra density at the subunit interface and P-site (Figure 24). Thus, the wild-type RqcH-co-immunoprecipitated 50S sample was suitable for a high-resolution data collection to get more structural information about the bound factor(s).

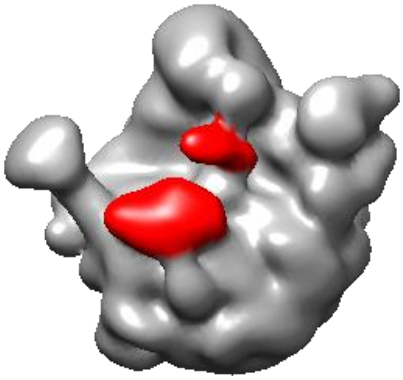

Figure 24: Low-resolution cryo-EM map obtained from the wild-type RqcH-50S sample. The map shows extra-ribosomal densities (red) at the ribosomal P-site and at the 50S subunit interface. The map consists of about 57k particle images and has a resolution of 17 Å. The data were collected at the Spirit TEM.

For high resolution data collection at the Tecnai G2 Polara microscope, the same sample concentration of 33nM as for low-resolution cryo-EM was used. A representative micrograph is shown in Figure 25.

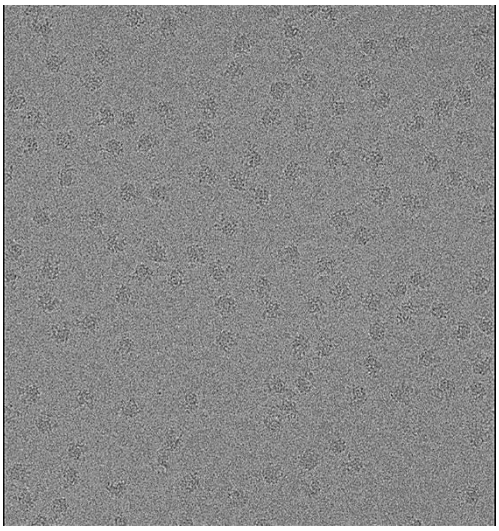

Figure 25: Representative electron micrograph obtained from the wild-type RqcH-50S sample and collected at the Polara TEM.

From 3931 automatically collected micrographs, 3544 were selected for data processing, on which 595,852 single particle images existed. To create an initial 3D reconstruction, the particle images were aligned using CryoSPARC's homogeneous refinement (Punjani et al., 2017). The subsequent 3D multiparticle sorting (Loerke et al., 2010) split the data into a 50S reconstruction containing a well-defined density for the P-tRNA (Figure 26, Tier 1, class I) and four additional artefactual reconstructions (Figure 26, Tier 1, class II – V). The class I particle images (Tier 1 in Figure 26) were used for focused classification (Penczek et al., 2006) using a mask for the P-site region which resulted into an empty 50S reconstruction and P-tRNA bound 50S reconstruction (Tier 2 in Figure 26). The P-tRNA containing particle images (Figure 26, Tier 2, class II) were further classified, again with mask for the P-site region, revealing the final map consisting of 44,212 particle images (Figure 26; Tier 3, class II). The final map was used for further analysis and interpretation.

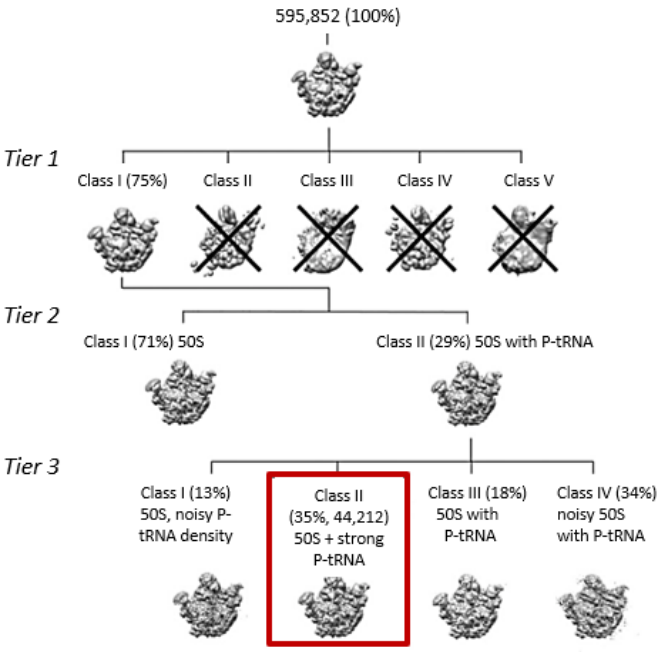

Figure 26: Computational classification of the cryo-EM dataset collected from the wild-type RqcH-50S sample. The number of particle images and structural features of reasonable maps in each Tier are indicated. Discarded classes are marked with a cross. The final map (red box) was further refined and used for modelling. This data was published in Lytvynenko et al, 2019.

The final map (Figure 26; class II, Tier 3) was refined to 3.8 Å using the FSC 0.143 criterion (Figure 27A). The local resolution of the map ranges from 3 Å to 15 Å (Figure 27B) as determined by ResMap (Kucukelbir et al., 2014).

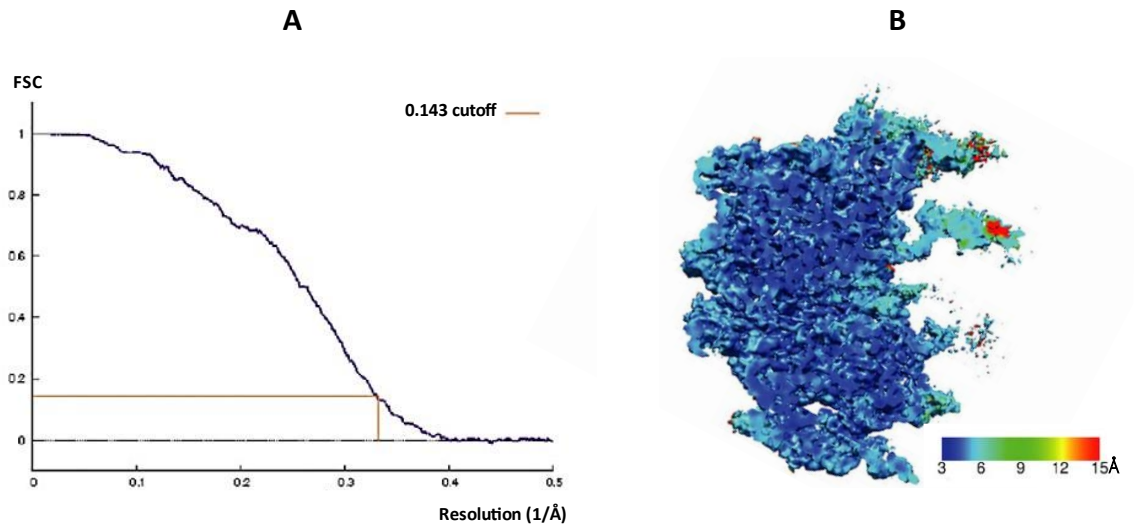

Figure 27: Resolution for the cryo-EM map obtained from the wild-type RqcH-50S sample. A) The overall resolution of the cryo-EM map was 3.8 Å using the Fourier shell correlation (FSC) cut-off at 0.143. B) The cross section through the cryo-EM map which is colored according to its local resolution. This data was published in Lytvynenko et al, 2019.

The cryo-EM map obtained from the wild-type RqcH-50S sample exhibits two extra-ribosomal densities: one is located at the 50S subunit interface which does not match the size of RqcH (Figure 28A), and the other density matches the size and shape of a P-tRNA (Figure 28B). The 50S subunit model obtained from a cryo-EM structure of the *B. subtilis* 70S ribosome complex (PDB-ID: 3J9W) docked into the map obtained from the wild-type RqcH-50S sample shows the presence of the P-site tRNA and lack of ribosomal helices H68, H69, H71 (Figure 28B).

The 3'CCA-end of the P-tRNA is linked to the nascent-peptide chain at the peptidyl-transfer center (PTC) as demonstrated in the cross-section of the cryo-EM map (Figure 28C). However, the 50S subunits co-purified with FLAG-tagged RqcH did not show a density for the factor RqcH. The presence of a nascent chain attached to the P-site tRNA indicates that active RqcH-50S complexes were purified. The absence of factor density may suggest that RqcH is bound to the 50S subunit in a highly flexible state. Another possibility explaining the lack of RqcH density could be the unstable RqcH binding to the 50S subunit, which caused RqcH falling off from the 50S subunit during purification.

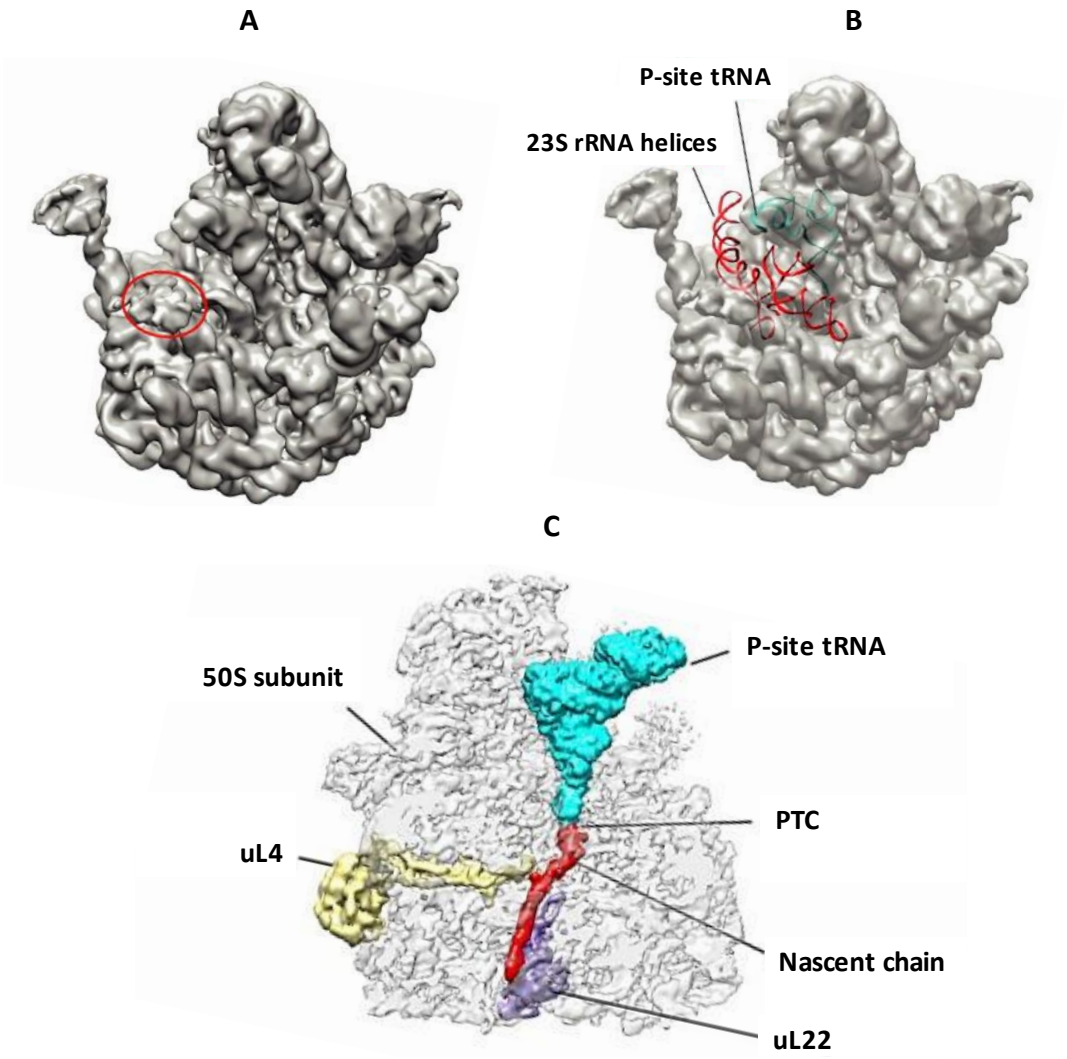

Figure 28: Final cryo-EM map obtained from the wild-type RqcH-50S sample. The map shows A) an unknown density (circled) at the ribosomal subunit interface and (B) a density at the P-site matching the size and shape of tRNA (cyan; PDB-ID: 3J9W) but lacking density for the ribosomal helices H68, H69, H71 (red, PDB-ID: 3J9W). (C) The cross-section of the cryo-EM map to show the linkage of the P-tRNA density with the nascent peptide (red) at the peptidyl-transferase center (PTC) and the ribosomal proteins uL4 (yellow) and uL22 (purple) marking the peptide exit tunnel. The cryo-EM density maps in A and B, and the densities for uL4 and uL22, the nascent peptide, and P-tRNA in Figure C are low-pass filtered for clarity. This data was published in Lytvynenko et al, 2019.

3.3 Mutant RqcH co-immunoprecipitates with 50S subunits

Since the structural analysis of the wild-type RqcH-co-immunoprecipitated 50S subunit complex did not show a density for this factor (see previous chapter 3.2), we used RqcH with a mutation in the NFACT-N domain (NFACT-N*, E121A, I122G, M123G) that co-purified with the 50S subunit as the wild-type RqcH but was not functional (Lytvynenko et al., 2019). It was hypothesized that the dysfunctionality of this mutant RqcH causes its stalling and stabilizing it in a certain RQC state, thus enabling its visualization on the 50S subunit by cryo-EM.

Like for the wild-type RqcH-50S sample, the purification of mutant RqcH-50S complex was done via FLAG-tagged RqcH protein by affinity chromatography from the *B. subtilis* cell lysate (chapter 2.2.1.2). The subsequent binding test confirmed to have purified mutant RqcH which was bound to 50S ribosomal proteins (Figure 29). This sample was used for the structural analysis using electron microscopy. Both purification and binding tests for the mutant RqcH-50S complex was done by Dr. Helge Paternoga.

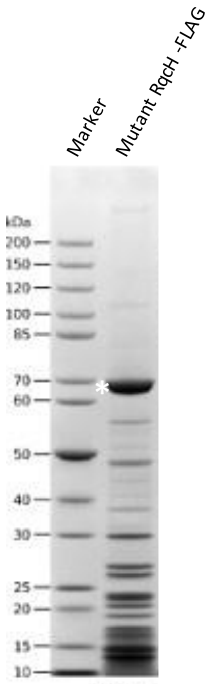

Figure 29: SDS-PAGE of mutant RqcH-co-immunoprecipitated 50S subunit complexes. The band corresponding to mutant RqcH-FLAG is indicated by an asterisk. Coomassie staining of the sample utilized for EM structural determination. The experiments were performed by Dr. Helge Paternoga.

3.4 Mutant RqcH-50S sample requires crosslinking for RqcH visualization

In a first attempt to visualize mutant RqcH on the 50S subunit, low-resolution EM experiments were performed. Using the SPIRIT TEM, two low-resolution cryo-EM data sets were collected. One data set from the untreated mutant RqcH-50S sample. And in case that the mutation will not reduce the conformational flexibility, a second data set was collected from the same sample but crosslinked with 0.5 % glutaraldehyde prior to plunge-freezing. The two samples were treated equally in terms of data collection and processing to facilitate a reasonable comparison afterwards.

For negative staining a concentration of 30ug/ml were used for both samples, the mutant RqcH-50S sample untreated and treated with 0.5% glutaraldehyde. The negative stain images show single particles matching the size and shape of 50S ribosomal subunits (Figure 30A and C), making both samples suitable for a cryo-EM analysis. The particle concentration on the micrograph obtained from the cryo-EM grid with crosslinked sample of a concentration of 91nM is ideal (Figure 30D). While for the untreated sample (45nM) more empty spots on the micrograph are visible, indicating to ideally increase the concentration, in case that further cryo-EM experiment will be performed (Figure 30B).

A) UANS-EM-image of mutant RqcH-50S

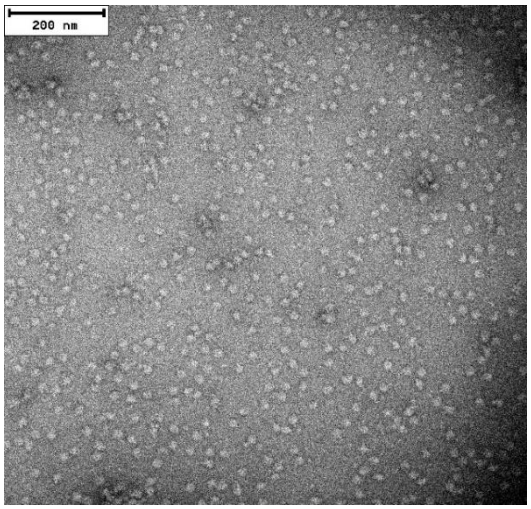

B) cryo-EM image of mutant RqcH-50S

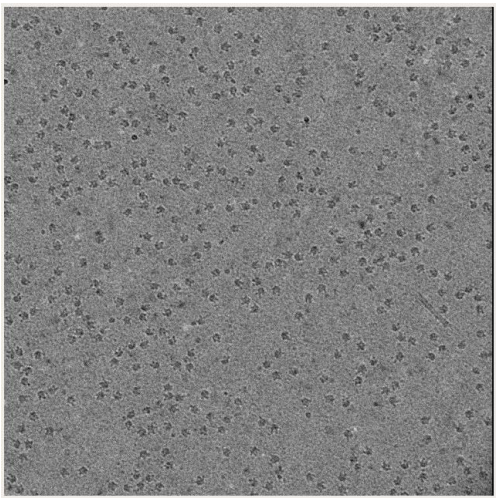

C) UANS-EM-image of mutant RqcH-50S crosslinked with 0.5% GA

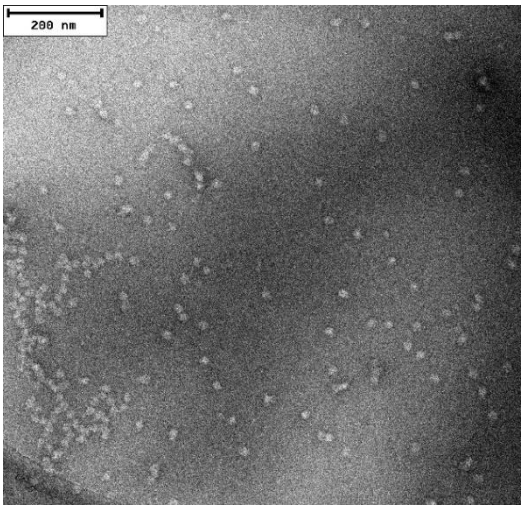

D) cryo-EM image of mutant RqcH-50S crosslinked with 0.5% GA

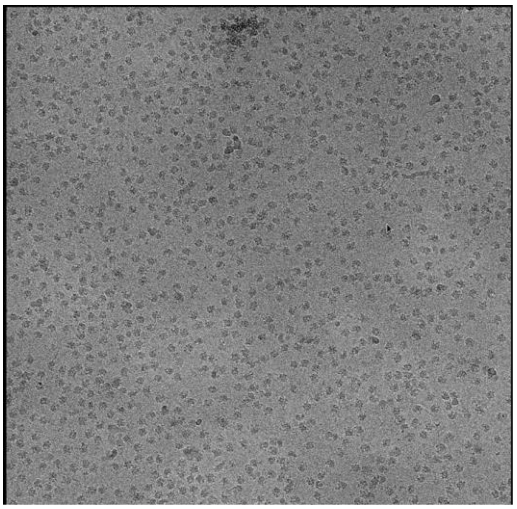

Figure 30: Electron micrographs obtained from the mutant RqcH-50S sample at the Spirit TEM. The negative contrast image for the untreated sample (A) and the sample crosslinked with 0.5% GA (C). The cryo-EM image for the untreated sample (B) and the sample crosslinked with 0.5% GA (D). GA= glutaraldehyde

For processing of the data obtained from the mutant RqcH-50S sample, the same strategy was applied as for the low-resolution wild-type RqcH-50S data (as described in chapters 2.4.3 - 2.4.4). Compared to the low-resolution cryo-EM data set of the wild-type RqcH-50S sample that revealed only one substate (see Figure 24), the data sets of the mutant RqcH-50S sample split into two substates which represent the 50S subunit with extra-ribosomal density at the subunit interface (Figure 31). The first substate of the non-crosslinked mutant sample (Figure 31 A substate I) matches the overall shape and features of the low-resolution map obtained from the wild-type RqcH-50S sample (Figure 24) for which RqcH couldn't be visualized (Figure 28).

However, the second substate, present in both mutant RqcH data sets (Figure 31A and B substate II) differ compared to that which was observed in the low-resolution wild-type map (Figure 24). In contrast to the wild-type structure (Figure 24), the density at the 50S subunit of the second substate is stronger and covers the subunit interface, the P-site and additionally the A-site. Since it is assumed that the RqcH factor is located around the ribosomal P- and A-site as it was observed for the eukaryotic RQC complexes (Shen et al., 2015; Shao et al., 2015), the second substate indicated the presence of RqcH. However, the second state has a poor defined extra ribosomal density that also indicates flexibility.

One substate (Figure 31B substate I) only observed in the crosslinked sample forms a 50S subunit with well-defined density that extends from the stalk-base towards the A-site, whose shape and position strongly resemble the NEMF ligand that also extends from the stalk base over the A-site in the eukaryotic RQC complex (Shao et al., 2015). This suggest that the bound RqcH visible as amorphous density (second substate in both mutant samples) requires additional crosslinking in order to form a well-defined factor density. Therefore, the crosslinked sample was used for a high-resolution collection at the Polara TEM.

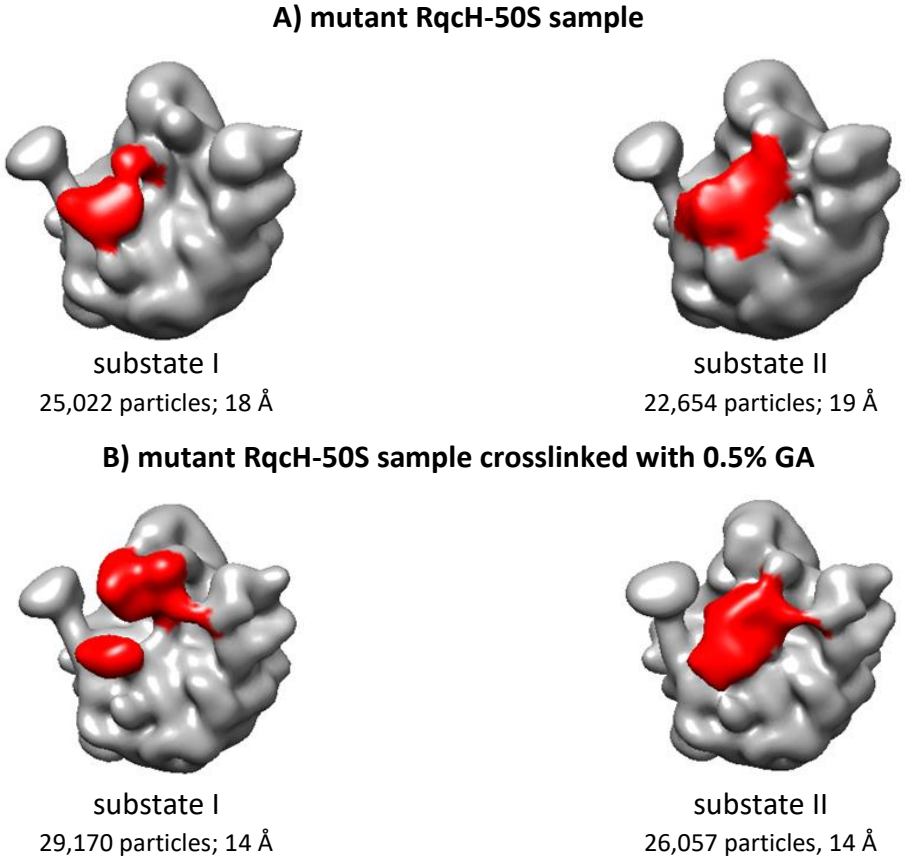

Figure 31: Low-resolution cryo-EM maps obtained from mutant RqcH-50S sample. A) Substate I and II of the mutant RqcH-50S sample. B) substate I and II of the mutant RqcH-50S sample crosslinked with 0.5% glutaraldehyde (GA) prior freezing.

3.5 Structural analysis of mutant RqcH-50S complexes

For high resolution data collection at the Tecnai G2 Polara microscope, the crosslinked mutant RqcH-50S sample was used, a representative micrograph is shown in Figure 32.

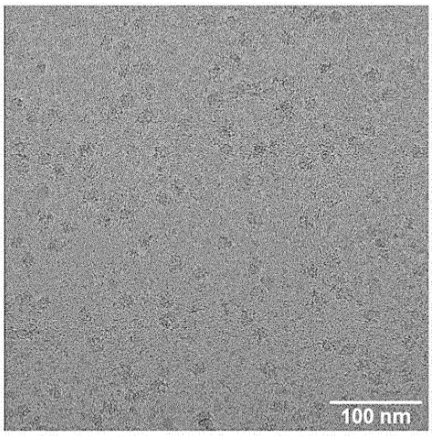

Figure 32: Electron micrograph obtained from the mutant RqcH-50S sample at the Polara-TEM. A representative micrograph from the RqcH-50S dataset.

After data collection, 6,137 micrographs were selected for pre-processing. A total number of 1,168,163 particle images were used for the initial 3D reconstruction using the ab initio procedure of CryoSPARC (Punjani et al., 2017). The artifactual 3-D reconstruction (class II formed by „junk“ particle images) was discarded. The 481,308 particle images of class I were aligned using a 30 Å low-pass filter generated from the 50S ribosomal subunit from *B. subtilis* (PDB ID: 3J9W; Sohmen et al., 2015) as reference using the homogenous refinement of CryoSPARC. Further image-processing steps were performed using CisTEM (Grant, Rohou and Grigorieff, 2018).

The 3-D classification assigned the particle images into five classes (Tier 1). The 3D reconstructions without or poorly resolved factor densities (class I, II, III, V) were discarded. The class IV particle images (Tier 1) which have formed a 50S structure with strong factor density split into four classes (Tier 2) using a focus mask for the factors (RqcH and tRNA). All resulting classes (Tier 2) contained density for the P-site tRNA. These classes represent 65% (Tier 2) from the total number of 481,308 particle images, which indicates that the majority of the particle images formed P-tRNA containing 50S-structures. This confirms that the 50S-P-site tRNA complex is a substrate for RqcH.

Only the classes with density for both factors (class I and III particle images, Tier 2) were subjected to a second round of focused classification revealing five classes (Tier 3). The class IV particle images (Tier 3) forming a 50S structure with poor factor density was discarded. The remaining classes showing strong factor density (class I, II, III, V, Tier 3) were subjected to a last round of focused classification. The resulting maps represent substates that differ slightly in the tRNA binding position (class I – V, Tier 4). The major subpopulation showing the best-defined factor density (class V, 101,370 particle images, Tier 4) were further refined and used for modelling. The final cryo-EM map (Figure 33B) has a global resolution of 3.1 Å corresponding to the 0.143 FSC cut-off (Figure 33D) and its local resolution ranges from 3 Å to 10 Å (Figure 33C).

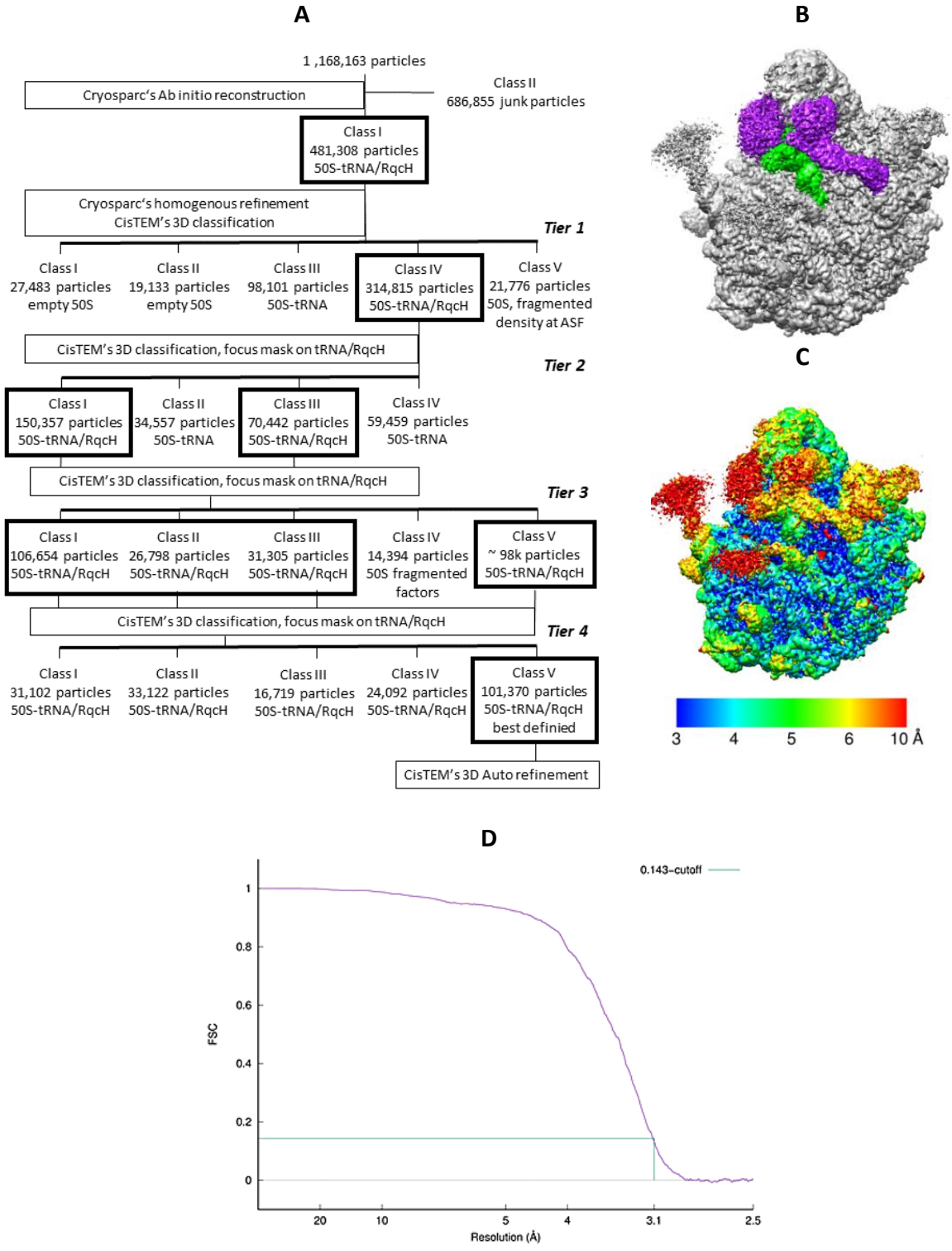

Figure 33: The classification scheme, final 3D reconstruction and resolution evaluation of the high-resolution data obtained from the mutant RqcH-50S sample. A) The classification scheme with indicated number of particle images and structural features for each class. Kept classes per tier are boxed, discarded classes are unboxed. B) The final cryo-EM map with colored densities for the mutant RqcH protein (purple), P-site tRNA (green) and 50S ribosomal elements (grey). C) Finale cryo-EM map colored by their local resolution ranging from 3 to 10 Å which is indicated by the color scale bar. D) The Global resolution of the cryo-EM map is 3.1 Å corresponding to the 0.143 FSC cut-off.

The final 3D reconstruction represents the ribosomal 50S subunit with strong extra-ribosomal densities matching the size and shape of the P-site tRNA and RqcH (Figure 33A and B). The density for RqcH extends from the stalk base over the ribosomal A-site towards the P-site bound tRNA that is attached to the nascent chain (Figure 34A and C). Even though the resolution of RqcH varies between 6 Å and 10 Å (Figure 33C), the complete density could be assigned unambiguously (Figure 34A and B). The domains of RqcH were assigned using existing crystal structures of the *S. suis* RqcH homolog as models (PDB ID: 5H3X and 5H3W, Musyoki et al., 2016).

The structure shows that binding of RqcH to the 50S subunit is facilitated by various interactions with ribosomal RNA and proteins. RqcH ‘s NFACT-N* and HhH are located at the central protuberance (CP) and above the anticodon arm of the P-tRNA (Figure 34A and C). The coiled-coil helices of RqcH span between P-site tRNA and the stalk base (rRNA helices H43/H44), and the NFACT-R domain interacts with helix 38 (H38) of the 23S rRNA (Figure 34A). Similar to the structure of the 50S complex that co-purified with wild-type RqcH (Figure 28B), the density for the ribosomal helices H68, H69 and H71 of canonical states is missing (Figure 34D).

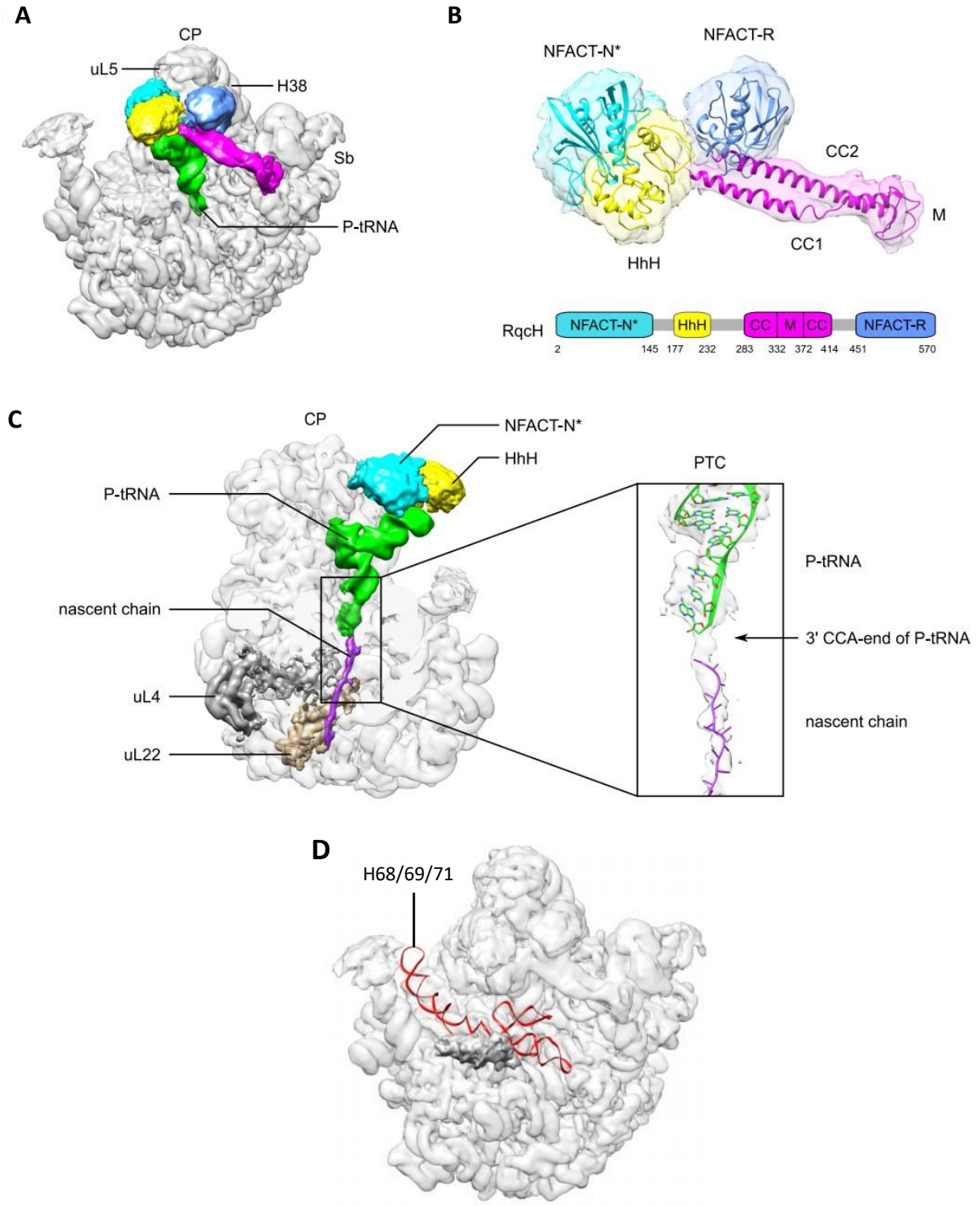

Figure 34: Cryo-EM reconstruction of the mutant RqcH-50S complex. A) Overview of the cryo-EM map shows the structural organization of RqcH (NFACT-N* (cyan), HhH (yellow), CC1-M-CC2 (magenta) and NFACT-R (blue)) when bound to the ribosomal 50S subunit (grey) and P-tRNA (green). The ribosomal protein uL5, central protuberance (CP), ribosomal helix 38 (H38) and stalk base (Sb; formed by H43 and H44) are indicated for orientation. The density map was low pass filtered to 6 Å for clarity. B) Extracted density of the cryo-EM map in (A) with the atomic model for RqcH. The individual domains of RqcH are indicated. C) Side view and transverse section of the cryo-EM map in A) reveal the peptide exit tunnel showing density for the nascent-chain (purple) and acceptor arm of the tRNA at the peptidyl transferase center (PTC). The ribosomal proteins uL4 (grey) and uL22 (tan) adjacent to the peptide exit

channel are indicated. The close-up view of the unfiltered density map reveals high fragmentation, caused by nascent-chain compositional heterogeneity. The density (transparent grey) and built atomic model display the connection between the nascent chain (purple) and the 3‘CCA end of the tRNA (green). D) Unknown amorphous density (dark grey) at the ribosomal subunit interface of the cryo-EM map in A). Rigid body fitting of the 23S rRNA from a *B. subtilis* 70S ribosome complex (PDB ID: 3J9W) indicates the absence of density for the ribosomal helices H68, H69, H71 (red) in the map.

3.5.1 HhH/CC1 regions of RqcH provide 50S-P-tRNA binding sites

Further modelling analysis proposed a rigid-body dock of the *B. subtilis* NFACT-N*-HhH homology model in which the NFACT-N* domain makes contact to uL5, while the HhH domains interact with the P-site tRNA’s anticodon loop (Figure 35A). This tentative assignment revealed a plausible orientation in which the distance of 12 Å between the C-terminal residue K281 of HhH and the residue K288 of CC1 could well occupy the six residues, A282 – Y287 (Figure 35A). The residues A282 – Y287 lack in the crystal structure of the *S. suis* RqcH homolog (PDB-ID: 5H3X and 5H3W, Musyoki et al., 2016).

The HhH lysines (K194, K209, K249) are in binding distance to the nucleotides A32, A31, A30 contained in the anticodon loop of the P-tRNA (Figure 35A) which agrees with its proposed function as a nucleic acid-binding domain (Doherty, 1996; Burroughs and Aravind, 2014; Shao, 2000).

The CC1 helix shows a clear association to the tRNA as well. Even though its associated density lacked side-chain information, the N-terminal CC1 region, K288-Q292 could be defined as a second binding interface to the tRNA at position 28,29 and 43 (Figure 35B).

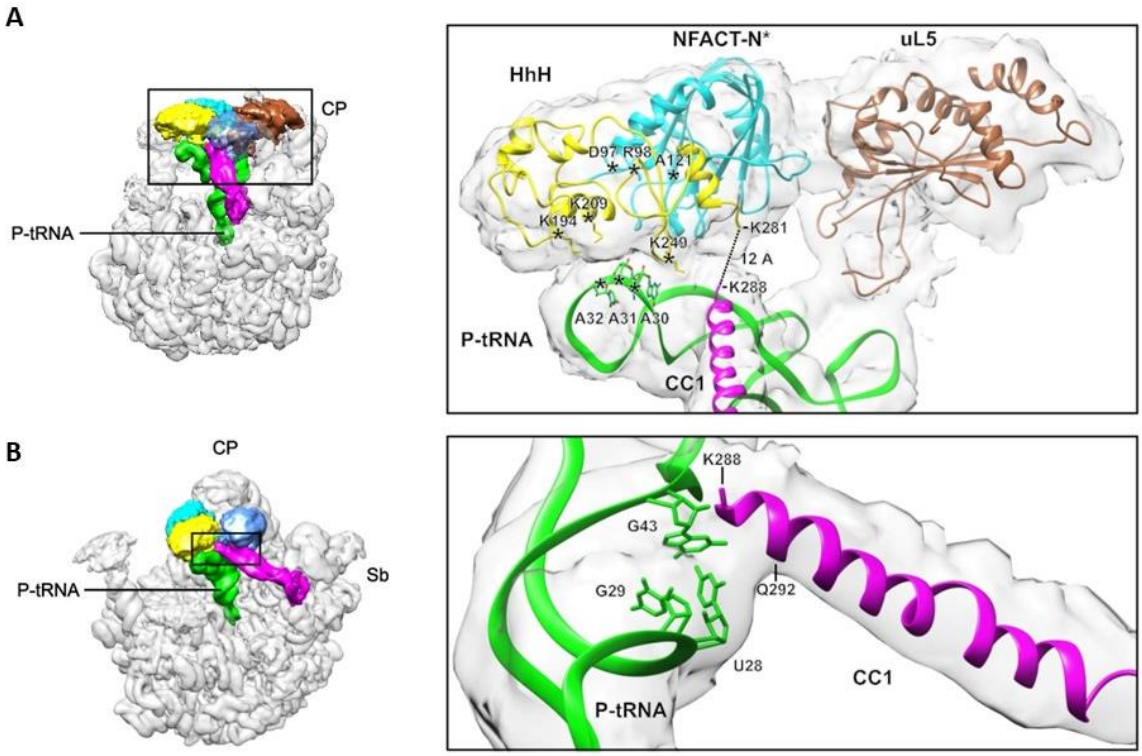

Figure 35: tRNA binding by NFACT-N-HhH and CC1 domains in the mutant RqcH-50S complex. (A) Side view of the cryo-EM map (low-pass filtered to 6 Å) with colored densities for uL5 (brown), tRNA (green) and RqcH (same color coding as in Figure 34A). Right side: Close-up of RqcH's HhH (yellow) and NFACT-N* domains (cyan). The HhH domains expose lysines (K) at position A30, A31, A32 of the anti-codon loop of the tRNA (green). The distance of 12 Å between the C-terminal residue K281 of HhH and residue K288 of CC1 matches the space to occupy the six missing residues (A282 – Y287). (B) Front view of the cryo-EM map in (A). Right side: Close-up of the tRNA (green) and CC1 (magenta). The N-terminal CC1 residues, K288-Q292 form a second binding interface for the tRNA at position U28, G29 and G43.

3.5.2 M-CC2 region and NFACT-R domain are crucial for RqcH function

In the mutant RqcH-50S structure, the density for the M-domain was suitable for modelling a region which was lacking in the crystal structure (PDB-ID: 5H3X and 5H3W, Musyoki et al., 2016). The M domain (L332-E371), modelled *de novo* from residues 332-357, establishes key contacts with the 50S subunit: the residues A334 and N335 interfaces the N-terminal residues of uL11, and residues D343, K344 and Q345 seem to interact with A2689 of the sarcin-ricin loop (SRL) of the 23S rRNA (Figure 36A, right panel).

The residues of CC2 that follow the M domain were placed confidently into the well-resolved density around the stalk base helices H44 and H43 (Figure 36A, middle panel). Here, polar (S370, Q374, Q381) and aromatic (F377) residues seem to engage in stacking and electrostatic interactions with nucleotides located at the tips of H43 and H44 (Figure 36A, middle panel).

Like F377, its neighboring Y376 is highly conserved among prokaryotes and might be functionally important, too (Lytvynenko et al., 2019).

An additional binding site of RqcH on the 23S rRNA relies on the NFACT-R domain, that is located at H38 (Figure 36B). The rigid body-docked NFACT-R model fits well the density and possesses arginine residues (R476, R480, R534) at the H38 interaction surface (C932, C933, U934, A935).

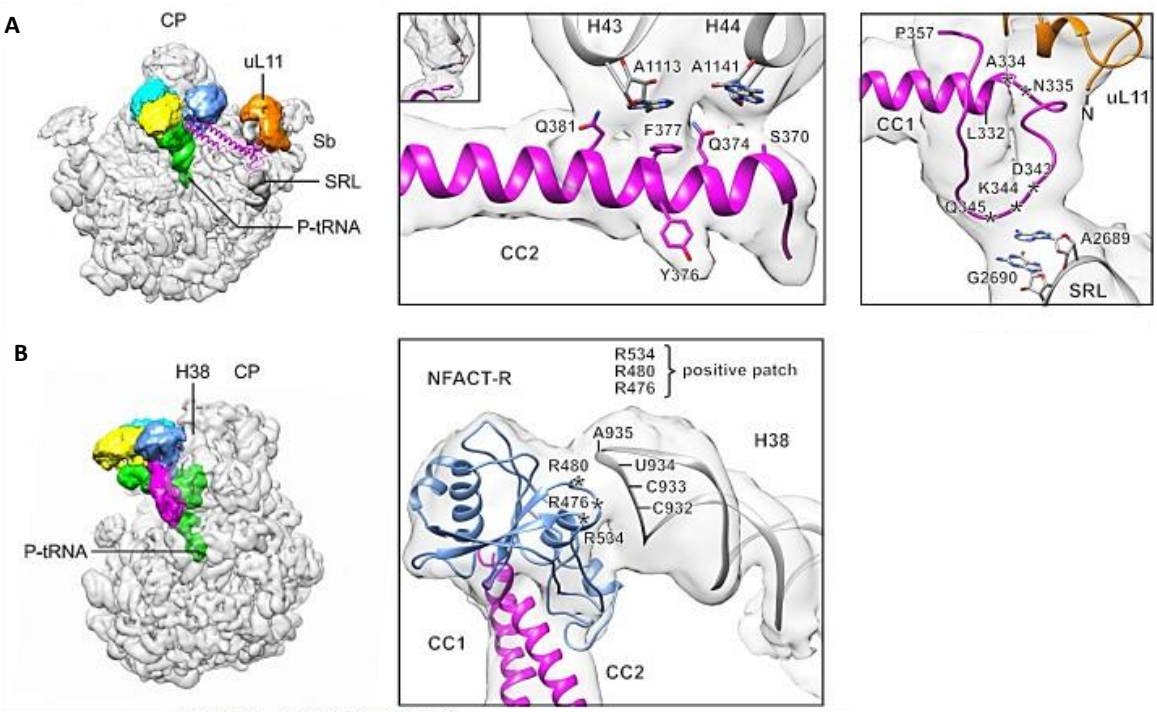

Figure 36: Interactions of M-CC2 and NFACT-R domains in the mutant RqcH-50S complex. A) Left panel: Front view of the cryo-EM map (low-pass filtered to 6 Å) of the mutant RqcH-50S complex showing the ribosomal environment (uL11 (orange), H43, H44 and SRL (dark grey)) of the M-CC2 region. Middle panel: The N-terminal residues of CC2, Q381, F377 and Q374, S370 interact with nucleotides located at the tips of H43 and H44 of the 23S rRNA, respectively. The inset shows the unfiltered density of the stacking interaction between F377 and A1113 of H43. Right panel: The M domain region (L332 - P357) contacts N terminal residues of uL11 via A334 and N335 and nucleotide A2689 of the SRL via polar or charged residues (D343, K344, Q345). B) Side view of the cryo-EM map in A). The rigid body-docked model of NFACT-R exposes arginine residues (indicated by asterisks) that interact with the phosphate backbone of H38 at position C932, C933, U934, A935.

To corroborate the tentative assignment of the CC2 region and NFACT-R domains into the density, their residues identified in the structure to be involved in 50S binding (Figure 36) are mutated. The following RqcH mutants were designed: YF376AA, in which CC2 residues Y376 and F377 were mutated to alanine, and the ‘patch’ mutant, in which the positive patch in the

NFACT-R domain consisting of the arginine residues R476, R480 and R534 were mutated, thereby forming the R476A R480A R534A triple mutant. The mutation and following biochemical experiments designed to test the contribution of the individual RqcH-50S docking sites were performed by Dr. Helge Paternoga.

The FLAG-tagged RqcH mutants introduced in the ΔrqcH strain are expressed at comparable levels to the wild-type control (Figure 37A). FLAG immunoprecipitation (IP) revealed a strong reduction of co-IP'ed ribosomal proteins for the YF376AA mutant and a smaller reduction for the patch mutant, compared to the wild-type (Figure 37A). In addition, the combination of the two mutations further decreased 50S binding compared to the YF376AA mutant alone, albeit to a small extent (Figure 37A).

Analysis of the co-IP'ed RNA species indicates that all mutants specifically interact with 50S subunits and are still able to bind to tRNA (Figure 37B, Lytvynenko et al., 2019). For the mutants, these tRNA species are enriched relative to the 23S rRNA, which is consistent with their reduced interaction with the 50S subunit (Figure 37A). The observation that RqcH-50S-coimmunoprecipitation for each mutant, the YF376AA and patch mutant, is decreased indicates a weakened 50S association compared to the wild-type RqcH. This suggest that the introduced mutations in RqcH destabilizes the 50S binding and this, in turn, reinforces the structural assignment of the CC2 residues, Y376 and F377 as well as NFACT-R residues, R476, R480 and R534 as 50S binding interfaces in RqcH.

Moreover, the CC2 YF376AA mutation impacts RqcH's ability for 50S binding to a greater extent, since the YF376AA mutant showed a significant reduction in immunoprecipitation of 50S ribosomal proteins compared with the NFACTR patch mutant (Figure 37A).

To test for *in vivo* phenotypes, the RqcH mutants were introduced in the ΔrqcH ΔssrA double deletion strain and checked for growth complementation at 45 °C (Figure 37C). SsrA is the *B. subtilis* gene for tmRNA and was co-deleted with RqcH to enhance the phenotype (Lytvynenko et al., 2019). In this experiment, the RqcH YF376AA mutant shows a strong defect in complementing the growth phenotype, whereas the patch mutant complements growth as efficiently as wild-type RqcH. The combination of the patch and YF376AA mutations results in a synthetic defect (Figure 37C), indicating that the patch mutant has reduced functionality when 50S association is weakened by the YF376AA mutations.

To further investigate the role of CC1-M-CC2 in 50S binding, a truncated RqcH mutant containing only this region of the protein (amino acids 282-415) was generated. This mutant was expressed at low levels compared to the wild-type, preventing functional analysis. Nevertheless, the results of FLAG IPs show that the RqcH$^{CC1\text{-}M\text{-}CC2}$ truncation co-precipitates with 50S subunits (Figure 37D and E), suggesting that the CC1-M-CC2 region can specifically target 50S subunits without binding to the P-site tRNA and H38.

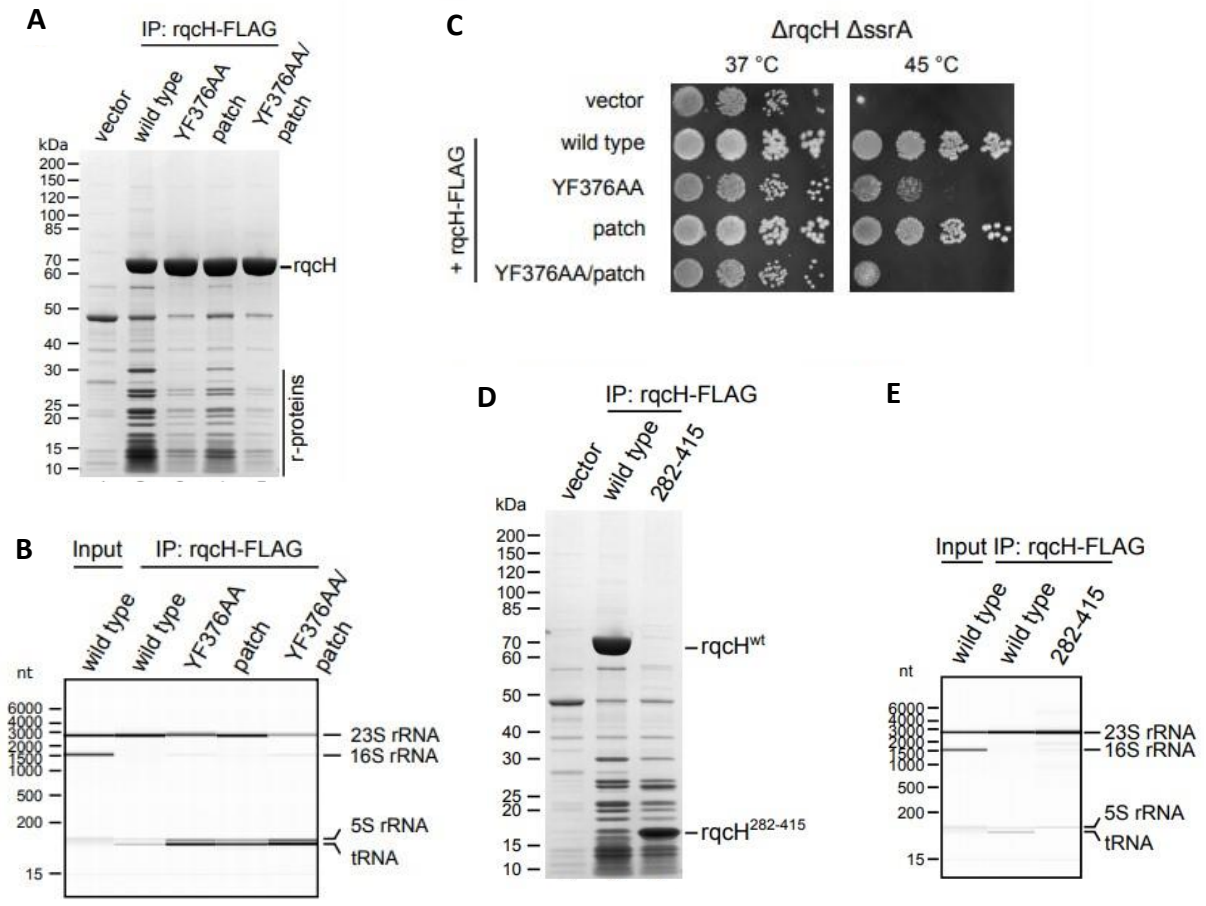

Figure 37: Biochemical analysis of CC2 and NFACT-R mutants. A) IP of RqcH-FLAG variants, eluates were analyzed by SDS-PAGE. r-proteins = ribosomal proteins. B) RNA extracted from rqcH-FLAG co-IPs was analyzed by capillary gel electrophoresis. The apparent increase of 5S rRNA over 23S rRNA for the mutant samples results from an overlay of the 5S rRNA and tRNA peaks. nt = nucleotide. C) Growth analysis of the ΔrqcH ΔssrA double deletion strain containing plasmids carrying rqcH-FLAG variants. D) IP of RqcH-FLAG variants including the RqcH$^{CC1\text{-}M\text{-}CC2}$ truncation, eluates were analyzed by SDS-PAGE. E) RNA extracted from the same IPs was analyzed by capillary gel electrophoresis. The experiments were performed by Dr. Helge Paternoga.

3.5.3 NFACT-R loops are essential for RqcH function

The NFACT-R domain is docked by the A-site, which suggested that it could contribute to A-site tRNA recruitment by 50S-bound RqcH for Ala-tailing (Lytvynenko et al., 2019). To test this

hypothesis, first a canonical A/A tRNA was fitted into our density map and checked whether the A-tRNA would clash with the NFACT-R domain in the conformation assumed in our structure.

There are two loops (loop 1: K430-Y431-L432-R433-P434; loop 2: K537-K538-P539-N540-G541-A542-K543) in the NFACT-R domain that would face an A/A tRNA but were not resolved in our reconstitution, suggesting flexibility (Figure 38). The globular portion of the NFACT-R domain would not clash with the A-tRNA and loops 1 and 2 of the NFACT-R domain are well positioned to accept the D-loop of incoming tRNAs. Notably, loop 2 residue G541 is in the same distance of 10 Å as H38 nucleotide G930 to G19 of the tRNA's D-loop (Figure 38 B), which is involved in A-tRNA-positioning during translocation (Yusupov, 2001). Furthermore, NFACT-R loop 1 residue Y431 is even closer and could also interact with the A-tRNA nucleotide G19 (Figure 38B).

In addition, RqcH-bound H38 is shifted compared to the 70S-EFG-pre-translocational state (Figure 38A) (Komoda et al., 2006).

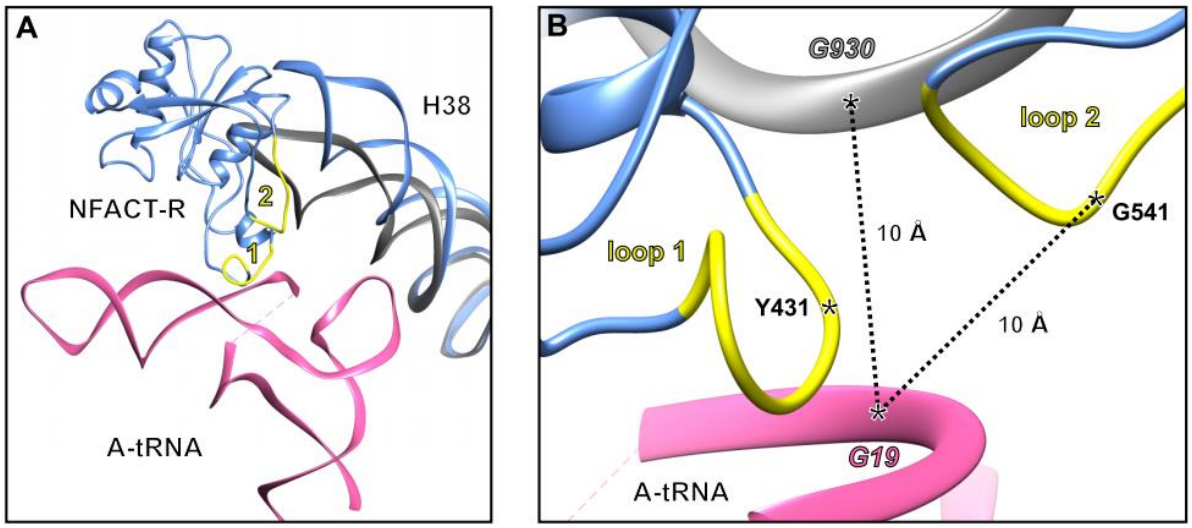

Figure 38: RqcH's NFACT-R domain features loops with functional significance at the ribosomal A-site. (A) Superposition of the loops (yellow, indicated as Loop 1 and Loop 2) from the docked NFACT-R crystal structure (PDB ID: 5H3W, Musyoki et al., 2016, blue) and H38 (blue, present structure) with the A-site tRNA (pink) and H38 (grey) of an EFG-70S pre-translocational state (PDB ID: 4WPO, Lin et al., 2015) upon a 23S rRNA alignment. (B) Close-up view of overlaid models in A) shows the distances between NFACT-R loops (yellow) or H38 (grey) and the A-tRNA (pink). NFACT-R Loop 2 residue G541 is in a similar distance to G19 of the A-tRNA as nucleotide G930 of H38 in the EFG-70S complex. NFACT-R's Loop 1 residue Y431 is located even closer to G19 of the A-tRNA.

To test whether the NFACT-R loops participate in A-tRNA recruitment, the two NFACT-R loops were mutated to glycine-serine stretches of equivalent length. Both loop 1 and loop 2 mutants are expressed at comparable level to the wild-type control (Figure 39A) and still bind specifically to 50S subunits and Ala-tRNA (Figure 39A and B). On the other hand, whereas individual loop mutants are nearly as effective as the wild-type in complementing growth of the ΔrqcH ΔssrA double deletion strain at 45 °C, a mutant with both loop mutations combined has a strong growth phenotype (Figure 39C). The mutation experiments show that NFACT-R loops are essential for the function of RqcH, most likely mediated by A-tRNA positioning.

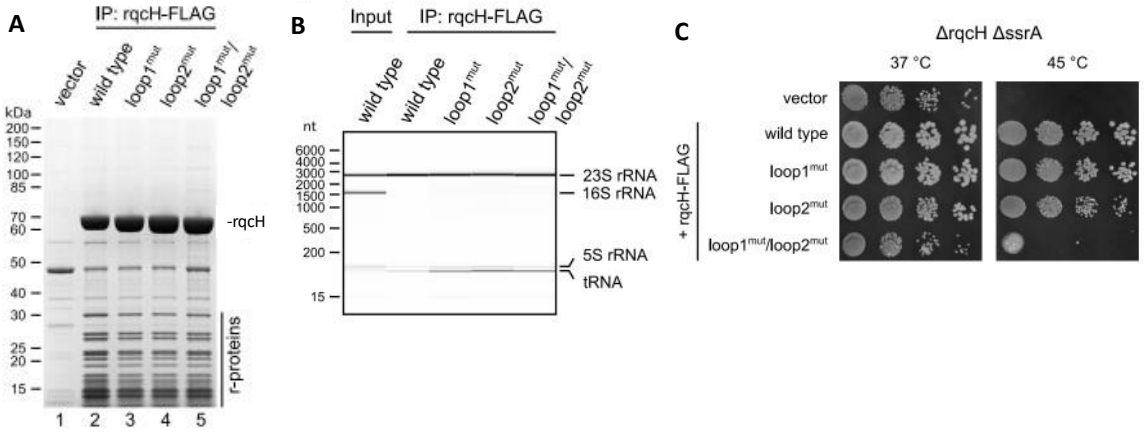

Figure 39: Biochemical analysis of RqcH's NFACT-R domain loops with functional significance at the ribosomal A-site. A) IP of RqcH-FLAG variants, eluates were analyzed by SDS-PAGE. r-proteins = ribosomal proteins. B) RNA extracted from rqcH-FLAG co-IPs was analyzed by capillary gel electrophoresis. nt = nucleotide. C) Growth analysis of the ΔrqcH ΔssrA double deletion strain containing plasmids carrying rqcH-FLAG variants. The experiments were performed by Dr. Helge Paternoga.

3.6 Cryo-EM analysis of the 70S-tmRNA-EF-G-FA sample

The 70S ribosome in complex with tmRNA-SmpB and EF-G is formed during translocation as part of the *trans*-translation cycle, which is described in the introduction (chapter 1.4.1). The first 70S-tmRNA-EF-G structure has been resolved to only 8.3 Å due to limited EM technologies at this time (Ramrath et al., 2012). The 70S-tmRNA-EF-G sample in this study was prepared using the antibiotic fusidic acid (FA) which stalls the EF-G-mediated translocation of the fMet-Ala-TLD-SmpB module and a $tRNA^{fMet}$ from the A and P to P and E sites, respectively. This antibiotic binds between domains I – III of EF-G after GTP hydrolysis has occurred (Gao et al., 2009). This stalls EF-G in its GDP form on the ribosome because FA binding blocks the conformational change of EF-G required for release from the ribosome (Gao et al., 2009; Ratje et al., 2010).

To achieve higher resolution and molecular understanding of the 70S-tmRNA-EF-G structure, the remaining cryo-EM grids of the study in Ramrath et al., 2012 were used for data collection at a Titan Krios electron microscope and re-analysis (see chapter 2.4).

In total 6584 micrographs were collected; a representative micrograph is shown in Figure 40 A. Image processing was done in CryoSPARC (Punjani et al., 2017) and SPIDER (Frank et al., 1996). Using multiparticle sorting (Loerke et al., 2010) and focused classification (Penczek et al., 2006), the particle images representing ribosomal subpopulations with well-defined factor densities were separated from subpopulations lacking or poorly resolved tmRNA densities. The data processing strategies are described in detail in Figure 40B.

The technically advanced microscopy conditions in combination with state-of-the-art image processing allowed the reconstruction of cryo-EM maps with global resolutions of 3.5 Å to 3.8 Å resolution (Figure 42). Compared to the previous cryo-EM study (Ramrath et al., 2012) revealing only one substate of intermediate resolution, the cryo-EM re-analysis of the 70S-tmRNA-EF-G-FA specimen revealed five substates (Figure 40) and each with improved resolution (Figure 42). Based on the presence or absence of the EF-G densities and position of the tmRNA densities, the final cryo-EM maps were assigned to distinct translocation states (Figure 40B, colored maps at the bottom of the classification scheme): the PAST-E TI POST (class 2.1.2.1), the PAST-E POST state (class 2.1.2.2), the tmRNA-PRE state (class 2.2.3), the tmRNA-TI-POST I state (class 3.3.3) and the tmRNA-TI-POST II state (class 3.4.3).

The final maps were further refined and used for modelling (see chapters 2.4.5 and 2.5). The structural details of the states are further described in the following chapter 3.7. In this work, the structures obtained from the 70S-tmRNA-EF-G-FA specimen were designated as tmRNA-PRE and tmRNA-TI-POST states to distinguish them from the canonical PRE and TI-POST states. Since the PAST-E states are unique for the tmRNA pathway, their names are kept in the next chapters.

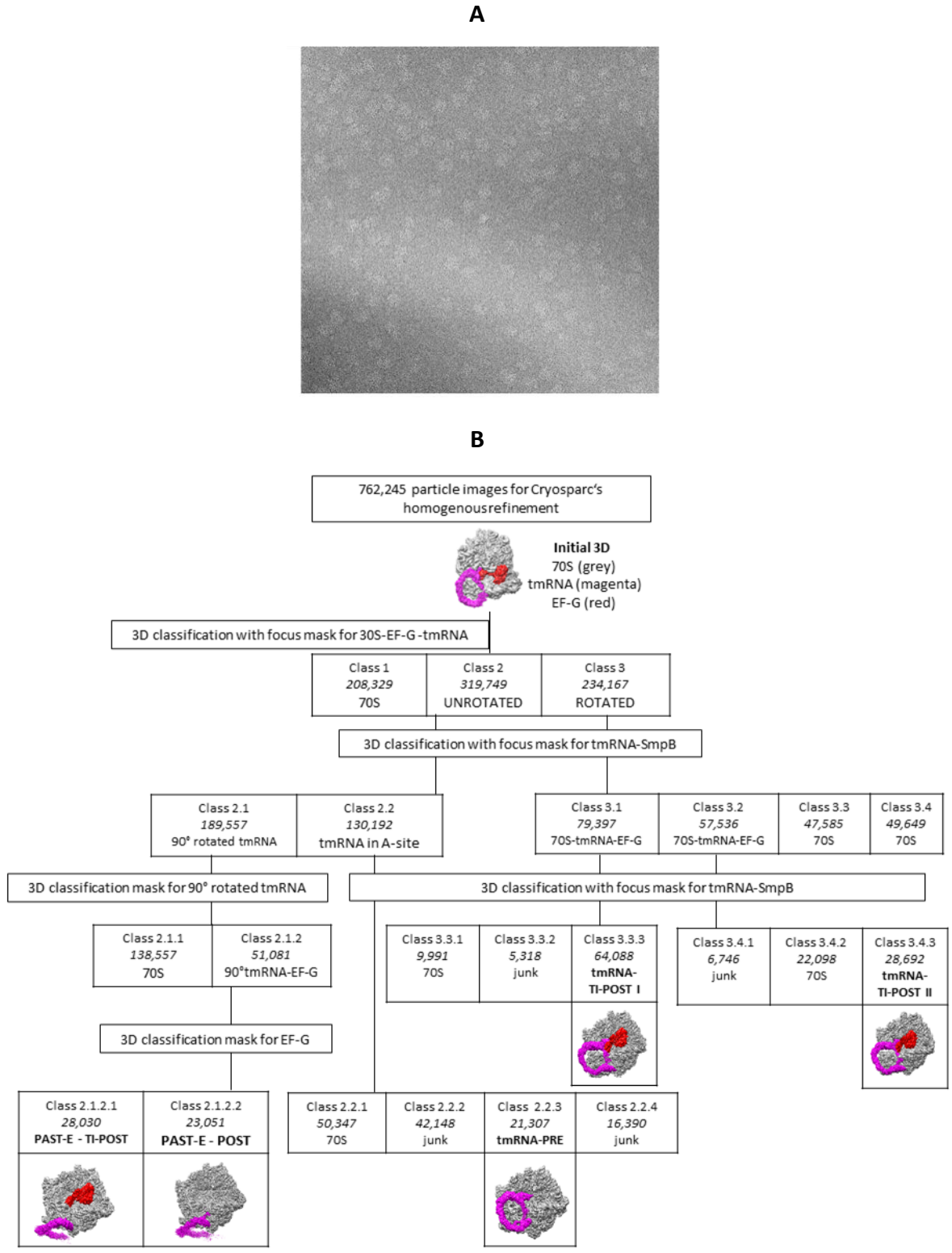

Figure 40: Representative micrograph and classification scheme for the cryo-EM data set obtained from the 70S-tmRNA-EFG-FA sample . A) Representative micrograph collected at the Titan Krios TEM. B) Classification scheme with indicated umber of particle images used for the 3D classification in each class. The initial 3D reconstruction of the 70S-tmRNA-EF-G-FA sample was obtained using the homogenous refinement of CryoSPARC (Punjani et al., 2017). In the first sorting step, the particle images were separated into three classes by applying a mask covering the ribosomal 30S subunit, tmRNA and EF-G: class 1 - an empty 70S substate, class 2 - unrotated 70S-tmRNA substate, and class 3 - rotated 70S-

tmRNA substate. The rotated and unrotated states were further classified separately using masks for the tmRNA-SmpB density. The unrotated state (class 2) split into two classes (2.1 and 2.2). The class 2.2 substate revealed a 70S ribosome with tmRNA in the ribosomal A-site. Further improvement of resolution and definition, achieved by classification of the class 2.2 particle images using a tmRNA-SmpB mask revealed the final cryo-EM map (class 2.2.3) and exclusion of particle images showing empty 70S ribosomes or maps consisting of images of bad quality (broken particle images or images with bad resolution, indicated as junk). The class 2.1 substate is a 70S with a 90° rotated tmRNA, a tmRNA configuration which was not seen before. The particles images in this class 2.1. were classified using a mask for the 90° rotated tmRNA which resulted into two substates, one empty 70S reconstruction and another 70S showing a strong density for the 90° rotated tmRNA and a weak density for EF-G. The differences in the intensities of the bound ligands, EF-G and tmRNA suggesting the class 2.1 substate is composed of more than one state (compositional heterogeneity). Therefore, the particles images were classified using a mask for EF-G. Indeed, this allowed the separation of a 70S with 90° rotated tmRNA with either presence of EF-G (class 2.1.2.1) or absence of EF-G (class 2.1.2.2). The particle images of the rotates states (class 3.1, and 3.2) were each subjected to focused classification using the tmRNA-SmpB mask to further improve their definitions achieved by exclusion of bad quality images. This resulted into the final populations (class 3.3.3 and 3.4.4) differing in the position of the tmRNA density at the first glance. The final maps (boxed) were further refined and used for modelling. The densities for the 70S ribosome (grey) tmRNA (magenta) and EF-G (red) in the initial and final maps are shown. The particle images in each class are indicated in italics.

3.7 Structural characterization reveals distinct 70S-tmRNA states

All extra-ribosomal densities could be identified, using appropriate models for each map (see also chapter 2.5 and table S2). The final maps with colored densities for their ligands (tRNAs, tmRNA, SmpB and/or EF-G) can be seen as an overview in Figure 41. In all five states, the full tmRNA molecule is resolved, albeit at different resolutions (Figure 42), caused by its conformational flexibility.

The tmRNA elements with poor or no ribosome contact, such as the mRNA-like domain (MLD), the pseudoknots (PKs) or only in case of the PAST-E-states, the tRNA-like domain (TLD), possess a higher degree of flexibility (indicated by its fragmented density and lower resolution, see Figure 42) than ribosome-bound tmRNA elements. The TLD of the tmRNA is associated with the core structure of SmpB in all states. The TLD/SmpB module is positioned at the 50S ribosomal A-site in the tmRNA-PRE state and at the 50S ribosomal P-site in the tmRNA-TI-POST states. In the PAST-E states, the TLD/SmpB module has left the ribosome and stays mostly associated via its MLD that occupies the complete mRNA channel.

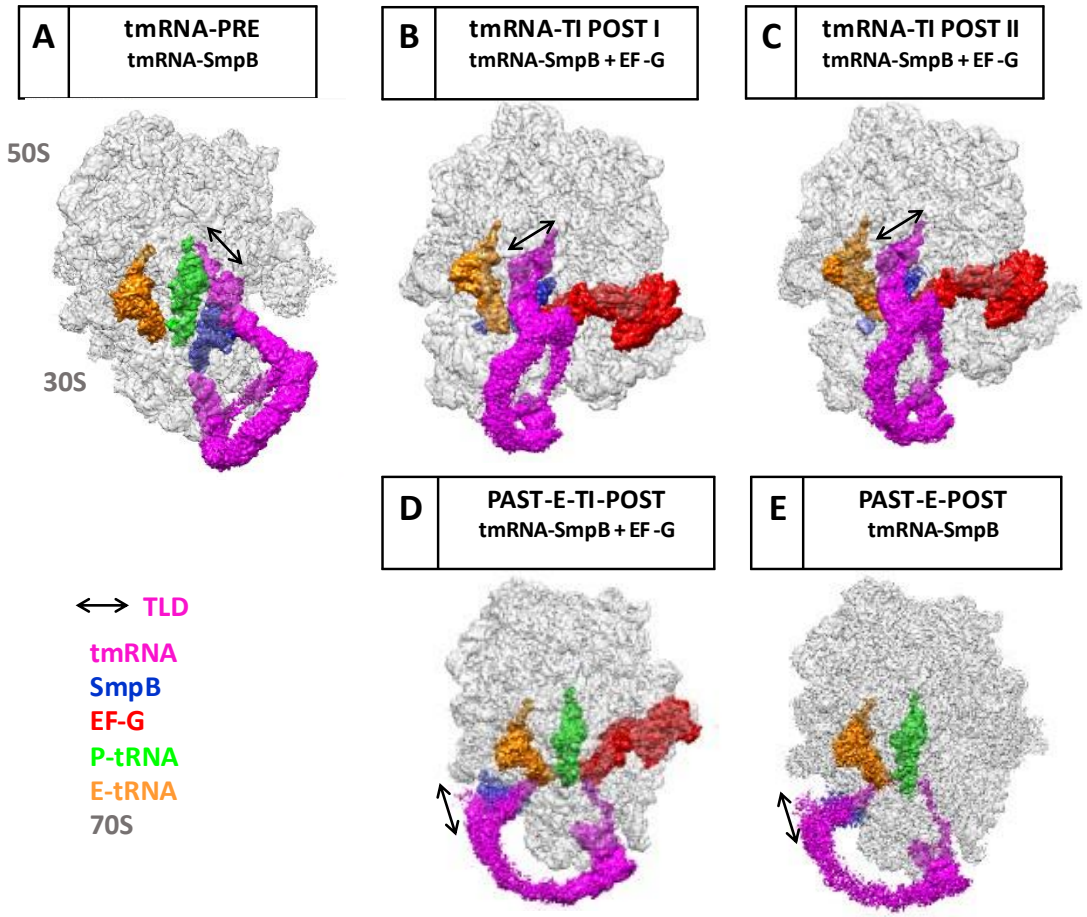

Figure 41: Overview of the cryo-EM maps of all 70S-tmRNA states. A) tmRNA-PRE, B) tmRNA TI-POST I, C) tmRNA-TI-POST II, D) PAST-E-TI-POST, E) PAST-E-POST. The densities were colored using their respective models built in this study.

The overall resolution of the final cryo-EM maps obtained from the 70S-tmRNA-EF-G-FA specimen range between 3.5 Å (tmRNA-TI-POST I), 3.7 Å (PAST-E-POST) and 3.8 Å (tmRNA-PRE, -TI-POST II and PAST-E-TI-POST) (Figure 42). Coloring the cryo-EM maps according to their local resolution revealed that the core elements of the ribosome reach local resolutions of 3 Å, while the resolution of the surface-exposed, flexible regions of the ribosome, and bound ligands (tmRNA-pseudoknots (PKs)/mRNA-like domain (MLD), tRNAs and small protein B (SmpB)) vary from 4 Å to 8 Å (Figure 42). The resolution allowed building of the atomic model for each ribosomal substate with a reasonable statistics and good map-to-model correlations (see Table S4).

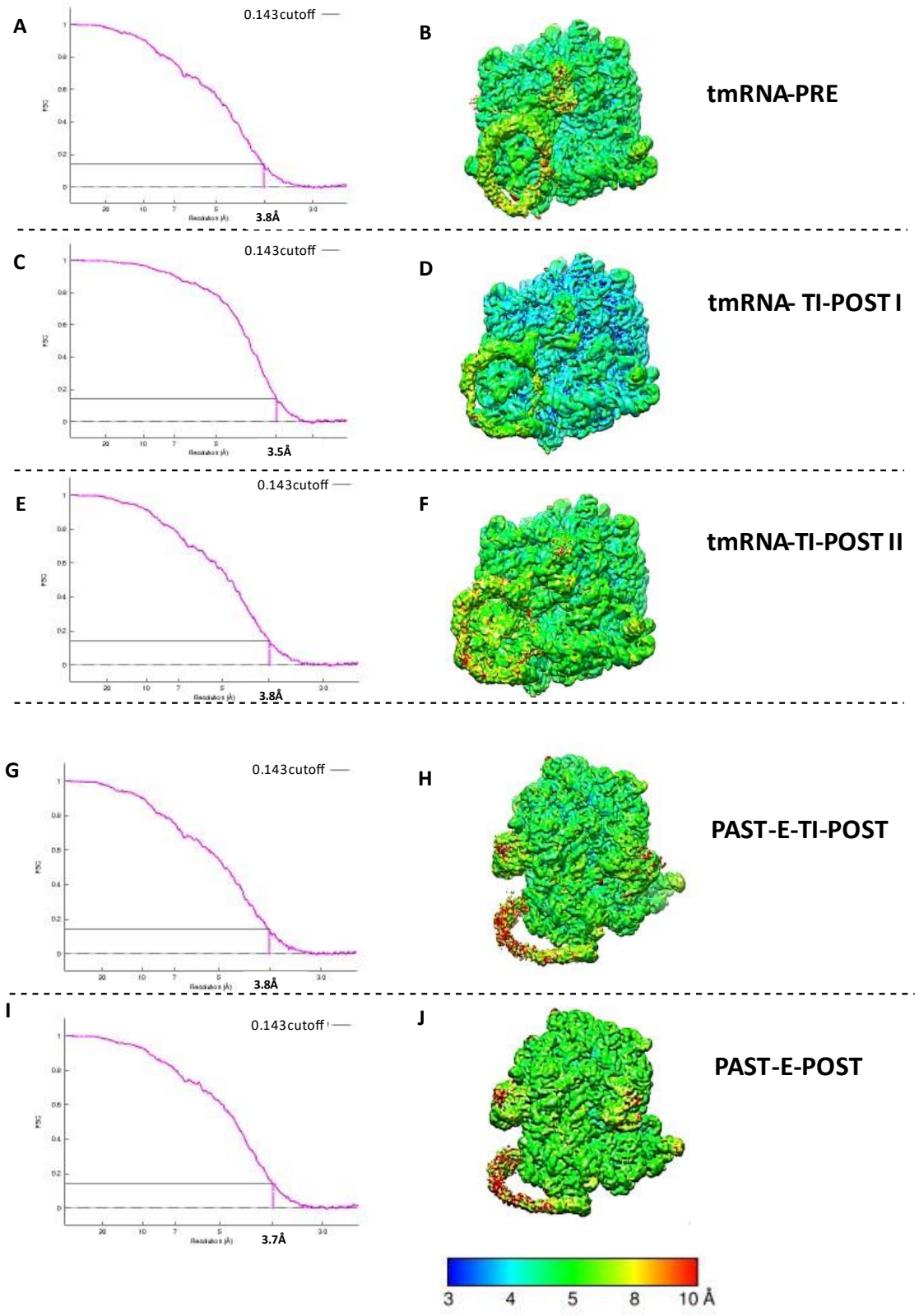

Figure 42: Map quality of all 70S-tmRNA states. A, C, E, G, and I: Fourier shell correlation (FSC) curves showing the global resolution of the maps. B, D, F, H, and J: Finale cryo-EM maps colored by their local resolution ranging from 3 Å to 10 Å indicated by the color scale bar.

To characterize the precise binding position of canonical tRNAs and tmRNA's TLD/SmpB module, their interaction with ribosomal 50S (23S rRNA) and 30S (16S rRNA) residues that contact the tRNA in A, P-, and E-site were analyzed. The classical A/A-tRNA binding position involves interaction of U955 (head a-site) of the 16S rRNA and G2553 of the 23S-RNA (Yusupov et al., 2001) (Figure 43). In the classical P/P-position the tRNA is contacted by A1229, G1338, G1339 (head p-site), and A790 (body p-site) of the 16S rRNA and G2551 as well as G2552 (A-loop) of the 23S rRNA. The classical E/E-tRNA position includes contacts of U788, A695 (body E-site) of the 16S rRNA and C2394, G2421 of the 23S rRNA.

In the tmRNA-PRE and PAST-E states the tRNAs are bound in classical P/P- and E/E - tRNA binding positions (Figure 43A, D and E). The ribosomal A-site in the PAST-E-states is empty, while in the tmRNA-PRE state it is occupied by the 3'CCA-end of the TLD at the 50S subunit and SmpB at the 30S subunit. Classical tRNA binding positions are observed in nonrotated ribosomes (as described in the introduction (chapter 1.2.3.1) as this is the case for the tmRNA-PRE and the PAST-E states.

In the tmRNA-TI-POST states, the 3'CCA- end of the TLD and canonical tRNA interact with the P-site (G2251 and G2252) and E-site (C2394 and G2421) of the 50S subunit, respectively (Figure 43B and C). From the perspective of the 30S subunit, the SmpB of the tmRNA-TI-POST states contact the p-site of the 30S body (A790) while maintaining 30S head a-site contact (U955). The canonical tRNA has p-site contact to the 30S head (A1229, G1338, and G1339), while binding the e-site of the 30S body (U788 and A695). Respectively, in the tmRNA-TI-POST states, the tRNA or tRNA-like entities are bound in intra-subunit ap/P and pe/E hybrid state conformation.

The formation of chimeric bound ap/P and pe/E tRNA-tRNAs is accompanied with the reversal movement of 30S head and body during EFG-induced translocation (as described in chapter 1.3.2.3). The characteristics of rotation in the tmRNA-TI-POST states are described in chapter 3.7.2.

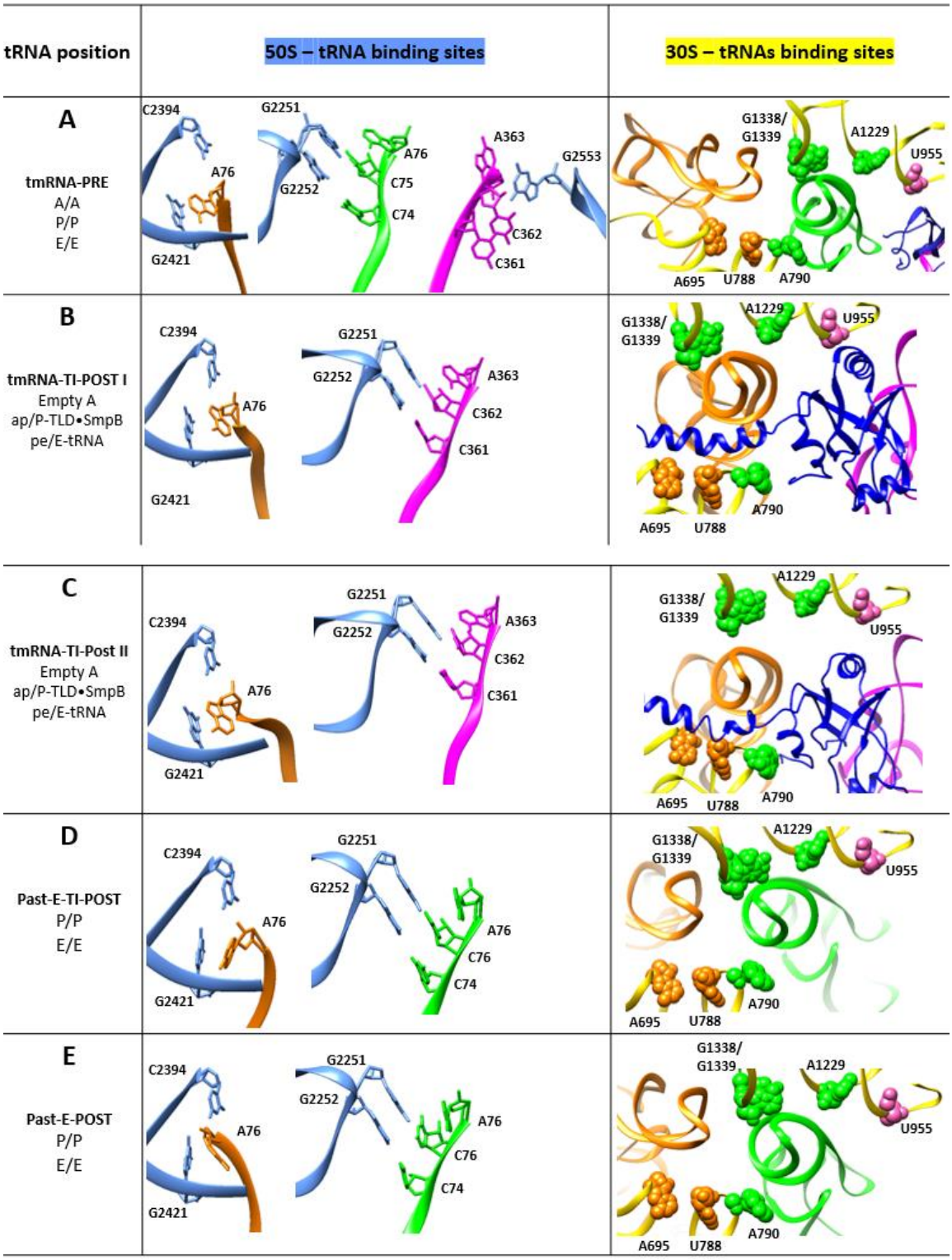

Figure 43: Ribbon presentation of the individual tRNA binding sites in the 70S-tmRNA states A) tmRNA-PRE, B) tmRNA-TI-POST I, C) tmRNA-TI-POST II, D) PAST-E-TI-POST, E) PAST-E-POST with indicated tRNA binding position on the ribosomal 50S and 30S subunit (left column). Middle column: The 23S (blue) rRNA residues of the 50S subunit that contact the tRNA in the A-site (G2553), P-site (G2251, G2252) and E-site (C2394, G2421) are displayed as sticks. Right column: The 16S (yellow) rRNA residues of the 30S subunit that contact the tRNAs in the A-site (pink, U955), P-site (green, A790, A1229, G1338, G1339) and E site (orange; A695, U788) are shown as spheres. The canonical E- and P-site tRNA are colored in orange and green, respectively. The tmRNA is colored in magenta and the SmpB protein is deep blue.

3.7.1 The tmRNA-PRE translocation shows TLD-SmpB mimicking a A/A-tRNA

The tmRNA-PRE translocation complex was produced by adding alanine-tmRNA–SmpB–EF-Tu–GTP to ribosomes with a fMet-tRNA^{fMet} at the P site and a truncated mRNA at the A site (see chapter 2.3.3). The subsequent EF-Tu-induced GTP hydrolysis and EF-Tu-GDP release form the 70S ribosome with tmRNA bound to the ribosomal A-site. This complex was used for the subsequent EF-G-induced translocation reaction, which was stalled using fusidic acid (FA) in order to form translocation intermediate states (defined, for example, by the presence of EF-G), therefore called 70S-tmRNA-EFG-FA sample.

However, the presence of a tmRNA-PRE translocation state indicates that the EF-G induced reaction did not fully lead to the turnover of the PRE complex reactant. But the high-resolution information of this by-product provide additional information about a structurally relevant state that forms before the translocation starts. The additional tRNA was bound in the ribosomal E-site (Figure 44A) due to the excess of deacylated tRNA^{fMet} in the reaction mix.

The comparison with a canonical PRE state (Demeshkina et al., 2012; PDB ID: 4v87) shows that overall binding and conformation of the bound tRNAs or TLD/SmpB are similar (Figure 44A). The acceptor end and elbow region of the canonical A-site tRNA is taken by the TLD of the tmRNA, while the anticodon stem loop is replaced by the core structure of SmpB. The mRNA of the tmRNA-PRE state interacts with the anticodon of the E-tRNA at position C34 and base-pairs with the anticodon of the P-tRNA via its start codon, A12, U13 and G14 (Figure 44B). The truncated codon (U15, A16) at the 3’end of the mRNA is positioned at the empty A-site (Figure 44B).

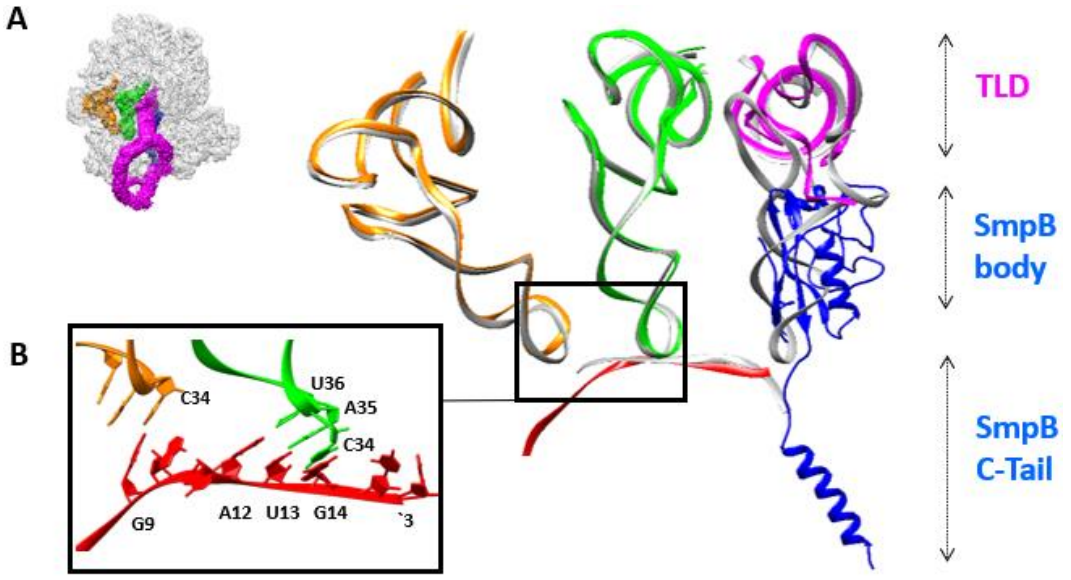

Figure 44: Comparison of the tRNA and TLD/SmpB in the tmRNA-PRE with the tRNAs in the canonical PRE state. A) Left: Orientation help showing the structure of the tmRNA-PRE state with the tRNA in the E-site (orange) and P- site (green) as well as TLD (magenta)-SmpB (blue) in the ribosomal A-site. Right: Comparison of the atomic models of the tmRNA-PRE structure (colored) and canonical PRE structure (grey; Demeshkina et al., 2012; PDB-ID: 4V87) upon an 50S alignment. B) Atomic model of the mRNA (red) extends along the binding sites of the E- tRNA (orange) and P-tRNA (green) and reaches the A-site via its 3'end.

The A-site binding of tmRNA-SmpB is stabilized by the interaction of the conserved residues, His22 and His136 of SmpB (Dong et al., 2002) and nucleotides A1493 and G530 of the 16S rRNA at the decoding center (DC), respectively (Figure 45A and B). The interaction of SmpB at the DC is supported by biochemical experiments showing that binding of SmpB at the A site protects DC nucleotides (Kurita et al., 2007; Nonin-Lecomte et al., 2009). However, compared to canonical decoding of tRNA, where G530, A1493 as well as A1492 participate in anticodon-codon recognition (Ogle et al., 2001), the tmRNA-PRE state does not involve A1492 the interaction with SmpB (Figure 45C).

Beside the imitation of the tRNAs ASL by SmpB's body, the C-terminal tail of SmpB mimics the mRNA by occupying its channel downstream of the A-site codon (Figure 45D). Similar to the mRNA (Wimberly et al., 2000), SmpB first passes through the RNA layer (h28, h34, h18), then reaches the proteins uS4 and uS5, and finally ends at the tmRNA-H5. The interaction of SmpB with the C1397 (h28) and U1196 (h34) may help to position SmpB correctly in the ribosomal A-site. Moreover, the interaction of charged residues in the C-terminal SmpB helix with the channel proteins uS4 and uS5, as well as with H5 stabilizes the tmRNA-SmpB in the PRE state in overall (Figure 45D).

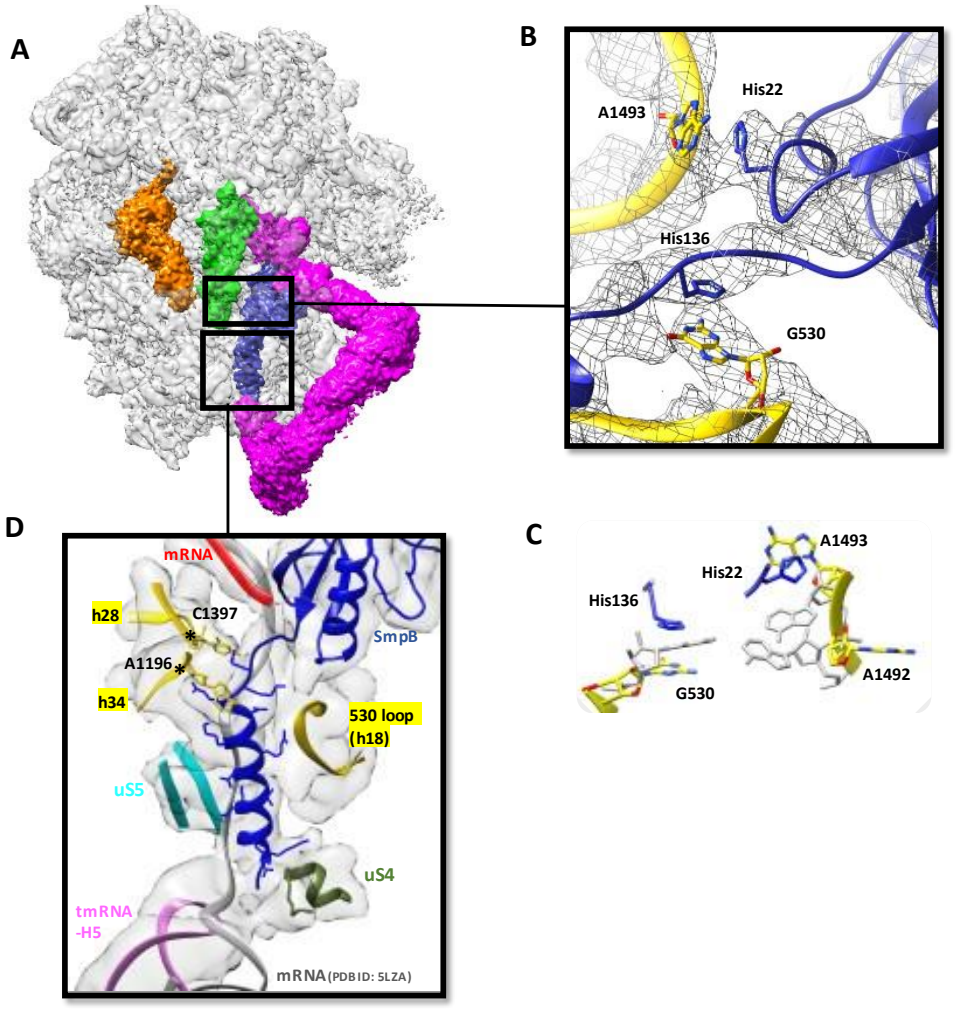

Figure 45: Interactions of SmpB within the tmRNA-PRE state. A) SmpB (blue) interacts at the ribosomal A-site (upper box) and the mRNA channel (lower box). B) Close-up views of the interaction of SmpB's residues His22 and His136 with the decoding nucleotides A1493 and G530, respectively. The map is presented as mesh. C) Comparison of the conformational configuration of A1492/A1493 and G530 at the decoding center in the present tmRNA-PRE state (colored) and a canonical decoding state (grey) after 50S alignment. D) The C-terminal tail of SmpB with its charged residues (blue sticks) interact with the mRNA channel downstream of the A-site codon and contact 16S RNA helices (h28, h34 and h18; yellow), ribosomal proteins uS5 (cyan), uS4 (olive) as well as tmRNA's H5 (orchid). The canonical mRNA (grey) after 50S alignment is shown for comparison. The map is shown transparent and in light grey.

Both, PK2 and H5 of the tmRNA contact the ribosome via proteins uS3, uS4 and uS5 at the ribosomal solvent side (Figure 46A). The interaction between the single-stranded RNA region from PK2 (nucleotides 183-185) and ribosomal protein uS3 (residues 73-84) anchors the tmRNA to the small subunit. The interactions of uS3 (residues 141-132), uS4, uS5, and SmpB's C-terminus (residue N157) with the tip of tmRNA's H5 blocks the entrance of the mRNA channel. The density emerging from H5 and extending to the PK1 corresponds to the MLD (Figure

46B) which is too fragmented for building an atomic model. However, considering the electron density alone, one can see clear interaction between the MLD and ribosomal helix h16 at A412-G413 and G423-G424 (Figure 46B, close-up view).

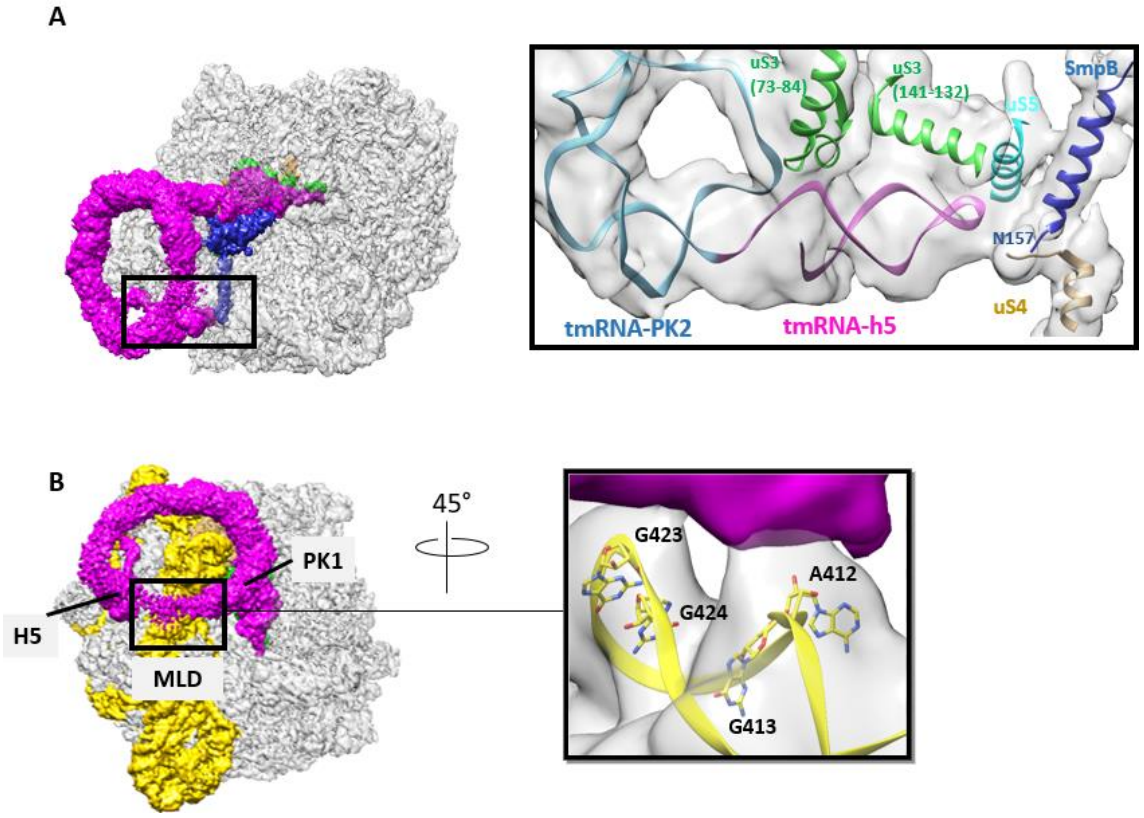

Figure 46: Interaction of PK2/H5 and MLD in the tmRNA-PRE complex. A) PK2 (sky blue) and H5 (orchid) is stabilized by uS3 (green), uS4 (tan), uS5 (cyan) as well as SmpB's C-terminus (blue) at the solvent side of the ribosome. B) Close-up of the MLD-h16 interaction, where helix h16 nucleotides A412, G413, G423, and G424 are represented as yellow sticks, embedded into their grey cryo-EM map. The maps were low-pass filtered (width: 5 Å) for clarity.

3.7.2 The tmRNA-TI-POST states show the tmRNA-SmpB during translocation

In comparison to the previous study of the same 70S-tmRNA-SmpB-EF-G-FA specimen that revealed only one TI-POST state (Ramrath et al., 2012), in the current cryo-EM study this state split into two substates, the tmRNA-TI-POST I and I state (Figure 40 and 41B and C). The presence of two substates allows a more accurate description of the tmRNA-TI-POST state as well as the molecular interactions of its bound ligands since both states are much better resolved (Figure 42C-F).

The two structures reveal that the translocation steps are dominated by movements of the 30S subunit relative to the 50S subunit, aimed for reestablishing the unrotated conformation

of a classical POST state: From tmRNA-TI-POST-I, the 30S body/platform rotates back reaching the tmRNA-TI-POST-II state that is very similar to the previously published tmRNA-TI-POST (30S subunit rotation: ~5°; 30S head swivel: ~19°; 30S head tilt: ~12°) at intermediate resolution obtained from the same sample (Ramrath et al., 2012). This conclusion was made after comparison of the degrees in 30S subunit and head rotation of the two translocation intermediates obtained from the 70S-tmRNA-SmpB-EF-G-FA sample (Figure 47A and B), which is described in the following text.

The structure of the tmRNA-TI-POST I state, is characterized by a 9° rotation of the 30S body/platform, measured relative to the 50S subunit as well as by the large 30S head swivel movement of about 20°, measured relative to the 30S body/platform (Figure 47A). These dimensions are compared with the dimensions of the classical/unrotated conformation of a *E. coli* 70S ribosomal complex (Dunkle et al., 2011). In contrast to the tmRNA-TI POST I (Figure 47A), the tmRNA-TI-POST II state (Figure 47B) reveals a less intensive rotation of the 30S body/platform of 4° and a similar 30S head swivel movement of about 20° in relation to the same unrotated 70S ribosomal complex as mentioned above (Dunkle et al., 2011).

Compared with a canonical TI-POST state (Ramrath et al., 2013), both states, the tmRNA-TI-POST I and II, exhibit an additional head tilt of 9° and 13°, respectively. The 30S head tilt measurement was performed around an axis that is roughly parallel to the mRNA, near the A- and P-site codons. The tilt movement distances the 30S head further from ribosomal 50S subunit. Compared to the classical state (Dunkle et al., 2011), the combination of all three motions (30S head tilt, swivel and intersubunit rotation) in the presented tmRNA-TI-POST states achieves a shift of the ribosomal elements of up to 50 Å (Figure 47A and B).

The conformation of the presented tmRNA-TI-POST-states resembles the canonical TI-POST state, which is characterized by a 4° 30S subunit rotation and 18° 30S head swivel (Ramrath et al., 2013) and it is in good agreement with related structural information (Zhou et al., 2013, 2014; Ratje et al., 2010). The head tilt was originally thought to be unique to tmRNA-70S structures, but has also been found in canonical 80S complexes (Flis et al., 2018) and predicted in MD simulation experiments with 70S translocation intermediate structures (Nguyen and Whitford, 2016).

Notably, during the 5° 30S subunit back-rotation, the 30S head continues the tilt forward movement of about 4° (Figure 47C). The enlarged tilt in the TI-POST II state enables overcoming barriers required for MLD loading during translocation (see chapter 4.2.4).

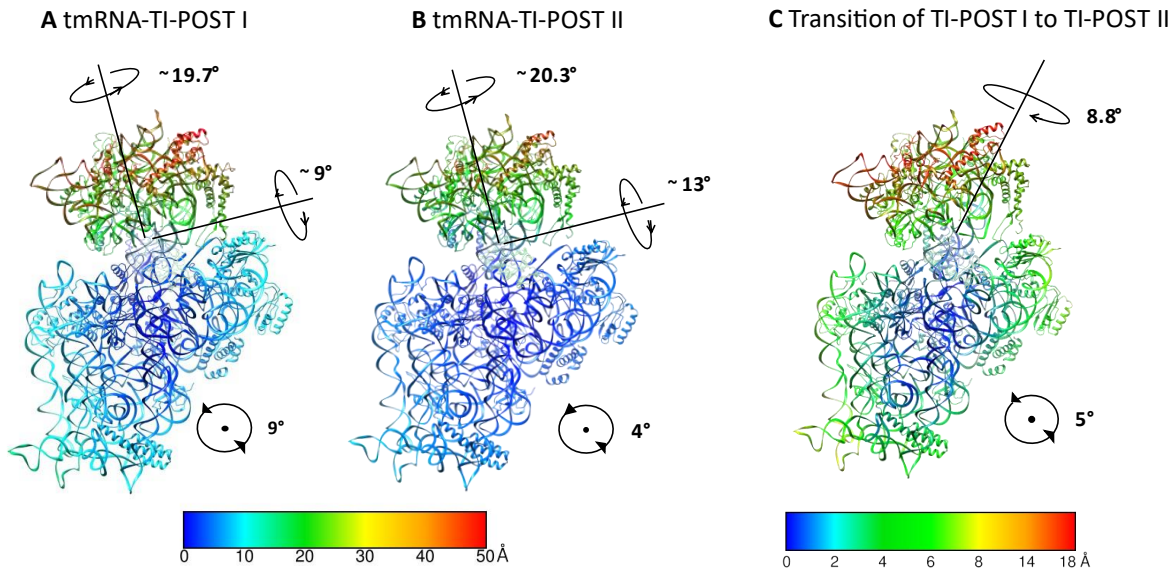

Figure 47: Rotation and tilting of the 30S elements in the tmRNA-TI-POST states. The 30S subunit viewed from the intersubunit space. A) and B) Shown are the degrees of the 30S subunit rotation, the 30S head swivel movement as well as 30S head tilt for the tmRNA-TI-POST I (A) and II (B), compared to the classical/unrotated conformation (Dunkle et al., 2011). C) Comparison of 30S head and body rotation of the tmRNA-TI-POST states by common 50S alignment. The intersubunit rotation happens along the vertical axis and the head rotation along the horizontal axis. Arrows indicate the direction of the rotations. Ribosomal elements are colored according to their structural movements relative to the classical conformation, from blue (less movement) to red (more movement) (Dunkle et al., 2011).

Interaction of SmpB within the tmRNA-TI-POST states

The superposition of the ligands from the tmRNA-TI-POST states and canonical TI-POST state upon a 50S alignment reveals similar position and conformation of the bound pe/E tRNAs, ap/P-tRNA or TLD and EF-G proteins (Figure 48C). However, there are small-scale differences to mention.

In contrast to the canonical TI-POST state (Ramrath et al., 2013), the anticodon steam loops (ASLs) of the pe/E-tRNA in the tmRNA-TI-POST states are slightly shifted (Figure 48C). The shifts are a consequence of the larger 30S body and head rotation in the tmRNA-TI-POST states (Figure 47), compared to the canonical TI-POST (2.5° 30S subunit rotation and 18° 30S head swivel). By following the 30S body rotation, ASL of the tRNA maintains the chimeric pe/E tRNA binding position on the 30S subunit.

The overlay of the ap/P site bound TLD/SmpB module with a canonic al ap/P tRNA shows a good overlap of their acceptor arms (Figure 48C). The difference in conformation within the elbow region/TΨC could result from the tmRNA-specific D-loop structure lacking the D-stem, which is becoming apparent in the tmRNA-TI POST states. The D-loop interacts with SmpB that matches the position of the ASL of the canonical ap/P tRNA.

In the canonical TI-POST state (Ramrath et al., 2013), the ASL of the ap/P-tRNA contacts the conserved loop I (residues 507–514 in E. coli EF-G) in domain IV of EF-G (Gao et al., 2009). In the presented tmRNA-TI-POST states, the SmpB mimics the ASL of the ap/P tRNA (Figure 48A and B) and thereby replaces the tRNA binding interface for EF-G as it was observed for the intermediate resolution tmRNA-TI-POST structure (Ramrath et al., 2012).

The improved resolutions of the present tmRNA-TI-POST states allows a visualization of the molecular details of the EFG/SmpB interaction around the decoding center (Figure 48A and B): EF-G is contacted at residue Y514 of domain IV by the residues F66 and Y55 of SmpB. The aromatic character at amino acid position 66 and 55 in SmpB is conserved among bacteria (Bessho et al., 2007) which indicates their importance during translocation.

The C-terminal tail of SmpB occupies the space which is normally taken by the mRNA upstream the A-site codon in the canonical TI-POST state (Figure 48C). The cryo-EM density corresponding to the C-terminal tail exhibits a helical form and is partially fragmented, indicating structural flexibility. Therefore, the model of SmpB's C-terminal helix was placed as a rigid body and refined once overall together with the final model. Like the mRNA in the canonical TI-POST (Ramrath et al., 2013), the SmpB C-terminal tail in the presented tmRNA-TI-POST structures interact with the anticodon loop of the bound tRNA (Figure 48A and B). In the rigid body-docked SmpB model of both tmRNA-TI-POST states I and II, SmpB's residue W147 and the conserved residue F25 are potential candidates for interaction with the E-site tRNA (Figure 48A and B).

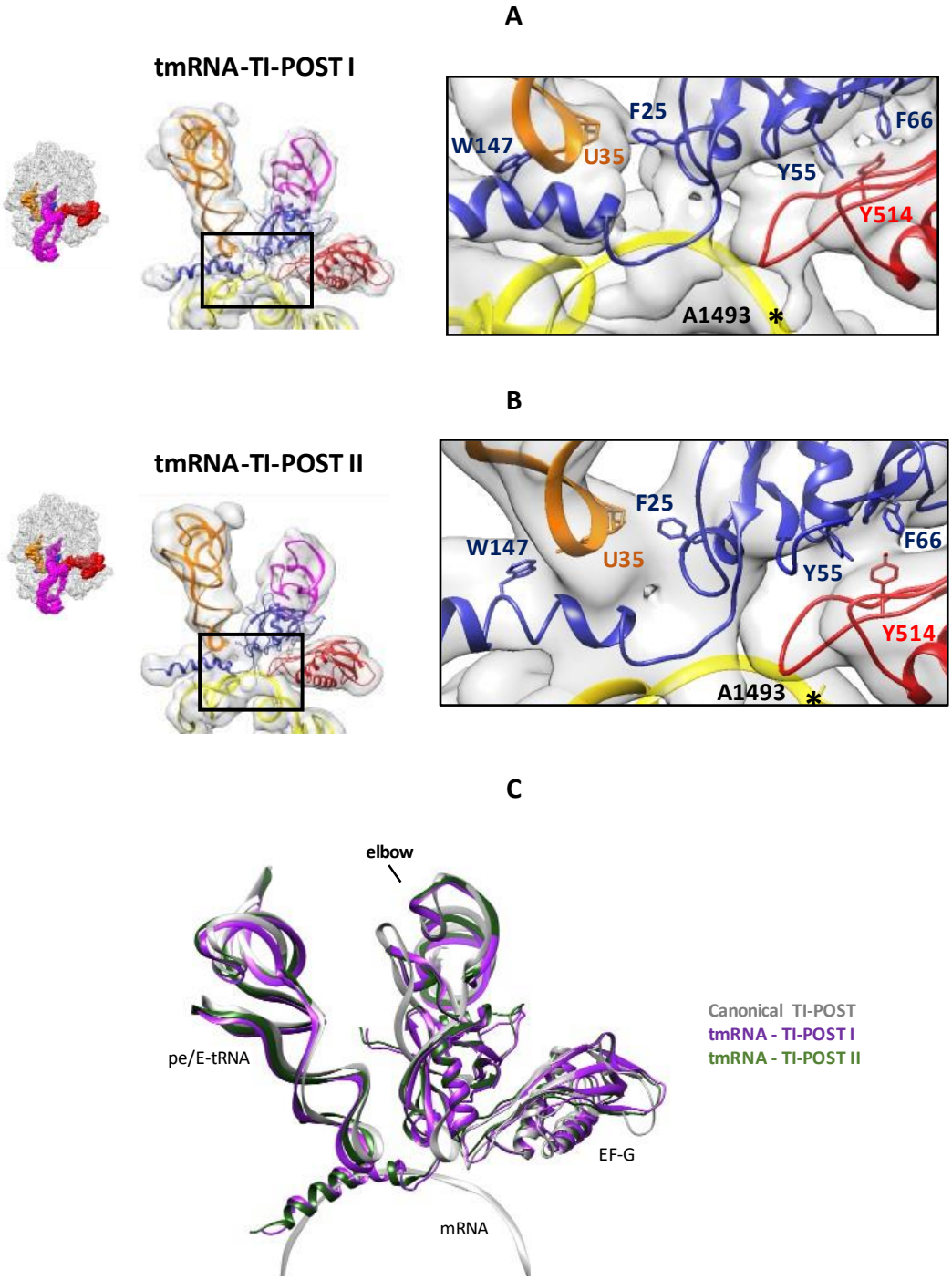

Figure 48: Interaction of SmpB's core structure within the tmRNA-TI-POST states. A and B: cryo-EM maps (gaussian low-pass filtered using a width of 2 Å) with corresponding model show the interaction of EF-G (red) and SmpB (blue). The nucleotide A1493 of the 30S decoding center at the A-site is indicated with an asterisk. The interacting residues of SmpB and E-tRNA as well as EF-G are displayed. C) Superposition of the ribosomal ligands in the presented tmRNA-TI-POST (state I in purple, state II in green) and the canonical TI-POST (in grey, Ramrath et al., 2013) after a 50S alignment.

Similar to the mRNA in the canonical TI-POST state (Ramrath et al., 2013), the C-terminal tail of SmpB in the presented tmRNA-TI-POST states passes through the 16S rRNA layers comprising helices h45, h28, h23, h24, and h44 (Figure 49). The C-terminal tail contacts the ribosomal

A-site (h44-C1400), P-site (h24-A790; h28-G926), and E-site (h23-G693; h45-A1534). The C-terminus of SmpB interacts with ribosomal protein uS7 (Figure 49A and B). In addition, there is an unassigned cryo-EM density which follows SmpB's C-terminus and occupies the space above the Shine-Dalgarno (SD) sequence of the 16S rRNA (pink density in Figure 49A and B). The unoccupied density close to the SD sequence may correspond to the truncated mRNA, which was displaced from the mRNA channel during the transition from the tmRNA-PRE to tmRNA-TI-POST state. Since the C-terminal residues of SmpB can interact with RNA as observed in the tmRNA-PRE state (Figure 45D), one can speculate that they are involved in the displacement of the mRNA in the tmRNA-TI-POST states. The SmpB C-terminal tail itself may bind the mRNA during its occupation into of the mRNA channel and thereby navigating the mRNA towards the mRNA exit channel.

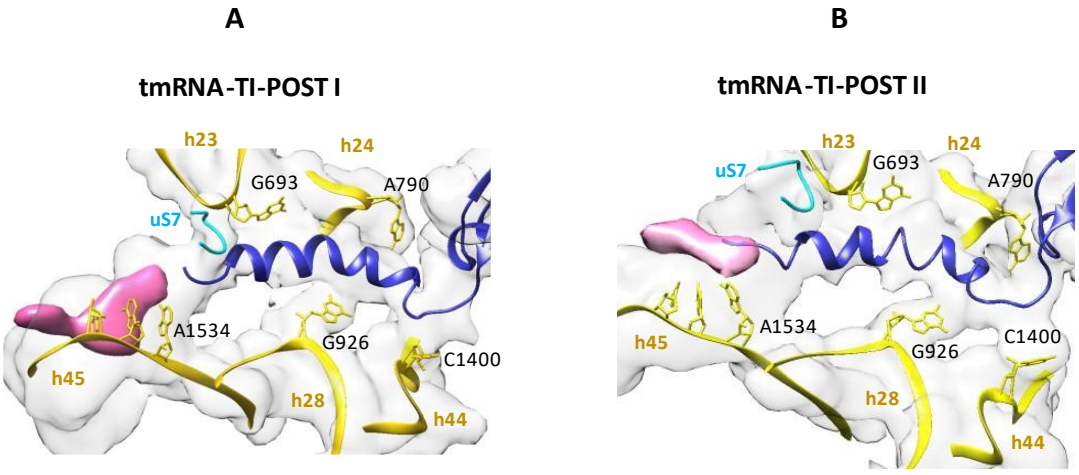

Figure 49: Interactions of SmpB's C-terminal tail within the tmRNA-TI-POST states. Cryo-EM maps (gaussian low-pass filtered using a width of 2 Å) for the tmRNA-TI-POST I (A) and tmRNA-TI-POST II (B) with atomic models for the SmpB's C-terminal region that goes through the 16S rRNA layer consisting of helices h45, h28, h23, h24, and h44 (yellow). The SmpB interacting residues of the 16SrRNA helices h44 (C1400), h28 (G926), h23 (G693), h24 (A790), and h45 (A1534) are represented as sticks. The unassigned density at SmpB's C-terminus is shown in pink.

Interaction of the mRNA-like domain within the tmRNA-TI-POST states

The mRNA-like domain (MLD) of the tmRNA is a key region of tmRNA, which contains an open reading frame that encodes a tag added to the incomplete peptide, thereby targeting it for proteolytic degradation. During translocation it is suggested that the MLD is loaded into the mRNA channel (Ramrath et al., 2012), required for resuming the translation of the open reading frame of the tmRNA. However, the MLD in Ramrath et al., 2012 couldn't be visualized. Notably, in both tmRNA-TI-POST states the density for the single-stranded MLD is visible, albeit its fragmentation and low-resolution of 5-10 Å (Figure 42C-F). This gives novel insights into the process of MLD loading during translocation.

The density for MLD in the tmRNA-TI-POST I and II structures can be clearly distinguished from the well-defined density of the ribosomal environment and therefore, suitable for tentative modeling (Figure 50A-D). The models of both tmRNA-TI-POST states reveal differences in the ribosomal environment and in position of their MLDs relative to the mRNA entry channel, which is located between the head and body of the small subunit (Figure 50).

The MLD of the tmRNA-TI-POST II state extends deeper into the mRNA channel as the MLD of the tmRNA-TI-POST I state (Figure 50E-F). Compared to the MLD of tmRNA-TI-POST I state that makes contact to 16S RNA helices, h16 and h18 and ribosomal protein uS3, the MLD of tmRNA-TI-POST II establishes additional contacts to protein uS4, uS5 and EF-G and helix h44. These MLD interactions within the mRNA channel observed for the tmRNA-TI-POST II state have also been found in the POST state tmRNA structure (Rae et al., 2019). This suggests that the tmRNA-TI-POST II state represents a later step in translocation than the tmRNA-TI-POST I state. This will be discussed further in chapter 4.2.5.

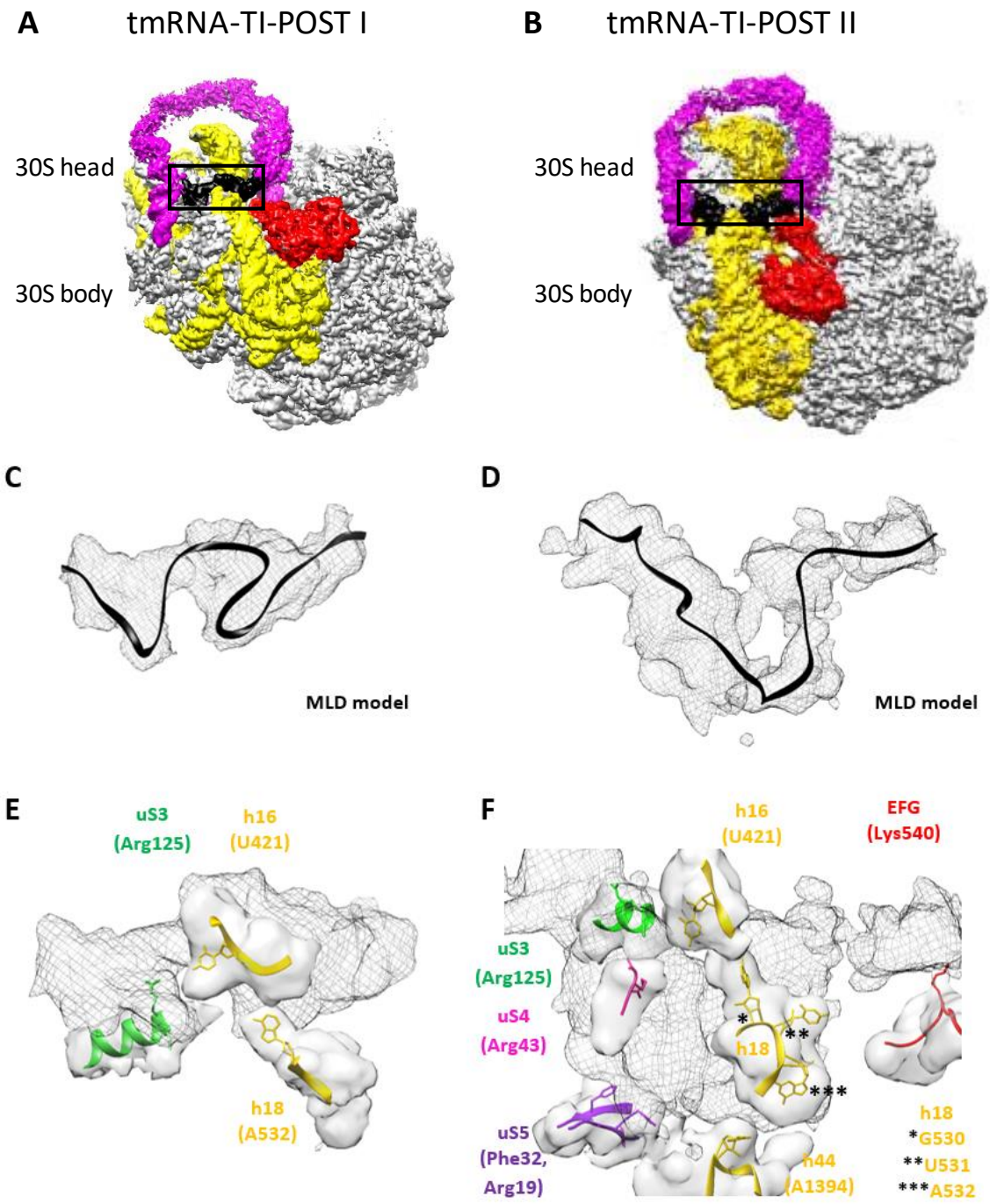

Figure 50: Structure and position of the MLD in the tmRNA-TI-POST states: A, B) cryo-EM maps of the tmRNA-TI-POST I (A) and tmRNA-TI-POST II (B) for orientation help with colored densities for the 16S rRNA (yellow), tmRNA (magenta), MLD (black, mRNA-like domain) and EF-G (red). C), D) Tentative model for MLD (black) and its corresponding density (black, mesh presentation) of the tmRNA-TI-POST I (C) and II (D). E), F) The extracted density of the MLD (same presentation as in C and D) of the TI-POST I (E) and TI-POST II (F). The molecular environment of the MLD on the ribosome (grey maps) are shown with their atomic models (ribbon presentation): 16S rRNA helices (yellow) h16, h18 and h44, ribosomal proteins uS3 (green), uS4 (pink), uS5 (purple) and EF-G (red). The nucleotides (U421, G530, U531, A532; A1394) and residues (Arg125, Arg43, Arg19, Phe32 and Lys540) that interact with the MLD are displayed as sticks. The map for the MLD in C-F) was obtained by Segmentation of the full map at a threshold of 0.5 using the Segger method (Pintilie and Chiu, 2012). The MLD maps were gaussian low-pass filtered (width: 4.0 Å). The grey maps were gaussian low-pass filtered (width: 1.0 Å).

The MLD in the tmRNA-TI-POST states is stably associated via PK2/H5 on the ribosome. In both tmRNA-TI-POST states, PK2 and H5 of the tmRNA maintain the contact to the same region of ribosomal proteins uS3 (Figure 51), as observed in the tmRNA-PRE state (Figure 46A). However, compared to the tmRNA-PRE state, the H5 of tmRNA additionally establishes a new interaction with ribosomal protein uS2 (Figure 51).

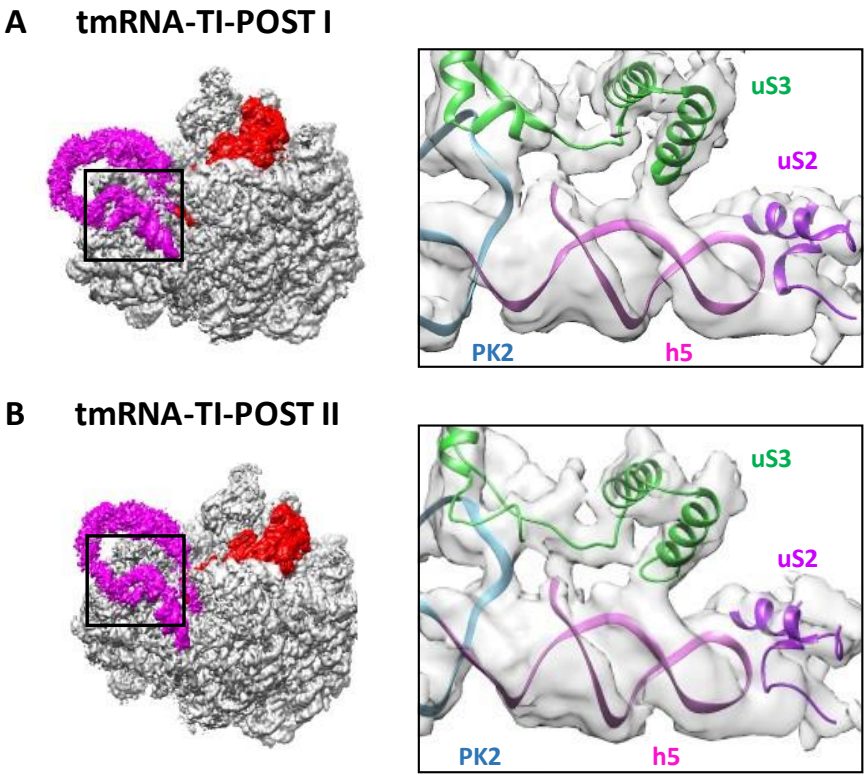

Figure 51: Interaction of PK2/H5 within the tmRNA-TI-POST states. A, B) Left: Cryo-EM maps of the tmRNA-TI-POST I (A) and tmRNA-TI-POST II (B) as orientation help with colored densities for the tmRNA (magenta) and EF-G (red). Right: Close-up views showing the models for the PK (blue) and h5 (orchid) of the tmRNA and ribosomal proteins uS3 (green), uS2 (purple) together with its corresponding density map (grey). The density maps in the close-ups were gaussian low-pass filtered (width: 2.0 Å).

3.7.3 The PAST-E states show tmRNA-SmpB in a next translocation round

The data analysis of the 70S-tmRNA-SmpB-EF-G-FA specimen revealed states with canonical tRNAs in the ribosomal E- and P-site and the tmRNA-SmpB located off the ribosome (Figure 53 A and C). This suggests that the TLD-SmpB must have passed at least a second translocation step. A further translocation would require the presence of an Ala-tRNA^{Ala} to decode the resume codon of the MLD in the A site. After binding of the Ala-tRNA^{Ala}, EF-G would then trans-

locate the peptidyl-tRNA^{Ala} into the P-site, moving tmRNA-SmpB to the E-site. However, instead binding of tmRNA-SmpB into the E-site, the TLD-SmpB module has moved past the E site resembling PAST-E states (Figure 53A and C).

Theoretically a second translocation cannot occur, since to Ala-tRNA^{Ala} is not present in the translocation reaction mix (see chapter 2.3.3). Only tRNA^{fMet} is available for a further translocation. However, the complementary AUG codon, required for tRNA^{fMet} binding, is not present in the ORF of the tmRNA (see chapter 1.4.1, Figure 13). The occurrence of a -1 or +1 frameshifting within the tmRNA also does not lead to the formation of an AUn codon. Another explanation for proceeding the translation using tRNA^{fMet} only could be the ribosomal bypassing, an EFG-mediated process where the ribosome slides along the noncoding mRNA (Klimova et al., 2019). This assumption is supported by the structural features specifying the initiator tRNA, tRNA^{fMet} observed in the PAST-E states (Figure 52).

A unique feature of the tRNA^{fMet} is three consecutive guanine cytosine (G:C) base pairs in its anticodon stem that form A-minor groove interactions with 16S rRNA nucleotides G1338 and A1339 (Figure 52; Lancaster and Noller, 2005; Moazed et al., 1995; Selmer et al., 2006). Thus, the PAST-E states do not represent physiological complexes but provide as models structural information about how a complex could form after second or later translocation.

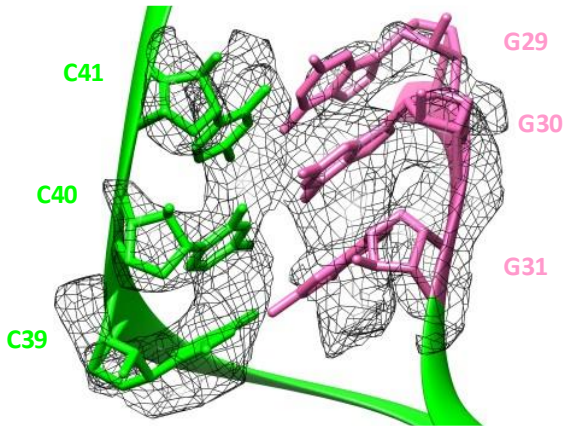

Figure 52: Specific feature of the initiator tRNA^{Met} of the PAST-E-TI-POST state. The density of the PAST-E-TI-POST state (as mesh) and atomic model showing the interaction of three G:C base pairs (G: pink; C: green), G29:C41, G30:C40, and G31:C39 of the initiator tRNA^{Met}.

The presented PAST-E states have reached the unrotated ribosomal conformation during the translocation. The PAST-E state, in which EF-G is dissociated from the ribosome (Figure 53C),

forms a POST translocation state, and therefore was referred to as PAST-E-POST state. The POST state formation in presence of fusidic acid is possible because this antibiotic was found to be a “slow inhibitor of the EF-G-GTPase” allowing a series of GTPase turnovers before complete inhibition of the 70S-EFG-GDP state (Seo et al., 2005). The second PAST -E state containing EF-G (Figure 53A), is an intermediate state (assigned as PAST-E-TI-POST) of a very late translocation step. Here fusidic acid has trapped EF-G in its GDP-bound-state on the PAST-E-TI-POST ribosome.

The PAST-E states are structurally almost identical, except for the presence or absence of EF-G (Figure 53). Compared to the tmRNA-PRE and TI-POST structures of this study, most parts of the tmRNA lost the connection to the ribosome explaining their high degree of fragmentation and low resolution (Figure 42G-J). Only areas associated with the ribosome, namely the PK2/H5 region and the MLD were suitable for tentative modelling. Therefore, the complete tmRNA was fitted as a rigid body, but manually refined only H5 (nucleotides G108-C137), MLD region (nucleotides G87-C107), and the single-stranded RNA of PK2 (nucleotides A177-C191).

The density occupying the mRNA channel was unambiguously assigned to the MLD (Figure 53A and C). In both PAST-E states the MLD makes interaction with the ribosomal elements (proteins uS3, uS4 and uS5 and 16SrRNA helices h23, h44, h28, and h16) and contact the anticodon stem loop of the P- and E-tRNAs. Based on the tentative MLD model, the resume codon (nucleotides G90, C91, A92) contacts the anticodon loop of the P-site tRNA at nucleotides A37 and A35 via base-stacking interactions (Figure 53B and D) indicating that the PAST-E states went through a second translocation.

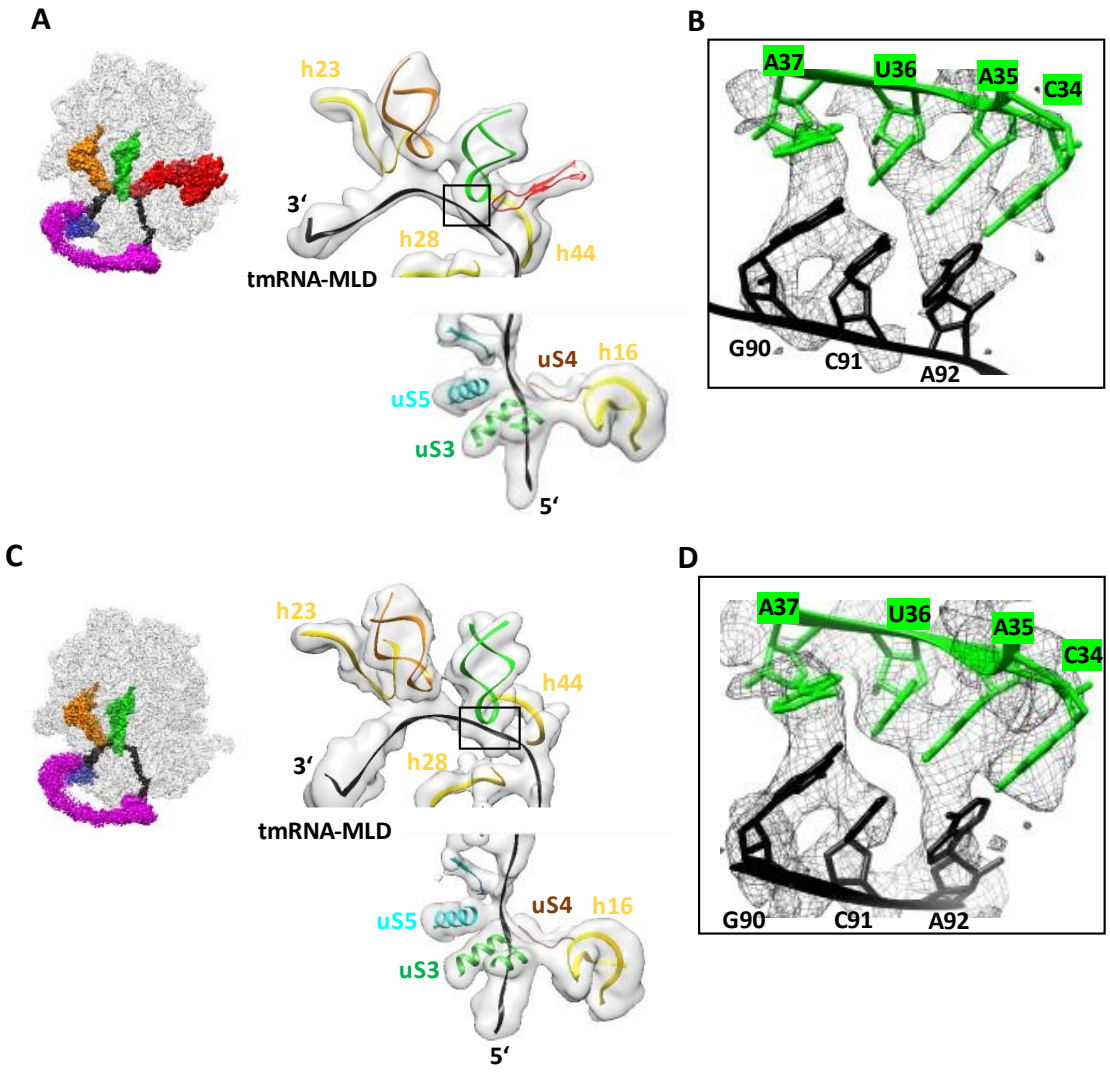

Figure 53: Interaction of the MLD within the PAST-E states. A, C) Left: cryo-EM maps of the PAST-E TI-POST I (A) and PAST-E POST (C) as orientation help with colored densities for the tmRNA (magenta with its MLD in black), SmpB (blue), E-tRNA (orange), P-tRNA (green) and EF-G (red). Right: Close-up view showing the extracted density (grey, gaussian low-pass filtered with width: 3.0 Å) and atomic models for the mRNA-like domain, MLD (black, 3’end and 5’end are indicated), E-tRNA (orange), P-tRNA (green), 16S rRNA (yellow) with indicated helices h23, h28, h44 and h16, EFG loop I of domain IV (red), ribosomal proteins uS5 (cyan), uS3 (lime green), and uS4 (brown). B), D) Density maps in mesh presentation and atomic models showing the interaction of the MLD with the P-site tRNA in the PAST-E TI-POST I (B) and PAST-E POST (D).

In both PAST-E states the tmRNA maintains contact to the ribosome via SmpB and PK2/H5. SmpB was assigned to a cryo-EM density, which connects the TLD and h26 and uS18 (Figure 54 A and B). Due to the high fragmentation of that density, only the core structure SmpB could be rigid body docked. The C-terminal region of SmpB is presumably very flexible since binding partners seem to be absent at this ribosome position. As observed for the tmRNA-TI-POST

structures in this study, the ribosomal proteins uS2 and uS3 anchor the PK2/H5 of the tmRNA at the solvent side of the ribosome (Figure 54C and D).

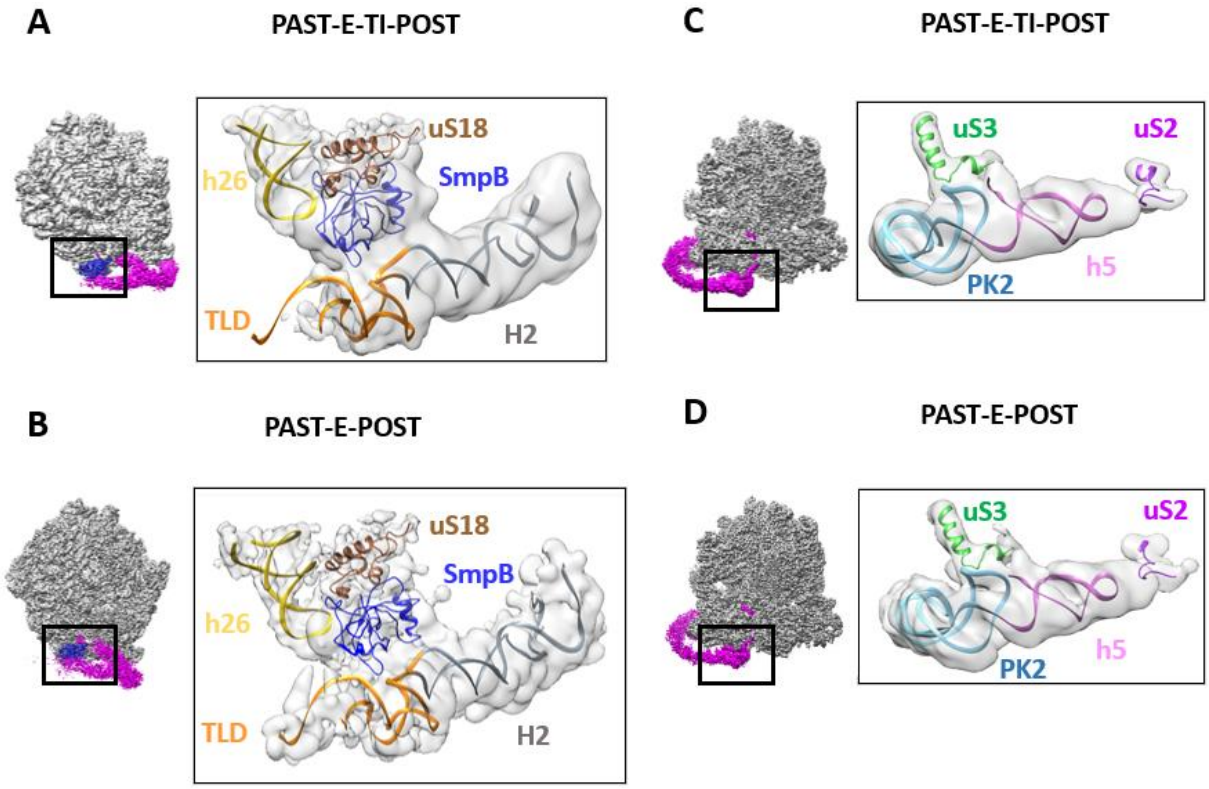

Figure 54: Interaction of SmpB and PK2/H5 within the PAST-E states. A, B) Left: cryo-EM maps of the PAST-E-TI-POST (A) and PAST-E-POST (B) as orientation help with colored densities for the tmRNA (magenta) and SmpB (blue). Right: Close-up views showing the atomic models for the SmpB (blue), TLD (orange), h2 (grey) and ribosomal protein uS18 (brown), 16SrRNA helix h26 (yellow) together with its corresponding density map (grey). C), D) Left: cryo-EM maps of the PAST-E-TI-POST (C) and PAST-E-POST (D) as orientation help with colored densities for the tmRNA (magenta). Right: Close-up views showing the models for the PK (blue) and H5 (orchid) of the tmRNA and ribosomal proteins uS3 (green), uS2 (purple) together with its corresponding density map (grey). The density maps in the close-ups were gaussian low-pass filtered (width: 2.0 Å for SmpB-TLD/h2 and uS3/uS2-PK2/h5, width: 1.0 Å for h26 and uS18).

Apart from the presence of tmRNA, both the ribosomal conformation and ligands (tRNAs and EF-G) are almost identical to the canonical TI-POST complex of a very late translocation step (Gao et al., 2009; Figure 55). As in the canonical TI-POST state, EF-G interacts with the P-tRNA and mRNA/MLD in the PAST-E-TI-POST state (Figure 55).

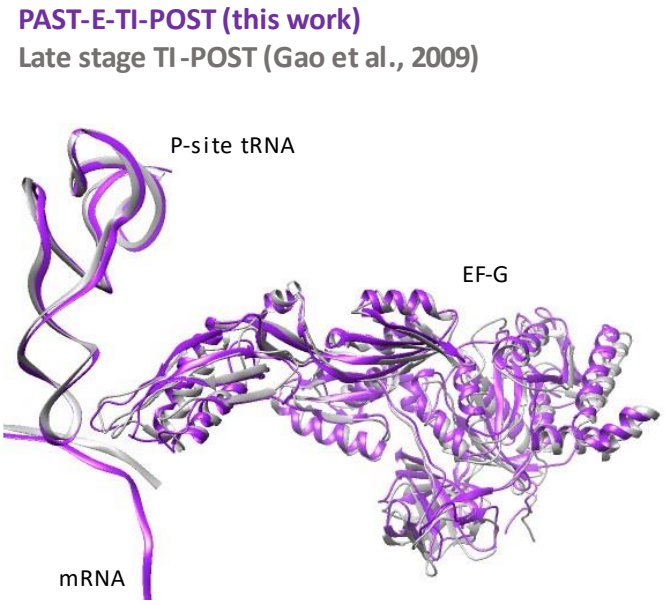

Figure 55: Comparison of the models of the PAST-E-TI-POST state with a canonical late-stage TI-POST state models. Superposition of PASTE-TI-POST state (purple) and the canonical late-stage TI-POST state (in grey, PDB-ID: 4V5F, Gao et al., 2009) upon a common 50S alignment.

The barriers within the PAST-E states which must be overcome for completion of MLD loading into the mRNA channel will be discussed in chapter 4.2.6.

4 Discussion

In this work, cryo-EM was used to investigate the structures involved in key translational surveillance pathways in bacteria: the *trans*-translation and ribosome-associated quality control (RQC). Both pathways result in the release of the stalled ribosomal complexes and degradation of the nascent polypeptide. In *trans*-translation, the ribosomes stalled on truncated mRNA are rescued by the tmRNA and its accessory protein SmpB (see also chapter 1.4.1). In RQC, the ribosomal P-tRNA-50S complexes stalled by the attached nascent chain are rescued under involvement of RqcH (see also chapter 1.4.2).

In this chapter the results of the structural and biochemical analysis of the RqcH-50S complexes (chapter 4.1) and cryo-EM analysis of the 70S-tmRNA complexes (chapter 4.2) will be discussed and put in context with the existing structures.

4.1 RqcH

RqcH functions in degradation of stalled ribosomal subunits (Lytvynenko et al., 2019). Similar to the yeast rescue factor Rqc2, RqcH mediates an mRNA-independent elongation of nascent chains blocking the 50S subunit but by adding C-terminal alanine extensions (Ala tailing) that marks the nascent chain for proteolytic degradation. As part of the study in Lytvynenko et al., 2019, the presented cryo-EM analysis of wild-type RqcH-co-immunoprecipitated 50S subunit purified from *B. subtilis* lysates indicated that RqcH binds large ribosomal subunits. The resulting cryo-EM structure with a resolution of 3.8 Å represented a 50S subunit bound to a P-tRNA that is associated with a nascent chain.

Even though RqcH density was lacking, this structure indicated that RqcH recognizes nascent chain stalled 50S subunits since this ribosomal complex co-immunoprecipitated with RqcH (Lytvynenko et al., 2019).

The subsequent analysis of mutant RqcH-co-immunoprecipitated 50S subunit complex and its additional crosslinking prior cryo-EM allowed visualization of the RqcH on the ribosomal 50S subunit. The structure with a resolution of 3.1 Å revealed how RqcH recognizes stalled ribosomal 50S subunits. Additional mutation experiments confirmed the essential 50S binding interfaces in RqcH observed in the structure.

After completion of our structural analysis, two publications appeared showing several bacterial RQC structures that differ in the binding mode that RqcH can adopt during the Ala-tail elongation cycle (Filbeck et al., 2021; Crowe-McAuliffe et al., 2021). These independent studies reached similar conclusions, namely that RqcH remains anchored to the 50S stem base via its CC1-M-CC2 region spanning the ribosomal A site, whereas its NFACT and HhH domains are more flexible and move around the bound tRNA. However, the presented mutant RqcH-50S structures differ in the details from the current available RQC structures.

4.1.1 RqcH recognizes the P-tRNA-50S complex as substrate

The analysis of the wild-type sample confirmed that RqcH co-immunoprecipitated with the 50S subunit. About 30% of the 50S particle images contained P-site tRNA density (Figure 26) and structural analysis revealed that the P-site tRNA was connected to nascent-chain density in the ribosomal peptide exit tunnel (Figure 28C). This suggests that the 50S subunit was involved in translation before it was bound by RqcH.

Therefore, RqcH was assumed to recognize the association of a P-tRNA with the ribosomal 50S subunit as a characteristic of the 50S blockade, in a similar way as observed for Rqc2 and NEMF that function in the eukaryotic RQC (Lyumkis et al., 2014; Shen et al., 2015; Shao et al., 2015).

The density that might correspond to RqcH was not apparent after *in silico* sorting (Figure 26). However, since the association of RqcH to 50S subunits was not affected (Lytvynenko et al. 2019), it was assumed that the RqcH is bound in a very flexible state to the 50S subunit.

4.1.2 Visualization of RqcH binding on the ribosomal 50S subunit

In the second attempt to visualize *B. subtilis* RqcH on the 50S subunit, RqcH with a mutation (E121A, I122G, M123G) in the NFACT-N domain (NFACT-N*) was used for the EM analysis. The initial low-resolution structures of the mutant (Figure 31A) revealed a stronger density for ligands at the 50S subunit interface compared to the low-resolution structure obtained from wild-type RqcH-co-purified particles (Figure 24). This indicated that the mutant RqcH has decreased the flexibility of RqcH when bound to the 50S surface.

But additional crosslinking using glutaraldehyde facilitated the visualization of RqcH binding to the nascent-chain stalled 50S subunit (Figure 31B substate I and Figure 34A-C). Like the wild-type (Figure 28B), the map of the mutant shows an extra density at the ribosomal subunit

interface (Figure 34D). This density may correspond to the missing helices H68, H69, and H71 which might have alternatively conformed as it was observed in 50S assembly intermediates (Nikolay et al., 2018). The key contacts of RqcH to the P-tRNA-50S complex are shown in Figure 56, which can be used as an overview for the following text. In the next chapters the domain rearrangement of RqcH observed in the presented mutant RqcH-50S complex is compared to similar structures found in the eukaryotic and prokaryotic RQC pathway.

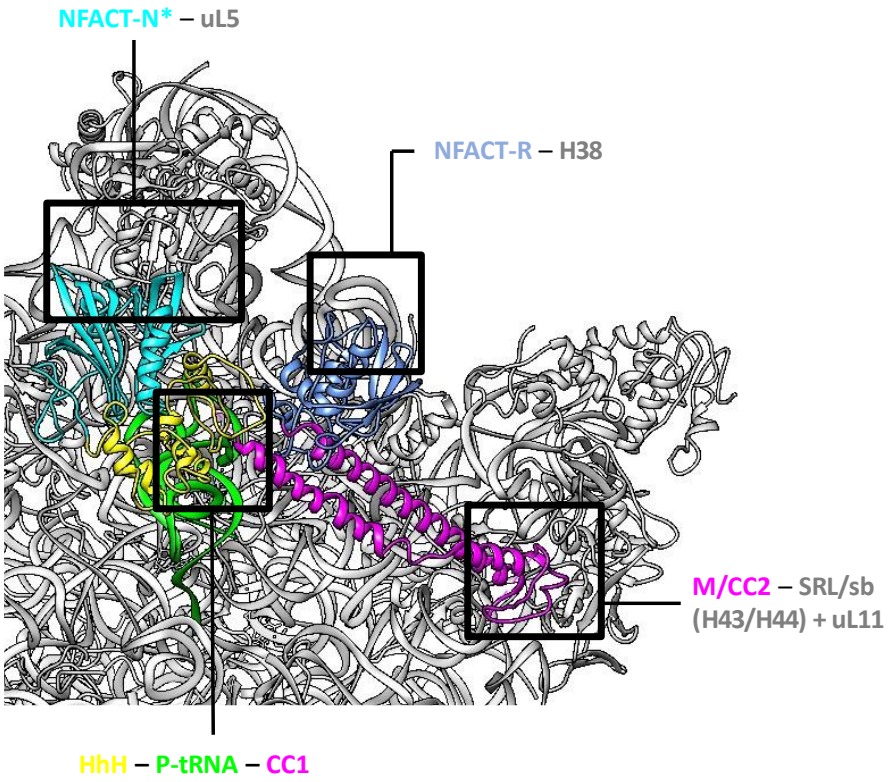

Figure 56: Key contacts of mutant RqcH with ribosomal elements and P-site tRNA. Shown is the atomic model of the mutant RqcH-50S complex from this work with ribosomal elements in grey, elements of RqcH are colored as indicated, and the P-site tRNA is green.

4.1.3 Comparison of the mutant RqcH-50S complex with current structures

The overall binding on the ribosomal LSU of the mutant RqcH, wild-type RqcH as well as eukaryotic orthologues (Rqc2 or NEMF) are similar (Figure 56 and Figure 57). They bind to the ribosomal large subunit (LSU) by spanning from the stalk base helices to the P-tRNA binding sites. In the prokaryotic RQC complexes, especially the M-CC2 region and the C-terminal lobe (NFACT-R) of RqcH interact in a highly similar manner with the stalk base/SRL and the helix H38 of the 23S rRNA of the LSU, respectively (Figure 56 and Figure 57).

Both eukaryotic RQC complexes are bound by the E3 ligase (Ltn1 in yeast or Listerin) which ubiquitylate the nascent polypeptide leaving the LSU as described in chapter 1.4.2. Compared to the mammalian RQC complex which binds only tRNA in the P-site, the yeast RQC complex contains both, a P-site and A-site tRNA. The two structures each represent likely a different functional state in the eukaryotic RQC.

The prokaryotic RQC structures differ regarding the binding of the N-terminal domains, NFACT-N and HhH (Figure 57). These domains are shifting relative to the anticodon arms of the bound tRNAs during Ala-tailing cycle. The C-terminal domain, NFACT-R was seen always bound to the 23S rRNA helix, H38, in all bacterial RQC structures (Filbeck et al., 2021; Crowe-McAuliffe et al., 2021, this work). Moreover, the recent studies observed an additional factor, RqcP which is bound to certain states occurring during the prokaryotic Ala-tailing cycle.

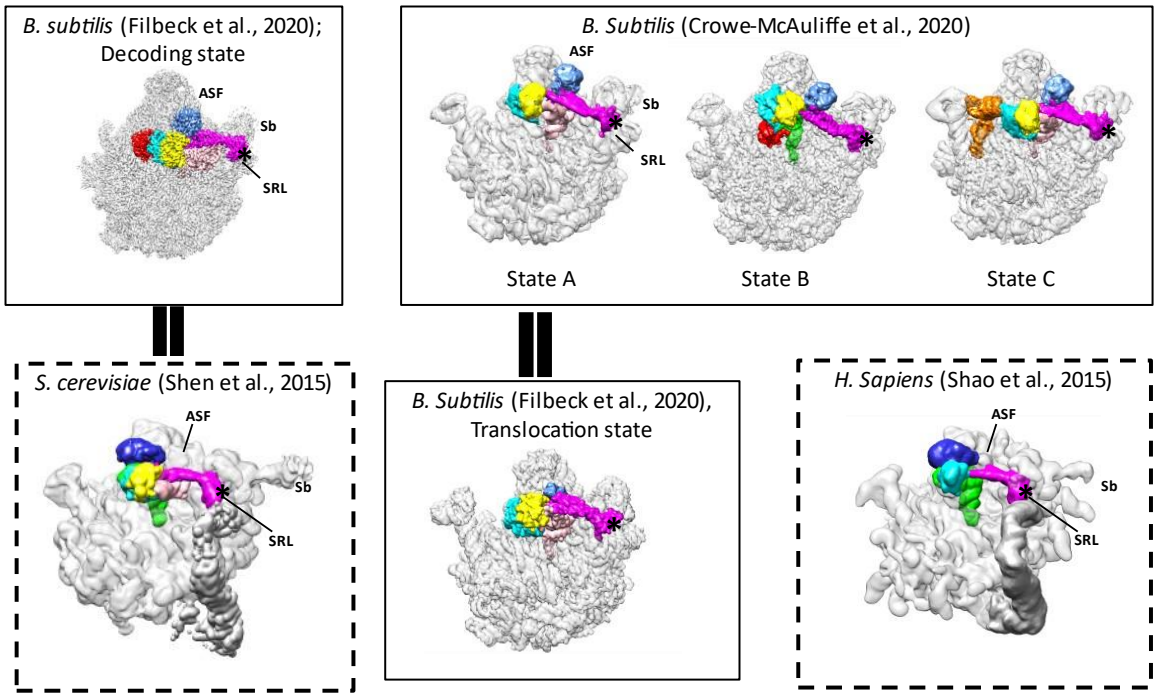

Figure 57: Current RQC structures. Dashed lines surround eukaryotic RQC structures. Equals sign indicate similar RQC states. The domains of RqcH (*B. subtilis*), NEMF (*H. sapiens*), Rqc2 (*S. cerevisiae*) are colored as followed: NFACT-N: cyan, HhH: yellow, CC1-M-CC2: magenta, NFACT-R: blue, NFACT-R+C (only in eukaryotic structures): dark blue. RqcP (is only present in prokaryotes) is red. The A-site tRNA is pink, P-site tRNA is green, E-site tRNA is orange and the ribosomal large subunit is light grey. The E3 ligase (Ltn1 or Listerin in grey) is only present in eukaryotic structures. The A-site finger (ASF), stalk base (Sb) and sarcin-ricin loop (SRL) are indicated for orientation. The M-domain in all structures is indicated with an asterisk.

In the next chapters I am going to describe all domains in detail and include the conclusion of the mutation experiment performed based on our structural results as well as the structural features of RQC complexes observed in independent studies.

4.1.4 RqcH M-CC2 region docks via stalk base/SRL/uL11 the 50S subunit

The CC1-M-CC2 domains itself do not require the N- and C-terminal domains of RqcH for 50S binding as shown by the preserved association to 50S after purification of FLAG-tagged CC1-M-CC2 truncation (Figure 37D and E). The mutation of the highly conserved Y376, F377 did not severely affect RqcH binding to the 50S subunit, either (Figure 37A and B). However, the functionality is impeded when those residues are mutated (Figure 37C). In particular, the F377-H43-A1113 stacking interaction (Figure 36A middle panel) appears to be essential for the Ala-tailing process, since this interaction was observed in all functional states in prokaryotes (Filbeck et al., 2021; Crowe-McAuliffe et al., 2021).

The binding of M-CC2 region to the same region on the 50S subunit (sb=CC2 contact, SRL/uL11=M domain contact) was found in all available structures (Figure 57; Filbeck et al., 2021; Crowe-McAuliffe et al., 2021; Shen et al., 2015, Shao et al., 2015) which indicates the significance of the M-CC2 region for both, prokaryotic and eukaryotic RQC. The stalk base/SRL occupied by the M-CC2 region in RQC-complexes is usually essential for binding of several GTPases during translation and ribosome biogenesis (Sergiev et al., 2005; Sato et al., 2005).

Consequently, structural superpositions of RqcH with two canonical GTPases (EF-G and ObgE) on the 50S subunit show a large steric clash (Figure 58). This shows that RqcH binding to the 50S subunit would prevent docking of canonical GTPases during the tailing reaction by occupying their binding interface (GTPase-associated center, GAC: H43, H44, uL11 and SRL). This implies that canonical translation factors are likely not involved in the cycle, because RqcH-M-CC2 stays bound to the GAC during the whole cycle. This is consistent with the finding that GTP binding, and hydrolysis were not required for CAT tail synthesis in yeast extracts (Defenouillère et al., 2013).

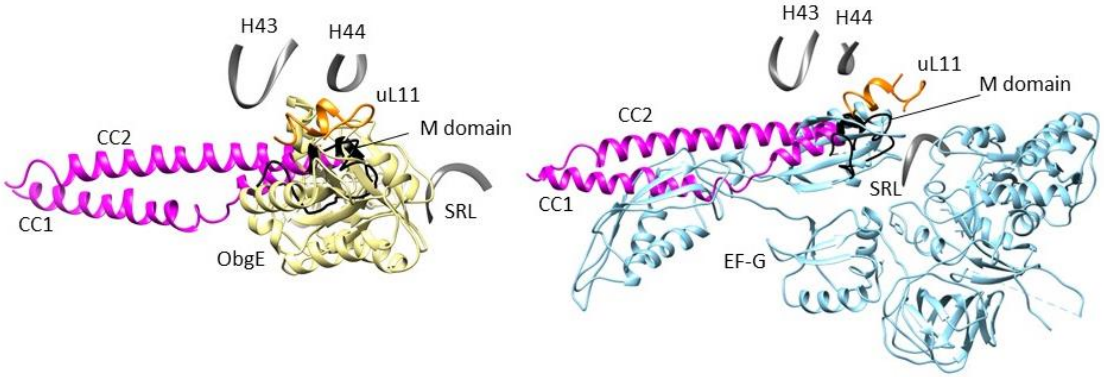

Figure 58: RqcH's CC1-M-CC2 and canonical GTPases interact with the GTPase-associated center. Superimposition of CC1-M-CC2 from the mutant RqcH-50S structure and ObgE (khaki) from an *E. coli* 50S structure (PDB ID: 4SCU) or EF-G (light blue) from an *E. coli* 70S structure (PDB ID: 4V5F) by a 23S rRNA alignment. The coiled-coil helices (CC1 and CC2, magenta) and M domain (black) clash with ObgE or EF-G, both positioned at the GTPase-associated center. The components, 23S rRNA helices H43, H44, the sarcin-ricin loop (SRL, grey) and uL11 (orange) of the GTPase-associated center are indicated.

4.1.5 RqcH NFACT-R domain docks via H38 to the 50S subunit

The rigid-body docked NFACT-R domain fits well the density that is located at H38, adjacent to the ribosomal A-site (Figure 36B). At this position, the NFACT-R domain would clash with the ribosomal protein uS13, a component of the 30S subunit that interacts with helix H38 (Figure 59) in order to form the inter-subunit bridge B1a within a 70S ribosome (Cukras and Green; 2005; Liu and Fredrick, 2016).

Like uS13, NFACT-R possesses arginine residues (R476, R480, R534) at the H38 interaction surface (C932, C933, U934, A935) (Figure 59 and 36B) suggesting the involvement of predominantly unspecific electrostatic interactions with the rRNA backbone. This is consistent with NFACT-R predicted to function in RNA binding (Burroughs and Aravind, 2014). Moreover, the identified H38 binding surface in the docked NFACT-R model is in perfect agreement with the binding surface observed in the decoding state of the wild-type RqcH-50S complex that involves the same arginine residues (R476, R480, R534) in the interaction with the tip of H38 (Filbeck et al. 2021).

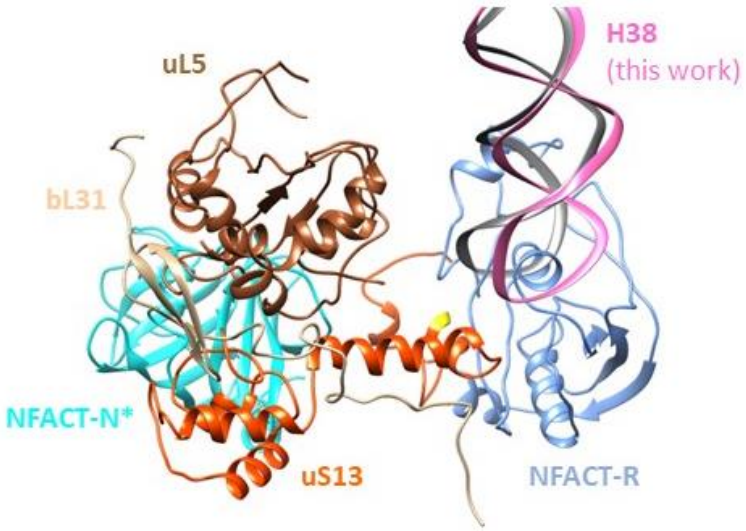

Figure 59: RqcH's NFACT domains overlap with uS13 protein within a 70S structure. Superimposition of the NFACT domains (NFACT-N*: cyan, NFACT-R: blue) from the mutant RqcH-50S structure and ribosomal protein uS13 (orange) from a *B. subtilis* 70S complex (PDB ID: 3J9W) by a 23S rRNA alignment. The arginine residues of uS13 (yellow), which interact with H38 (grey) in order to form inter-subunit bridge B1a, clash with NFACT-R. The N-terminal loop of uS13 involved in the formation of bridge B1b (that includes uL5 (brown) and bL31 (light brown) as further bridge components) overlaps with NFACT-N*.

While the globular domain of NFACT-R is interacting with H38, its loops are well positioned to replace A-tRNA-interacting nucleotides of ribosomal helix H38 during Ala-tailing (Figure 38). This suggests that NFACT-R's loops might be able to sense and stabilize the tRNA in the A-site in the absence of the small ribosomal subunit. This view is supported by the mutational analysis of flexible loops in the NFACT-R domain that would project towards an A-site tRNA (Figure 39). The double loop mutant shows a strong defect in rescuing growth of the ΔrqcH ΔssrA double deletion strain (Figure 39C) without affecting RqcH binding (Figure 39A and B). This suggests that the NFACT-R loops are critical for the function of RqcH, presumably mediated by A-tRNA positioning.

4.1.6 RqcH NFACT-N-HhH domains and CC1 contribute to P-tRNA binding

The introduction of the EIM mutation (NFACT-N*) did not destabilize the interaction of RqcH with the 50S subunit (Lytvynenko et al., 2019). The NFACT-N* mutant of RqcH is defective in tRNA binding, it thus appears that the NFACT-N domain is dispensable for recognizing obstructed 50S subunits, whereas an intact NFACT-N domain is essential for Ala-tRNA binding (Lytvynenko et al., 2019).

In the present structure NFACT-N was placed near but not in binding distance to the anticodon arm of the tRNA (Figure 35A). Due to the limited resolution of the NFACT-N-HhH density (Figure 33C) only surface-exposed residues are used for the interpretation of the binding mode of the NFACT-N-HhH domains. The structure reveals a state in which the NFACT-N domain would be available to recruit Ala-tRNA via the exposed residues D97 and R98 (Figure 35A). The DR residues, together with the EIM residues of NFACT-N were shown to form a binding pocket for the anticodon loops of P-tRNAs (Shao et al., 2015; Crowe-McAuliffe et al., 2021) or A-tRNAs (Filbeck et al., 2021).

The tRNAs that are interacting with NFACT-N are found to be additionally stabilized by CC1 as well as HhH in all structures. The binding pattern of the N-terminal CC1 region and HhH residues interacting with the anticodon loop of the tRNA (Figure 35B) is very similar to that observed in wild-type RqcH structures (Crowe-McAuliffe et al., 2021; Filbeck et al., 2021). However, compared to wild-type structures, the P-site tRNA does not interact with NFACT-N* in the presented structure (Figure 35). This may prevent an interaction with the factor RqcP, which was seen in interaction with NFACT-N in prokaryotic wild-type RqcH complexes (Crowe-McAuliffe et al., 2021; Filbeck et al., 2021).

4.1.7 Mutant RqcH-50S complex represents an initial recognition state

Recent cryo-EM studies identified the action both protein factors, RqcH and RqcP on peptidyl-tRNA obstructed 50S subunits as sufficient to execute the whole elongation cycle without the small ribosomal subunit or mRNA. Even though some states of the elongation are discovered, the mechanistic details are poorly understood. For example, it is not clear how the Ala-tRNA^{Ala} is recruited to the stalled 50S complex resulting after splitting or resulting from a previous Ala tailing cycle (Crowe-McAuliffe et al., 2021). Moreover, it remains unclear how the completion of the translocation cycle is achieved, where it is assumed that RqcP rebinding shifts the A/P

bound tRNA into the ribosomal P-site in order to form the POST state (Filbeck et al., 2021; Crowe-McAuliffe et al., 2021).

The two independent studies obtained one common structure - the 50S-RqcH complex with a A/P-like tRNA and both defined it as a state before final translocation which requires RqcP for completion. Their model mechanism for the formation of the A/P-like state involves the action of both, RqcH and RqcP and start with the tRNA delivery to a stalled 50S complex in which the P-site tRNA is supposed to be stabilized by RqcP (Filbeck et al., 2021; Crowe-McAuliffe et al., 2021).

In both Ala-tailing models they assume that binding of RqcP is required to fully translocate the A/P like tRNA attached to RqcH to the P-site, thereby resembling a post-translocation like state (state B) observed in Crowe-McAuliffe et al., 2021 only. This state is most similar to our structure with the difference that RqcP is not bound (Figure 60A). Compared to the RqcH in state B, the RqcH in the presented structure is about 31 Å rotated relative to the tRNA. This difference may be caused by the absence of RqcP, which stabilizes the NFACT-N domain around the anticodon of the P-tRNA (Figure 60B).

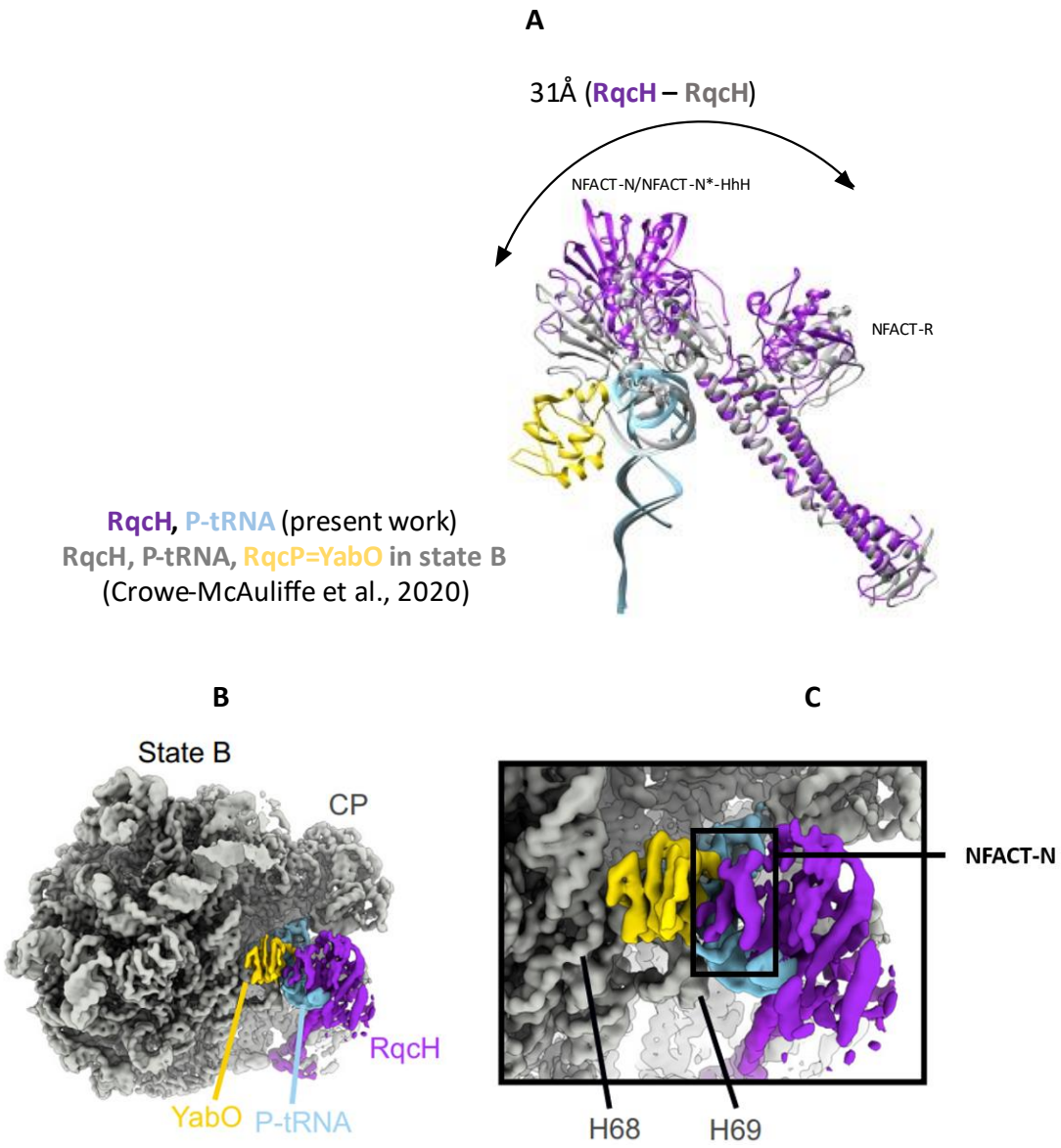

Figure 60: Comparison of RqcH in translocation state B and in the presented mutant RqcH-50S state. A) Superimposition of RqcH (present work, purple) with RqcH of state B (PDB-ID: 7AS8, grey) by tRNA alignment (P-tRNA: blue, present work). The NFACT-N and HhH domains and C-terminal NFACT-R are shifted by about 31 Å relative to the P-site bound tRNA. B) This figure was taken from Crowe-McAuliffe et al., 2021 and shows in the close-up view that YqbO (=RqcP) binds both the H69 and RqcH's NFACT-N domain. Left: Overview of the 50S ribosomal subunit (grey) bound to RqcH (purple), P-site tRNA (blue) and YabO (=RqcP, yellow).

Compared to the state B, defined as post-translocation like state in Crowe-McAuliffe et al., 2021, the presented state most likely represents an initial recognition state since the RqcH NFACT-N* mutant is defective in tRNA binding and Ala-tailing (Lytvynenko et al., 2019). This implies, unlike to what is proposed in Crowe-McAuliffe et al., 2021, the P-tRNA do not require stabilization by RqcP before RqcH binding. This is also consistent with the biochemical experiments in Filbeck et al., 2021, which showed that RqcP is not required for RqcH recruitment.

Therefore, it can be assumed that RqcP becomes important only after the recognition of the P-tRNA-50S complex.

However, it has been shown that RqcP is required together with RqcH for Ala synthesis (Filbeck et al., 2021). RqcP was observed to contact 23S rRNA helices H68 and H69, NFACT-N and the P-tRNA (Filbeck et al., 2021; Crowe-McAuliffe et al., 2021; Figure 60B and C). In our structures, the binding of RqcP is probably not possible, because these 23S rRNA helices exhibiting an alternatively conformation which most likely formed due to a low the concentration of magnesium used for sample preparation (see chapter 2.2.6). A sufficient magnesium environment is mandatory for the formation of the RNA tertiary structure (Draper, 2004). In the other studies (Filbeck et al., 2021; Crowe-McAuliffe et al., 2021), a much higher magnesium concentration was used, which prevented the formation of the state we have observed.

Although it cannot be excluded that our complex is an artificial complex, because RqcH is mutated and the functional helices are missing, this structure may represent a complex that shows how the binding of RqcH to the 50S may look like.

The assumption that the presented mutant RqcH-50S complex is an initial recognition state, together with the observation that the NFACT domains have a dynamic character, which was also observed in the other studies (state B* in Crowe-McAuliffe et al., 2021, or translocation state, Figure 57), leads to an alternative hypothesis. In this hypothesis, the elongation in prokaryotic RQC starts at an initial recognition RqcH-P-tRNA-50S state, unlike the other studies that begin with a RqcP-RqcH-PtRNA-50S state. In the initial recognition state, the CC1 domain forms a primary barrier preventing the delivery or binding of an A-tRNA (Figure 61).

This barrier may be removed by the cooperative interaction of RqcH and RqcP on the stalled 50S complex. Binding of RqcP may induce movement of the NFACT-N domain only towards the anticodon of the P-tRNA. The domain rearrangement in RqcH similarly as observed in state B* with highly flexible NFACT-domains (Crowe-McAuliffe et al., 2021) might be followed by the adjacent CC1 helix. This results in a hypothetical PRE tRNA sensing state - a likely transient state since it was not observed yet (Figure 61). In this state, the NFACT-R loops that replace helix 38 are accessible to sense and/or coordinate an incoming A-tRNA (Figure 38) which appears necessary for a processive tailing reaction (Figure 39C).

Sensing the occupancy of a tRNA in the A-site may trigger rearrangement in RqcH, leading to re-blocking of the ribosomal A-site and formation of A-tRNA sensing state (Figure 61) with

tRNA bound to the ribosomal A-site, like the decoding complex in Filbeck et al., 2021 (Figure 57). Additional experiments are needed to show how a newly delivered tRNA is sensed within the prokaryotic RQC.

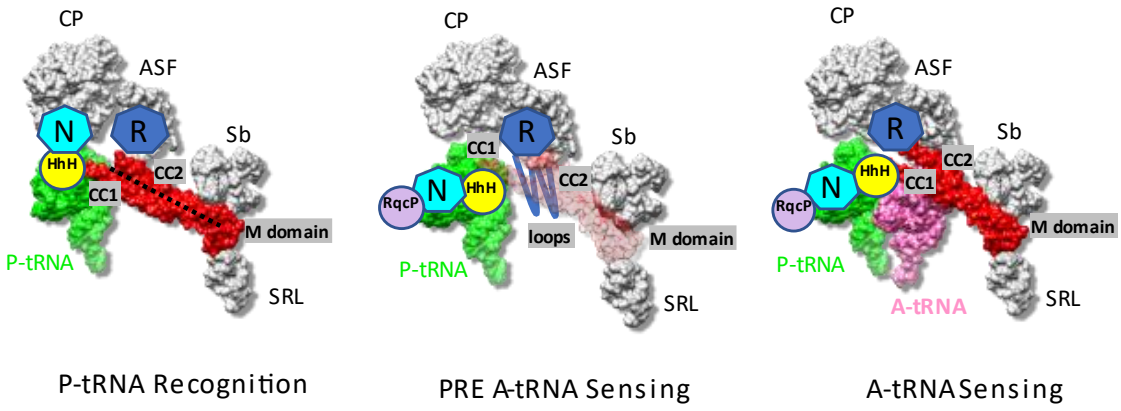

Figure 61: A hypothetical PRE A-tRNA sensing state might be result after RqcP binding and movement of the NFACT-N-HhH domains only towards the anti-codon of the P-tRNA. Consequently, the adjacent CC1 helix would follow, thereby providing space which is required to for sensing a new A-tRNA.

4.2 Discussion tmRNA

The structural analysis of the 70S-tmRNA-EF-G-FA sample revealed five different structures with resolutions between 3.5 Å and 3.8 Å. The tmRNA-PRE state represents a state before the first translocation starts. The two tmRNA-POST states are intermediates formed during the first translocation. The PAST-E states, the PAST-E-TI-POST and PAST-E-POST, are derived from later translocation steps. The structures provide detailed molecular insights into the process by which the large tmRNA and its adapter protein SmpB pass through the ribosome and accomplish correct MLD loading.

However, when our structural analysis of the 70S-tmRNA-EF-G-FA sample completed, a publication appeared showing cryo-EM maps tmRNA-structures from *E. coli* at resolutions of 3 Å to 4 Å (Rae et al., 2019). They obtained three tmRNA structures: one state that formed before translocation, the A-site complex, and two states that formed after the first translocation, and second translocation, the P-site complex, and the PAST-E site complex, respectively.

The PAST-E-site complex and A-site complex in Rae et al., 2019 are very similar to our PAST-E-POST and tmRNA-PRE state, respectively. Comparison of these structures revealed complementary results. However, the translocation has not been explored in this study and also the

process of MLD loading were elusive. The MLD of the tmRNA replaces the dysfunctional mRNA of stalled ribosomes and encodes a resume codon and a stop codon required for performing the translation *in trans*. The MLD is fully loaded within the mRNA channel by two translocation steps: first tmRNA translocation into the P-site and second, tmRNA translocation through the E-site.

Moreover, during the translocation, the intermediate tmRNA states must overcome the following barriers: (i) intersubunit bridges B1a and B1b for the passage of tmRNA's helix H2, (ii) the 30S-site latch for MLD-loading into the mRNA entry channel and (iii) the E-site latch for MLD-loading into the mRNA exit channel.

The structural rearrangement required for translocation and MLD loading are accomplished by a combination of 30S subunit rotation and 30S-head swiveling/tilting as well as EF-G release.

4.2.1 The tmRNA-PRE structure - the state before translocation starts

The tmRNA-PRE complex represents the state right after accommodation of TLD/SmpB into the ribosomal A-site and thus it is also referred to as the accommodation state. Comparison with a high-resolution crystal structure of the pre-accommodated tmRNA complex from *T. Thermophilus* reveals that the binding position of the C-terminal helix of SmpB is maintained during accommodation, while the TLD and SmpB body moves into the A/A-position to place its 3'CCA-end into the peptidyl transferase center (PTC) (Neubauer et al., 2009) (Figure 62A and Figure 44A).

Comparison of the presented tmRNA-PRE structure with the A-site complex (also referred to as accommodated state) from *E. coli* described in an independent study (Rae et al., 2019) show that the position of SmpB is in good agreement, while the acceptor ends of the TLD at the ribosomal 50S subunit differ (Figure 62A). The overlay of the A-site complex with a canonical hybrid PRE complex (Rundlet et al., 2021) indicates that the position of the acceptor ends match suggesting that the A-site complex is an accommodated state with the TLD-SmpB in A/P hybrid binding position (Figure 62B). Thus, the tmRNA-PRE structure presented here with TLD-SmpB module in classical A/A binding position forms another high-resolution structure in the *trans*-translation pathway.

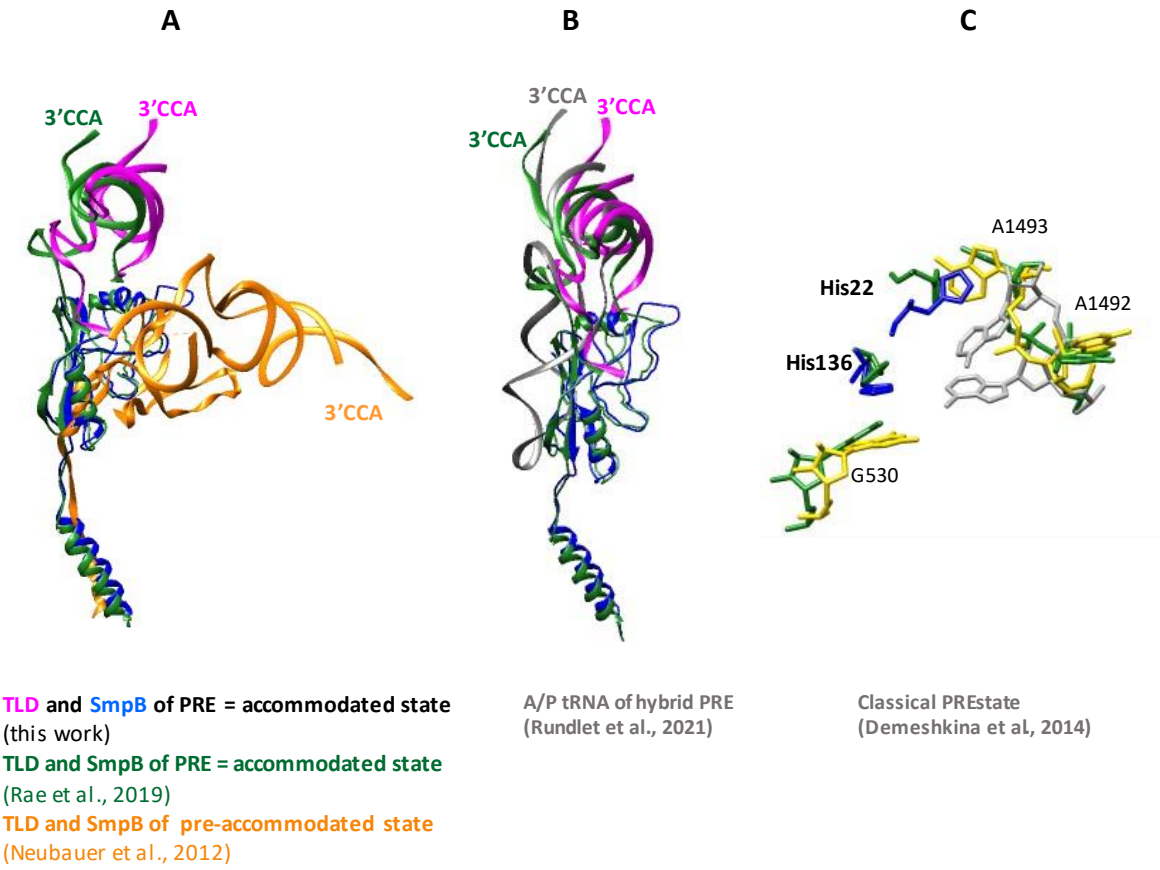

Figure 62: Comparison of TLD/SmpB of the tmRNA-PRE and pre-accommodated tmRNA state and canonical PRE state tRNAs. A) Overlay of the atomic models of the TLD-SmpB module of accommodated states (this work and Rae at al., 2019; PDB-ID: 6Q97) and pre-accommodated state (Neubauer at al., 2012; PDB-ID: 4V8Q) upon a common 50S alignment. B) Overlay of the atomic models of the TLD-SmpB module of accommodated states (this work and Rae at al., 2019; PDB-ID: 6Q97) and A/P hybrid-tRNA Rundlet et al., 2021; PDB-ID: 7N2U) upon a common 50S alignment. C) Comparison of the conformational configuration of A1492/A1493 and G530 at the decoding center in the present tmRNA-PRE state (colored), the accommodated state (green, Rae et al., 2019) and a canonical PRE state (grey; Demeshkina et al., 2012; PDB ID: 4v87) after 50S alignment.

The process by which the tmRNA-SmpB is delivered to stalled ribosomes by EF-Tu was described in Neubauer et al., 2012. In this study, they observed that in the absence of codon-anticodon base pairing, the interaction of SmpB core residues His22 and His136 with the decoding nucleotides G530, A1493, respectively, are sufficient to facilitate decoding (see also chapter 1.3.2.1). After decoding they observed the tRNA-like entity (tmRNA-TLD and SmpB core) in the A/T-position (Figure 62A, Neubauer et al., 2012) in complex with EF-Tu stalled with kirromycin that prevents EF-Tu release and the accommodation of the 3'CCA-end of the tmRNA into the PTC of the ribosomal A-site. However, it was not clear what happens after accommodation with tmRNA-SmpB at the decoding center.

In the presented tmRNA-PRE state, the accommodated state, the residues His22 and His136 of SmpB interacts with the decoding center nucleotides A1493 and G530, respectively (Figure 45A and B). This observation is in good agreement with the interaction of SmpB and A1493/G530 observed in the A-site complex (Rae et al., 2019). Since the interaction of SmpB with the same decoding nucleotides is also observed in the pre-accommodated tmRNA complex (Neubauer et al., 2009), it is suggested that the G530/A1493 interaction is maintained during TLD-SmpB accommodation. However, compared to canonical decoding of tRNA, where G530, A1493 as well as A1492 participate in anticodon-codon recognition (Ogle et al., 2001), the SmpB interaction in the pre-accommodated (Neubauer et al., 2009) and accommodated tmRNA states (present work and Rae et al., 2019) do not involve A1492 (Figure 62C).

4.2.2 tmRNA-SmpB translocation into the P-site requires an open bridge B1a

The movement of the tmRNA from the ribosomal A-site to the P-site requires the disruption of the intersubunit bridge B1a, which is formed by the A-site finger (ASF) and ribosomal protein uS13 (see also chapter 1.2.3.3). The tmRNA-PRE state shows a closed B1a conformation that prevents the passage of helix 2 (H2) of the tmRNA (Figure 63A). However, the tmRNA-TI-POST states exhibit an open B1a conformation, which allows tmRNA-H2 movement into the P-site (Figure 63B and C). The distances measured between the B1a-forming elements is 51 Å in the tmRNA-TI-POST I and 43 Å in the tmRNA-TI-POST II state, respectively.

The smaller space in the tmRNA-TI-POST II state results from the 5° 30S body back-rotation (Figure 47). In comparison with canonical TI-POST (Ramrath et al., 2013), where the 30S head swivel of 19° alone causes a 25 Å separation of the B1a elements, the additional 30S head tilt in tmRNA-TI-POST states enlarges the B1a gap significantly. This extra-wide B1a opening is essential for tmRNA-H2 passage during the ratchet movement as proposed in Weis et al., 2010 and Ramrath et al., 2012.

After translocation of the TLD-SmpB module into the P-site, the B1a gap amounts back to 25 Å as it is observed in the tmRNA-POST state in Rae et al., 2019 (Figure 63D). However, compared to a classical POST state (Dunkle et al., 2011), where the B1a bridge is closed (~ 7 Å), the tmRNA-POST state (Rae et al., 2019) still exhibits a larger B1a gap providing the space required for stabilization and positioning the tmRNA-H2 between the two ribosomal subunits.

Notably, during and after tmRNA-H2 passage through bridge B1a, the pseudoknot 1 (PK1) remains associated with the ASF (Figure 63B-D). The importance of the PK1-ASF contact has already been demonstrated by PK1/ASF mutation experiments, which showed that PK1, but not other PK ring elements, and a functional ASF are required for tmRNA function (Nameki et al., 2000, Crandall et al., 2010).

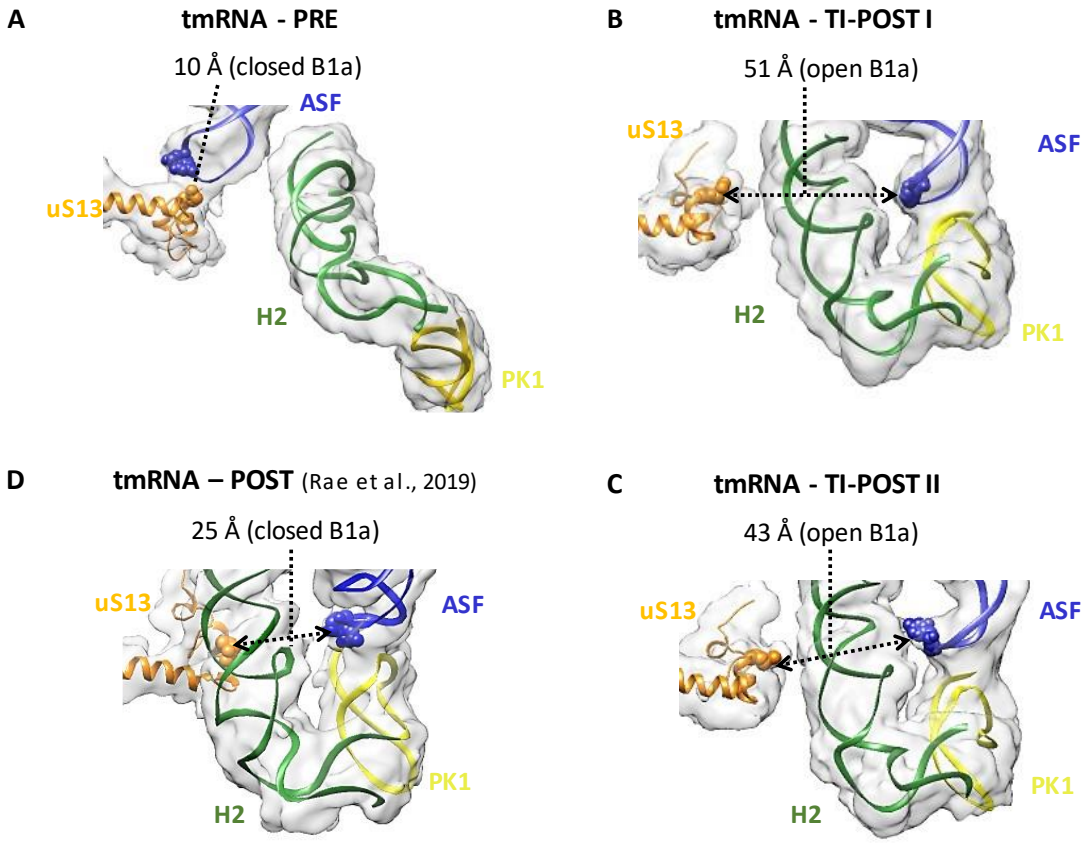

Figure 63: Conformation of bridge B1a in the tmRNA structures. A) tmRNA-PRE (this work), B) tmRNA-TI-POST state I (this work), C) tmRNA-TI-POST state II (this work) and D) tmRNA-POST state (Rae et al., 2019). Shown are the cryo-EM densities (grey) and corresponding atomic models for the tmRNA helix H2 (green), PK1 (yellow) and B1a-forming elements uS13 (orange) and the ASF (blue). The distances were measured between the B1a forming elements, uS13-Arg92 (orange spheres) and H38-C889 (blue spheres). The density maps were gaussian low-pass filtered (width: 1.0 Å for tmRNA-PRE, -TI-POST states and width: 2.0 Å for tmRNA-POST state).

4.2.3 During translocation the SmpB C-terminal tail leaves the mRNA entry channel

During tmRNA translocation into the P site, the C-terminal tail of SmpB flips into the mRNA exit channel and vacates the space of the mRNA entry channel for occupation by the mRNA-like domain (MLD). In both tmRNA-TI-POST states the C-terminal tail remains alpha-helical and is positioned within the mRNA exit channel in a similar manner as observed in the tmRNA-POST

state (Rae et al., 2019; Figure 64). However, in contrast to the tmRNA-POST state (Rae et al., 2019) there is a significant difference in the position of SmpB's loop K131-H136 (Figure 64). The loop has shifted towards the A-site after translocation in order to position the MLD resume codon properly into the empty A-site to form the tmRNA-POST state (Figure 67B; Rae et al., 2019).

Since both tmRNA-TI-POST structures representing a certain temporary state and further intermediates states are likely to be present as observed for the canonical TI-POST states (Ramrath et al. 2013; Zhou et al., 2013, 2014, 2019), it cannot be excluded that SmpB tail takes over additional intermediate positions. As soon as the C-terminal tail of SmpB leaves the mRNA channel, it can be occupied by the mRNA-like domain (MLD) of the tmRNA, which occurs in a stepwise manner (see next chapters).

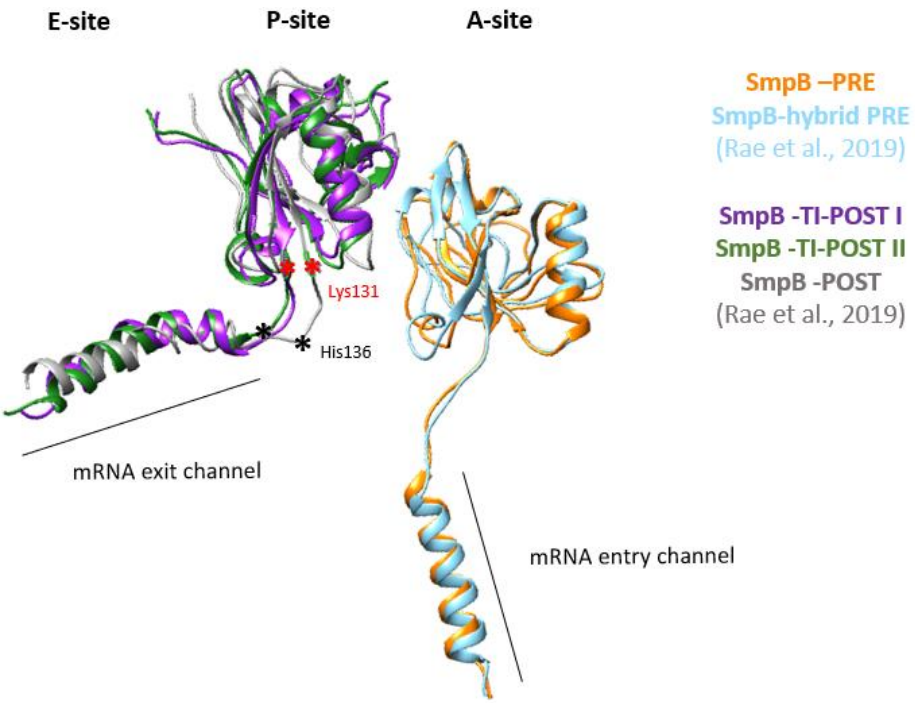

Figure 64: Comparison of SmpB's C-terminal tail before, during and after translocation of the tmRNA into the P-site. A) In the tmRNA-PRE state (orange), the C-terminal tail of SmpB is positioned in the mRNA-entry channel in a similar way as observed for the hybrid PRE state (blue, Rae at al., 2019). In the tmRNA-TI-POST states (purple, green) and POST state (grey, Rae et al., 2019), the SmpB C-terminal tail is located within the mRNA exit channel.

4.2.4 tmRNA movement before MLD enters the ribosomal 30S latch

A physical barrier that prevents the mRNA-like domain (MLD) to enter the mRNA channel is formed by helix H5 of the tmRNA in the PRE-translocation state (see tmRNA-PRE state in Figure 65). During translocation, the tmRNA-H5 moves by about 20 Å freeing the mRNA entrance and subsequently interacting with uS2 at the surface of the 30S subunit (Figure 65). The interaction of H5 with uS2 may stabilize the PK ring during MLD loading.

Together with PK2, the helix H5 of the tmRNA is additionally stabilized at the ribosomal solvent side by uS3 (Figure 46A, Figure 51, Figure 54C and D). The high conservation of uS3 (Ramrath et al., 2012) and PK2 (Hudson et al., 2014) as well as their maintained interaction observed in all tmRNA states (Ramrath et al., 2012; Weis et al., 2010; Neubauer et al., 2014; Rae et al., 2019) highlights their function during the movement of the tmRNA through the ribosome.

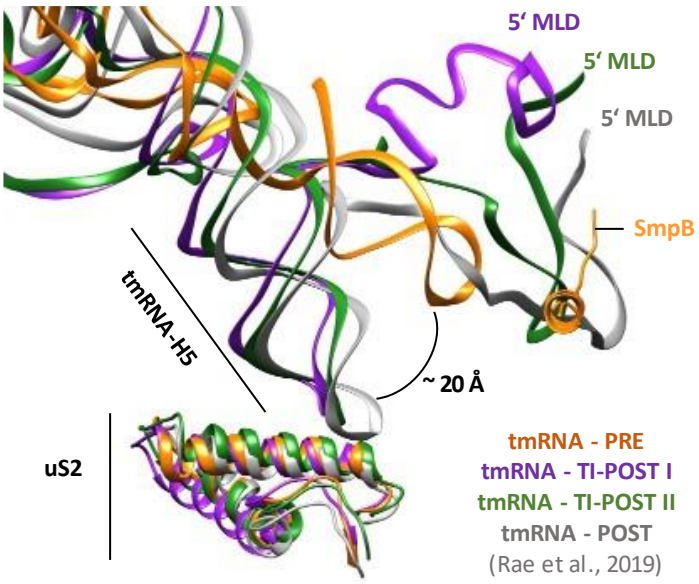

Figure 65: Position of helix H5 and MLD of the tmRNA before, during and after translocation. Superposition of helix H5 of the tmRNA by a common 50S alignment. The tmRNA's H5 moves about 20 Å during the transition from the tmRNA-PRE state complex (orange) to the tmRNA-TI-POST complexes (state I: purple and state II: green), facilitating the MLD to pass through the space which was previously filled by the tail of SmpB (orange). The interaction between H5 and uS2 observed in tmRNA-TI-POST states is maintained in the tmRNA-POST state (grey, Rae at al., 2019).

As seen in previous cryo-EM reconstructions of pre-accommodated (Neubauer at al., 2012), PRE-translocated (Rae et al., 2019) and fully translocated tmRNA (Weis et al., 2010; Fu et al., 2010), the conformation of the pseudoknots (PK1-4) in the presented tmRNA-PRE and -TI-POST states mostly remains the same (Figure 41A-C). However, during tmRNA transition from

the A-site (Figure 66A) towards the P-site (Figure 66B-D), the tmRNA's H5 enlarges its distances relative to PK1, providing more space for the MLD extension. Both, the tmRNA-H5 and PK1 anchor the MLD on the solvent exposed side and intersubunit side on the ribosome, respectively.

The tentative MLD models for the tmRNA-TI-POST states reveal differences in their position relative to the ribosomal 30S latch (Figure 66B and C). The 30S latch is a dynamic area of the mRNA entry channel that is formed by helix h34 in the 30S head and the G530 nucleotide of h18 in the 30S body, respectively. Opening of the 30S latch is a consequence of the 30S head movement in the tmRNA-TI POST states that allows the MLD to enter the mRNA channel (Figure 66B and C). This is similar to eukaryotic translation initiation complexes, in which enlarging the gap between the 40S head and body latch components facilitates mRNA docking into the mRNA entry binding channel (Sokabea and Frasera, 2017; Passmore et al., 2007).

The presented tmRNA-TI-POST states show an open 30S latch conformation defined by the distance of more than 20 Å between G530 of h18 and h34 seen in the previous tmRNA-TI-POST structure (Ramrath et al., 2012). In contrast, the tmRNA structures with unrotated ribosomal conformation, such as tmRNA-PRE (Figure 45), in which the mRNA channel is occupied by the C-terminal tail of SmpB, or tmRNA-POST (Rae et al., 2019), in which the channel has just been loaded with MLD, do not require access to the mRNA entry channel and open 30S latch conformation (Figure 66A and D).

Even though the 30S latch of both tmRNA-TI-POST states is sufficiently wide open for the MLD to enter the mRNA channel, the MLD passed the 30S latch is only observed in the tmRNA-TI-POST II state. The combination of a larger 30S head rotation and starting back rotation in the tmRNA-TI-POST II state (Figure 47B) likely causes the MLD entry into the mRNA channel.

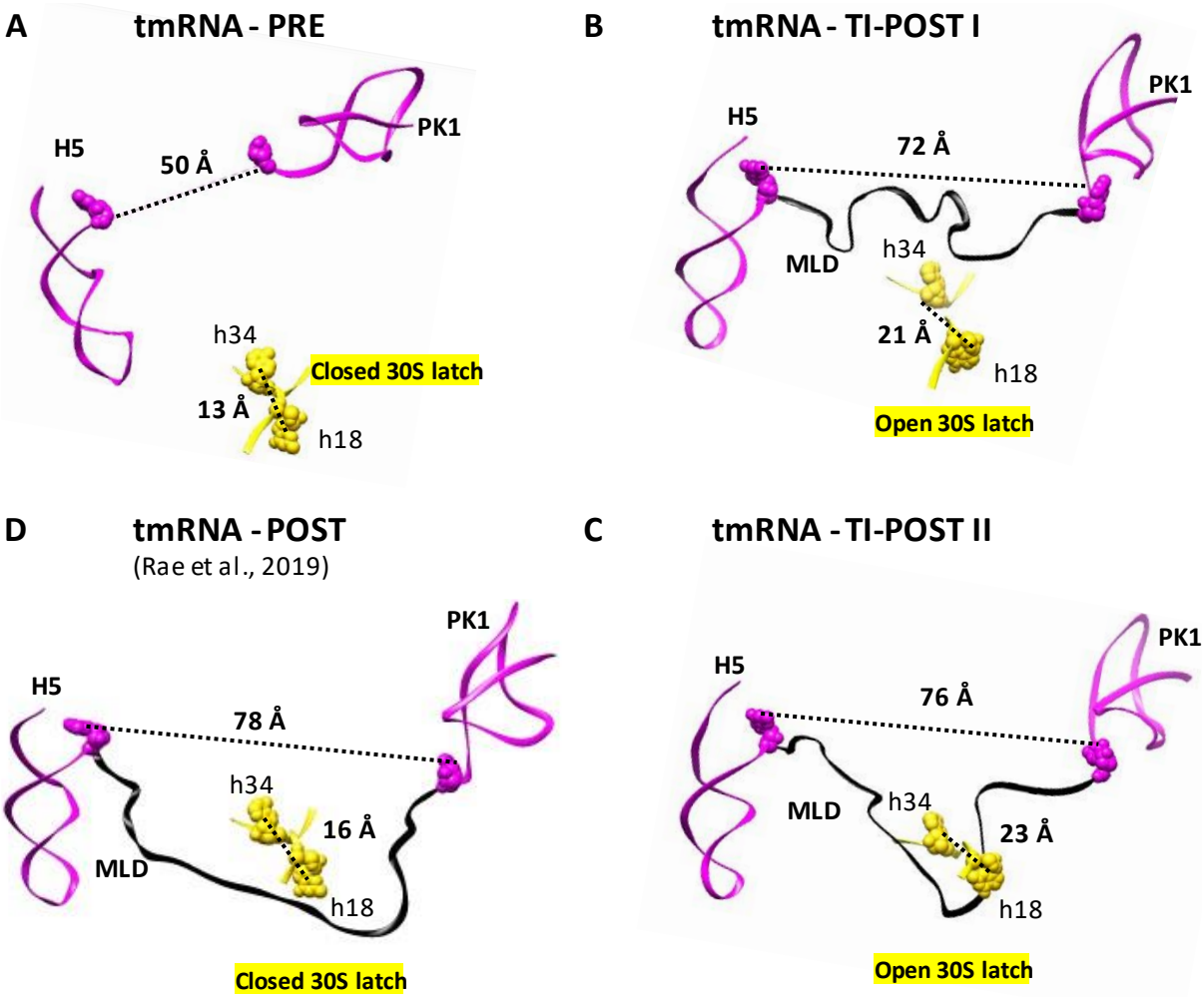

Figure 66: 30S-latch opening and MLD unfolding. A) tmRNA-PRE state, B) tmRNA-TI-POST I state, C) tmRNA-TI-POST II and D) tmRNA-POST state (Rae et al., 2019). Shown are the models for the 30S latch components h34 and h18 (yellow) and the tmRNA (magenta). The 30S latch distances were measured between nucleotide C1055 of h34 and G530 of the h18, both shown as yellow spheres. The nucleotides C78 of PK1 and G108 of H5 enclosing the MLD (black) used for measurement are shown as pink spheres.

4.2.5 MLD loading requires 30S subunit/head rotation and EF-G-release

The sustained interaction of MLD with protein uS3 observed in the tmRNA-TI-POST (this study and Ramrath et al., 2012) suggest that particularly this 30S head protein contribute to MLD navigation into the mRNA channel during translocation (Figure 67A). In contrast, the 30S body elements, uS4, uS5, h18, and h44 participate in MLD stabilization only after initial (tmRNA-TI-POST II in Figure 67A) or completed MLD insertion (tmRNA-POST in Figure 67A; Rae et al., 2019). Moreover, the ribosomal proteins uS3, uS4 identified to have helicase activity, are likely to involve in MLD unwinding as suggested for the mRNA (Takyar et al. 2005).

To finalize MLD loading in the first translocation step, the resume codon of the MLD must be positioned correctly into the decoding site for restarting the translation in *trans*. Biochemical experiment with tmRNA mutants of *E. coli* showed that five nucleotides upstream of the resume codon in the MLD are critical for establishing the reading frame (Lee et al., 2001; Konno et al., 2007). This region of the resume codon was shown to interacts with SmpB at the ribosomal A-site within the tmRNA-POST structure (Figure 67B; Rae et al., 2019).

Comparison with the tmRNA-POST state (Rae et al., 2019) shows that EF-G in the tmRNA-TI-POST states clashes with the MLD five nucleotides upstream the resume codon (Figure 67B). Moreover, the upstream nucleotides contacting SmpB's residues, Thr110 and Lys134, observed in the tmRNA-POST state (Rae et al., 2019) are too far away to interact with MLD during translocation (Figure 67B-C). This suggests that an interaction of MLD with SmpB within the ribosomal A-site is achieved during back-rotation and after EF-G-release from the tmRNA-TI-POST states. Since the EF-G-release in canonical translocation occurs after finalized 30S body and head back rotation, it is obvious that the EF-G-release in the presented tmRNA TI-POST states represents one of the last steps of MLD loading and subsequent initiation of the *trans*-translation process.

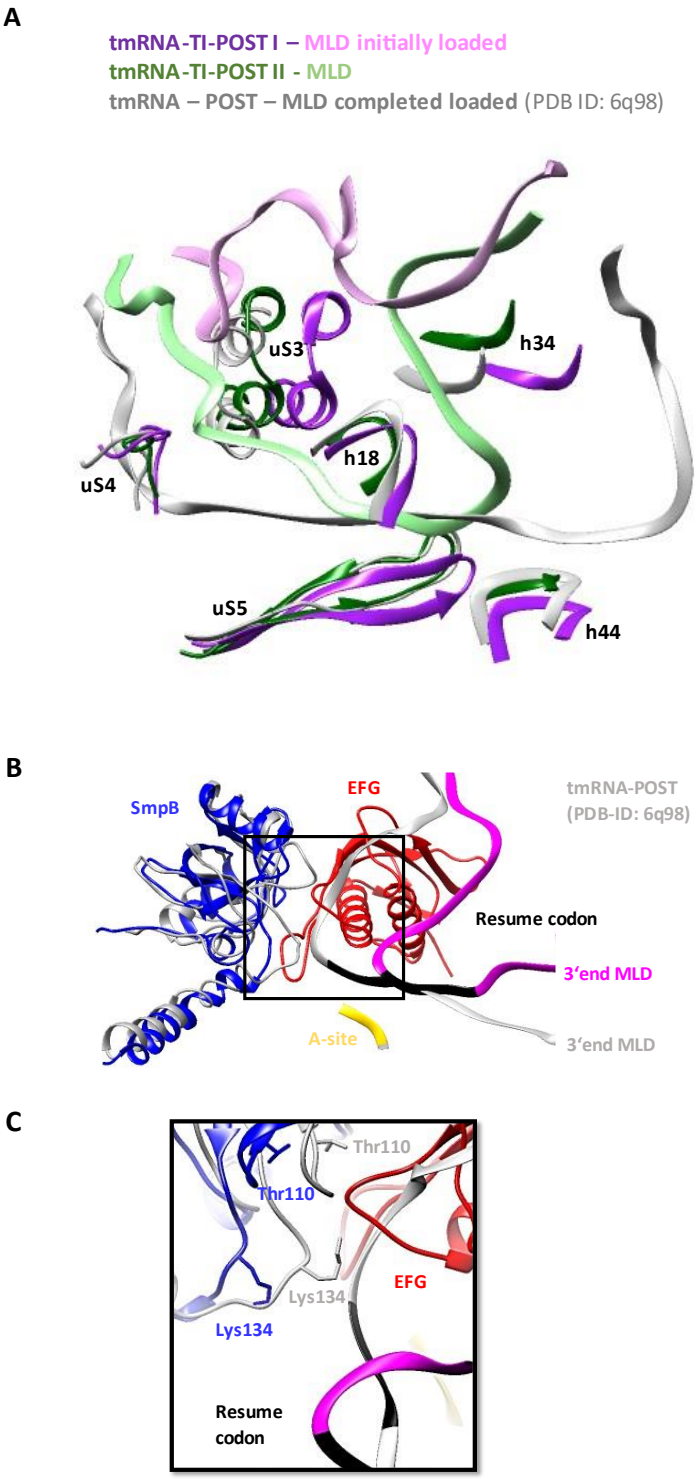

Figure 67: Comparison of MLD and SmpB position in the presented tmRNA-TI-POST states and a tmRNA-POST state. A) Superposition of MLD of tmRNA-POST I (pink), tmRNA-TI-POST II (green), and tmRNA-POST state (grey, PDB-ID: 6q98, Rae et al., 2019) by common 30S body alignment. The 30S elements surrounding the MLD are indicated. B) Superposition of the tmRNA-POST (grey, PDB-ID: 6q98, Rae et al., 2019) and the tmRNA-TI-POST II (MLD in magenta, EF-G in red, SmpB in blue, A-site in yellow) upon a 50S alignment. The resume codon (black) and 3'end of the MLD are indicated. C) Close up view from B) shows the residues of SmpB, Tyr110 and Lys134 of the tmRNA-TI-POST II state are not

in binding distance to interact with the MLD upstream of the resume codon. The same Color code was used as in B).

4.2.6 Second translocation completes MLD loading into the mRNA channel

The conformation and binding of tmRNA-SmpB in both PAST-E states are in good agreement with the recently published PAST-E state of *in vitro* constituted tmRNA-SmpB-P-tRNA-70S complex (Rae et al., 2019) (Figure 68). This reinforces the hypothesis that the ribosome slide along the mRNA without requiring interaction anticodon shifted the tRNA into the P-site, thereby forming a state that resembles a physiological state.

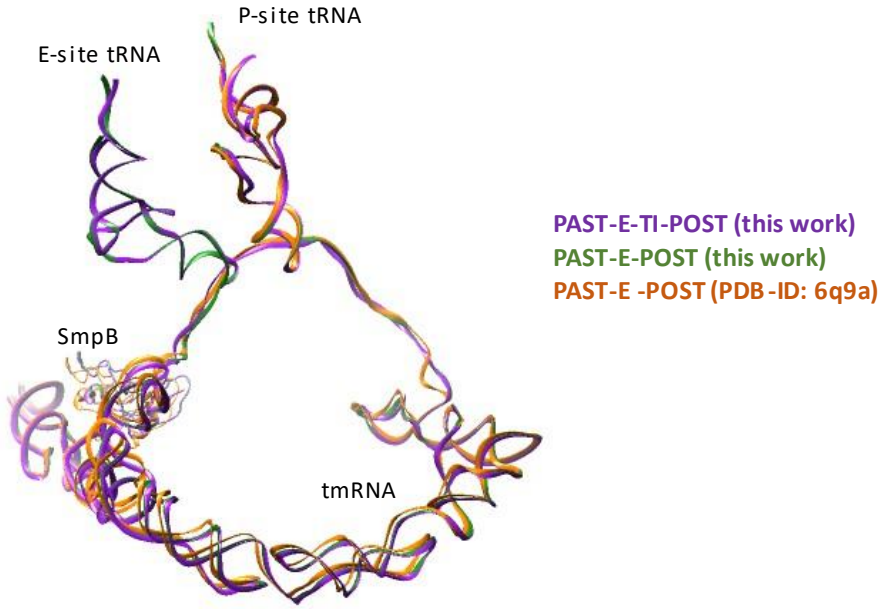

Figure 68: Comparison of tmRNA-PAST-E models with a similar model. Superposition of the tmRNA, SmpB, P-site and E-site tRNA in the PAST-E-TI-POST state (purple), PAST-E-POST state (green) and PAST-E-state (in orange; Rae et al., 2019) upon a common 50S alignment reveal a good match.

The first translocation cycle brings the tmRNA in the P site and the translation resume codon of the tmRNA in the A-site (Figure 69A, Rae at al., 2019). The second translocation moves the resume codon of MLD into the P-site but resembles an unexpected state where the tmRNA has passed the E-site (Figure 69A; Figure 53A and C). However, even though tmRNA-SmpB-binding in the E-site is skipped in the *trans*-translation, the presence of EF-G in the intermediate PAST-E state (Figure 53A) indicates that the translocation of MLD into the P-site occurred in a canonical manner.

For tmRNA translocation from the P-site towards the E-site, the most obvious ribosomal barrier to overcome is the intersubunit bridge B1b formed by protein uS13 of the small subunit and

uL5 as well as bL31 of the large subunit (Figure 69B, see also chapter 1.2.3.3). The larger gap between the B1b-forming elements observed in the tmRNA-TI-POST-II of this study would sterically favor the movement of the tmRNA towards the E-site (Figure 69C). This suggest that the same structural rearrangement occurring during the first step, may take place during the second translocation, too, allowing the tmRNA-SmpB in the P-site (Rae at al., 2019) to pass through bridge B1b. However, a binding into the E-site would require structural rearrangement within the tmRNA. Assuming the ribosome adopts the unrotated conformation as observed in the tmRNA-POST state after the second translocation, the PK1 domain of the tmRNA would sterically clash with the central protuberance when fitting the TLD of the tmRNA into the ribosomal E-site (Rae et al., 2019).

For complete MLD loading, a structural constriction, called the E-site latch, has to be opened. The E-site latch is formed by the 30S head protein uS7 and 30S body elements, protein uS11 and G693 of 16S rRNA helix h23 (Figure 69D). The E-site latch in the tmRNA-TI-POST II states exhibits a larger distance separating G693 and protein uS7, compared with the PAST-E-POST state (Figure 69E). Similar to the 30S latch, the widening of the E-site latch is probably accomplished by the large tilting movement of the 30S head allowing the tmRNA to pass the E-site.

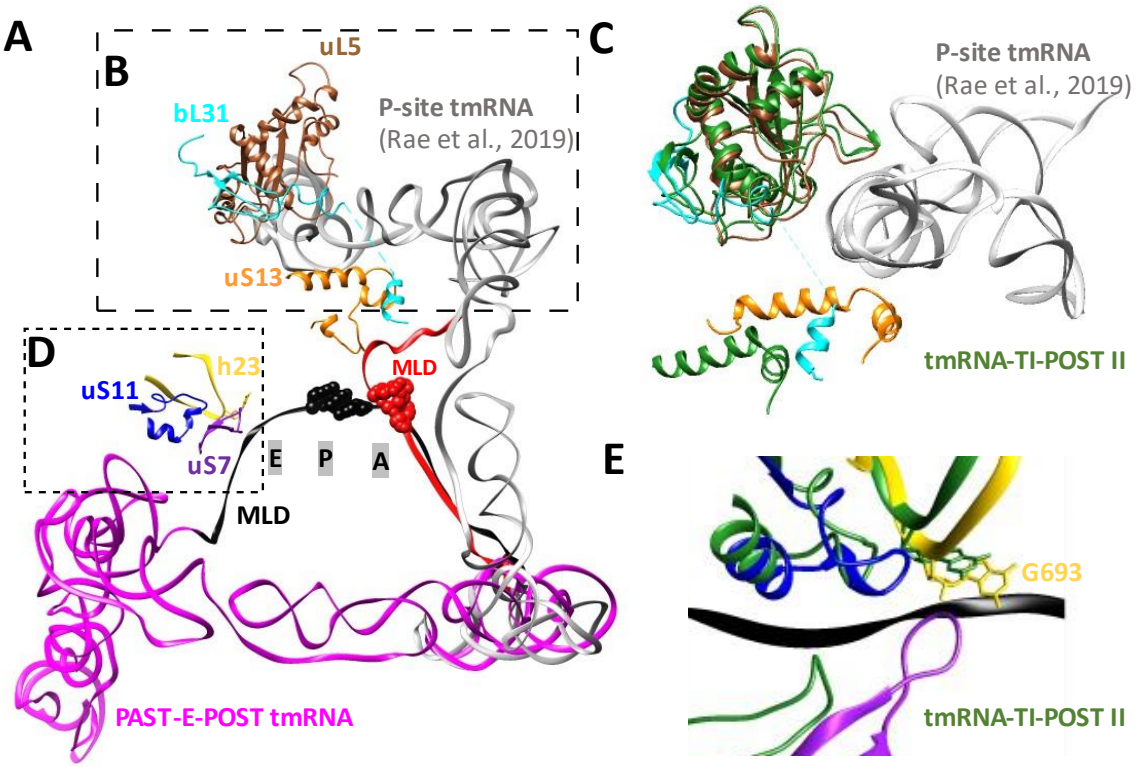

Figure 69: The overcoming barriers, bridge B1b and E-site latch, for the tmRNA to complete MLD loading and to form the PAST-E states. A) Superposition of the P-site tmRNA (in grey, Rae et al., 2019) with its MLD (red) and resume codon (red spheres) and the PAST-E-POST tmRNA with its MLD (black)

and resume codon (black spheres) by a common 50S alignment. The ribosomal tRNA binding sites are indicated as A, P and E. B) Conformation of bridge B1b (uL5 in brown, bL31 in cyan, uS13 in orange) of the POST state (Rae et al., 2019). C) Superposition of the B1b bridges of the POST state (Rae et al., 2019; same coloring as in B)) and tmRNA-TI-POST II state (green) by a 50S alignment. D) Conformation of the E-site latch (nucleotide G693 of the 16S rRNA helix h23 in yellow, uS11 in blue, uS7 in purple) of the PAST-E-POST state. E) Superposition of the E-site latch components of the PAST-E-POST-state (same coloring as in D) and tmRNA-TI-POST II state (green) after 50S alignment.

5 Conclusions

This work focused on the structural investigation of key steps involved in the prokaryotic pathways to rescue stalled ribosomal complexes - the ribosome-associated quality control (RQC) and the *trans*-translation.

The cryo-EM structure obtained from wild-type RqcH co-purified 50S subunits lacked RqcH density but suggested that the nascent chain-stalled 50S complex is a bound by RqcH. These results provided complementary evidence for RqcH's role in prokaryotic RQC in Lytvynenko et al. 2019. The following cryo-EM analysis of the mutant RqcH-50S complex crosslinked with glutaraldehyde enabled the visualization of all domains of RqcH (NFACT-N-HhH, CC1-M-CC2 and NFACT-R) on P-tRNA-nascent chain-50S subunits.

Docking of RqcH to the ribosomal 50S subunit is achieved largely by the M-CC2 region, with the functional analysis suggesting that the CC1-M-CC2 region alone is able to anchor RqcH to the 50S subunit and CC2-ribsomal stalk base interaction as essential for the function of RqcH.

Comparison with all existing RQC structures shows that the M-CC2 region is always bound around the GTPase associated center which suggest this region in all Rqc2 homologous (NEMF, Rqc2 and RqcH) generally forms a stable anchor to the large ribosomal subunit. Whereas the N- and C-terminal lobes (NFACT-N-HhH and NFACT-R/C) in prokaryotic and eukaryotic RQC complexes seem to have a dynamic character and can move around more during the catalysis cycle.

The interaction of the NFACT-R domain with the ribosomal A-site finger was observed in all prokaryotic structures which indicate its functional relevance for RqcH during the whole catalysis cycle. Moreover, our structure-function analysis suggests that the NFACT-R domain assists in tRNA positioning during the tailing reaction.

Compared to prokaryotic wilde-type RQC structures, the P-tRNA binding by mutant RqcH occurs without the involvement of the NFACT-N* domain that is defective in tRNA binding. This implies that the NFACT-N domain is dispensable for RqcH binding to the P-site tRNA bound to 50S subunits. Since the RqcH mutant is disabled in its function (Lytvynenko et al., 2019), the structure likely represents an initial recognition state within the Ala-tailing cycle. However,

appropriate experiments must follow in order to prove the presence of such an initial recognition state within the prokaryotic RQC pathway.

The cryo-EM structures obtained from the 70S-tmRNA-EF-G-FA specimen provide insights of the structural barriers which must overcome during the translocation of the *trans*-translation. Moreover, the tmRNA-TI-POST structures answer one outstanding question, namely what conformational changes of SmpB takes place during translocation. The C-terminal tail of SmpB in the tmRNA-TI-POST states remains α-helical, but flips to the empty A-site, and occupies the mRNA exit channel and thereby anchoring tmRNA-SmpB in the ap/P position on the ribosome. However, whether the C-terminal SmpB tail also occupies other intermediate positions not seen in our structures remains to be investigated.

During the first translocation tmRNA-H5 moves away from its position at the A-site in the tmRNA-PRE state facilitating the MLD to enter the mRNA entry channel before occupied by the SmpB C-terminal tail. The MLD is subsequently threaded through the 30S-latch into the mRNA channel in a stepwise manner. This occurs during 30S head tilting in the tmRNA-TI-POST states and is assisted by ribosomal elements (uS3, uS4, uS5, h16, h18, and h44). The positioning of the resume codon of the MLD properly into the P-site is accomplished by a complete 30S back rotation and subsequent EF-G-release, thereby ending the first translocation cycle.

The second EF-G mediated translocation moves the tRNAs and mRNA forward by one codon. However, the tmRNA in the resulting state does not mimic a tRNA in the E-site since it was found passed the ribosomal E-site which is consistent with similar structures. To accomplish full MLD loading, the tmRNA's passage through the intersubunit bridge B1b and MLD insertion through the E-site latch is achieved in the second translocation. However, it is unclear whether complete mRNA loading requires an extra-large 30S head rotation during the second translocation, too but it would be one option to disrupt the E-site latch barrier.

However, many questions remain about the exact nature of MLD loading during the tmRNA-SmpB translocations withing the *trans*-translation. The results presented here provide a structural framework for designing future experiments to address these unanswered questions.

6 Supplement

Supplementary tables.

Table S1: Used templates for building the mutant RqcH-50S model.

Factor	Chain ID	Source of the model
23S rRNA	A	PDB ID: 3j9W
5S rRNA	B	PDB ID: 3j9W
tRNA	C	PDB ID: 3WQZ
uL2	D	PDB ID: 3j9W
uL3	E	
uL4	F	
uL5	G	
uL6	H	
uL10	I	
uL11	J	
uL13	K	
uL14	L	
uL15	M	
uL16	N	
bL17	O	
uL18	P	
bL19	Q	
bL20	R	
bL21	S	
uL22	T	
uL23	U	
uL24	V	
bL27	W	
uL29	X	
uL30	Y	
bL31	Z	

Factor	Chain ID	Source of the model
bL32	1	
bL33	2	
bL34	3	
bL35	4	
bL36	5	
Nascent chain	6	Built *de novo*
RqcH	7	PDB ID: 5H3X Rigid-body dock PDB ID: 5H3W M: Built *de novo*
		PDB ID: 5H3W Rigid body dock
RqcH-Sequence		Uniprot ID: O34693

Table S2: Used templates for building the tmRNA-70S models.

		Source of model (PDB-ID)		
Factor	**Chain ID**	**PRE**	**TI-POST-I and II**	**PAST-E- TI-POST and POST**
23S rRNA	1	6q97	6q97	6q9a
5S rRNA	2			
16S rRNA	3			
mRNA	4	Sequence shown in chapter 2.3.3	n.p.	n.p.
P-tRNA	5	6q97	6q98	6q97
E-tRNA	6	6q97		6q97
tmRNA	7	6q97	6q98	6q9a
SmpB	8	6q97	6q98	6q9a
uL2	A	6q97	6q98	6q9a
uL3	B			
uL4	C			
uL5	D			
uL6	E			
bL9	F			
uL10	G			
uL11	H			
uL13	I			
uL14	J			
uL15	K			
uL16	L			
bL17	M			
uL18	N			
L19	O			
bL20	P			
bL21	Q			
uL22	R			
uL23	S			
uL24	T			
bL25	U			
bL27	V			

		Source of model (PDB-ID)		
Factor	**Chain ID**	**PRE**	**TI-POST-I and II**	**PAST-E- TI-POST and POST**
bL28	W			
uL29	X			
uL30	Y			
bL31	Z			
bL32	a			
bL33	b			
bL34	c			
bL35	d			
bL36	e			
uS2	f			
uS3	g			
uS4	h			
uS5	i			
bS6	j			
uS7	k			
uS8	l			
uS9	m			
uS10	n			
uS11	o			
uS12	p			
uS13	q			
uS14	r			
uS15	s			
bS16	t			
uS17	u			
bS18	v			
uS19	w			
bS20	x			
bS21	y			
EF-G	z	n.p.	4v9m	For POST only:4v9m

n.p.: not present

Table S3: Statistics for the atomic models of mutant RqcH-50S structure.

Mutant RqcH-50S		
Cross-resolution (Map-to-Model)	FSC cutoff at 0.5	3.2 Å
All-Atoms Contacts	Clashscore, all atoms	4.59
Protein Geometry	Poor rotamers	7.07%
	Favored rotamers	84.47%
	Ramachandran outliers	0.05%
	Ramachandran favored	93.00%
	Rama distribution Z-score	-0.61 ± 0.11
	Molprobity score	2.33
	Cβ deviations > 0.25 Å	0.03%
	Bad bonds	0.00%
	Bad angles	0.04%
Peptide Omegas	Cis Prolines	0.00%
	Cis nonProlines	0.19%
	Twisted Peptides	0.08%
Nucleic Acid Geometry	Probably wrong sugar puckers	0.40%
	Bad backbone conformations	18.12%
	Bad bonds	0.00%
	Bad angles	0.02%
Low-resolution Criteria	CaBLAM outliers	5.0%
	CA Geometry outliers	1.25%

Table S4: Statistics for the atomic models of tmRNA-70S structures.

		tmRNA-PRE	**tmRNA-TI-POST I**	**tmRNA-TI-POST II**	**PAST-E-TI-POST**	**PAST-E-POST**
Cross-resolution (Map-to-Model)	FSC cutoff at 0.5	3.8 Å	3.6 Å	3.9 Å	3.8 Å	3.8 Å
All-Atoms Contacts	Clashscore, all atoms	9.92	9.45	11.81	9.95	9.4
Protein Geometry	Poor rotamers	1.42%	1.18%	0.28%	2.15%	1.64%
	Favored rotamers	92.47%	93.22%	93.52%	91.90%	93.26%
	Ramachandran outliers	0.03%	0.02%	0.09%	0.03%	0.00%
	Ramachandran favored	97.04%	93.60%	93.37%	96.57%	97.33%
	Rama distribution Z-score	-0.61 ± 0.11	-0.46 ± 0.11	-0.54 ± 0.11	-0.17 ± 0.11	-0.56 ± 0.11
	Molprobity score	1.80	1.98	2.0	1.99	1.79
	Cβ deviations > 0.25Å	0.00%	0.00%	0.03%	0.00%	0.00%
	Bad bonds	0.00%	0.00%	0.00%	0.00%	0.00%
	Bad angles	0.00%	0.03%	0.03%	0.00%	0.00%
Peptide Omegas	Cis Prolines	1.60%	0.00%	0.00%	1.28%	1.49%
	Cis nonProlines	0.00%	0.02%	0.02%	0.02%	0.02%
	Twisted Peptides	0.00%	0.02%	0.02%	0.01%	0.00%
Nucleic Acid Geometry	Probably wrong sugar puckers	0.00%	1.26%	1.24%	0.89%	0.89%
	Bad backbone conformations	21.45%	16.57%	21.98%	20.34%	19.87%
	Bad bonds	0.00%	0.00%	0.00%	0.00%	0.00%
	Bad angles	0.01%	0.03%	0.03%	0.01%	0.00%
Low-resolution Criteria	CaBLAM outliers	2.3%	4.9%	4.8%	2.7%	2.7%
	CA Geometry outliers	0.62%	1.35%	1.30%	0.94%	0.78%

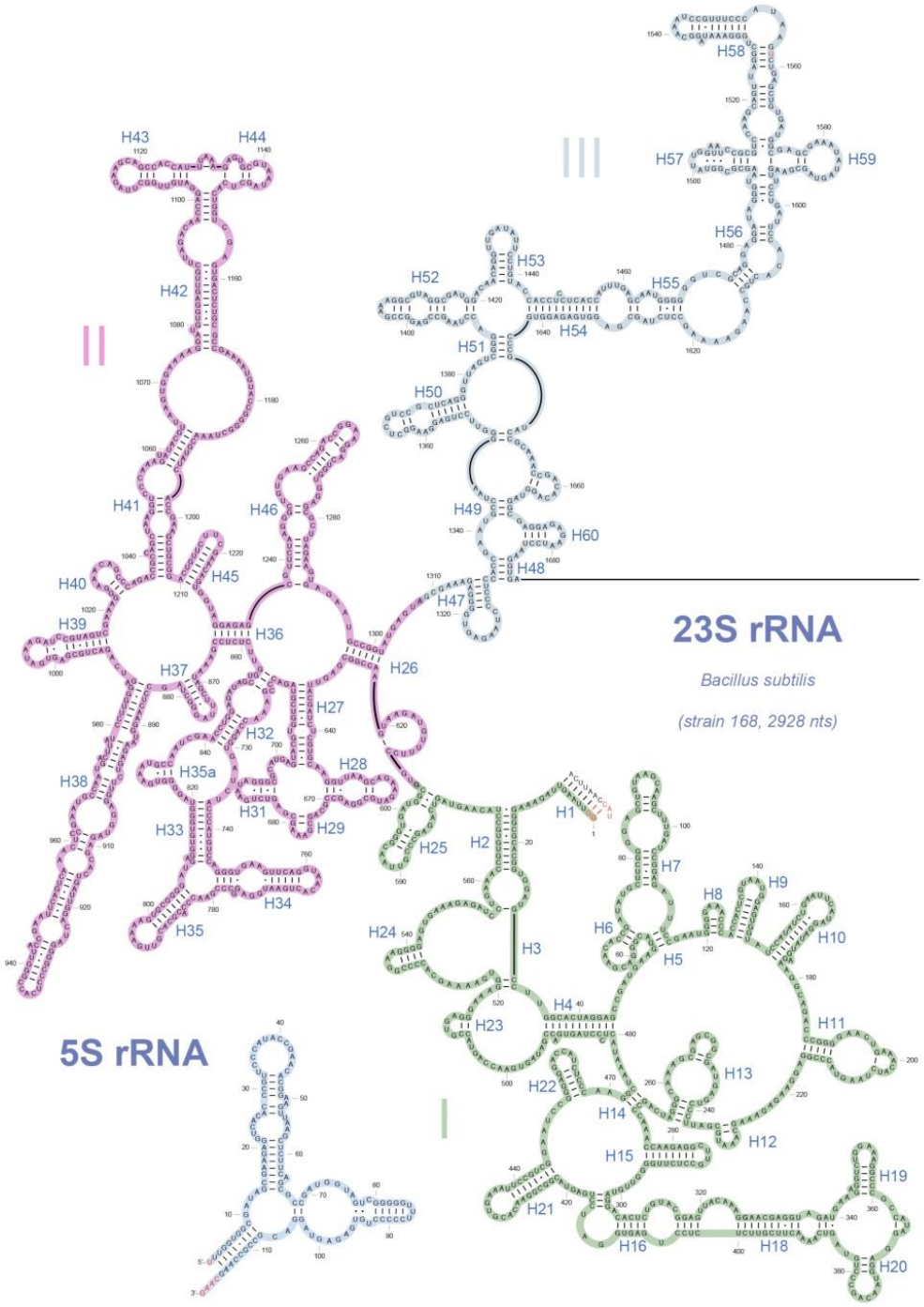
23S rRNA
Bacillus subtilis
(strain 168, 2928 nts)
5S rRNA
I
II
III
H1
H2
H3
H4
H5
H6
H7
H8
H9
H10
H11
H12
H13
H14
H15
H16
H18
H19
H20
H21
H22
H23
H24
H25
H26
H27
H28
H29
H31
H32
H33
H34
H35
H35a
H36
H37
H38
H39
H40
H41
H42
H43
H44
H45
H46
H47
H48
H49
H50
H51
H52
H53
H54
H55
H56
H57
H58
H59
H60

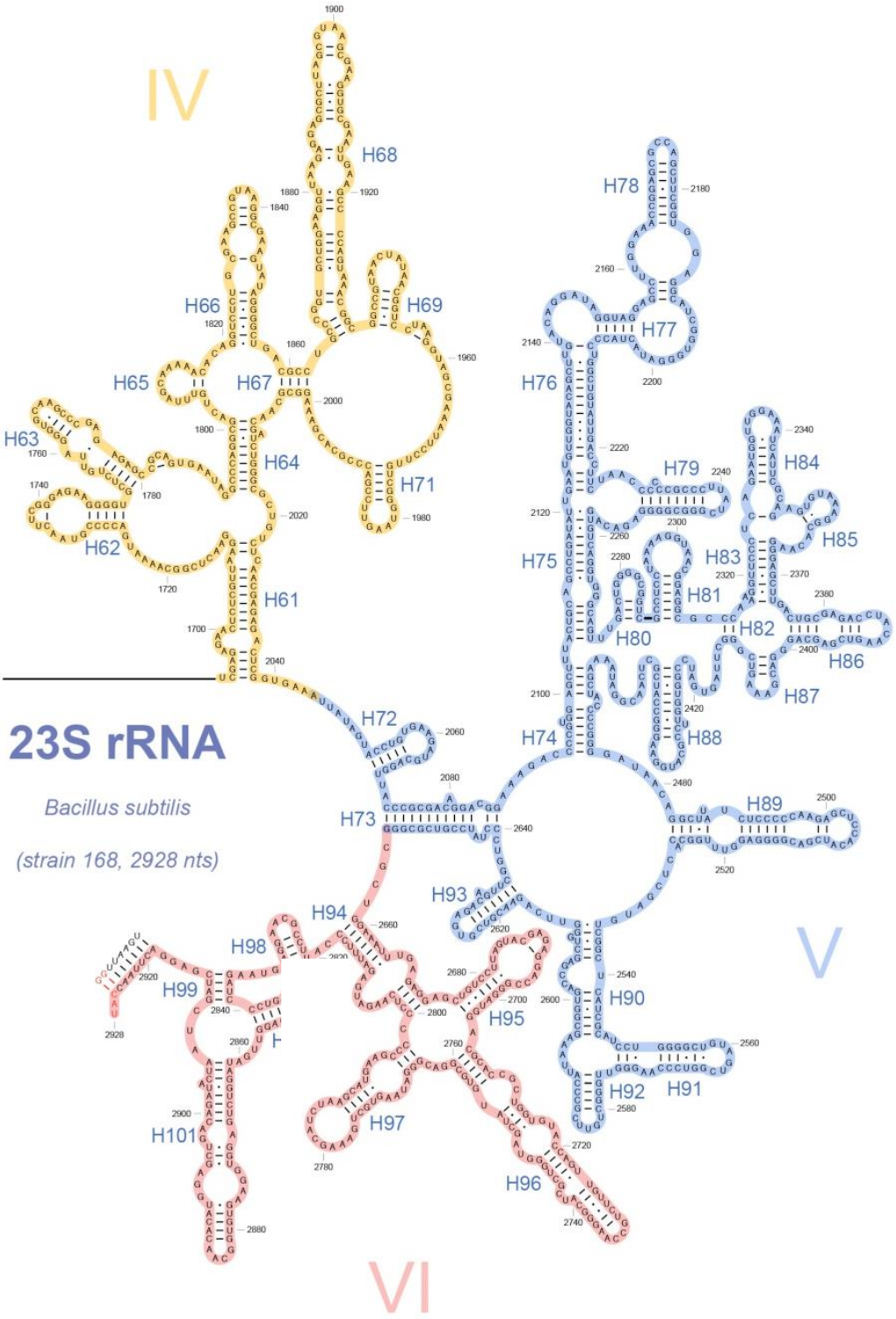

Figure S1: Secondary structure of the *B. subtilis* 5S and 23S rRNA. Images were taken Sohmen et al., 2015.

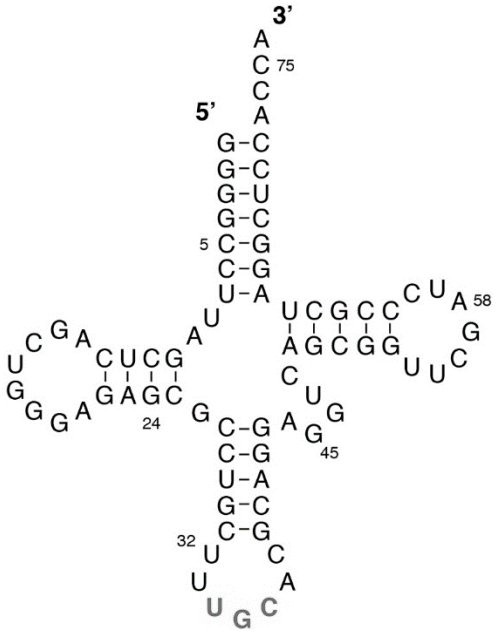

Figure S2: Secondary structure of the *B. subtilis* tRNA^{Ala}. Figure was adapted from Lytvynenko et al., 2019.

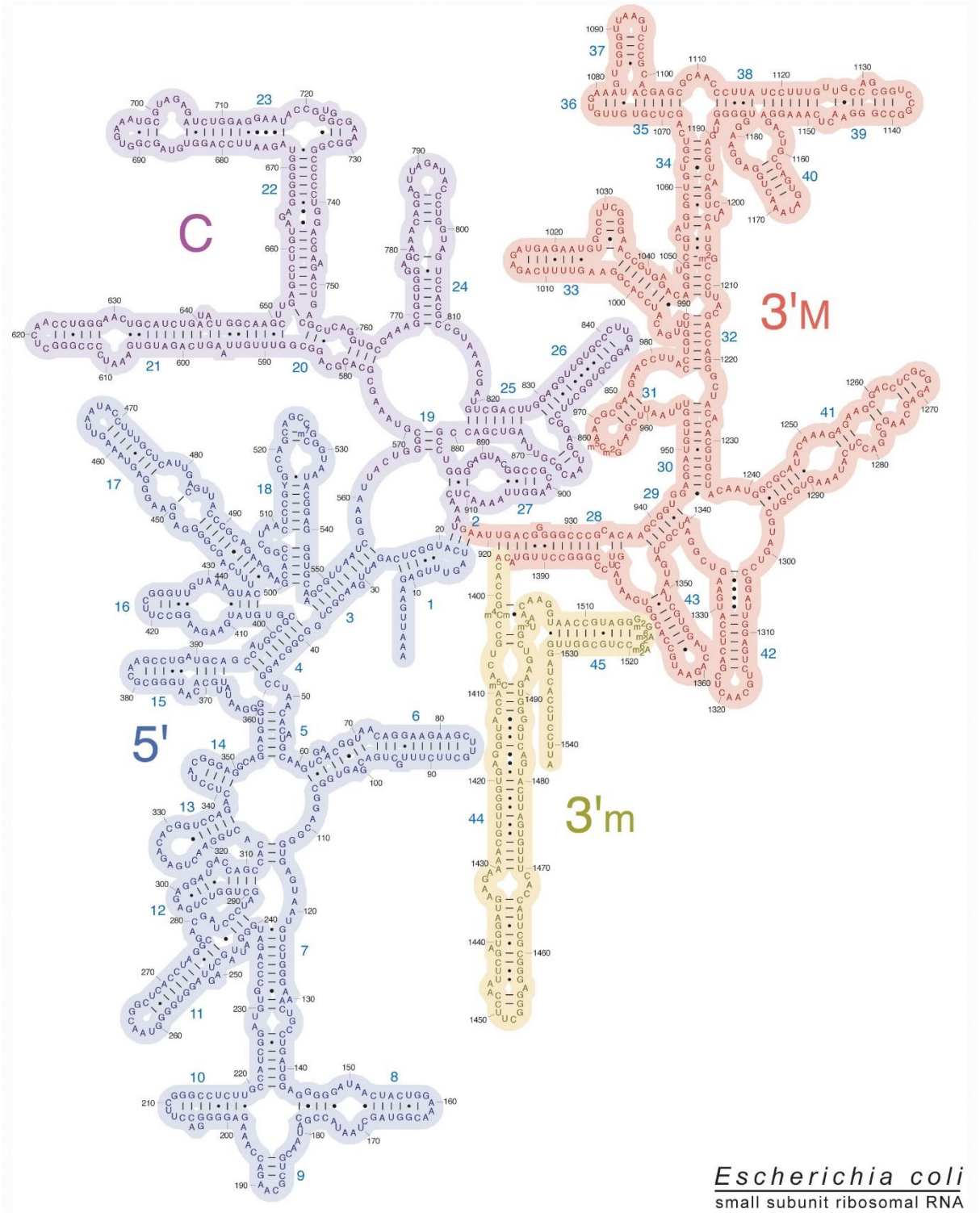

Figure S3: Secondary structure of the *E. coli* 16S rRNA. Image was downloaded from http://rna.ucsc.edu/rnacenter/ribosome_images.html.

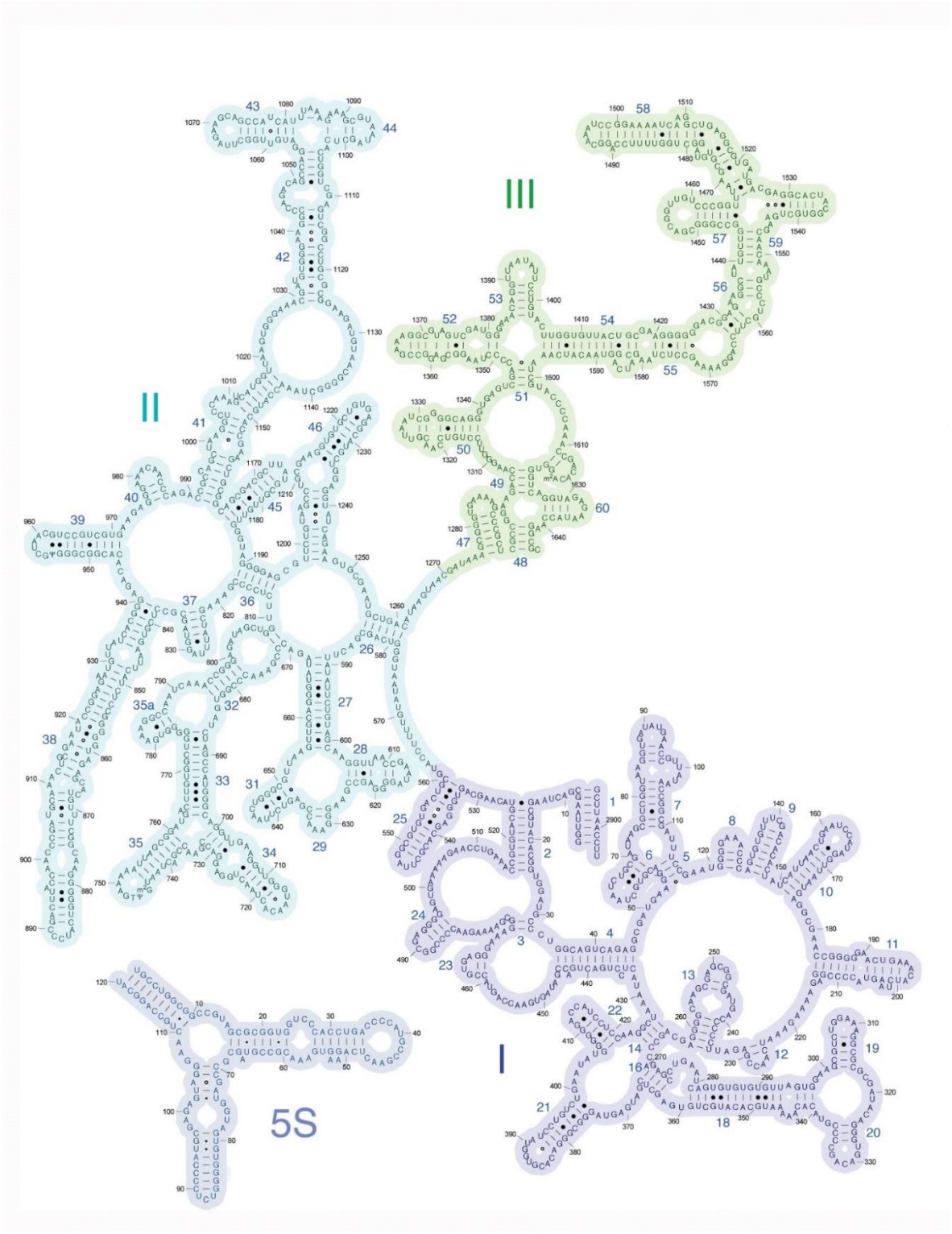
I
II
III
5S

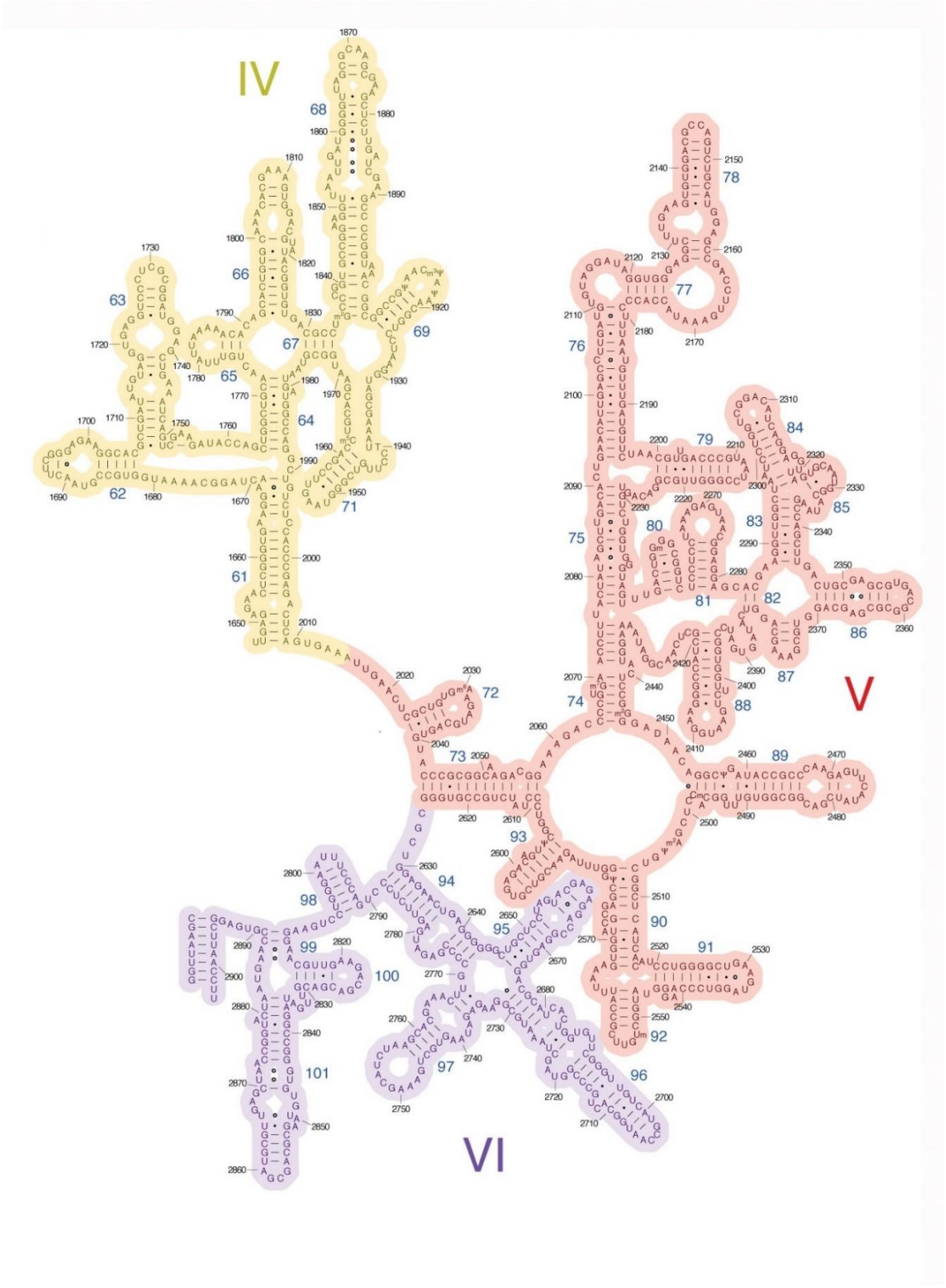

Figure S4: Secondary structure of the *E. coli* 5S and 23S rRNA. Image was downloaded from http://rna.ucsc.edu/rnacenter/ribosome_images.html.

Figure S5: Secondary structure of the *E. coli* tRNA^{Met}. Figure was adapted from Schmitt et al., 1998.

7 References

Adams, P. D., Afonine, P. V., Bunkóczi, G., Chen, V. B., Davis, I. W., Echols, N., ... & McCoy, A. J. (2010). PHENIX: a comprehensive Python-based system for macromolecular structure solution. Acta Crystallographica Section D: Biological Crystallography, 66(2), 213-221.

Adio, S., Senyushkina, T., Peske, F., Fischer, N., Wintermeyer, W., & Rodnina, M. V. (2015). Fluctuations between multiple EF-G-induced chimeric tRNA states during translocation on the ribosome. Nature communications, 6(1), 1-11.

Ævarsson, A., Brazhnikov, E., Garber, M., Zheltonosova, J., Chirgadze, Y., Al-Karadaghi, S., ... & Liljas, A. (1994). Three-dimensional structure of the ribosomal translocase: elongation factor G from Thermus thermophilus. The EMBO journal, 13(16), 3669-3677.

Agirrezabala, X., Lei, J., Brunelle, J. L., Ortiz-Meoz, R. F., Green, R., & Frank, J. (2008). Visualization of the hybrid state of tRNA binding promoted by spontaneous ratcheting of the ribosome. In Single-Particle Cryo-Electron Microscopy: The Path Toward Atomic Resolution: Selected Papers of Joachim Frank with Commentaries (pp. 416-423).

Anger, A. M., Armache, J. P., Berninghausen, O., Habeck, M., Subklewe, M., Wilson, D. N., & Beckmann, R. (2013). Structures of the human and Drosophila 80S ribosome. Nature, 497(7447), 80-85.

Antoun, A., Pavlov, M. Y., Lovmar, M., & Ehrenberg, M. (2006). How initiation factors maximize the accuracy of tRNA selection in initiation of bacterial protein synthesis. Molecular cell, 23(2), 183-193.

Antoun, A., Pavlov, M. Y., Lovmar, M., & Ehrenberg, M. (2006). How initiation factors tune the rate of initiation of protein synthesis in bacteria. The EMBO journal, 25(11), 2539-2550.

Arnaud, M., Chastanet, A., & Débarbouillé, M. (2004). New vector for efficient allelic replacement in naturally nontransformable, low-GC-content, gram-positive bacteria. *Applied and environmental microbiology*, *70*(11), 6887-6891.

Bammes, B. E., Rochat, R. H., Jakana, J., & Chiu, W. (2011). Practical performance evaluation of a 10k× 10k CCD for electron cryo-microscopy. Journal of structural biology, 175(3), 384-393.

Ban, N., Nissen, P., Hansen, J., Moore, P. B., & Steitz, T. A. (2000). The complete atomic structure of the large ribosomal subunit at 2.4 Å resolution. Science, 289(5481), 905-920.

Barends, S., Björk, K., Gultyaev, A. P., de Smit, M. H., Pleij, C. W., & Kraal, B. (2002). Functional evidence for D-and T-loop interactions in tmRNA. FEBS letters, 514(1), 78-83.

Behrmann, E., Loerke, J., Budkevich, T. V., Yamamoto, K., Schmidt, A., Penczek, P. A., ... & Spahn, C. M. (2015). Structural snapshots of actively translating human ribosomes. Cell, 161(4), 845-857.

Belardinelli, R., Sharma, H., Peske, F., Wintermeyer, W., & Rodnina, M. V. (2016). Translocation as continuous movement through the ribosome. RNA biology, 13(12), 1197-1203.

Bengtson, M. H., & Joazeiro, C. A. (2010). Role of a ribosome-associated E3 ubiquitin ligase in protein quality control. nature, 467(7314), 470-473.

Ben-Shem, A., de Loubresse, N. G., Melnikov, S., Jenner, L., Yusupova, G., & Yusupov, M. (2011). The structure of the eukaryotic ribosome at 3.0 Å resolution. Science, 334(6062), 1524-1529.

Berg JM, Tymoczko JL, Stryer L., New York: W H Freeman; 2002. Biochemistry. 5th edition. Section 29.5

Bessho, Y., Shibata, R., Sekine, S. I., Murayama, K., Higashijima, K., Hori-Takemoto, C., ... & Yokoyama, S. (2007). Structural basis for functional mimicry of long-variable-arm tRNA by transfer-messenger RNA. Proceedings of the National Academy of Sciences, 104(20), 8293-8298.

Blanchard, S. C., Kim, H. D., Gonzalez, R. L., Puglisi, J. D., & Chu, S. (2004). tRNA dynamics on the ribosome during translation. Proceedings of the National Academy of Sciences, 101(35), 12893-12898.

Bommer, U., Burkhardt, N. I. L. S., Jünemann, R., Spahn, C. M., Triana-Alonso, F. J., & Nierhaus, K. H. (1997). Ribosomes and polysomes. Subcellular Fractionation-A Practical Approach.

Borg, A., Pavlov, M., & Ehrenberg, M. (2016). Complete kinetic mechanism for recycling of the bacterial ribosome. Rna, 22(1), 10-21.

Brandman, O., Stewart-Ornstein, J., Wong, D., Larson, A., Williams, C. C., Li, G. W., ... & Weissman, J. S. (2012). A ribosome-bound quality control complex triggers degradation of nascent peptides and signals translation stress. Cell, 151(5), 1042-1054.

Brilot, A. F., Chen, J. Z., Cheng, A., Pan, J., Harrison, S. C., Potter, C. S., ... & Grigorieff, N. (2012). Beam-induced motion of vitrified specimen on holey carbon film. Journal of structural biology, 177(3), 630-637.

Brilot, A. F., Korostelev, A. A., Ermolenko, D. N., & Grigorieff, N. (2013). Structure of the ribosome with elongation factor G trapped in the pretranslocation state. Proceedings of the National Academy of Sciences, 110(52), 20994-20999.

Burroughs, A. M., & Aravind, L. (2014). A highly conserved family of domains related to the DNA-glycosylase fold helps predict multiple novel pathways for RNA modifications. RNA biology, 11(4), 360-372.

Buskirk, A. R., & Green, R. (2017). Ribosome pausing, arrest and rescue in bacteria and eukaryotes. Philosophical Transactions of the Royal Society B: Biological Sciences, 372(1716), 20160183.

Campbell, M. G., Cheng, A., Brilot, A. F., Moeller, A., Lyumkis, D., Veesler, D., ... & Grigorieff, N. (2012). Movies of ice-embedded particles enhance resolution in electron cryo-microscopy. Structure, 20(11), 1823-1828.

Cannone, J. J., Subramanian, S., Schnare, M. N., Collett, J. R., D'Souza, L. M., Du, Y., ... & Pande, N. (2002). The comparative RNA web (CRW) site: an online database of comparative sequence and structure information for ribosomal, intron, and other RNAs. BMC bioinformatics, 3(1), 2.

Canonaco, M. A., Calogero, R. A., & Gualerzi, C. O. (1986). Mechanism of translational initiation in prokaryotes: evidence for a direct effect of IF2 on the activity of the 30 S ribosomal subunit. FEBS letters, 207(2), 198-204.

Carter, A. P., Clemons, W. M., Brodersen, D. E., Morgan-Warren, R. J., Hartsch, T., Wimberly, B. T., & Ramakrishnan, V. (2001). Crystal structure of an initiation factor bound to the 30S ribosomal subunit. Science, 291(5503), 498-501.

Chen, C., Cui, X., Beausang, J. F., Zhang, H., Farrell, I., Cooperman, B. S., & Goldman, Y. E. (2016). Elongation factor G initiates translocation through a power stroke. Proceedings of the National Academy of Sciences, 113(27), 7515-7520.

Chen, C., Stevens, B., Kaur, J., Cabral, D., Liu, H., Wang, Y., ... & Cooperman, B. S. (2011). Single-molecule fluorescence measurements of ribosomal translocation dynamics. Molecular cell, 42(3), 367-377.

Chen, Y., Feng, S., Kumar, V., Ero, R., & Gao, Y. G. (2013). Structure of EF-G–ribosome complex in a pretranslocation state. Nature structural & molecular biology, 20(9), 1077-1084.

Chen, Y., Kaji, A., Kaji, H., & Cooperman, B. S. (2017). The kinetic mechanism of bacterial ribosome recycling. Nucleic acids research, 45(17), 10168-10177.

Chiu, W., & Glaeser, R. M. (1976). Factors affecting high resolution fixed-beam transmission electron microscopy. Ultramicroscopy, 2, 207-217.

Chou, F. C., Richardson, J. S., & Das, R. (2012). ERRASER, a powerful new system for correcting RNA models. Computl Crystallogr. Newslett, 3, 35-36.

Chou, F. C., Sripakdeevong, P., Dibrov, S. M., Hermann, T., & Das, R. (2013). Correcting pervasive errors in RNA crystallography through enumerative structure prediction. Nature methods, 10(1), 74.

Choy, J. S., Aung, L. L., & Karzai, A. W. (2007). Lon protease degrades transfer-messenger RNA-tagged proteins. Journal of bacteriology, 189(18), 6564-6571.

Connell, S. R., Takemoto, C., Wilson, D. N., Wang, H., Murayama, K., Terada, T., ... & Dabrowski, M. (2007). Structural basis for interaction of the ribosome with the switch regions of GTP-bound elongation factors. Molecular cell, 25(5), 751-764.

Cornish, P. V., Ermolenko, D. N., Noller, H. F., & Ha, T. (2008). Spontaneous intersubunit rotation in single ribosomes. Molecular cell, 30(5), 578-588.

Crandall, J., Rodriguez-Lopez, M., Pfeiffer, M., Mortensen, B., & Buskirk, A. (2010). rRNA mutations that inhibit transfer-messenger RNA activity on stalled ribosomes. Journal of bacteriology, 192(2), 553-559.

Crick, F. (1970). Central dogma of molecular biology. Nature, 227(5258), 561-563.

Crick, F. H. C. (1966). Codon-anticodon pairing: the wobble hypothesis.

Crick, F., Barnett, L., Brenner, S., & Watts-Tobin, R. J. (1961). General nature of the genetic code for proteins.

Crowe-McAuliffe, C., Takada, H., Murina, V., Polte, C., Kasvandik, S., Tenson, T., ... & Hauryliuk, V. (2021). Structural basis for bacterial ribosome-associated quality control by RqcH and RqcP. Molecular Cell, 81(1), 115-126.

Cukras, A. R., & Green, R. (2005). Multiple effects of S13 in modulating the strength of intersubunit interactions in the ribosome during translation. Journal of molecular biology, 349(1), 47-59.

Czworkowski, J., Wang, J., Steitz, T. A., & Moore, P. B. (1994). The crystal structure of elongation factor G complexed with GDP, at 2.7 A resolution. The EMBO journal, 13(16), 3661-3668.

De Bruijn, W. C., Sorber, C. W. J., Gelsema, E. S., Beckers, A. L. D., & Jongkind, J. F. (1993). Energy-filtering transmission electron microscopy of biological specimens. Scanning microscopy, 7(2), 24.

Defenouillère, Q., Yao, Y., Mouaikel, J., Namane, A., Galopier, A., Decourty, L., ... & Fromont-Racine, M. (2013). Cdc48-associated complex bound to 60S particles is required for the clearance of aberrant translation products. Proceedings of the National Academy of Sciences, 110(13), 5046-5051.

Demeshkina, N., Jenner, L., Westhof, E., Yusupov, M., & Yusupova, G. (2012). A new understanding of the decoding principle on the ribosome. Nature, 484(7393), 256-259.

Diaconu, M., Kothe, U., Schlünzen, F., Fischer, N., Harms, J. M., Tonevitsky, A. G., ... & Wahl, M. C. (2005). Structural basis for the function of the ribosomal L7/12 stalk in factor binding and GTPase activation. Cell, 121(7), 991-1004.

Doherty, A. J., Serpell, L. C., & Ponting, C. P. (1996). The helix-hairpin-helix DNA-binding motif: a structural basis for non-sequence-specific recognition of DNA. Nucleic acids research, 24(13), 2488-2497.

Dong, G., Nowakowski, J., & Hoffman, D. W. (2002). Structure of small protein B: the protein component of the tmRNA–SmpB system for ribosome rescue. The EMBO journal, 21(7), 1845-1854.

Dorner, S., Brunelle, J. L., Sharma, D., & Green, R. (2006). The hybrid state of tRNA binding is an authentic translation elongation intermediate. Nature structural & molecular biology, 13(3), 234-241.

Draper, D. E. (2004). A guide to ions and RNA structure. Rna, 10(3), 335-343.

Dubochet, J., & McDowall, A. W. (1981). Vitrification of pure water for electron microscopy. Journal of Microscopy, 124(3), 3-4.

Dubochet, J., Lepault, J., Freeman, R. B. J. A., Berriman, J. A., & Homo, J. C. (1982). Electron microscopy of frozen water and aqueous solutions. Journal of Microscopy, 128(3), 219-237.

Dubochet, J., Adrian, M., Chang, J. J., Homo, J. C., Lepault, J., McDowall, A. W., & Schultz, P. (1988). Cryo-electron microscopy of vitrified specimens. Quarterly reviews of biophysics, 21(2), 129-228.

Dunkle, J. A., Wang, L., Feldman, M. B., Pulk, A., Chen, V. B., Kapral, G. J., ... & Cate, J. H. D. (2011). Structures of the bacterial ribosome in classical and hybrid states of tRNA binding. Science, 332(6032), 981-984.

Emsley, P., Lohkamp, B., Scott, W. G., & Cowtan, K. (2010). Features and development of Coot. Acta Crystallographica Section D: Biological Crystallography, 66(4), 486-501.

Erickson, H. P., & Klug, A. (1971). Measurement and compensation of defocusing and aberrations by Fourier processing of electron micrographs. Philosophical Transactions of the Royal Society of London. B, Biological Sciences, 261(837), 105-118.

Ermolenko, D. N., & Noller, H. F. (2011). mRNA translocation occurs during the second step of ribosomal intersubunit rotation. Nature structural & molecular biology, 18(4), 457-462.

Feng, B., Mandava, C. S., Guo, Q., Wang, J., Cao, W., Li, N., ... & Sanyal, S. (2014). Structural and functional insights into the mode of action of a universally conserved Obg GTPase. PLoS biology, 12(5).

Felden, B., Himeno, H., Muto, A., McCUTCHEON, J. P., Atkins, J. F., & Gesteland, R. F. (1997). Probing the structure of the Escherichia coli 10Sa RNA (tmRNA). *Rna*, *3*(1), 89-103.

Filbeck, S., Cerullo, F., Paternoga, H., Tsaprailis, G., Joazeiro, C. A., & Pfeffer, S. (2021). Mimicry of canonical translation elongation underlies alanine tail synthesis in RQC. Molecular Cell, 81(1), 104-114.

Fischer, N., Konevega, A. L., Wintermeyer, W., Rodnina, M. V., & Stark, H. (2010). Ribosome dynamics and tRNA movement by time-resolved electron cryomicroscopy. Nature, 466(7304), 329-333.

Flis, J., Holm, M., Rundlet, E. J., Loerke, J., Hilal, T., Dabrowski, M., ... & Budkevich, T. V. (2018). tRNA translocation by the eukaryotic 80S ribosome and the impact of GTP hydrolysis. Cell reports, 25(10), 2676-2688.

Frank, J. (1975). Averaging of low exposure electron micrographs of non-periodic objects. In Single-Particle Cryo-Electron Microscopy: The Path Toward Atomic Resolution: Selected Papers of Joachim Frank with Commentaries (pp. 69-72).

Frank, J. (2006). Three-dimensional electron microscopy of macromolecular assemblies: visualization of biological molecules in their native state. Oxford university press.

Frank, J., & Agrawal, R. K. (2000). A ratchet-like inter-subunit reorganization of the ribosome during translocation. Nature, 406(6793), 318–322.

Frank, J., Gao, H., Sengupta, J., Gao, N., & Taylor, D. J. (2007). The process of mRNA–tRNA translocation. Proceedings of the National Academy of Sciences, 104(50), 19671-19678.

Frank, J., Radermacher, M., Penczek, P., Zhu, J., Li, Y., Ladjadj, M., & Leith, A. (1996). SPIDER and WEB: processing and visualization of images in 3D electron microscopy and related fields. Journal of structural biology, 116(1), 190-199.

Frank, J., Verschoor, A., & Boublik, M. (1981). Computer averaging of electron micrographs of 40S ribosomal subunits. Science, 214(4527), 1353-1355.

Frank, J., Zhu, J., Penczek, P., Li, Y., Srivastava, S., Verschoor, A., ... & Agrawal, R. K. (1995). A model of protein synthesis based on cryo-electron microscopy of the E. coli ribosome. Nature, 376(6539), 441-444.

Fu, J., Hashem, Y., Wower, I., Lei, J., Liao, H. Y., Zwieb, C., ... & Frank, J. (2010). Visualizing the transfer-messenger RNA as the ribosome resumes translation. The EMBO journal, 29(22), 3819-3825.

Fu, Z., Kaledhonkar, S., Borg, A., Sun, M., Chen, B., Grassucci, R. A., ... & Frank, J. (2016). Key intermediates in ribosome recycling visualized by time-resolved cryoelectron microscopy. In Single-Particle Cryo-Electron Microscopy: The Path Toward Atomic Resolution: Selected Papers of Joachim Frank with Commentaries (pp. 516-525).

Gasteiger, E., Hoogland, C., Gattiker, A., Wilkins, M. R., Appel, R. D., & Bairoch, A. (2005). Protein identification and analysis tools on the ExPASy server. The proteomics protocols handbook, 571-607.

Gao, H., Sengupta, J., Valle, M., Korostelev, A., Eswar, N., Stagg, S. M., ... & Frank, J. (2003). Study of the structural dynamics of the E. coli 70S ribosome using real-space refinement. Cell, 113(6), 789-801.

Gao, H., Zhou, Z., Rawat, U., Huang, C., Bouakaz, L., Wang, C., ... & Sanyal, S. (2007). RF3 induces ribosomal conformational changes responsible for dissociation of class I release factors. Cell, 129(5), 929-941.

Gao, N., Zavialov, A. V., Li, W., Sengupta, J., Valle, M., Gursky, R. P., ... & Frank, J. (2005). Mechanism for the disassembly of the posttermination complex inferred from cryo-EM studies. Molecular cell, 18(6), 663-674.

Gao, Y. G., Selmer, M., Dunham, C. M., Weixlbaumer, A., Kelley, A. C., & Ramakrishnan, V. (2009). The structure of the ribosome with elongation factor G trapped in the posttranslocational state. Science, 326(5953), 694-699.

Giegé, R. (2008). Toward a more complete view of tRNA biology. Nature structural & molecular biology, 15(10), 1007-1014.

Giudice, E., & Gillet, R. (2013). The task force that rescues stalled ribosomes in bacteria. Trends in biochemical sciences, 38(8), 403-411.

Giudice, E., Macé, K., & Gillet, R. (2014). Trans-translation exposed: understanding the structures and functions of tmRNA-SmpB. Frontiers in microbiology, 5, 113.

Godefroy-Colburn, T., Wolfe, A. D., Dondon, J., Grunberg-Manago, M., Dessen, P., & Pantaloni, D. (1975). Light-scattering studies showing the effect of initiation factors on the reversible dissociation of Escherichia coli ribosomes. Journal of molecular biology, 94(3), 461-478.

Gold, L., Pribnow, D., Schneider, T., Shinedling, S., Singer, B. S., & Stormo, G. (1981). Translational initiation in prokaryotes. Annual Reviews in Microbiology, 35(1), 365-403.

Goralski, T. D., Kirimanjeswara, G. S., & Keiler, K. C. (2018). A new mechanism for ribosome rescue can recruit RF1 or RF2 to nonstop ribosomes. MBio, 9(6), e02436-18.

Grigoriadou, C., Marzi, S., Kirillov, S., Gualerzi, C. O., & Cooperman, B. S. (2007). A quantitative kinetic scheme for 70 S translation initiation complex formation. Journal of molecular biology, 373(3), 562-572.

Grigorieff, N. (2016). Frealign: an exploratory tool for single-particle cryo-EM. Methods in enzymology, 579, 191-226.

Gualerzi, C. O., Brandi, L., Caserta, E., La Teana, A., Spurio, R., Tomšic, J., & Pon, C. L. (2000). Translation initiation in bacteria. The ribosome: Structure, function, antibiotics, and cellular interactions, 475-494.

Hanawa-Suetsugu, K., Takagi, M., Inokuchi, H., Himeno, H., & Muto, A. (2002). SmpB functions in various steps of trans-translation. Nucleic acids research, 30(7), 1620-1629.

Hanszen, K. J. (1971). The optical transfer theory of the electron microscope: fundamental, principles and applications. Advanced Optical and Electron Microscopy, 4, 1.

Harauz, G., & van Heel, M. (1986). Exact filters for general geometry three-dimensional reconstruction. Optik., 73(4), 146-156.

Harms, J., Schluenzen, F., Zarivach, R., Bashan, A., Gat, S., Agmon, I., ... & Yonath, A. (2001). High resolution structure of the large ribosomal subunit from a mesophilic eubacterium. Cell, 107(5), 679-688.

Henderson, R., & Unwin, P. N. T. (1975). Three-dimensional model of purple membrane obtained by electron microscopy. Nature, 257(5521), 28-32.

Herman, C., Thévenet, D., Bouloc, P., Walker, G. C., & D'Ari, R. (1998). Degradation of carboxy-terminal-tagged cytoplasmic proteins by the Escherichia coli protease HflB (FtsH). Genes & development, 12(9), 1348-1355.

Himeno, H., Kurita, D., & Muto, A. (2014). tmRNA-mediated trans-translation as the major ribosome rescue system in a bacterial cell. Frontiers in genetics, 5, 66.

Hirashima, A., & Kaji, A. (1973). Role of elongation factor G and a protein factor on the release of ribosomes from messenger ribonucleic acid. Journal of Biological Chemistry, 248(21), 7580-7587.

Hohn, M., Tang, G., Goodyear, G., Baldwin, P. R., Huang, Z., Penczek, P. A., ... & Ludtke, S. J. (2007). SPARX, a new environment for Cryo-EM image processing. Journal of structural biology, 157(1), 47-55.

Holley, R. W., Everett, G. A., Madison, J. T., & Zamir, A. (1965). Nucleotide sequences in the yeast alanine transfer ribonucleic acid. Journal of Biological Chemistry, 240(5), 2122-2128.

Horan, L. H., & Noller, H. F. (2007). Intersubunit movement is required for ribosomal translocation. Proceedings of the National Academy of Sciences, 104(12), 4881-4885.

Hudson, C. M., Lau, B. Y., & Williams, K. P. (2014). Ends of the line for tmRNA-SmpB. Frontiers in microbiology, 5, 421.

Hussain, T., Llácer, J. L., Wimberly, B. T., Kieft, J. S., & Ramakrishnan, V. (2016). Large-scale movements of IF3 and tRNA during bacterial translation initiation. Cell, 167(1), 133-144.

Huter, P., Müller, C., Arenz, S., Beckert, B., & Wilson, D. N. (2017). Structural basis for ribosome rescue in bacteria. Trends in biochemical sciences, 42(8), 669-680.

Ibba, M., & Söll, D. (2000). Aminoacyl-tRNA synthesis. Annual review of biochemistry, 69(1), 617-650.

Inada, T. (2017). The ribosome as a platform for mRNA and nascent polypeptide quality control. Trends in biochemical sciences, 42(1), 5-15.

Ito, K., Blasbalg, R., Hussain, S. M., & Mitchell, D. G. (2000). Portal vein and its tributaries: evaluation with thin-section three-dimensional contrast-enhanced dynamic fat-suppressed MR imaging. Radiology, 215(2), 381-386.

Jakobsen, C. G., Søgaard, T. M. M., Jean-Jean, O., Frolova, L. Y., & Justesen, J. (2001). Identification of eRF3b, a Human Polypeptide Chain Release Factor with eRF3 Activity in vitroand in vivo. Molecular Biology, 35(4), 575-583.

Janssen, B. D., & Hayes, C. S. (2012). The tmRNA ribosome-rescue system. Advances in protein chemistry and structural biology, 86, 151-191.

Joazeiro, C. A. (2017). Ribosomal stalling during translation: providing substrates for ribosome-associated protein quality control. Annual review of cell and developmental biology, 33, 343-368.

Karzai, A. W., Susskind, M. M., & Sauer, R. T. (1999). SmpB, a unique RNA-binding protein essential for the peptide-tagging activity of SsrA (tmRNA). The EMBO journal, 18(13), 3793-3799.

Keiler, K. C. (2015). Mechanisms of ribosome rescue in bacteria. Nature Reviews Microbiology, 13(5), 285-297.

Keiler, K. C., & Feaga, H. A. (2014). Resolving nonstop translation complexes is a matter of life or death. Journal of bacteriology, 196(12), 2123-2130.

Keiler, K. C., Waller, P. R., & Sauer, R. T. (1996). Role of a peptide tagging system in degradation of proteins synthesized from damaged messenger RNA. Science, 271(5251), 990-993.

Kelley, L. A., Mezulis, S., Yates, C. M., Wass, M. N., & Sternberg, M. J. (2015). The Phyre2 web portal for protein modeling, prediction and analysis. Nature protocols, 10(6), 845.

Khade, P. K., Shi, X., & Joseph, S. (2013). Steric complementarity in the decoding center is important for tRNA selection by the ribosome. Journal of molecular biology, 425(20), 3778-3789.

Kim, S. H., Quigley, G. J., Suddath, F. L., McPherson, A., Sneden, D., Kim, J. J., ... & Rich, A. (1973). Three-dimensional structure of yeast phenylalanine transfer RNA: folding of the polynucleotide chain. Science, 179(4070), 285-288.

Klimova, M., Senyushkina, T., Samatova, E., Peng, B. Z., Pearson, M., Peske, F., & Rodnina, M. V. (2019). EF-G–induced ribosome sliding along the noncoding mRNA. Science advances, 5(6), eaaw9049.

Knoll, M., & Ruska, E. (1932). Das elektronenmikroskop. Zeitschrift für physik, 78(5), 318-339.

KoMINE, Y. U. R. I. K. O., Kitabatake, M., Yokogawa, T., Nishikawa, K., & Inokuchi, H. (1994). A tRNA-like structure is present in 10Sa RNA, a small stable RNA from Escherichia coli. Proceedings of the National Academy of Sciences, 91(20), 9223-9227.

Komoda, T., Sato, N. S., Phelps, S. S., Namba, N., Joseph, S., & Suzuki, T. (2006). The A-site finger in 23 S rRNA acts as a functional attenuator for translocation. Journal of Biological Chemistry, 281(43), 32303-32309.

Konevega, A. L., Fischer, N., Semenkov, Y. P., Stark, H., Wintermeyer, W., & Rodnina, M. V. (2007). Spontaneous reverse movement of mRNA-bound tRNA through the ribosome. Nature structural & molecular biology, 14(4), 318-324.

Konno, T., Kurita, D., Takada, K., Muto, A., & Himeno, H. (2007). A functional interaction of SmpB with tmRNA for determination of the resuming point of trans-translation. Rna, 13(10), 1723-1731.

Koo, B. M., Kritikos, G., Farelli, J. D., Todor, H., Tong, K., Kimsey, H., ... & Gross, C. A. (2017). Construction and analysis of two genome-scale deletion libraries for Bacillus subtilis. Cell systems, 4(3), 291-305.

Korostelev, A., Ermolenko, D. N., & Noller, H. F. (2008). Structural dynamics of the ribosome. Current opinion in chemical biology, 12(6), 674-683.

Korostelev, A., Trakhanov, S., Laurberg, M., & Noller, H. F. (2006). Crystal structure of a 70S ribosome-tRNA complex reveals functional interactions and rearrangements. Cell, 126(6), 1065-1077.

Koukos, P. I., & Bonvin, A. M. J. J. (2019). Integrative modelling of biomolecular complexes. Journal of molecular biology.

Kozak, M. (1999). Initiation of translation in prokaryotes and eukaryotes. Gene, 234(2), 187-208.

Kozak, M. (2005). Regulation of translation via mRNA structure in prokaryotes and eukaryotes. Gene, 361, 13-37.

Krüger, D. M., Neubacher, S., & Grossmann, T. N. (2018). Protein–RNA interactions: structural characteristics and hotspot amino acids. RNA, 24(11), 1457-1465.

Kucukelbir, A., Sigworth, F. J., & Tagare, H. D. (2014). Quantifying the local resolution of cryo-EM density maps. Nature methods, 11(1), 63-65.

Kühlbrandt, W. (2014). Microscopy: cryo-EM enters a new era. Elife, 3, e03678.

Kühlbrandt, W. (2014). The resolution revolution. Science, 343(6178), 1443-1444.

Kurita, D., Muto, A., & Himeno, H. (2010). Role of the C-terminal tail of SmpB in the early stage of trans-translation. Rna, 16(5), 980-990.

Kurita, D., Sasaki, R., Muto, A., & Himeno, H. (2007). Interaction of SmpB with ribosome from directed hydroxyl radical probing. Nucleic acids research, 35(21), 7248-7255.

Lagerkvist, U. L. F. (1978). " Two out of three": an alternative method for codon reading. Proceedings of the National Academy of Sciences, 75(4), 1759-1762.

Lancaster, L., & Noller, H. F. (2005). Involvement of 16S rRNA nucleotides G1338 and A1339 in discrimination of initiator tRNA. Molecular cell, 20(4), 623-632.

Lee, S., Ishii, M., Tadaki, T., Muto, A., & Himeno, H. (2001). Determinants on tmRNA for initiating efficient and precise trans-translation: some mutations upstream of the tag-encoding sequence of Escherichia coli tmRNA shift the initiation point of trans-translation in vitro. Rna, 7(7), 999-1012.

Li, X., Mooney, P., Zheng, S., Booth, C. R., Braunfeld, M. B., Gubbens, S., ... & Cheng, Y. (2013). Electron counting and beam-induced motion correction enable near-atomic-resolution single-particle cryo-EM. Nature methods, 10(6), 584-590.

Lin, J., Gagnon, M. G., Bulkley, D., & Steitz, T. A. (2015). Conformational changes of elongation factor G on the ribosome during tRNA translocation. Cell, 160(1-2), 219-227.

Lindahl, M., Svensson, L. A., Liljas, A., Sedelnikova, S. E., Eliseikina, I. A., Fomenkova, N. P., ... & Muranova, T. A. (1994). Crystal structure of the ribosomal protein S6 from Thermus thermophilus. The EMBO Journal, 13(6), 1249-1254.

Liu, Q., & Fredrick, K. (2016). Intersubunit bridges of the bacterial ribosome. Journal of molecular biology, 428(10), 2146-2164.

Loerke, J., Giesebrecht, J., & Spahn, C. M. (2010). Multiparticle cryo-EM of ribosomes. Methods in enzymology, 483, 161-177.

Lorenz, C., Lünse, C. E., & Mörl, M. (2017). tRNA modifications: impact on structure and thermal adaptation. Biomolecules, 7(2), 35.

Lytvynenko, I., Paternoga, H., Thrun, A., Balke, A., Müller, T. A., Chiang, C. H., ... & Joazeiro, C. A. (2019). Alanine tails signal proteolysis in bacterial ribosome-associated quality control. Cell, 178(1), 76-90.

Lyumkis, D., Brilot, A. F., Theobald, D. L., & Grigorieff, N. (2013). Likelihood-based classification of cryo-EM images using FREALIGN. Journal of structural biology, 183(3), 377-388.

Lyumkis, D., dos Passos, D. O., Tahara, E. B., Webb, K., Bennett, E. J., Vinterbo, S., ... & Joazeiro, C. A. (2014). Structural basis for translational surveillance by the large ribosomal subunit-associated protein quality control complex. Proceedings of the National Academy of Sciences, 111(45), 15981-15986.

Malhotra, S., Träger, S., Dal Peraro, M., & Topf, M. (2019). Modelling structures in cryo-EM maps. Current opinion in structural biology, 58, 105-114.

Martemyanov, K. A., & Gudkov, A. T. (2000). Domain III of elongation factor G from Thermus thermophilus is essential for induction of GTP hydrolysis on the ribosome. Journal of Biological Chemistry, 275(46), 35820-35824.

Mastronarde, D. N. (2005). Automated electron microscope tomography using robust prediction of specimen movements. Journal of structural biology, 152(1), 36-51.

McMullan, G., Faruqi, A. R., Clare, D., & Henderson, R. (2014). Comparison of optimal performance at 300 keV of three direct electron detectors for use in low dose electron microscopy. Ultramicroscopy, 147, 156-163.

McMullan, G., Faruqi, A. R., Henderson, R., Guerrini, N., Turchetta, R., Jacobs, A., & Van Hoften, G. (2009). Experimental observation of the improvement in MTF from backthinning a CMOS direct electron detector. Ultramicroscopy, 109(9), 1144-1147.

Milazzo, A. C., Cheng, A., Moeller, A., Lyumkis, D., Jacovetty, E., Polukas, J., ... & Potter, C. S. (2011). Initial evaluation of a direct detection device detector for single particle cryo-electron microscopy. Journal of structural biology, 176(3), 404-408.

Miller, M. R., & Buskirk, A. R. (2014). An unusual mechanism for EF-Tu activation during tmRNA-mediated ribosome rescue. Rna, 20(2), 228-235.

Milne, J. L., Borgnia, M. J., Bartesaghi, A., Tran, E. E., Earl, L. A., Schauder, D. M., ... & Subramaniam, S. (2013). Cryo-electron microscopy–a primer for the non-microscopist. The FEBS journal, 280(1), 28-45.

Milón, P., & Rodnina, M. V. (2012). Kinetic control of translation initiation in bacteria. Critical reviews in biochemistry and molecular biology, 47(4), 334-348.

Milon, P., Carotti, M., Konevega, A. L., Wintermeyer, W., Rodnina, M. V., & Gualerzi, C. O. (2010). The ribosome-bound initiation factor 2 recruits initiator tRNA to the 30S initiation complex. EMBO reports, 11(4), 312-316.

Milon, P., Konevega, A. L., Gualerzi, C. O., & Rodnina, M. V. (2008). Kinetic checkpoint at a late step in translation initiation. Molecular cell, 30(6), 712-720.

Moazed, D., & Noller, H. F. (1989). Intermediate states in the movement of transfer RNA in the ribosome. Nature, 342(6246), 142-148.

Moazed, D., Samaha, R. R., Gualerzi, C., & Noller, H. F. (1995). Specific protection of 16 S rRNA by translationalinitiation factors. Journal of molecular biology, 248(2), 207-210.

Moffat, J. G., Tate, W. P., & Lovett, P. S. (1994). The leader peptides of attenuation-regulated chloramphenicol resistance genes inhibit translational termination. Journal of bacteriology, 176(22), 7115-7117.

Mohan, S., & Noller, H. F. (2017). Recurring RNA structural motifs underlie the mechanics of L1 stalk movement. Nature communications, 8(1), 1-11.

Moore, S. D., & Sauer, R. T. (2007). The tmRNA system for translational surveillance and ribosome rescue. Annu. Rev. Biochem., 76, 101-124.

Müller, C., Crowe-McAuliffe, C., & Wilson, D. N. (2021). Ribosome Rescue Pathways in Bacteria. Frontiers in Microbiology, 12, 558.

Munro, J. B., Altman, R. B., O'Connor, N. & Blanchard, S. C. Identification of two distinct hybrid state intermediates onthe ribosome. Mol. Cell25, 505–517(2007).

Munro, J. B., Wasserman, M. R., Altman, R. B., Wang, L., & Blanchard, S. C. (2010). Correlated conformational events in EF-G and the ribosome regulate translocation. Nature structural & molecular biology, 17(12), 1470-1477.

Munro, J.B., Sanbonmatsu, K.Y., Spahn, C.M.T., and Blanchard, S.C. (2009a). Navigating the ribosome's metastable energy landscape. Trends Biochem. Sci. 34, 390–400.

Musyoki, A. M., Shi, Z., Xuan, C., Lu, G., Qi, J., Gao, F., ... & Liu, C. (2016). Structural and functional analysis of an anchorless fibronectin-binding protein FBPS from Gram-positive bacterium Streptococcus suis. Proceedings of the National Academy of Sciences, 113(48), 13869-13874.

Naganuma, M., Sekine, S. I., Chong, Y. E., Guo, M., Yang, X. L., Gamper, H., ... & Yokoyama, S. (2014). The selective tRNA aminoacylation mechanism based on a single G• U pair. Nature, 510(7506), 507.

Nakane, T., Kotecha, A., Sente, A., McMullan, G., Masiulis, S., Brown, P. M., ... & Scheres, S. H. (2020). Single-particle cryo-EM at atomic resolution. Nature, 587(7832), 152-156.

Nameki, N., Tadaki, T., Himeno, H., & Muto, A. (2000). Three of four pseudoknots in tmRNA are interchangeable and are substitutable with single-stranded RNAs. FEBS letters, 470(3), 345-349.

Neubauer, C., Gillet, R., Kelley, A. C., & Ramakrishnan, V. (2012). Decoding in the absence of a codon by tmRNA and SmpB in the ribosome. Science, 335(6074), 1366-1369.

Nguyen, K., & Whitford, P. C. (2016). Steric interactions lead to collective tilting motion in the ribosome during mRNA–tRNA translocation. Nature communications, 7(1), 1-9.

Nikolay, R., Hilal, T., Qin, B., Mielke, T., Bürger, J., Loerke, J., ... & Spahn, C. M. (2018). Structural visualization of the formation and activation of the 50S ribosomal subunit during in vitro reconstitution. Molecular cell, 70(5), 881-893.

Nissen, P., Hansen, J., Ban, N., Moore, P. B., & Steitz, T. A. (2000). The structural basis of ribosome activity in peptide bond synthesis. Science, 289(5481), 920-930.

Nissen, P., Kjeldgaard, M., Thirup, S., Polekhina, G., Reshetnikova, L., Clark, B. F., & Nyborg, J. (1995). Crystal structure of the ternary complex of Phe-tRNAPhe, EF-Tu, and a GTP analog. Science, 270(5241), 1464-1472.

Noller, H. F., Hoffarth, V., & Zimniak, L. (1992). Unusual resistance of peptidyl transferase to protein extraction procedures. Science, 256(5062), 1416-1419.

Nonin-Lecomte, S., Germain-Amiot, N., Gillet, R., Hallier, M., Ponchon, L., Dardel, F., & Felden, B. (2009). Ribosome hijacking: a role for small protein B during trans-translation. EMBO reports, 10(2), 160-165.

Ogle, J. M., Brodersen, D. E., Clemons, W. M., Tarry, M. J., Carter, A. P., & Ramakrishnan, V. (2001). Recognition of cognate transfer RNA by the 30S ribosomal subunit. Science, 292(5518), 897-902.

Ogle, J. M., Murphy IV, F. V., Tarry, M. J., & Ramakrishnan, V. (2002). Selection of tRNA by the ribosome requires a transition from an open to a closed form. Cell, 111(5), 721-732.

Orlova, E. V., & Saibil, H. R. (2011). Structural analysis of macromolecular assemblies by electron microscopy. Chemical reviews, 111(12), 7710-7748.

Palade, G. E. (1955). A small particulate component of the cytoplasm. The Journal of Cell Biology, 1(1), 59-68.

Pape, T., Wintermeyer, W., & Rodnina, M. V. (1998). Complete kinetic mechanism of elongation factor Tu-dependent binding of aminoacyl-tRNA to the A site of the E. coli ribosome. The EMBO journal, 17(24), 7490-7497.

Passmore, L. A., Schmeing, T. M., Maag, D., Applefield, D. J., Acker, M. G., Algire, M. A., ... & Ramakrishnan, V. (2007). The eukaryotic translation initiation factors eIF1 and eIF1A induce an open conformation of the 40S ribosome. Molecular cell, 26(1), 41-50.

Penczek, P. A. (2010). Image restoration in cryo-electron microscopy. Methods in enzymology, 482, 35-72.

Penczek, P. A., Frank, J., & Spahn, C. M. (2006). A method of focused classification, based on the bootstrap 3D variance analysis, and its application to EF-G-dependent translocation. Journal of structural biology, 154(2), 184-194.

Penczek, P. A., Kimmel, M., & Spahn, C. M. (2011). Identifying conformational states of macromolecules by eigen-analysis of resampled cryo-EM images. Structure, 19(11), 1582-1590.

Peske, F., Kuhlenkoetter, S., Rodnina, M. V., & Wintermeyer, W. (2014). Timing of GTP binding and hydrolysis by translation termination factor RF3. Nucleic acids research, 42(3), 1812-1820.

Peske, F., Rodnina, M. V., & Wintermeyer, W. (2005). Sequence of steps in ribosome recycling as defined by kinetic analysis. Molecular cell, 18(4), 403-412.

Petry, S., Weixlbaumer, A., & Ramakrishnan, V. (2008). The termination of translation. Current opinion in structural biology, 18(1), 70-77.

Pettersen, E. F., Goddard, T. D., Huang, C. C., Couch, G. S., Greenblatt, D. M., Meng, E. C., & Ferrin, T. E. (2004). UCSF Chimera—a visualization system for exploratory research and analysis. Journal of computational chemistry, 25(13), 1605-1612.

Prabhakar, A., Capece, M. C., Petrov, A., Choi, J., & Puglisi, J. D. (2017). Post-termination ribosome intermediate acts as the gateway to ribosome recycling. Cell reports, 20(1), 161-172.

Punjani, A., Rubinstein, J. L., Fleet, D. J., & Brubaker, M. A. (2017). cryoSPARC: algorithms for rapid unsupervised cryo-EM structure determination. Nature methods, 14(3), 290-296.

Rae, C. D., Gordiyenko, Y., & Ramakrishnan, V. (2019). How a circularized tmRNA moves through the ribosome. Science, 363(6428), 740-744.

Ramadoss, N. S., Alumasa, J. N., Cheng, L., Wang, Y., Li, S., Chambers, B. S., Chang, H., Chatterjee, A. K., Brinker, A., Engels, I. H., & Keiler, K. C. (2013). Small molecule inhibitors of trans-translation have broad-spectrum antibiotic activity. Proceedings of the National Academy of Sciences of the United States of America, 110(25), 10282–10287.

Ramrath, D. J., Yamamoto, H., Rother, K., Wittek, D., Pech, M., Mielke, T., ... & Spahn, C. M. (2012). The complex of tmRNA–SmpB and EF-G on translocating ribosomes. Nature, 485(7399), 526-529.

Ramrath, D.J.F., Lancaster, L., Sprink, T., Mielke, T., Loerke, J., Noller, H.F., and Spahn, C.M.T. (2013). Visualization of two transfer RNAs trapped in transit during elongation factor G-mediated translocation. Proc. Natl. Acad. Sci. U. S. A. 110, 20964–20969.

Ratje, A. H., Loerke, J., Mikolajka, A., Brünner, M., Hildebrand, P. W., Starosta, A. L., ... & Whitford, P. C. (2010). Head swivel on the ribosome facilitates translocation by means of intra-subunit tRNA hybrid sites. Nature, 468(7324), 713-716.

Rodnina, M. V. (2018). Translation in prokaryotes. Cold Spring Harbor perspectives in biology, 10(9), a032664.

Rohou, A., & Grigorieff, N. (2015). CTFFIND4: Fast and accurate defocus estimation from electron micrographs. Journal of structural biology, 192(2), 216-221.

Rose, A. (1946). A unified approach to the performance of photographic film, television pickup tubes, and the human eye. Journal of the Society of Motion Picture Engineers, 47(4), 273-294.

Rosenthal, P. B., & Henderson, R. (2003). Optimal determination of particle orientation, absolute hand, and contrast loss in single-particle electron cryomicroscopy. Journal of molecular biology, 333(4), 721-745.

Rundlet, E. J., Holm, M., Schacherl, M., Natchiar, S. K., Altman, R. B., Spahn, C. M., ... & Blanchard, S. C. (2021). Structural basis of early translocation events on the ribosome. Nature, 595(7869), 741-745.

Salsi, E., Farah, E., & Ermolenko, D. N. (2016). EF-G activation by phosphate analogs. Journal of molecular biology, 428(10), 2248-2258.

Sato, A., Kobayashi, G., Hayashi, H., Yoshida, H., Wada, A., Maeda, M., ... & Wada, C. (2005). The GTP binding protein Obg homolog ObgE is involved in ribosome maturation. Genes to Cells, 10(5), 393-408.

Savelsbergh, A., Katunin, V. I., Mohr, D., Peske, F., Rodnina, M. V., & Wintermeyer, W. (2003). An elongation factor G-induced ribosome rearrangement precedes tRNA-mRNA translocation. Molecular cell, 11(6), 1517-1523.

Savelsbergh, A., Rodnina, M. V., & Wintermeyer, W. (2009). Distinct functions of elongation factor G in ribosome recycling and translocation. Rna, 15(5), 772-780.

Scheres, S. H. (2012). RELION: implementation of a Bayesian approach to cryo-EM structure determination. Journal of structural biology, 180(3), 519-530.

Scheres, S. H. (2015). Semi-automated selection of cryo-EM particles in RELION-1.3. Journal of structural biology, 189(2), 114-122.

Scheres, S. H. (2016). Processing of structurally heterogeneous cryo-EM data in RELION. Methods in enzymology, 579, 125-157.

Schluenzen, F., Tocilj, A., Zarivach, R., Harms, J., Gluehmann, M., Janell, D., ... & Yonath, A. (2000). Structure of functionally activated small ribosomal subunit at 3.3 Å resolution. cell, 102(5), 615-623.

Schmeing, T. M., & Ramakrishnan, V. (2009). What recent ribosome structures have revealed about the mechanism of translation. Nature, 461(7268), 1234-1242.

Schmeing, T. M., Huang, K. S., Strobel, S. A., & Steitz, T. A. (2005). An induced-fit mechanism to promote peptide bond formation and exclude hydrolysis of peptidyl-tRNA. Nature, 438(7067), 520-524.

Schmeing, T. M., Huang, K. S., Kitchen, D. E., Strobel, S. A., & Steitz, T. A. (2005a). Structural insights into the roles of water and the 2′ hydroxyl of the P site tRNA in the peptidyl transferase reaction. *Molecular cell*, *20*(3), 437-448.

Schmeing, T. M., Moore, P. B., & Steitz, T. A. (2003). Structures of deacylated tRNA mimics bound to the E site of the large ribosomal subunit. Rna, 9(11), 1345-1352.

Schmid, M. F., Sherman, M. B., Matsudaira, P., Tsuruta, H., & Chiu, W. (1999). Scaling structure factor amplitudes in electron cryomicroscopy using X-ray solution scattering. Journal of structural biology, 128(1), 51-57.

Schmitt, E., Panvert, M., Blanquet, S., & Mechulam, Y. (1998). Crystal structure of methionyl-tRNAfMet transformylase complexed with the initiator formyl-methionyl-tRNAfMet. *The EMBO Journal*, *17*(23), 6819-6826.

Schröder, R. R. (1992). Zero-loss energy-filtered imaging of frozen-hydrated proteins: model calculations and implications for future developments. Journal of microscopy, 166(3), 389-400.

Schuette, J. C., Murphy IV, F. V., Kelley, A. C., Weir, J. R., Giesebrecht, J., Connell, S. R., ... & Spahn, C. M. (2009). GTPase activation of elongation factor EF-Tu by the ribosome during decoding. The EMBO journal, 28(6), 755-765.

Schuwirth, B. S., Borovinskaya, M. A., Hau, C. W., Zhang, W., Vila-Sanjurjo, A., Holton, J. M., & Cate, J. H. D. (2005). Structures of the bacterial ribosome at 3.5 Å resolution. Science, 310(5749), 827-834.

Selmer, M., Dunham, C. M., Murphy, F. V., Weixlbaumer, A., Petry, S., Kelley, A. C., ... & Ramakrishnan, V. (2006). Structure of the 70S ribosome complexed with mRNA and tRNA. Science, 313(5795), 1935-1942.

Semenkov, Y. P., Rodnina, M. V., & Wintermeyer, W. (2000). Energetic contribution of tRNA hybrid state formation to translocation catalysis on the ribosome. Nature structural biology, 7(11), 1027-1031.

Seo, H. S., Abedin, S., Kamp, D., Wilson, D. N., Nierhaus, K. H., & Cooperman, B. S. (2006). EF-G-dependent GTPase on the ribosome. Conformational change and fusidic acid inhibition. Biochemistry, 45(8), 2504-2514.

Seo, H. S., Kiel, M., Pan, D., Raj, V. S., Kaji, A., & Cooperman, B. S. (2004). Kinetics and thermodynamics of RRF, EF-G, and thiostrepton interaction on the Escherichia coli ribosome. Biochemistry, 43(40), 12728-12740.

Sergiev, P. V., Bogdanov, A. A., & Dontsova, O. A. (2005). How can elongation factors EF-G and EF-Tu discriminate the functional state of the ribosome using the same binding site?. FEBS letters, 579(25), 5439-5442.

Shaikh, T. R., Gao, H., Baxter, W. T., Asturias, F. J., Boisset, N., Leith, A., & Frank, J. (2008). SPIDER image processing for single-particle reconstruction of biological macromolecules from electron micrographs. Nature protocols, 3(12), 1941-1974.

Shao, S., Brown, A., Santhanam, B., & Hegde, R. S. (2015). Structure and assembly pathway of the ribosome quality control complex. Molecular Cell, 57(3), 433-444.

Shao, X., & Grishin, N. V. (2000). Common fold in helix–hairpin–helix proteins. Nucleic Acids Research, 28(14), 2643-2650.

Shareghi, P., Wang, Y., Malmberg, R., & Cai, L. (2012, June). Simultaneous prediction of RNA secondary structure and helix coaxial stacking. In BMC genomics (Vol. 13, No. S3, p. S7). BioMed Central.

Shen, P. S., Park, J., Qin, Y., Li, X., Parsawar, K., Larson, M. H., ... & Brandman, O. (2015). Rqc2p and 60S ribosomal subunits mediate mRNA-independent elongation of nascent chains. Science, 347(6217), 75-78.

Shimokawa-Chiba, N., Müller, C., Fujiwara, K., Beckert, B., Ito, K., Wilson, D. N., & Chiba, S. (2019). Release factor-dependent ribosome rescue by BrfA in the Gram-positive bacterium Bacillus subtilis. Nature communications, 10(1), 1-14.

Shine, J., & Dalgarno, L. (1974). The 3’-terminal sequence of Escherichia coli 16S ribosomal RNA: complementarity to nonsense triplets and ribosome binding sites. Proceedings of the National Academy of Sciences, 71(4), 1342-1346.

Shoemaker, C. J., & Green, R. (2012). Translation drives mRNA quality control. Nature structural & molecular biology, 19(6), 594.

Shoji, S., Walker, S. E., & Fredrick, K. (2006). Reverse translocation of tRNA in the ribosome. Molecular cell, 24(6), 931-942.

Shoji, S., Walker, S. E., & Fredrick, K. (2009). Ribosomal translocation: one step closer to the molecular mechanism. ACS chemical biology, 4(2), 93-107.

Sievers, A., Beringer, M., Rodnina, M. V., & Wolfenden, R. (2004). The ribosome as an entropy trap. Proceedings of the National Academy of Sciences, 101(21), 7897-7901.

Slonczewski, Joan; Foster, John Watkins (2009). Microbiology: An Evolving Science. New York: W.W. Norton. ISBN 9780393978575.

Sohmen, D., Chiba, S., Shimokawa-Chiba, N., Innis, C. A., Berninghausen, O., Beckmann, R., ... & Wilson, D. N. (2015). Structure of the Bacillus subtilis 70S ribosome reveals the basis for species-specific stalling. Nature communications, 6, 6941.

Sokabe, M., & Fraser, C. S. (2017). A helicase-independent activity of eIF4A in promoting mRNA recruitment to the human ribosome. Proceedings of the National Academy of Sciences, 114(24), 6304-6309.

Spahn, C. M., & Penczek, P. A. (2009). Exploring conformational modes of macromolecular assemblies by multiparticle cryo-EM. Current opinion in structural biology, 19(5), 623-631.

Spahn, C. M., Gomez-Lorenzo, M. G., Grassucci, R. A., Jørgensen, R., Andersen, G. R., Beckmann, R., ... & Frank, J. (2004). Domain movements of elongation factor eEF2 and the eukaryotic 80S ribosome facilitate tRNA translocation. The EMBO journal, 23(5), 1008-1019.

Spahn, C.M.T., Gomez-Lorenzo, M.G., Grassucci, R.A., Jørgensen, R., Andersen, G.R., Beckmann, R., Penczek, P.A., Ballesta, J.P.G., and Frank, J. (2004a). Domain movements of elongation factor eEF2 and the eukaryotic 80S ribosome facilitate tRNA translocation. EMBO J. 23, 1008–1019.

Spahn, C.M.T., Jan, E., Mulder, A., Grassucci, R.A., Sarnow, P., and Frank, J. (2004b). Cryo-EM visualization of a viral internal ribosome entry site bound to human ribosomes: the IRES functions as an RNA-based translation factor. Cell 118, 465–475.

Spiegel, P. C., Ermolenko, D. N., & Noller, H. F. (2007). Elongation factor G stabilizes the hybrid-state conformation of the 70S ribosome. Rna, 13(9), 1473-1482.

Spirin, A. S. (1985). Ribosomal translocation: facts and models. Progress in nucleic acid research and molecular biology, 32, 75-114.

Sprink, T., Ramrath, D. J., Yamamoto, H., Yamamoto, K., Loerke, J., Ismer, J., ... & Spahn, C. M. (2016). Structures of ribosome-bound initiation factor 2 reveal the mechanism of subunit association. Science advances, 2(3), e1501502.

Stark, H., Mueller, F., Orlova, E. V., Schatz, M., Dube, P., Erdemir, T., ... & van Heel, M. (1995). The 70S Escherichia coli ribosome at 23 Å resolution: fitting the ribosomal RNA. Structure, 3(8), 815-821.

Stark, H., Rodnina, M. V., Rinke-Appel, J., Brimacombe, R., Wintermeyer, W., & van Heel, M. (1997). Visualization of elongation factor Tu on the Escherichia coli ribosome. Nature, 389(6649), 403-406.

Suloway, C., Pulokas, J., Fellmann, D., Cheng, A., Guerra, F., Quispe, J., ... & Carragher, B. (2005). Automated molecular microscopy: the new Leginon system. Journal of structural biology, 151(1), 41-60.

Sun, J., & Li, H. (2010). How to operate a cryo-electron microscope. Methods in enzymology, 481, 231-249.

Takyar, S., Hickerson, R. P., & Noller, H. F. (2005). mRNA helicase activity of the ribosome. Cell, 120(1), 49-58.

Tang, G., Peng, L., Baldwin, P. R., Mann, D. S., Jiang, W., Rees, I., & Ludtke, S. J. (2007). EMAN2: an extensible image processing suite for electron microscopy. Journal of structural biology, 157(1), 38-46.

Taylor, K. A., & Glaeser, R. M. (1974). Electron diffraction of frozen, hydrated protein crystals. Science, 186(4168), 1036-1037.

Thon, F. (1966). Zur Defokussierungsabhängigkeit des Phasenkontrastes bei der elektronenmikroskopischen Abbildung. Zeitschrift für Naturforschung A, 21(4), 476-478.

Uemura, S., Dorywalska, M., Lee, T. H., Kim, H. D., Puglisi, J. D., & Chu, S. (2007). Peptide bond formation destabilizes Shine–Dalgarno interaction on the ribosome. Nature, 446(7134), 454-457.

Ushida, C., Himeno, H., Watanabe, T., & Muto, A. (1994). tRNA-like structures in 10Sa RNAs of Mycoplasma capricolum and Bacillus subtilis. Nucleic acids research, 22(16), 3392-3396.

Valle, M., Sengupta, J., Swami, N. K., Grassucci, R. A., Burkhardt, N., Nierhaus, K. H., ... & Frank, J. (2002). Cryo-EM reveals an active role for aminoacyl-tRNA in the accommodation process. The EMBO journal, 21(13), 3557-3567.

Valle, M., Zavialov, A., Sengupta, J., Rawat, U., Ehrenberg, M., & Frank, J. (2003). Locking and unlocking of ribosomal motions. In Single-Particle Cryo-Electron Microscopy: The Path Toward Atomic Resolution: Selected Papers of Joachim Frank with Commentaries (pp. 347-358).

Verma, R., Oania, R. S., Kolawa, N. J., & Deshaies, R. J. (2013). Cdc48/p97 promotes degradation of aberrant nascent polypeptides bound to the ribosome. elife, 2, e00308.

Voorhees, R. M., Weixlbaumer, A., Loakes, D., Kelley, A. C., & Ramakrishnan, V. (2009). Insights into substrate stabilization from snapshots of the peptidyl transferase center of the intact 70S ribosome. Nature structural & molecular biology, 16(5), 528-533.

Wade, R. H. (1992). A brief look at imaging and contrast transfer. Ultramicroscopy, 46(1-4), 145-156.

Wallin, I. E. (1922). On the nature of mitochondria. I. Observations on mitochondria staining methods applied to bacteria. II. Reactions of bacteria to chemical treatment. American Journal of Anatomy, 30(2), 203-229.

Wasserman, M. R., Alejo, J. L., Altman, R. B., & Blanchard, S. C. (2016). Multiperspective smFRET reveals rate-determining late intermediates of ribosomal translocation. Nature structural & molecular biology, 23(4), 333-341.

Weis, F., Bron, P., Giudice, E., Rolland, J. P., Thomas, D., Felden, B., & Gillet, R. (2010). tmRNA–SmpB: a journey to the centre of the bacterial ribosome. The EMBO journal, 29(22), 3810-3818.

Weis, F., Bron, P., Rolland, J. P., Thomas, D., Felden, B., & Gillet, R. (2010). Accommodation of tmRNA–SmpB into stalled ribosomes: A cryo-EM study. Rna, 16(2), 299-306.

Whitford, P. C., Geggier, P., Altman, R. B., Blanchard, S. C., Onuchic, J. N., & Sanbonmatsu, K. Y. (2010). Accommodation of aminoacyl-tRNA into the ribosome involves reversible excursions along multiple pathways. Rna, 16(6), 1196-1204.

Wiener, N. (1964). Extrapolation, interpolation, and smoothing of stationary time series: with engineering applications (Vol. 8). Cambridge, MA: MIT press.

Wilson, D. N., & Nierhaus, K. H. (2007). The weird and wonderful world of bacterial ribosome regulation. Critical reviews in biochemistry and molecular biology, 42(3), 187-219.

Wimberly, B. T., Brodersen, D. E., Clemons, W. M., Morgan-Warren, R. J., Carter, A. P., Vonrhein, C., ... & Ramakrishnan, V. (2000). Structure of the 30S ribosomal subunit. Nature, 407(6802), 327-339.

Yip, K. M., Fischer, N., Paknia, E., Chari, A., & Stark, H. (2020). Atomic-resolution protein structure determination by cryo-EM. Nature, 587(7832), 157-161.

Yusupov, M. M., Yusupova, G. Z., Baucom, A., Lieberman, K., Earnest, T. N., Cate, J. H. D., & Noller, H. F. (2001). Crystal structure of the ribosome at 5.5 Å resolution. Science, 292(5518), 883-896.

Yusupova, G., Jenner, L., Rees, B., Moras, D., & Yusupov, M. (2006). Structural basis for messenger RNA movement on the ribosome. Nature, 444(7117), 391-394.

Zavialov, A. V., Buckingham, R. H., & Ehrenberg, M. (2001). A posttermination ribosomal complex is the guanine nucleotide exchange factor for peptide release factor RF3. Cell, 107(1), 115-124.

Zavialov, A. V., Mora, L., Buckingham, R. H., & Ehrenberg, M. (2002). Release of peptide promoted by the GGQ motif of class 1 release factors regulates the GTPase activity of RF3. Molecular cell, 10(4), 789-798.

Zhang, K. (2016). Gctf: Real-time CTF determination and correction. Journal of structural biology, 193(1), 1-12.

Zhang, K., Li, M., & Sun, F. (2011). Gautomatch: an efficient and convenient gpu-based automatic particle selection program. Unpublished manuscript.

Zhang, Y., Lu, P. H., Rotunno, E., Troiani, F., van Schayck, J. P., Tavabi, A. H., ... & Ravelli, R. G. B. (2021). Single-particle cryo-EM: alternative schemes to improve dose efficiency. Journal of Synchrotron Radiation, 28(5).

Zheng, S. Q., Palovcak, E., Armache, J. P., Verba, K. A., Cheng, Y., & Agard, D. A. (2017). MotionCor2: anisotropic correction of beam-induced motion for improved cryo-electron microscopy. Nature methods, 14(4), 331-332.

Zhou, J., Lancaster, L., Donohue, J. P., & Noller, H. F. (2013). Crystal structures of EF-G–ribosome complexes trapped in intermediate states of translocation. Science, 340(6140).

Zhou, J., Lancaster, L., Donohue, J. P., & Noller, H. F. (2014). How the ribosome hands the A-site tRNA to the P site during EF-G–catalyzed translocation. Science, 345(6201), 1188-1191.

Zhou, J., Lancaster, L., Trakhanov, S., and Noller, H.F. (2012). Crystal structure of release factor RF3 trapped in the GTP state on a rotated conformation of the ribosome. RNA 18, 230–240.

Zhu, J., Penczek, P. A., Schröder, R., & Frank, J. (1997). Three-dimensional reconstruction with contrast transfer function correction from energy-filtered cryoelectron micrographs: procedure and application to the 70sescherichia coliribosome. Journal of structural biology, 118(3), 197-219.

8 Publication

Lytvynenko, I., Paternoga, H., Thrun, A., Balke, A., Müller, T. A., Chiang, C. H., ... & Joazeiro, C. A. (2019). **Alanine tails signal proteolysis in bacterial ribosome-associated quality control**. *Cell*, *178*(1), 76-90.